QUANTIFICATION OF WATER MASS TRANSFORMATIONS IN THE ARKONA SEA – IMPACT OF OFFSHORE WIND FARMS

QUANTAS-OFF

Final Report

Authors:

Hans Burchard[1], Alfred Leder[2], Mark Markofsky[3],

Richard Hofmeister[1], Frank Hüttmann[2], Hans Ulrich Lass[1],

Jan-Erik Melskotte[2], Peter Menzel[1,2], Volker Mohrholz[1],

Hannes Rennau[1], Stefan Schimmels[3],

Artur Szewczyk[1], and Lars Umlauf[1]

1. Leibniz Institute for Baltic Sea Research Institute Warnemünde at the University of Rostock
2. Chair of Fluid Mechanics, University of Rostock
3. Institut of Fluid Mechanics and Environmental Physics in Civil Engineering, Leibniz Universität Hannover

Warnemünde, Rostock & Hannover, June 2010

Federal Ministry for the
Environment, Nature Conservation
and Nuclear Safety

The project onto which this report is based has been funded by the German Federal Ministry for the Environment, Nature Conservation and Nuclear Safety under project reference numbers 0329957, 0329957A and 0329957B. The authors are responsible for the contents of this publication.

Contents

Chapter 1

Introduction

1.1 Baltic inflow events and their ecological role

Due to its topography with narrow and shallow connections to the world ocean (via Kattegat, Skagerrak and the North Sea) in the western part and with its relatively deep basins further east (see Fig. 1.1), the Baltic Sea ecosystem is specifically vulnerable. The natural oceanographic boundaries between the Kattegat and the Baltic Sea Proper are the Darss Sill (0.8 km^2 cross section and 18 m sill depth) and the Drogden Sill (0.1 km^2 cross section; 7 m sill depth) - see Fig. 1.2.

The first of a chain of a Baltic Sea basins looking from the west is the Arkona Basin (AB). To enter AB water has to pass through the Drogden Sill or through the Darss Sill (see Fig. 1.2). In the western part of the basin there is a shoal area, Kriegers Flak, with depths from 17 to 40 meters. The inflowing waters normally tend to flow around the Kriegers Flak both along the northern and southern flanks. The AB is 45 meters deep in its deepest place and is connected with the Bornholm Basin (BB) by the Bornholm Channel. The BB has an almost round shape with a diameter of about 80 km and a maximum depth of about 100 m. East of the BB there is a Słupsk Furrow. It is a channel like basin with width of nearly 80 km in the east-west direction and depths of 110 meters in the deepest place. In the northeast direction Słupsk Furrow is connected to the Eastern Gotland Basin (EGB). EGB is the largest and the central of all Baltic Sea basins. It is enclosed by a 150 m isobath and has a maximum depth of about 250 meters. In the east of EGB the Gulf of Riga is located. North of EGB the Farö Deep continues the chain-like alignments of the basins. In the Western Gotland Basin (WGB), separated from EGB by the island of Gotland there is the Landsort Deep, the deepest place in the Baltic Sea with depths up to 490 meters. The easternmost part of the Baltic Sea is the Gulf of Finland with an east-west extension, whereas northernmost part is the Gulf of Bothnia with north-south extension. The Gulf of Bothnia consist of the Bothnian

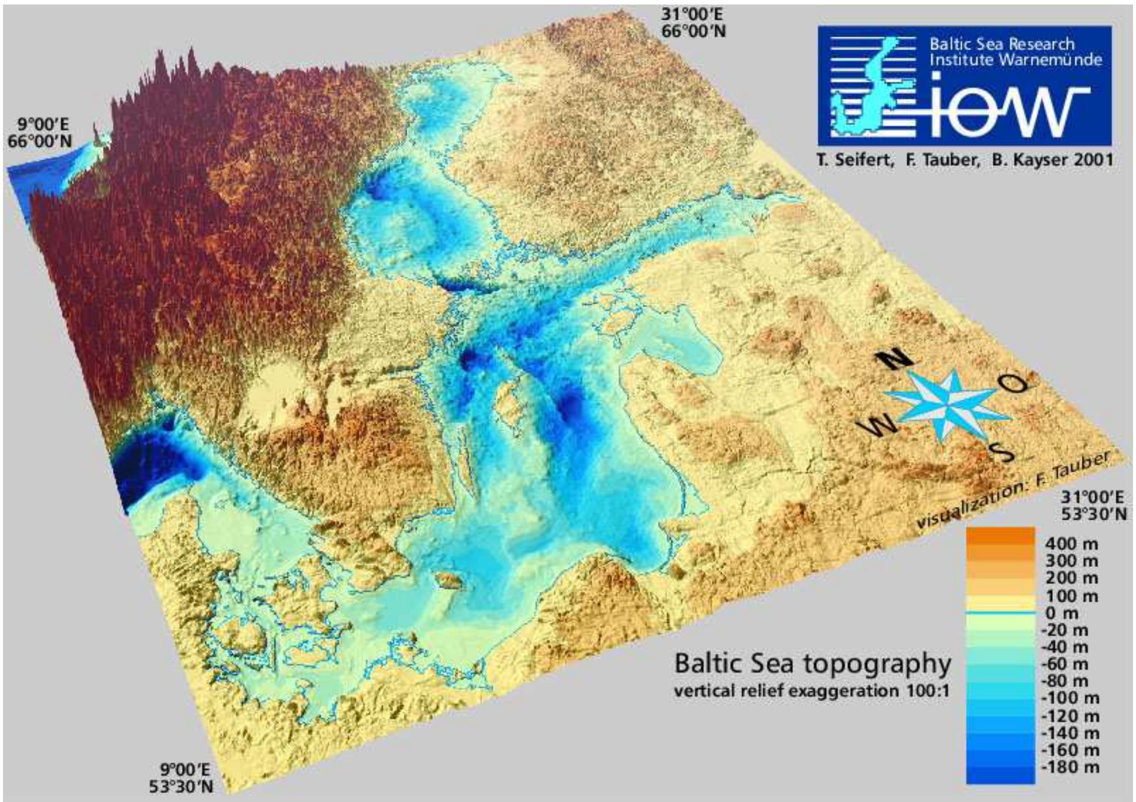

Figure 1.1: Bathymetry of the Baltic Sea.

Sea in the south and the Bay of Bothnia in the North.
Due to the permanently stable stratification of the Baltic Sea, resulting from a balance of freshwater supply from rivers and atmospheric evaporation difference and salt water supply from the North Sea, the deeper parts of the basins are cut off from direct mixing with surface waters.
Major Baltic inflow events (MBIs) are known as the only process for the ventilation of the Baltic Sea deep waters (*Wyrtki*, 1954; *Matthäus and Franck*, 1992; *Lass and Matthäus*, 1996; *Lehmann et al.*, 2004; *Feistel et al.*, 2006; *Reissmann et al.*, 2009). MBIs can be divided into baroclinic ones (driven by baroclinic pressure gradients especially horizontal salinity differences) and barotropic ones (driven by barotropic pressure gradients, especially sea-level differences). In recent years, major barotropic inflows, driven by a substantial sea level difference between the Kattegat and the Baltic Sea and persistent westerly winds, occurred in 1993 and 2003. Exceptionally strong baroclinic inflows, driven by the horizontal density gradient between the Kattegat and the Baltic Sea have been observed during the summers of 2002 and 2003 (*Feistel et al.*, 2003, 2004). These fairly rare, but significant events enter the Baltic

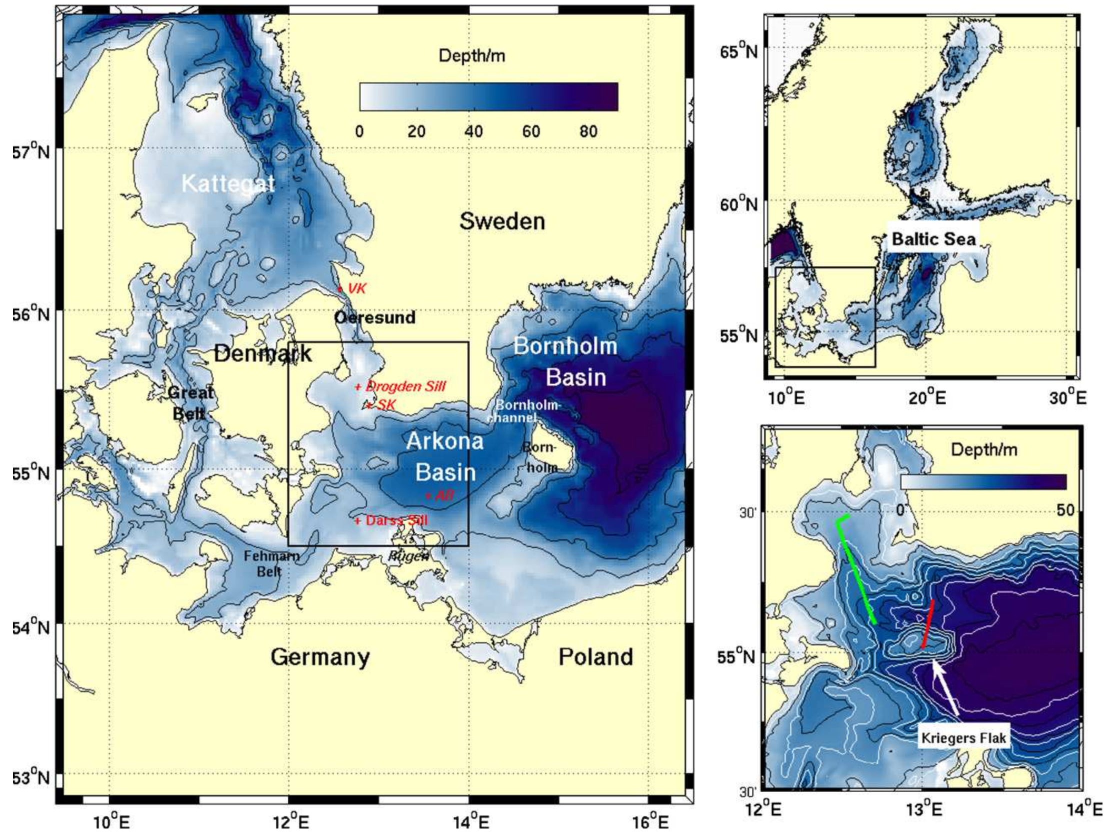

Figure 1.2: Map of the Baltic Sea showing the domain of the Baltic Sea model (upper right panel), the domain of the Western Baltic Sea model (left panel) and the area of the Drogden Sill and Kriegers Flak area (lower right panel). The positions of the Drogden Sill, Darss Sill (DS) and Arkona Buoy (AB) stations are shown in the left map as well as the locations of the coastal gauges in Viken (VK) and Skanör (SK). The Baltic Sea, and the Western Baltic Sea model has model has an open boundary in the Skagerrak at 9^o E, open boundaries between Kattegat and Skagerrak at 57^o 30' N and east of the Bornholm Sea at 16^o 30' E.

Sea mostly over the Belt Sea and Darss Sill and typically change the hydrography in the deep waters of the Gotland basin.
Stigebrandt (2003) has sketched a conceptual model for the vertical circulation in the central Baltic Sea. In Fig. 1.3 this overview is refined by listing all known relevant vertical mixing and transport processes in the Baltic Sea.
Episodic overflows over the Belt Sea sills transport saline water into the entrance areas of the Baltic Sea where they form dense bottom currents. Those are subject to entrainment of less saline ambient water lowering their salinity and thus their density. Once the density of the bottom currents equals the density of the ambient water (due to entrainment and deeper propagation) they interleave with the am-

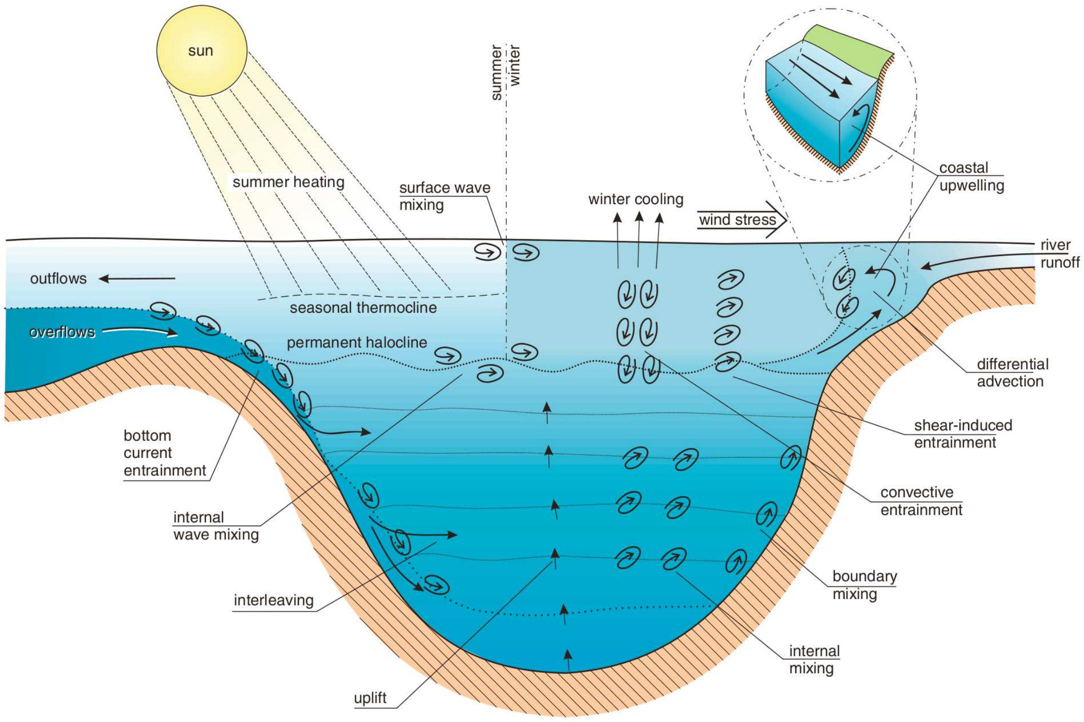

Figure 1.3: Scheme of vertical mixing and transport processes in the Baltic Sea. This figure has been taken from *Reissmann et al.* (2009).

bient water masses and ventilate them. Because of volume conservation the deep inflows generate a compensating uplift of the water column in the central Baltic Sea. Vertical turbulent transport is enhanced by internal mixing due to inertial waves and internal wave breaking, as well as by mesoscale Baltic Sea eddies (the so-called Beddies). The latter may also contribute to boundary mixing when they propagate towards the sloping sea bed. Other potential boundary mixing effects are internal wave breaking at the sloping sea bed or shear-induced convection, or near-bottom currents induced by inflow events. Coastal upwelling has the potential of transporting sub-halocline water towards the surface and irreversibly mixing them into less saline surface water due to differential advection. During winter surface cooling will establish statically unstable stratification leading to convective entrainment of surface water into the halocline. Similarly, the surface wind stress causes shear-induced entrainment into the halocline. During summer the halocline is protected against entrainment from above by a seasonal thermocline below which internal-wave mixing erodes the halocline. Finally, surface waves generate near-surface turbulence and modify the surface mixed layer in a complex way. Breaking surface waves inject turbulence into the surface mixed layer and thus have a strong impact on the near-surface dynamics.

Smaller inflow events, which typically enter the Baltic Sea first and most effectively via the Sound and the Drogden Sill (see Fig. 1.2 for coastlines, bathymetry and geographical names), occur several times per year and are vital for the ventilation of intermediate layers in the Bornholm Basin, are of similar importance. Such medium-intensity inflow events are essential for the maintenance of a suitable habitat for cod egg development in the halocline area of the Bornholm Basin (*Mohrholz et al.*, 2006). On their way over the sills through the Arkona Basin over the Bornholm Channel and into the Bornholm Basin, the medium intensity inflows propagate as dense bottom currents, and are thus subject to entrainment of overlaying brackish waters which reduce their density and thus decrease the density of the isopycnal surface at which they sandwich into the halocline of the Bornholm Basin. This turbulent mixing and entrainment has only been investigated in detail in recent years. Furthermore, human constructions in the pathway of the inflowing saline waters in the region of the Western Baltic Sea have the potential to additionally mix these bottom waters. *Kouts and Omstedt* (1993) analysed from long term hydrographic observations that the volume of dense bottom water increases by 53% due to entrainment in the Arkona Basin. *Lass and Mohrholz* (2003) hypothesised that the major mixing mechanism is differential advection (denser water sheared over fresher water) in the front region of the intermittent dense bottom currents and estimated a mixing related volume increase of dense bottom water by 30% for the passage from Drogden Sill to the Bornholm Channel. *Liljebladh and Stigebrandt* (1996) and *Lass and Mohrholz* (2003) investigated in detail the pool state of the Arkona Basin, during which a large amount of dense water is passively stored as a few meter thick layer in the eastern flat-bottom part of the Arkona Basin.

As the Baltic Sea is too fresh for most marine species and too salty for most freshwater species, most pelagic and benthic species experience physiological stress. Changes in salinity and oxygen concentrations may therefore have a considerable impact on species distributions, food webs and life-histories (*Meier et al.*, 2006).

The eutrophic Baltic Sea produces large amounts of organic matter sinking into the stratified deeper water where it mineralised and thus lowers the oxygen concentration in the water. During stagnation periods, i.e. between major salt water inflows into the Baltic Sea, large areas of the Baltic Sea deep water may be depleted from oxygen, not allowing presence of any higher life forms. Additionally, high amounts of phosphate are released from sediments under oxygen-depleted water masses, which favour, after been mixed up into the euphotic zone near the sea surface, massive summer blooms of toxic cyanobacteria.

Deoxygenation is an example for sensitive non-linear processes in the Baltic Sea. Under varying climate input a sensitive non-linear response, built on a cascade of physical and biogeochemical processes, leads to very different ecosystem states. This output depends on the changing redox condition in the winter column.

1.2 Offshore wind farms in the Western Baltic Sea

To reduce greenhouse gas emissions substantially, it is the goal of the German Federal government to increase the portion of power generated from renewable energies to at least 20% until 2020 (*BMU* (2007). Since use of water and sun for power generation is limited, as well as space for land-based wind turbines, the establishment of offshore wind farms in the German EEZ areas in the North Sea and the Baltic Sea is planned (Fig. 1.4). Neighbouring countries such as Denmark have comparable goals (*TRM* (2005)). While additional vertical mixing due to offshore wind farms in the well-mixed coastal waters of the German Bight (South-Eastern North Sea) have an negligible impact on the marine ecosystem, there may be significant effects for the stratified, almost tide-less Western Baltic Sea.

It was first discussed by *Lass* (2003), that structures such as foundations of wind turbines assembled in offshore wind farms could induce additional vertical mixing in stratified shear flow (see Fig. 1.5). Such a wind farm induced dilution of the inflowing water could result in a decreased ventilation of the halocline in the Baltic Sea (see Fig. 1.1). As a result of this, the region of oxygen depletion in the Baltic Sea could be extended to higher levels in the water column, with drastic environmental consequences for pelagic and benthic organisms.

It is the goal of the present study to quantify this impact.

1.3 Objectives of the QuantAS projects

1.3.1 QuantAS consortium

In order to quantify the natural and anthropogenic mixing of Baltic Sea inflow events, an international consortium of oceanographers was established in May 2004, with members from Germany, Denmark, Poland and Sweden (see Fig. 1.6). The aim of the consortium was to jointly carry out research in support of unravelling the mixing processes in the Western Baltic Sea. The initiative was named QuantAS, which stands for *Quantification of Mater Mass Transformations in the Arkona Sea*. Two German projects were proposed, QuantAS-Nat for studying natural mixing (funded by the German Research Foundation, 2005-2010), and QuantAS-Off for studying the potential effect of offshore wind farms (funded by the German Federal Ministry for the Environment, Nature Conservation and Nuclear Safety, 2004-2009).

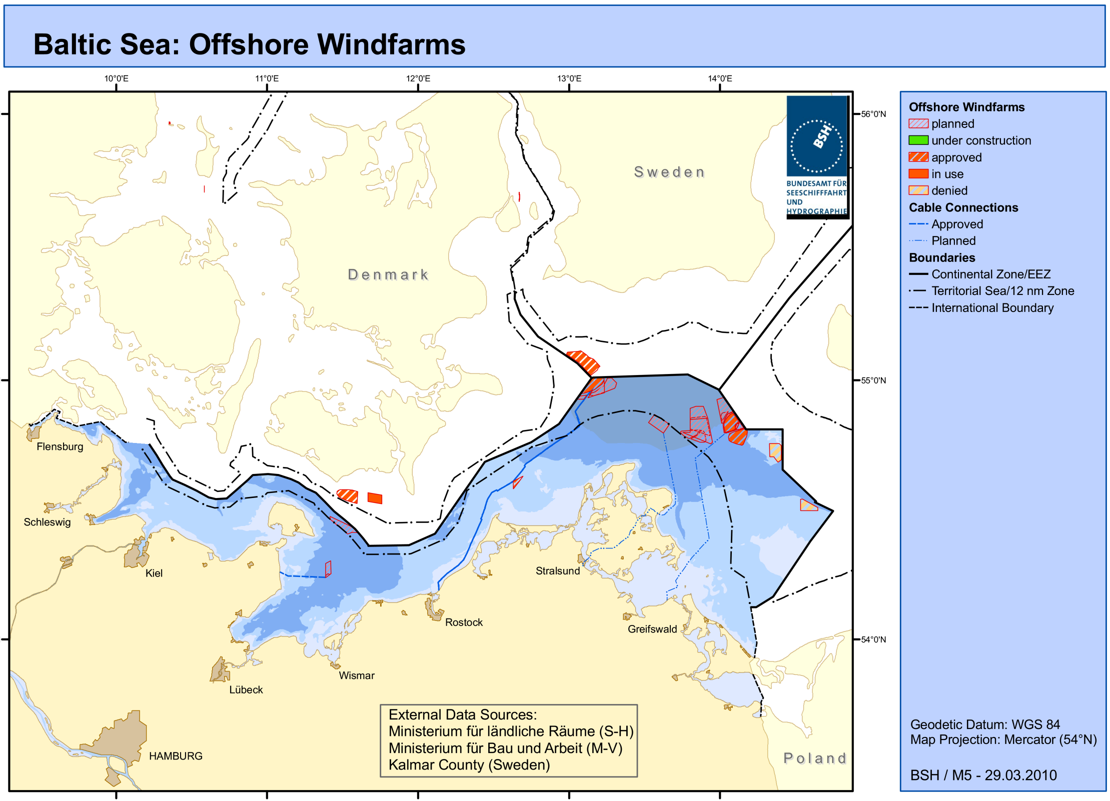

http://www.bsh.de/en/Marine_uses/Industry/CONTIS_maps/index.jsp

Figure 1.4: Distribution of existing, approved, planned and rejected offshore wind farms in the Western Baltic Sea. This map has been downloaded from the webpages of the BSH.

Both projects were closely interlinked. QuantAS-Off was a project cluster coordinated by Leibniz Institute for Baltic Sea Research in Warnemünde with the Chair of Fluid Mechanics at the University of Rostock (laboratory experiments) and the Fluid Mechanics Institute of the Leibniz University of Hannover (Computational Fluid Dynamics, simulations) as partners. As subcontractors for the QuantAS-Off project ISW Wassermesstechnik (Germany, turbulence measurements), the Institute for Oceanography of Polish Academy of Science (Poland, hydrographic observation) and wiglaf.dk (Denmark, numerical model setup) were chosen.

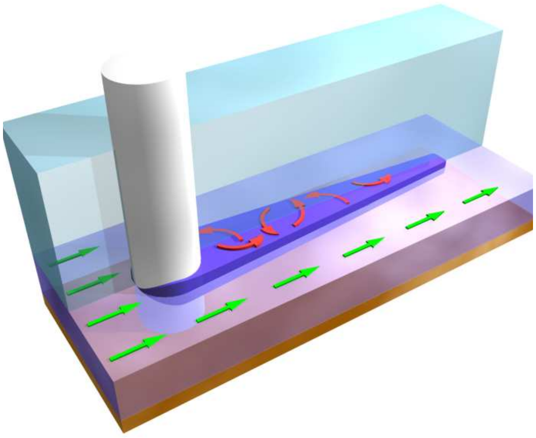

Figure 1.5: Sketch of how a structure in stratified shear flow could induce additional vertical mixing. Graphics: Jan Donath (IOW).

Figure 1.6: Members of the QuantAS consortium as established in May 2004 at IOW. From left: Volker Mohrholz (IOW), Anders Stigebrandt (University of Gothenburg, Sweden), Gerd Becker (BSH, Hamburg), Jürgen Sellschopp (FWG, Kiel), Ralph Wasserthal (BSH, Hamburg), Jan Piechura (IOPAN, Sopot, Poland), Hartmut Prandtke (ISW Wassermesstechnik, Fünfseen), Hans Burchard (IOW), Alfred Leder (University of Rostock), Ole Petersen (DHI, Hørsholm, Denmark), Karsten Bolding (BB, Asperup, Denmark), Werner Ziehlke (University of Hannover), Siegfried Krüger (IOW), and Hans Ulrich Lass (IOW). The Danish Maritime Safety Administration (DaMSA) was joining the consortium later.

This report focusses on the results of QuantAS-Off, but additionally presents many of the QuantAS-Nat results as background information. For the water mass transformation studies in the Arkona Sea, results from QuantAS-Nat and QuantAS-Off cannot be completely separated.

1.3.2 Social Impact

Any offshore construction has an impact of the surrounding water bodies. In the case of offshore wind farms constructed in the connecting waters between the North Sea and the Baltic Proper, this may not only have a local impact but may also significantly influence the dynamics of the whole Baltic Sea. The ecosystem of the Baltic Sea is under permanent stress due to the narrow connection to the North Sea and over-fertilisation from agriculture anyway, leading to extensive regions of oxygen depletion. It is thus an ethical duty of those who are planning offshore structures such as wind farms and bridges to ensure that their constructions have no significant impact on the Baltic Sea ecosystem. This attitude lead to the so-called zero blocking solution for the construction of large bridges over the Great Belt and the Sound in the 1990s, see *Hansen and Møller* (1989a) and *Stigebrandt* (1992), meaning that no changes of the transport of water and salt between the Baltic Sea and the North Sea should occur.

1.3.3 The Fehmarn Belt project: a spin-off from QuantAS-Off

QuantAS-off is connected to the hydrodynamic part of the Fehmarn Belt project (FEHY), which investigates the flow resistance from marine substructures as well as the associated mixing caused by the planned Fehmarn Belt link. This part of the project is mainly carried out by the QuantAS consortium partners Danish Hydraulic Institute in Hørsholm (Denmark) and IOW. The Fehmarn Belt link will connect the German island of Fehmarn with the Danish island of Lolland by crossing the 18-kilometre wide Fehmarn Belt in the Baltic Sea. Currently (April 2010), a bridge solution is preferred over the more expensive bridge solution. The elements of such a bridge may disturb the current and the stratification like foundations of offshore wind turbines. However, these constructions are closer to each other in distance compared to turbines in offshore wind farms. Another characteristics of a bridge is that the entire cross section (here: Fehmarn Belt) is covered by pylons such that water masses cannot flow around the construction as it is possible in offshore wind farms.

Major parts of the FEHY work at IOW will be related to past QuantAS activities as they are documented in this report, such as field observations in the

Western Baltic Sea, including intensive observations parallel to the Western Great Belt bridge, high-resolution realistic numerical modelling of the Western Baltic Sea, with and without impact of offshore structures, and development of suitable parameterisations of structure-induced impacts on stratification and mixing.

1.3.4 QuantAS-Off key questions

The key questions of QuantAS-Off as formulated in the 2004 proposal were:

- How much will dense and oxygen-rich bottom currents through the Arkona Sea into the Baltic Sea be obstructed and diluted by underwater constructions such as foundations of offshore wind farms ?
- Which influence do these water mass transformations have on the flux (and its distribution) of oxygen-rich North Sea water into the basins of the Baltic Sea such as the Bornholm Basin and the Gotland Basin ?
- Which recommendations for the location, layout and extent of off-shore wind farms can be given to the authorities responsible for approving the erection of offshore wind farms ?

The approach to answer these complex questions was to construct a proper parameterisation of mixing of inflow events tailor-made for the Western Baltic Sea and to carry out a number of numerical experiments for the Western Baltic Sea with this parameterisation implemented.

These parameterisations had to fit into hydrostatic models for the Western Baltic Sea, i.e. into models which are able to reproduce the dynamics of the Western Baltic Sea over periods of several years, with the consequence that smaller scales cannot be reproduced. The calibration of such parameterisations was one of the most complicated tasks within the project. Therefore, first of all, QuantAS-Off needed to be strongly interconnected with QuantAS-Nat, for understanding the natural processes, see WP 1 in Fig. 1.7 for main results. Secondly, the interaction between stratified (and sheared) currents with structures needed to be studied in detail. For this central part, a strategy based on field studies, laboratory studies and local model studies of structure induced mixing had been chosen (see WP 2 in Fig. 1.7).

Once these parameterisations had been developed and calibrated, they were implemented into the model for the Western Baltic Sea in order to quantify the additional mixing effects of wind farms by comparing model results with and without wind farm parameterisation (WP 3). In the final WP 4, numerical experiments were carried out with various wind farm densities and distributions for giving recommendations for future planning

1.3.5 Description of Workpackages

Here the tasks of the four workpackages are briefly described. For full details see the original proposal. The logical structure of the QuantAS projects is also shown in Fig. 1.7.

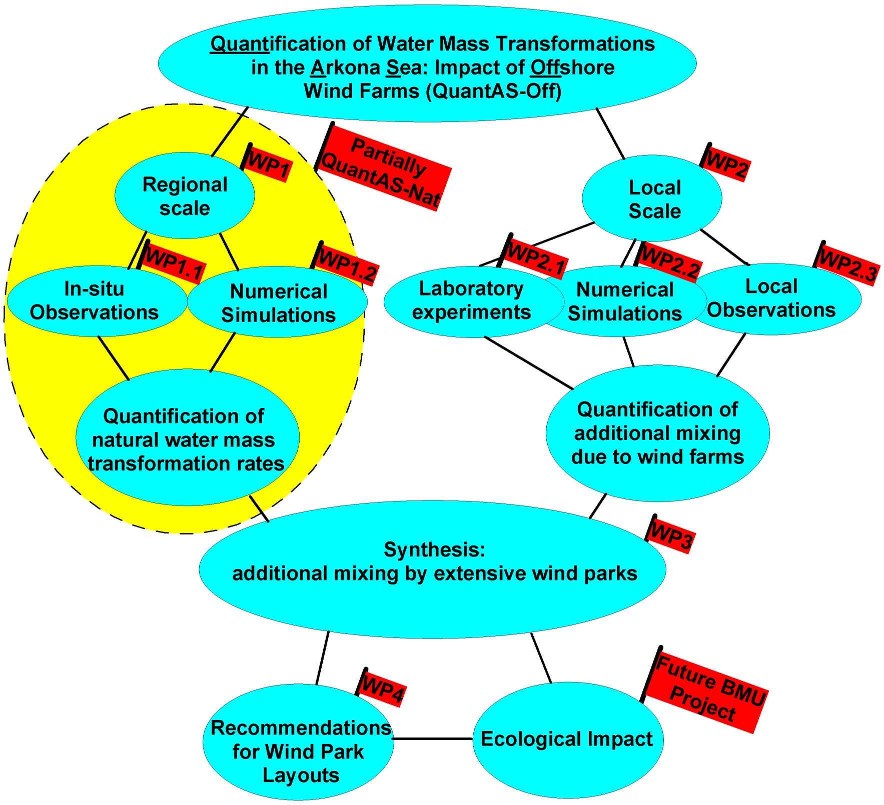

Figure 1.7: Diagram showing the organisation of QuantAS-Off and its relation to other projects.

WP1 Natural Pathways

1. In-situ Observations
2. Numerical Modelling

The four workpackages are briefly described here and references are made to the sections of this report containing the results are made:

WP1 Natural Pathways. The first workpackage dealt with investigations of the present transport and mixing processes in the Arkona Sea by means of observational (WP1.1) and modelling (WP1.2) techniques. The major portion of this activity was carried out in the framework of QuantAS-Nat.

WP1.1 In-situ Observations. In-situ observations of dense water inflow events into the Baltic Sea were difficult to carry out, since these events occur episodically. Three types of observations were carried out: ship-based observations, moorings and the use of monitoring data from the MARNET stations on Darss Sill and in the Arkona Basin, which IOW operates for Bundesamt für Seeschifffahrt und Hydrographie (BSH - see Marnet website at `www.bsh.de`) and monitoring stations in the Drogden Sill and in the Great Belt operated by Danish Maritime Safety Administration (DaMSA - see webpage `www.frv.dk`). The results obtained in this part of the project are described in sect. 2.1.

WP1.2 Numerical Modelling. Idealised and realistic model simulations with GETM (General Estuarine Transport Model, see sect. 1.4.2) were carried out for the Arkona Sea and the adjacent basins and straits. Idealised experiments with stationary forcing were used for investigating the locations of the principal pathways of inflowing dense water. The results obtained in this part of the project are described in sect. 2.2.

WP2 Near-field Human Impact. The direct impact of the offshore constructions on the surrounding water body is mediated due to friction between flowing water and the surface of the construction. This generates small-scale shear and vorticity in the water which results in turbulent mixing. In the wake of the construction a van Karman strait may establish leading to mixing at distances of several diameters of the construction. Since these effects are difficult to quantify, laboratory (WP2.1) and numerical (WP2.2) experiments of cylindric or similar constructions in stratified shear flow were carried out and compared to each other. Furthermore, field observations of mixing at underwater obstacles were made.

WP2.1 Laboratory Experiments. For the laboratory experiments, it was a major challenge to generate a well-controlled dense bottom current in a laboratory plume. For this purpose a new flume had been constructed by the project partner MST (University of Rostock) allowing for continuous measurements during sufficient time interval. The results obtained in this part of the project are described in sect. 3.1.

WP2.2 Small-scale Numerical Modelling. For the near-field numerical modelling the hydrostatic assumption as usually made for ocean models is not valid any more. For experiments with underwater constructions a model using Reynolds Averaged Navier-Stokes (RANS) equations was applied and upscaled to natural dimensions. In the vicinity of the underwater construction, a high resolution was needed, further away coarser resolution was unavoidable in order to give reasonable computational effort. Situations similar to the laboratory experiment (see WP2.1) were chosen for the numerical simulations. This work was carried out by the project partner FMI (University of Hannover). Additionally a Large Eddy Simulation (LES) model of the laboratory scale had been implemented by MST. The results obtained in this part of the project are described in sect. 3.2.

WP2.3 Field observations of anthropogenic mixing. At first ship wrecks which have a size and height above bed which is comparable to underwater constructions of wind turbines were planned to be investigated in means of turbulence dissipation measurements, high-resolution ADCP measurements and standard CTD observations. Since it was impossible to find a suitable ship wreck in the area field observation nearby the western part of the Great Belt Link were taken by IOW in cooperation with the QuantAS consortium members FWG Kiel, University of Gothenburg and DaMSA. These observations also included turbulence dissipation measurements, high-resolution ADCP measurements and standard CTD observations. The results obtained in this part of the project are described in sect. 3.3.

WP3 Far-field Human Impact. The impact of offshore wind farms on the dynamics of the deeper basins of the Baltic Sea could only be estimated by means of regional numerical models. In such models drag and mixing effects of wind farms can be added or removed and their impact studied. For the regional modelling, parameterisations for the effect of wind farms were constructed (WP3.1). For doing so, the results of WP2 were analysed and used. Once parameterisations for underwater constructions had been found, these were implemented into regional models for the Western Baltic Sea (including the Bornholm Sea, WP3.2) for estimating the impact of offshore wind farms on the stratification and oxygen ventilation. Originally, it was planned to set up a model simulation for the entire Baltic Sea to study the impact of offshore wind farms on that scale, but this was cancelled later due to the only small impact on the scale of the Bornholm Sea.

WP3.1 Parameterisations for Wind Farms. The way how the effect of underwater constructions of wind turbines or whole wind farms is parameterised in a regional scale ocean model depends on the underlying horizontal grid and its spatial resolution. The strategy was to include a quadratic friction term in the whole water column due to offshore structures, and to allow for structure-induced turbulence production which in turn increases mixing. This lead to an extension of the existing two-equation turbulence closure model used in GETM. In idealised setups of GETM (see sect. 1.4.2) which were the basis for the regional modelling, various parameterisations were tested. The results obtained in this part of the project are described in sect. 4.2.

WP3.2 Medium-Range Impact (Bornholm Sea). The Bornholm Sea, into which the dense bottom waters flow directly from the Arkona Sea without being hampered by a sill, is the area which may be most directly affected by additional mixing in the Arkona Sea. Thus, regional model impact study concentrated on that region. The results obtained in this part of the project are described in sect. 4.5.

WP3.3 Long-Range Impact (Baltic Proper). As a major result it was found that the impact of even extreme wind farms coverage in the Arkona Sea on the hydrography of the Bornholm Basin was relatively small, the originally planned impact assessment simulations for the entire Baltic Sea were skipped.

WP4 Specific Risk Assessment. Numerical experiments were carried out with two different spatial distributions of wind farms (WP4.1).

WP4.1 Numerical Experiments with Various Wind Farm Designs. Once suitable parameterisations for offshore wind farms had been found (WP3.1), sensitivity studies with two spatial wind farm distributions and two degrees of mixing efficiency were carried out. As a realistic distribution scenario, the actual planning scenario was implemented. This considered the wind farm projects in the German EEZ, but also those in the Danish and the Swedish EEZ. Furthermore, a worst case scenario study with wind farms covering a large area in the pathway of inflowing dense bottom water was carried out. The results obtained in this part of the project are described in sect. 4.5.

WP4.2 Division of Arkona Sea into Risk Class Areas. Since even the impact of a very extensive wind farm coverage was very small, the division of the Arkona Sea into risk class areas could be skipped.

1.4 Oceanographic methods

In the framework of the QuantAS projects Baltic Sea inflow events were investigated by means of in-situ measurements from research vessels and moorings. Furthermore, intensive numerical model simulation with a regional numerical model have been carried out. These methods are described in this section. The methods applied for the laboratory experiments and the local scale modelling are described in detail in the respective sections of chapter 3.

1.4.1 Observational methods

1.4.1.1 CTD measurements

Conductivity-Temperature-Depth (CTD) instruments have become essential platforms in measuring water hydrographic quantities such as salinity, temperature and density as function of pressure and depth. CTD instruments measure three important parameters directly in situ - conductivity, temperature and pressure. Since conductivity depends on salinity, temperature and pressure, the salinity can be determined by means of a CTD probe. A typical CTD probe is shown in Fig. 1.13a. Different deployment techniques of measurements using CTD were used during the QuantAS project:

- The CTD is cast while the ship is drifting or held in one position. This is the most basic CTD measurement method and gives a vertical profile of water hydrographic quantities underneath the research vessel. Exemplary salinity profile deduced using this measurements method is shown in Fig. 1.8 (top two panels).

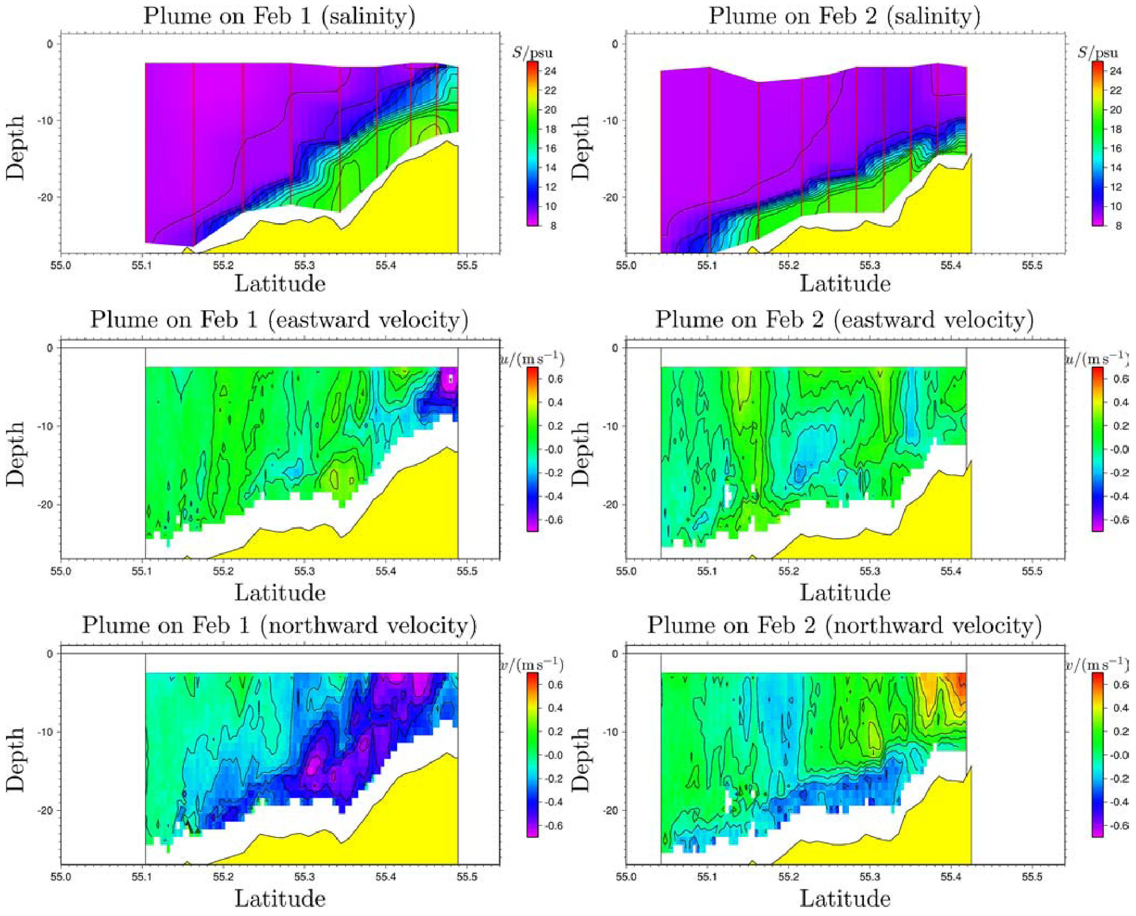

Figure 1.8: Observed salinity on a north-south transect south from Drogden Sill, deduced from CTD profiles. The red lines show the positions of the single CTD profiles. This figure was obtained from *Burchard et al.* (2005).

- A high-resolution profiling method is used e.g. during the cruises of the Polish Academy of Science research vessel R/V Oceania. Here, the CTD probe is mounted parallel to the surface/seabed, inside of a metal framework. Underneath the cage a heavy, metal chain is attached. The main purpose of the chain is to increase the weight (the CTD probe will fall faster, which increases the measurements resolution). Also, the chain helps to determine when the CTD is approaching the seabed. Measurement data are collected while the vessel is cruising and the CTD probe is moved up and down. It has to be taken into account that the up-going velocity depends on the winch speed. When it is above some threshold it causes the problem with disturbances of the water around the CTD sensor, i.e. measurements are conterminated by deeper waters entraining into the wake of the probe. To correct this error, for the area with the corrupted data, up-going casts were removed and replaced with the down-going casts proceeding them. In Fig. 1.9 the salinity data for one of the problematic transects obtained by R/V Oceania is shown, before and after removing of the corrupted up-going casts.

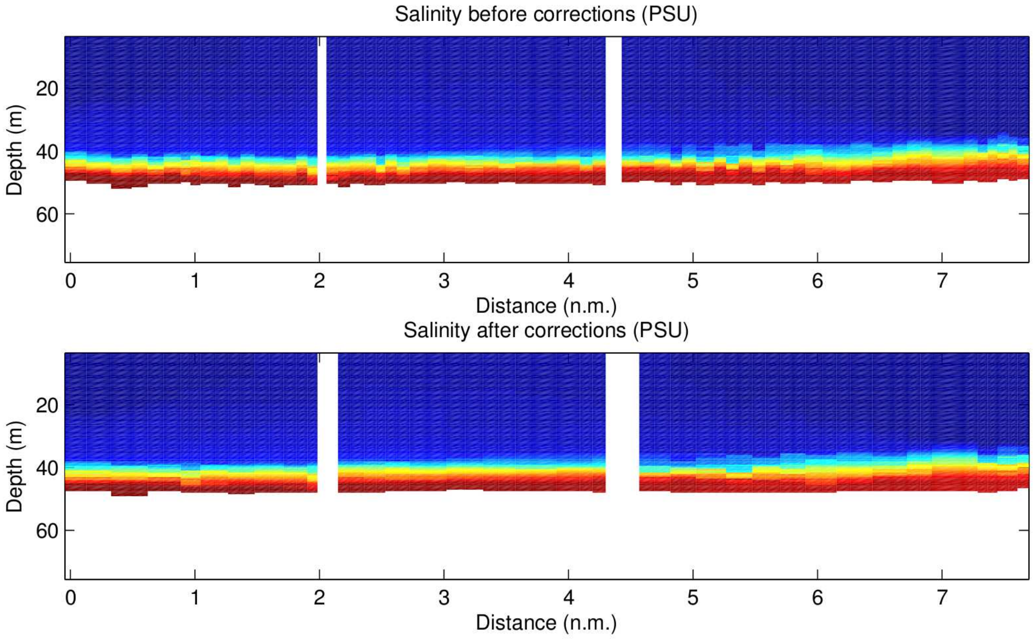

Figure 1.9: The original salinity data obtained from R/V Oceania (upper panel) and the data after removing up-going casts (lower panel) and replacing them with down-going casts. In the corrected data no zig-zagging of isopycnals is visible, but spatial resolution is lower. The figure was obtained from *Szewczyk* (2009).

- Using CTD chain (*Sellschopp*, 1997) towed behind the ship. A CTD chain consists of many CTD sensors aligned on a cable, which by inductive coupling provides the power for the sensor electronics and the data transfer between underwater sensors and deck unit. Each sensor fin is an autonomous CTD device. The vertical resolution of the acquired two-dimensional property fields is defined by the distance between sensor fins. The horizontal resolution of a towed CTD chain is the product of the towing speed and the duration of a polling cycle, which is typically two seconds. The maximum towing speed must be adjusted to the breaking strength of the towing cable. An exemplary CTD temperature data obtained via CTD chain measurements are given in Fig. 1.10.

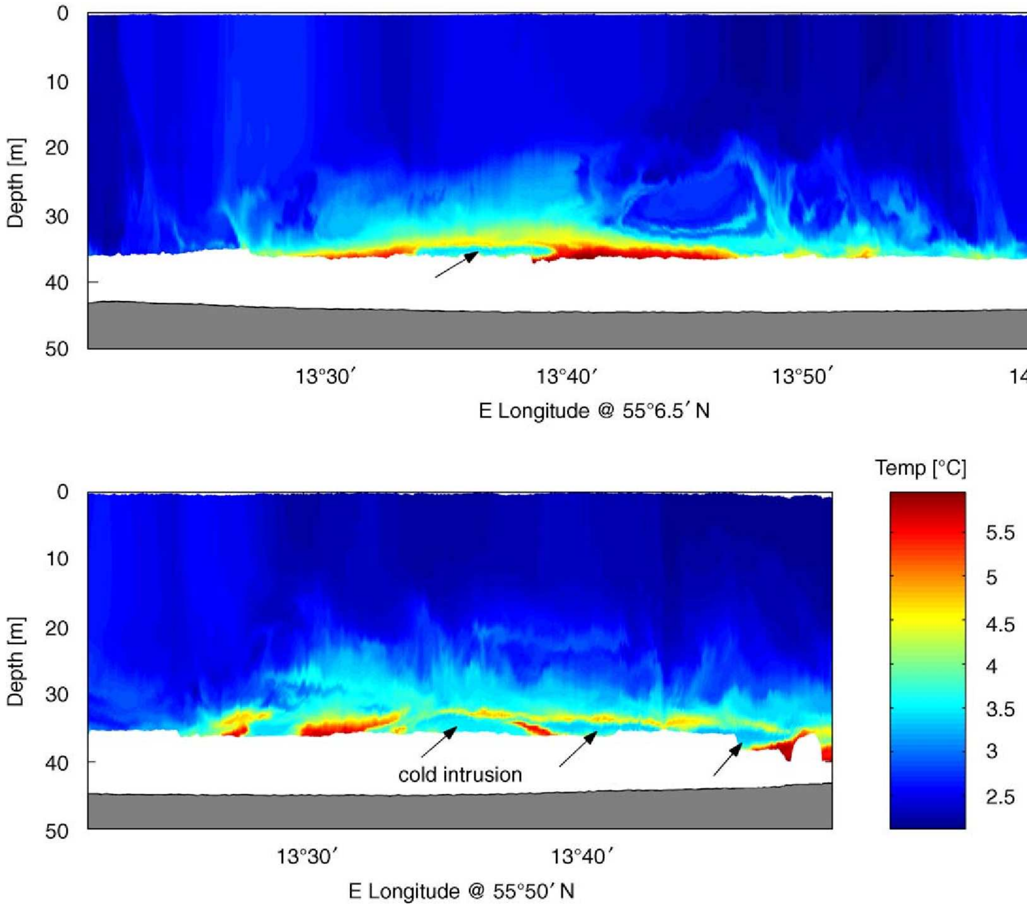

Figure 1.10: Exemplary temperature data obtained via the CTD chain measurement from *Sellschopp et al.* (2006). The residual saline bottom layer is hardly touched by the towed instrument except where the interface is uplifted in two cyclonic eddies. A cold intrusion, indicated by arrows, is present in the halocline at 35 m depth. The figure was obtained from *Sellschopp et al.* (2006).

- CTD sensors are attached to a mooring at various depths. The measurements are taken permanently while the buoy is deployed, see sect. 1.4.1.4 for details.

1.4.1.2 ADCP measurements

ADCPs (Acoustic Doppler Current Profilers) are exploiting the Doppler effect by transmitting sound at a fixed frequency and listening to echoes returning from sound scatterers in the water. These sound scatterers are small particles or plankton that reflect the sound back to the ADCP. Scatterers (such as zooplankton) are everywhere in the ocean. They float in the water and on average they move at the same velocity as the water. Sound scatters in all directions from scatterers. Most of the sound goes forward, unaffected by the scatterers. The small amount that reflects back is Doppler shifted. When sound scatterers move away from the ADCP, the sound they record is Doppler-shifted to a lower frequency proportional to the relative velocity between the ADCP and scatterer. The backscattered sound then appears to the ADCP as if the scatterers were the sound source.
Typically, ADCPs have four beams with their direction inclined by 20° - 20° from the vertical. Projected to a horizontal plane, they are orthogonal to each others. by means of trigonometric relations, the along-beam currents speeds are converted into a 3D vector (eastern, northern, and vertical component). To account for the ship movement, the ADCP uses bottom tracking or data from the Global Positioning System (GPS). A typical ADCP is shown in Fig. 1.13b.
In the QuantAS projects, ADCPs have been installed in the following ways:

- The vessel-mounted ADCPs in which the transducer is permanently installed on the hull and collects data while the ship moves (Fig. 1.11a)
- ADCP is towed behind the ship. The floating device features adjustable depth of the transducer below the water surface and adjustable beam direction (horizontal, vertical) of the echosounder (Fig. 1.11a)
- ADCP transducer installed underneath the buoy that measures velocities of the water column beneath the buoy (Fig. 1.11b)
- ADCP transducer installed on the seabed, looking up to the surface. It measures velocities of the water column over the device

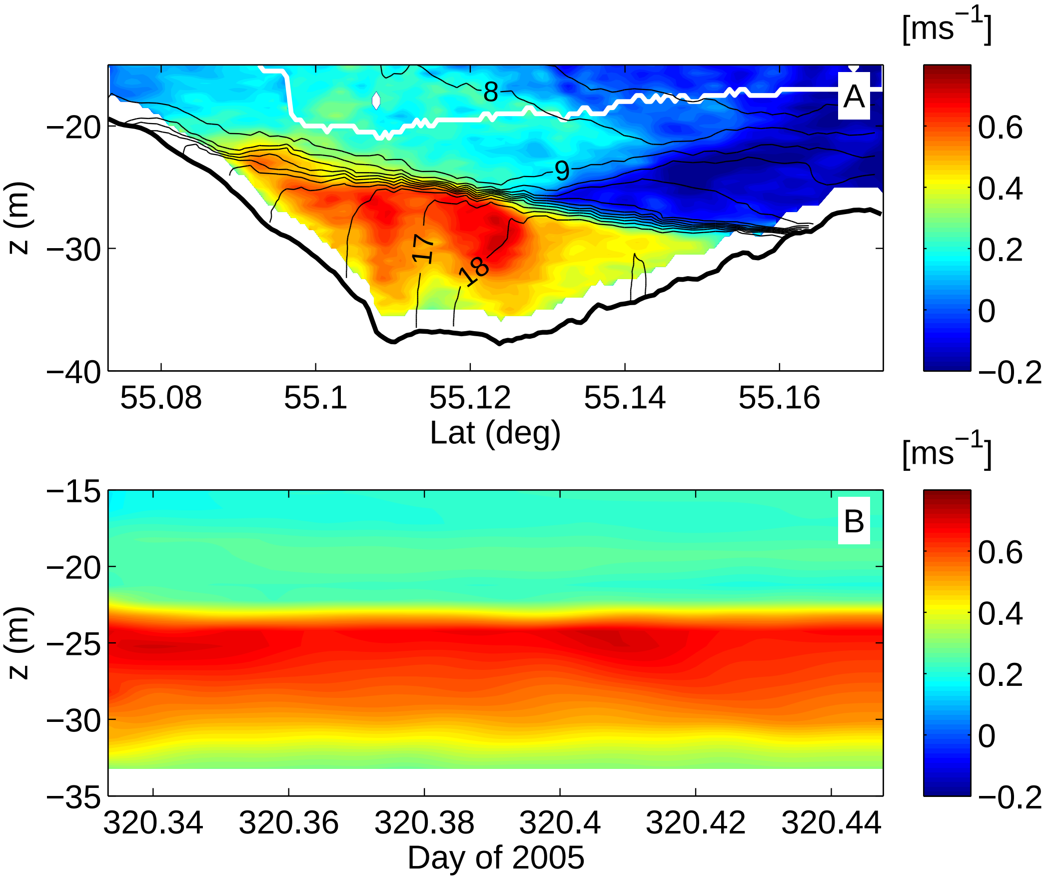

Figure 1.11: (a) Velocity data obtained from combined ADCP measurements: ADCP mounted underneath the vessel and ADCP towed behind the vessel. The white line indicates the position of the first bin of the towed and lowered ADCP. Data above this line are derived from the vessel-mounted ADCP. (b) 30 minute low-pass filtered velocities measured by the moored ADCP. The figure was obtained from *Umlauf et al.* (2007).

The echo from a hard surface such as the bottom or sea surface is so much stronger than the echo from scatterer in the water, so the bottom/surface layer will contain contaminated data. Normally data from distances too close to the surface (when looking up) or bottom (when looking down) should be rejected. Fig. 1.12 shows a transducer with the beam angle oriented 30^o from vertical. For the 30^o transducer, the echo through the side lobe facing the bottom returns to the ADCP at the same time as the echo from the main lobe at 85% of the distance to the bottom. This means data from the last 15% of the range to the surface can be contaminated. The effect is the same for an ADCP at the surface pointing down to the bottom.

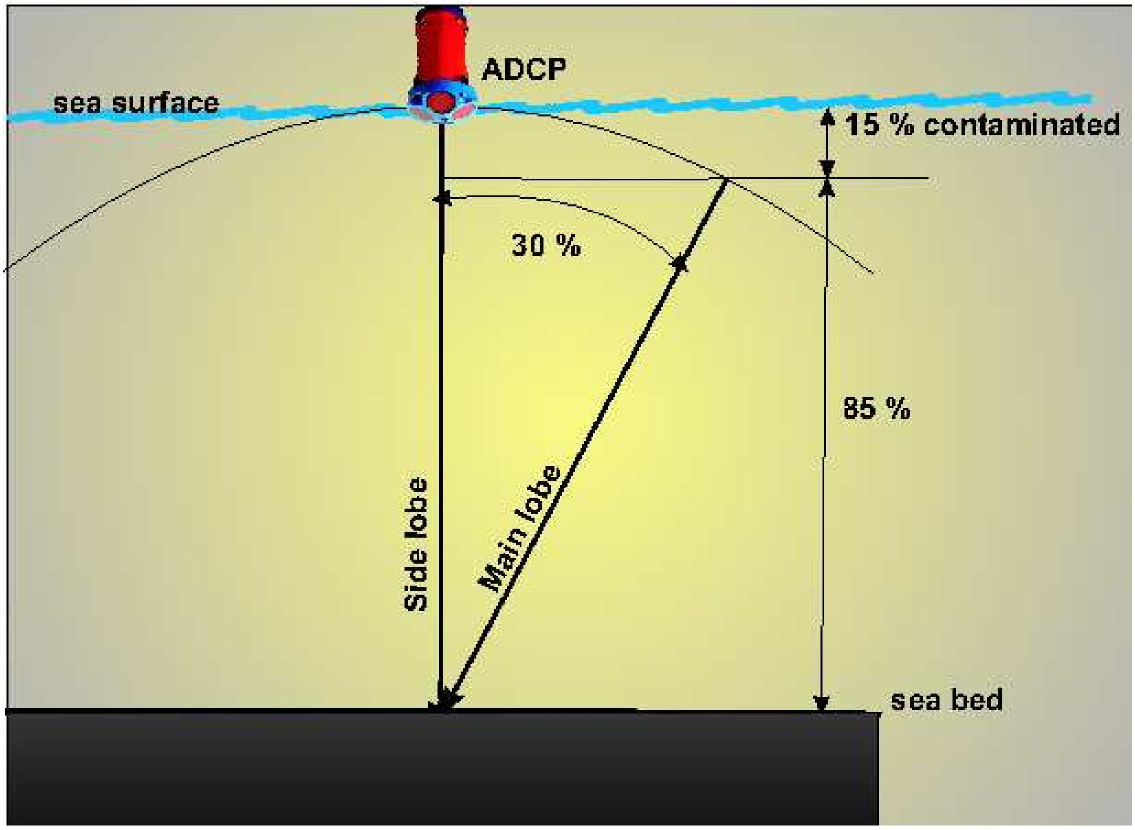

Figure 1.12: The relationship between transducer beam angle and the thickness of the contaminated layer at the surface. The figure was taken from *Szewczyk* (2009).

1.4.1.3 MSS measurements

The MSS (Micro-Structure Sonde) Profiler is a developed operational micro-structure measuring system, specially designed for marine and limnic turbulence measurements. The profiler can be used for sinking and uprising measurements and is equipped with a current shear sensor and various other probed including CTD. The upper detection limit is depending on the geometry of the shear sensor.

Small scale turbulence causes vertical fluxes of mass and energy of dissolved and suspended material in stratified waters. These fluxes directly influence larger scale physical, chemical, and biological processes in the aquatic environment. The dissipation rate of turbulent kinetic energy is a key parameter to quantify the level of turbulence and the resulting mixing processes in natural waters. Based on dissipation rate measurements, vertical diffusion coefficients and flux rates as well as friction velocities can be estimated.

The MSS is an instrument for simultaneous micro-structure and precision measurements of physical parameters in marine and limnic waters. It is designed for vertical profiling within the upper 100 m. The data are transmitted via electrical cable to an on board unit and further to a data acquisition PC. It is operated via a dedicated winch, avoiding disturbing effects caused by cable tension (vibrations) and the ships movement by keeping the cable slack.

The sinking velocity is calculated from the pressure and time channels. The dissipation rate ε, assuming isotropic turbulence in the dissipation range, is calculated from the shear values using the relation

$$\varepsilon = 7.5\nu(\frac{\partial \bar{u}}{\partial z})^2 \tag{1.1}$$

where ν is the kinematic viscosity of water (calculated as a function of water temperature) and $\partial u/\partial z$ is the vertical shear of the horizontal velocity component projected to the direction of sensitivity of the shear probe. (*Mohrholz et al.*, 2008).

The velocity shear variance is calculated by integrating the power spectrum in the wave number range from 2 to 30 cpm (cycles per m). The limitation of the high wave number cut off to 30 cpm is due to narrow band vibration peaks in the wave number range above 30 cpm resulting from eddy generation at the probe guard of the profiler. The low wave number cut off at 2 cpm is to eliminate contributions from low frequent tumbling motions of the profiler (*Mohrholz et al.*, 2008).

An MSS Profiler is shown in Fig. 1.13c. Some examples of the MSS measurements are given in Figs. 2.7 and 2.8 in the sect. 2.1.3.

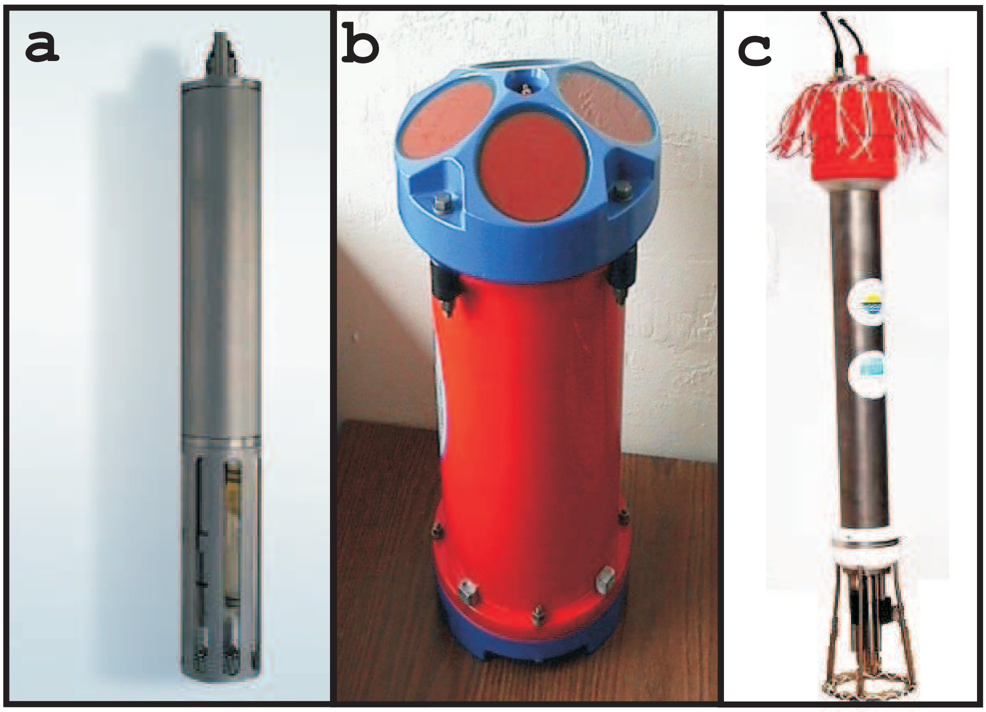

Figure 1.13: Conductivity, Temperature, Depth (CTD) probe (a), Advanced Doppler Current Profiler (ADCP) (b) and Micro-Structure Sonde (MSS) (c).

1.4.1.4 Moorings

In order to obtain long time series of hydrographic conditions acoustic current profilers (ADCP) and strings of CTDs were deployed at two locations in the vicinity of the Drogden Sill. The Kriegers Flak North mooring (KFN) was located in a channel like trench downstream of the Drogden Sill. The second mooring was deployed at the south eastern edge of Kriegers Flak (KFS). At both positions an identical design of the moorings was used. The current field was observed using a bottom mounted upward looking 600kHz ADCP. It gathered averaged current profiles with a vertical resolution of 1m and a sampling interval of 1h. Each averaged current profile consists of 300 subprofiles measured over a period of 5 minutes in order to prevent an aliasing by surface waves. The standard deviation of the averaged current profiles was about $0.4\,\mathrm{cm\,s^{-1}}$. The measurements cover the entire water column except the blank ranges near the bottom (2m) and the surface (3m). The strings of CTDs were composed of SeaBird instruments SBE16 SeaCat, SBE37 MicroCat and SeaStar temperature recorders (see tab. 1.1 for detailed information on mounting depth and measured parameters). The vertical distribution of the instruments was optimised according to the expected stratification. Prior and after each deployment

Name/ Position	**Position**	**Temperature sensor depth (m)**	**Conductivity sensor depth(m)**	**Current profile range(m)**
Kriegers Flak north (KFN)	55^o 07'06"N 13^o 00'37"E	11.5, 22.5, 27.5, 30.0, 32.5, 34.0, 35.5, 37.5	11.5, 22.5, 27.5, 32.5, 35.5, 37.5	4.0 – 38.0
Kriegers Flak southeast (KFSE)	54^o 58'62"N 13^o 12'02"E	12.0, 26.0, 31.0, 36.0, 39.0, 41.0, 43.0	12.0, 26.0, 31.0, 39.0 43.0	5.0 – 38.0
Bornholm Gatt (BG)	55^o 16'50"N 14^o 33'00"E	50.3	50.3	4.0 – 48.0

Table 1.1: Measuring depth of temperature, salinity and current data at time series stations.

all instruments were calibrated. Its accuracy could be kept in range of +/- 0.01K for temperature and +/- 0.01 PSU for salinity. A third mooring was deployed for 6 month duration at the Bornholm Channel (BGE). This station consists of an upward looking 300kHz WHADCP and a SBE37 CTD mounted in a trawl resistant bottom frame. The collected data set consists of full depth current profiles and near bottom temperature and salinity observations.

1.4.1.5 Cruises

In the framework of the QuantAS projects the following cruises organised by members of the QuantAS consortium:

- From 26.01.2004 to 13.02.2004 with research vessel *Helmsand*, chief scientist: Jürgen Sellschopp from FWG.
- From 06.02.2005 to 25.02.2005 with research vessel *Alkor*, chief scientist: Frank Janssen from IOW.
- From 05.02.2005 to 12.02.2005 with research vessel *Oceania*, chief scientist: Piotr Wieczorek from IOPAN.
- From 01.03.2005 to 10.03.2005 with research vessel *Oceania*, chief scientist: Piotr Wieczorek from IOPAN.
- From 07.11.2005 to 22.11.2005 with research vessel *Oceania*, chief scientist: Piotr Wieczorek from IOPAN.
- From 16.11.2005 to 29.11.2005 with research vessel *Professor Albrecht Penck*, chief scientist: Hans Burchard from IOW.

- From 23.01.2006 to 08.02.2006 with research vessel *Alkor*, chief scientist: Volker Mohrholz from IOW.
- From 03.04.2006 to 13.04.2006 with research vessel *Professor Albrecht Penck*, chief scientist: Hans Ulrich Lass from IOW.
- From 26.06.2006 to 30.06.2006 with research vessel *Professor Albrecht Penck*, chief scientist: Siegfried Krüger from IOW.

1.4.2 Numerical model

The numerical model GETM (*Burchard and Bolding* (2002), `www.getm.eu`) which has been applied for the regional model simulations of the Western Baltic Sea is a fully baroclinic and hydrostatic ocean model using general vertical coordinates. The model is implemented using the Arakawa C-grid (*Arakawa and Lamb*, 1977) for horizontal discretisation. For horizontal discretisation the characteristic numerical features of GETM are the mode splitting between the fast barotropic and the much slower baroclinic mode, the high-order advection schemes for tracer and momentum-advection (*Pietrzak*, 1998) and the possibility in applying various different turbulence closure models due to the implementation of the well-tested state-of-the-art turbulence model GOTM (General Ocean Turbulence Model, see `http://www.gotm.net`, *Burchard et al.* (1999) and *Umlauf et al.* (2005)). The turbulence closure model used for the coastal model setup is the k-ε model with transport equations for the turbulent kinetic energy (TKE), k, and the turbulence dissipation rate, ε. As second-moment closure, the model suggested by *Cheng et al.* (2002) is used. For calculating the internal pressure gradient the nonconservative Density-Jacobian scheme suggested by *Shchepetkin and McWilliams* (2003) is applied. For more details of the numerical model, see *Burchard et al.* (2009).
The advection of momentum and tracers is implemented using a directional-split scheme meaning that advection is calculated with subsequent full (or half) steps in x- and y -direction and a full step in z-direction. This makes it very simple to extract the amount of numerical mixing in each spatial direction of advection whereas the vertical physically induced diffusion of salinity is calculated as an own operational step after calculation of an intermediate tracer field (*Burchard and Rennau*, 2008; *Rennau and Burchard*, 2009). Open boundary conditions are applied using surface elevation and scalars (temperature and salinity).
Another feature of GETM to avoid the CFL criterion for explicit advection schemes being violated is that whenever the Courant number is larger than unity, the vertical advection time step is divided by the the next integer larger than the Courant number to calculate the vertical advection iteratively with a reduced time step.

The model simulation of the Western Baltic Sea had been carried out on a clus-

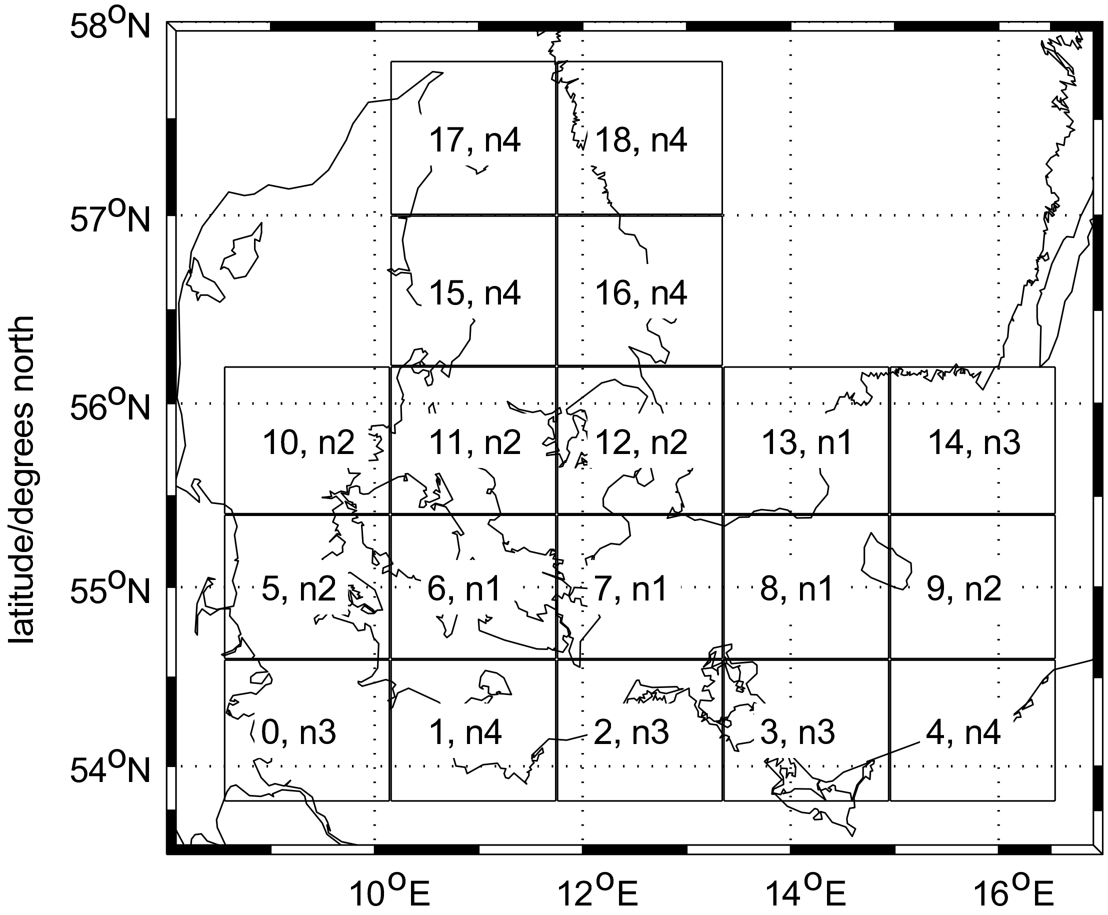

Figure 1.14: Domain decomposition map for the GETM simulation. The 19 subdomains (numbered 0-18) are allocated to the four available nodes of the LINUX-Cluster (with two processors each) in a way that the loads and communication times are balanced in an optimal way. The figure was taken from *Burchard et al.* (2009).

ter with 4 node dual-processor machines. The communication between the nodes was set up via a 100 MBits/s ethernet. The load-balancing in the parallel setup is achieved by aiming at a similar number of wet points on each computer in the cluster. This way the computational burden for the computers is balanced. Furthermore, neighbouring subdomains are - when possible - on the same computer node in order to minimise the traffic between nodes, see Fig. 1.14 for the distribution of subdomains to nodes.

Chapter 2

Results for natural mixing (IOW)

2.1 Field observations

2.1.1 Detection of medium-intensity inflow events by field observation.

Sellschopp et al. (2006) present results of a ship survey in the Arkona Sea that covered the period before, during and after a medium-intensity inflow of saline water in January/February 2004. These were the first detailed observation of such an event. Fixed monitoring stations, CTD stations and towed CTD-chain tracks used for the inflow event observation are given in Fig. 2.1.

The surface elevation differences that had driven the described inflow were caused by regional wind patterns (*Gustafsson and Andersson*, 2001). Westerly winds tend to raise the Kattegat sea level and lower the Arkona Sea level, thereby causing inflows, whereas easterly winds tend to cause outflows. The frictional balance has been confirmed by several studies (e.g. *Jakobsen et al.* (1997); *Green and Stigebrandt* (2002)), which have shown that the flow through the Sound can be well described by a quadratic friction law of type

$$\eta_N - \eta_S = KQ|Q| \tag{2.1}$$

where $\eta_N - \eta_S$ is the total sea level difference from south to north, which is taken to be equal to the water level difference, Q is the southward volume flux, and K is the specific resistance. *Jakobsen et al.* (1997) estimated the volume fluxes from ADCP measurements from the Drogden and Flinten Channels, and used sea level data from Hornbæk and Viken to the North and Rødvig and Skanör to the south. They found the average value for the specific resistance to be $K = 2.26 \times 10^{-12}\mathrm{s}^2\ \mathrm{m}^{-5}$. This value was used by *Sellschopp et al.* (2006) to calculate the volume fluxes from observed sea level differences between Viken and Skanör for the last half of

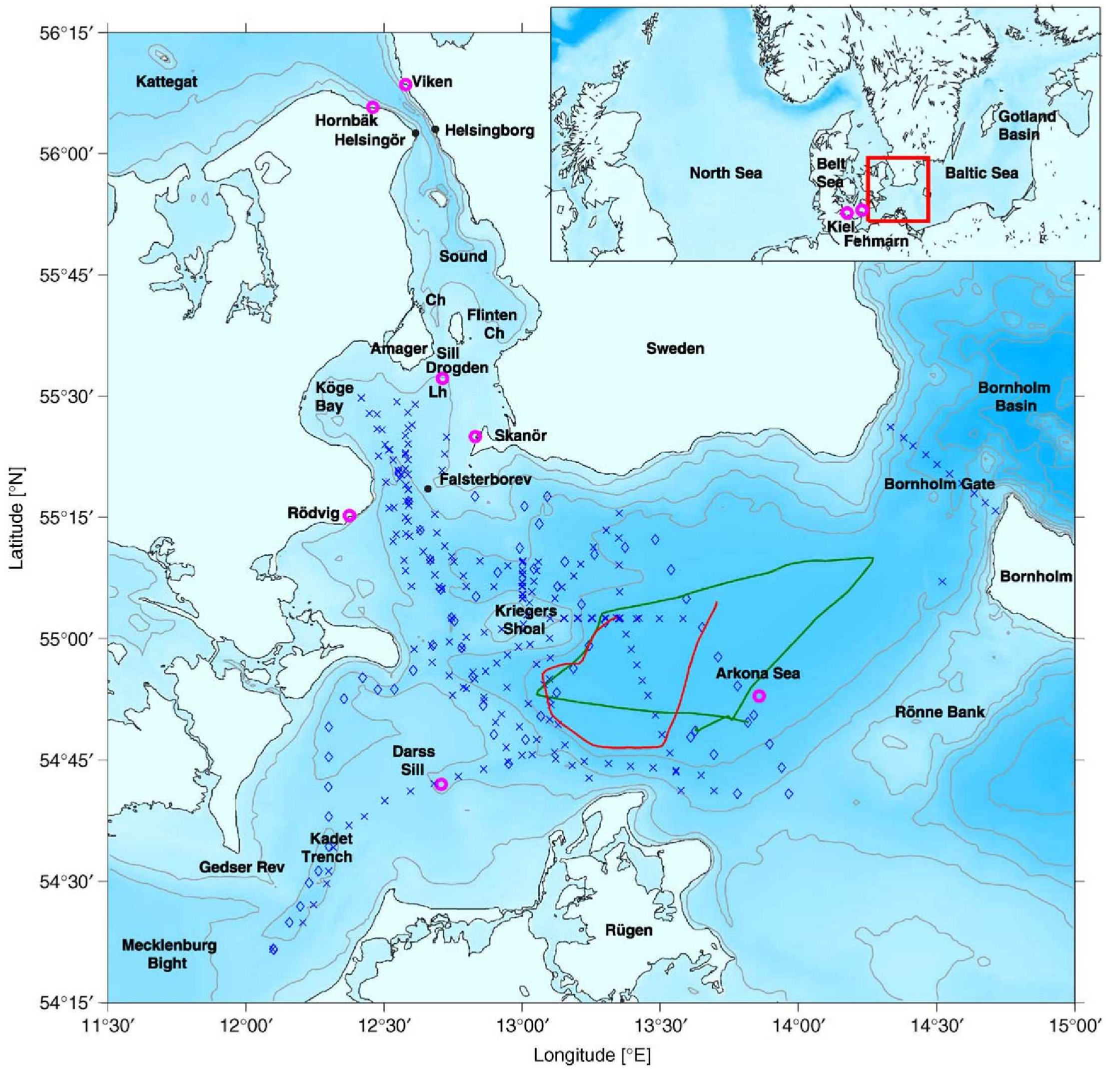

Figure 2.1: Topography of the Arkona Sea with bathymetry lines every 10 m, fixed monitoring stations (bold line rings), CTD stations before (diamonds) and after (crosses) the inflow event, towed CTD-chain tracks before (closed loop) and after (U-shaped) the inflow event observed by *Sellschopp et al.* (2006).

January and the first half of February 2004 (Fig. 2.2).

During the last half of January 2004 winds were variable (Fig. 2.2), causing no prolonged inflows or outflows through the Sound. Remainders of previous overspills had sufficient time to leave through the southern exit of the Sound. Bottom salinity exceeding 11 psu was nowhere found between Drogden Sill and Kriegers Flak. On January 26, winds turned to westerly directions at about 10 m s^{-1} and remained in westerly directions until February 11. The flows through the Sound reacted directly

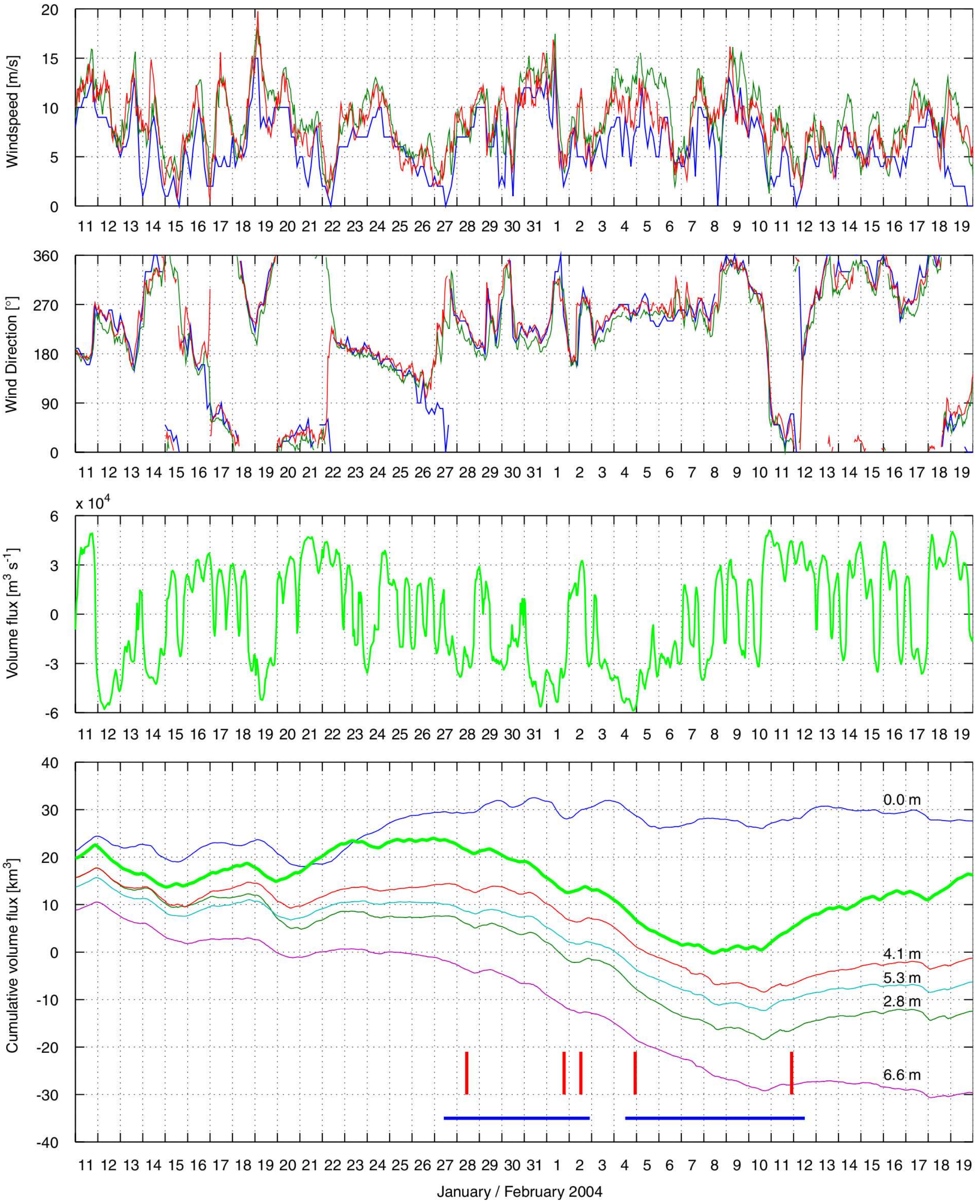

Figure 2.2: Time series of wind speed, wind direction from the Darss Sill Station (red), the Arkona Sea Station (green), and from Falsterbo (blue), and northward volume fluxes calculated from observed sea levels at Viken and Skanör (see Fig. 2.1) by means of eq. 2.1. Thin lines in the last panel are accumulated northward currents at Drogden lighthouse at different depths multiplied by a 0.08 km^2 cross-section. The bold curve is accumulated volume flux from the panel above. Horizontal bars at the bottom of the panel indicate two phases of the cruise . The instants of time when CTD sections in the southern Sound were obtained are marked by five vertical bars. This figure was taken from *Sellschopp et al.* (2006).

to the new wind field and became predominantly southward, which is clearly seen in the cumulated inflow curve. On February 1, a saline plume extending about 30 km south of the Sound was observed moving southward.

Sellschopp et al. (2006) observed, that after several weeks of rest or oscillations with periods too short to flush the connections between Kattegat and the Arkona Sea, all higher salinity water had left the shallower parts north-west of Kriegers Flak. The halocline separating the Baltic Sea surface water with salinities of around 8.5 psu and bottom water with salinity in excess of 15 psu was at 35-40 m depth, about 5 m above the bottom of the Arkona Basin. Temperature fine structure in the halocline and above showed various inflows in the distant or close past before the described observations. The advancement of the inflow forefront and the retreat of older bottom water as observed a few days after the inflow had begun, illustrated that the deepest parts of the basin were flooded in an early stage of the event.

In the saline water layer in the southern Sound, in the branches north and west of Kriegers Flak and in the Bornholm Channel *Sellschopp et al.* (2006) observed current velocities of the order 0.5 m s^{-1} and up to 1 m s^{-1}. Pycnoclines showed geostrophic balance in the transverse current direction. North of Kriegers Flak the densest bottom water was found on the left side of the current (see also sect. 2.1.3 and 2.1.4 for the description of the transverse structure of the bottom current). Another strong current setting east along the coast of Rügen consisted of water from the Darss Sill, a mixture of Baltic surface water and saline bottom water which had been present in the bottom layer of the Mecklenburg Bight before.

Turbulence measurements described by *Sellschopp et al.* (2006) showed high dissipation rates in the bottom plume and the pycnocline north of Kriegers Flak. Eddy diffusivity was large except within the depth range of the pycnocline and directly above and very large in the bottom layer.

2.1.2 Spatio-temporal evolution of the dense bottom currents.

In fact, until before the QuantAS consortium was established, the propagation of medium intensity inflow events had not been directly observed.

It was by idealised numerical model simulations that the pathways of Drogden Sill inflow events have first been hypothesised. By using different numerical models, and in contrast to the assumptions of *Lass and Mohrholz* (2003), *Burchard et al.* (2005) and *Lass et al.* (2005) found that the preferred pathway of such dense bottom currents should be southward from the Drogden Sill, with a turn to the east at about 55°10'N, such that the saline water flows along the channel north of Kriegers Flak from where it enters the dense bottom pool in the eastern Arkona Basin.

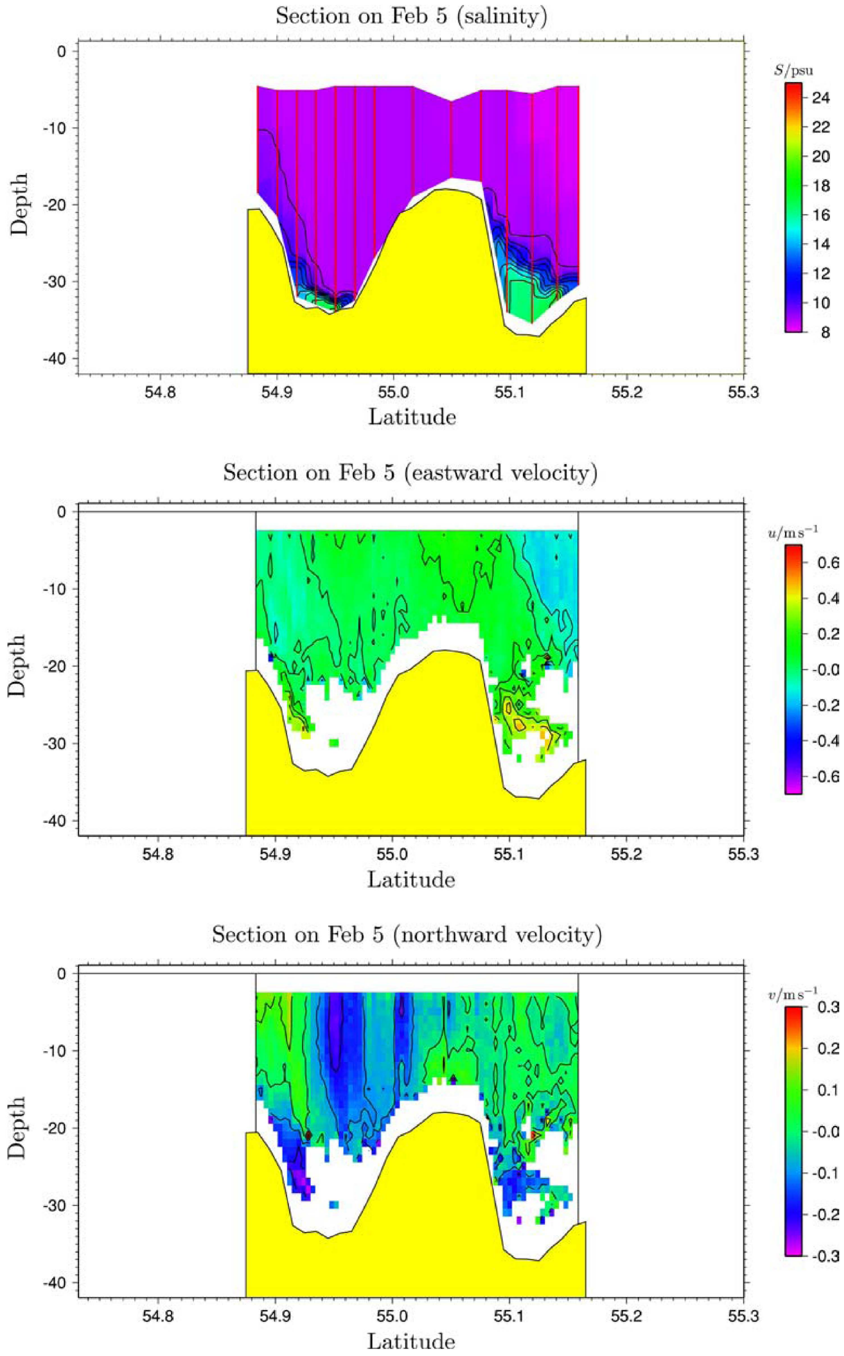

Section on Feb 5 (salinity)

Section on Feb 5 (eastward velocity)

Section on Feb 5 (northward velocity)

Figure 2.3: Observed salinity and current velocity on a north-south transect across Kriegers Flak deduced from CTD profiles and ADCP observations, respectively. The observations were taken on February 5, 2004 from 10:45 to 15:31 h. The red lines show the positions of the single CTD profiles. The figure has been taken from *Burchard et al.* (2005).

Observations in January/February 2004 indeed confirmed this predicted behaviour (*Burchard et al.*, 2005; *Sellschopp et al.*, 2006)). Knowing the major pathways of dense bottom currents into the Baltic Sea helps to identify locations which are less suitable for the erection of offshore wind farms, since there dilution effects due to structure-flow interaction would be relatively large. The salinity and velocities for the medium-intensity inflow in 2004 are given in Fig. 2.3 for the trenches north and south of Kriegers Flak. It is clear from this figure that, as predicted by means of the numerical model, the preferred pathway of the inflow is north of Kriegers Flak. This observation was also confirmed by *Szewczyk* (2009), see next paragraph.

The medium-intensity inflow in November 2005 was observed in detail by R/V Oceania operated by QuantAS project partner Institute for Oceanography of Polish Academy of Science (IOPAN). In Fig. 2.4 CTD and ADCP transects taken by the R/V Oceania are shown. The data were investigated and compared with the GETM model by *Szewczyk* (2009). Fig. 2.5 gives a qualitative impression about the situation in the Arkona Basin during and after the inflow. The inflow started in the beginning of November. Shown are simulated bottom salinities on November 6, 12, 18 and 30, 2005. The lines mark the inflow propagation as observed in the in-situ measurements. Red lines marks the warmer part of the inflow with salinities up to 17 PSU, whereas the green one the following, colder part with salinities up to 25 PSU.

Model simulations of the propagation of this inflow into the Western Baltic Sea are described in more details in sect. 2.2.1 and 2.2.2.

2.1.3 Direct observation of the dense bottom currents in the Arkona Basin and Bornholm Channel.

Umlauf et al. (2007), *Umlauf and Arneborg* (2009a), *Umlauf and Arneborg* (2009b) and *Reissmann et al.* (2009) presented cross-sectional high-resolution observations of the medium-intensity inflow event occurring in November 2005 in the channel north of Kriegers Flak, including data for temperature, salinity, current speed and direction, and the turbulent dissipation rate.

The observations of the transverse structure of the density current reveal a distinct transverse circulation pattern as it has been observed by *Paka et al.* (1998) for the Słupsk Furrow east of the Bornholm Basin. It is obvious from the observations by *Umlauf et al.* (2007) that turbulent entrainment is significantly modified by this transverse structure of the dense bottom current. MSS (see section 1.4.1.3) transects made by *Umlauf et al.* (2007) are shown in Fig. 2.6.

The transverse structure of the dissipation rate, ε, across the channel obtained from repeated casts of the micro-structure profiler is displayed in Fig. 2.7. It shows four clearly distinct regions.

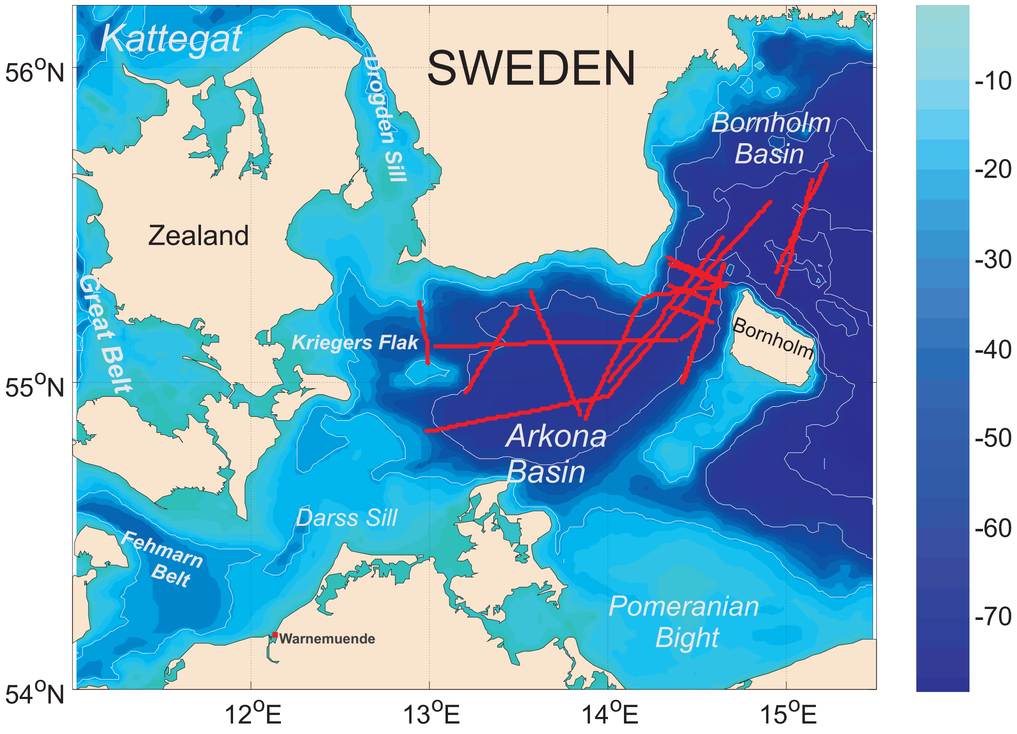

Figure 2.4: Transects taken by R/V Oceania during the November 2005 cruise (red lines). This figure has been taken from *Szewczyk* (2009).

Clearly visible was a vigorously turbulent gravity current with dissipation rates reaching $\varepsilon \approx 10^{-4}$ W kg^{-1}, separated by a strongly stratified but turbulent interface from the quiescent ambient fluid with dissipation rates several orders of magnitude lower. Turbulence in the gravity current exhibited a rich internal structure.

Most obvious and physically most intuitive are the strongly enhanced dissipation rates (Fig. 2.7) in the bottom boundary layer (region I), which can be shown to decrease away from the sediment in good agreement with the law of the wall. Increased near-bottom dissipation rates have also been observed in other gravity currents (*Wesson and Gregg*, 1995; *Johnson et al.*, 1994; *Peters and Johns*, 2005, 2006), and have been attributed to the effect of bottom friction. In the central part of the plume, boundary layer turbulence is separated from the turbulent interface (region II) by the nearly quiescent region III - the core of the plume with very low dissipation rates. This quiet core approximately coincides with the region of maximum speed, a fact that is surprising only at first glance: near the velocity maximum, the

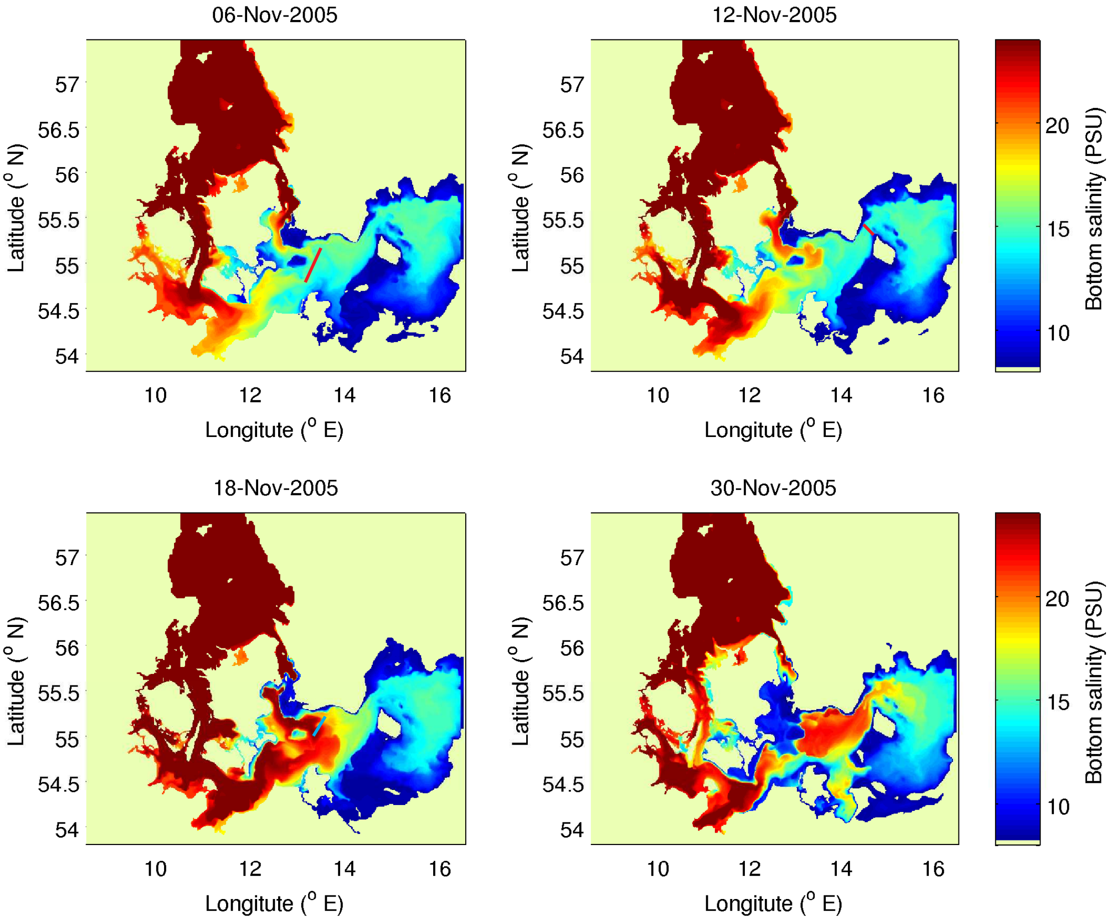

Figure 2.5: Simulated bottom salinity in the Arkona Basin during the medium intensity inflow in November 2005. Clockwise starting from the left-upper panel data from: 6th, 12th, 18th an 30th of November 2005 are displayed. The lines mark the inflow propagation as observed in the in-situ measurements. Red colour marks the warmer part of the inflow with salinities up to 17 PSU, whereas the green one the following, colder part with salinities up to 25 PSU. This figure has been taken from *Szewczyk* (2009)

.

shear, and therefore the shear production of turbulent kinetic energy, is small, and turbulence has insufficient energy supply to overcome the relatively weak stratification.

Above this local minimum of turbulence, the data revealed a turbulent interface (region II) with consistently enhanced dissipation levels, often exceeding 10^{-6} W kg^{-1}. This local maximum of turbulence has also been identified in the same channel in the single-station turbulence measurements presented by *Arneborg et al.*

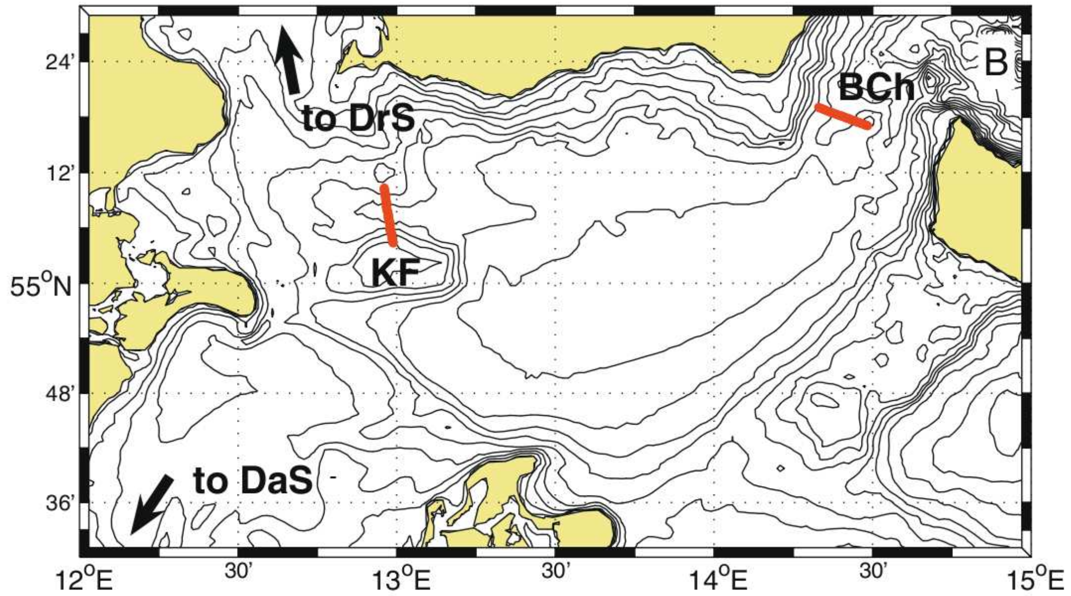

Figure 2.6: Detailed map the Arkona Basin. The arrows in map indicate the direction to the Darss Sill (DaS) and Drogden Sill (DrS). Indicated in red are the transects north of Kriegers Flak (KF) and across the Bornholm Channel (BCh), shown in Figs. 2.7 and 2.8, respectively. The bathymetry is drawn in contours with a spacing of 5 m, the inner contour in the Arkona Basin is at 45 m depth. The Fig. was taken from *Reissmann et al.* (2009).

(2007) and *Sellschopp et al.* (2006), as well as in other gravity currents observed by *Johnson et al.* (1994) and *Fer* (2006). Since, in contrast to the bottom boundary layer, interfacial turbulence had been associated with a strong density gradient, the contribution of this region to the overall entrainment was dominant.
A remarkable asymmetry in mixing was apparent between the southern and northern edges of the gravity current. Whereas at the northern edge, the vertical structuring of the dissipation rate as described above persisted until the interface intersects with the bottom, at the southern edge (region IV) high dissipation rates could be observed throughout the gravity current. Described dissipation pattern was also observed by *Umlauf et al.* (2007) for the Bornholm Channel (Fig. 2.8).
Results obtained by *Umlauf et al.* (2007) clearly demonstrate that the assumption of a constant entrainment velocity across a rotating gravity current is a rather coarse approximation. The observed asymmetry was related to rotational effects also manifested in the asymmetry of the interface thickness and the generation of a strong across-channel density gradient. This structure was similar to what we have seen during additional observations in similar channels in 2004 - 2006, and

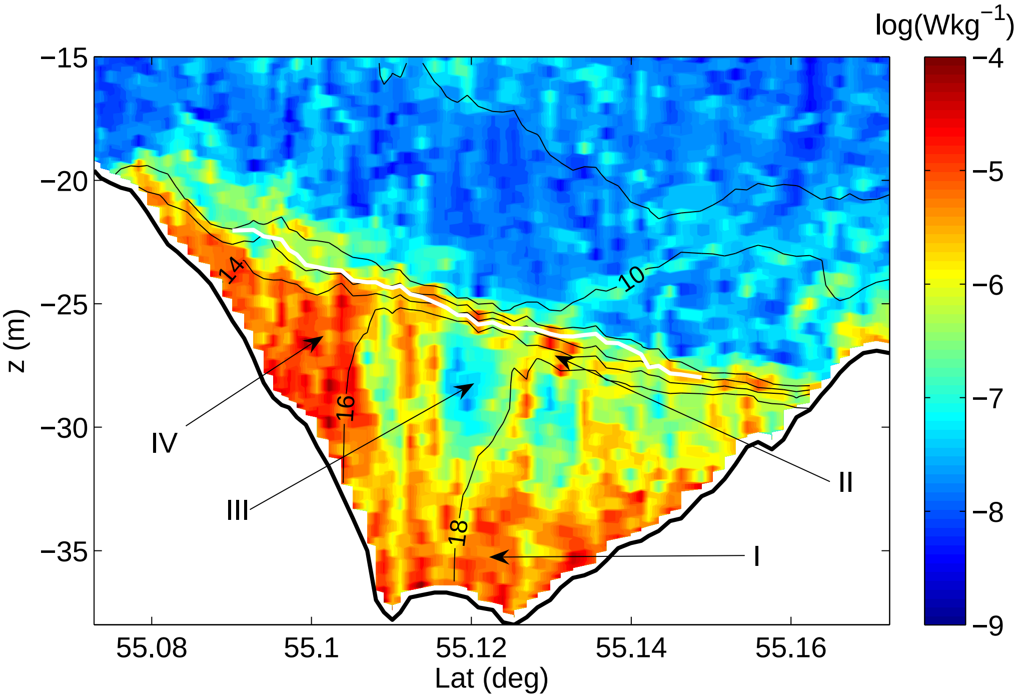

Figure 2.7: Decadal logarithm of the dissipation rate (colours), and contours of potential density σ_t (for clarity plotted here only at 2 kg m^{-3} intervals). Roman numbers indicate dynamical regimes discussed in the text. The Fig. was taken from *Umlauf et al.* (2007).

therefore appeared to be a stable result. The transverse structure of the dense bottom current was further investigated inside of the QuantAS project by *Umlauf and Arneborg* (2009b) (see section 2.1.4), and then numerically reproduced by *Umlauf et al.* (2010) (see section 2.2.3).

2.1.4 Analysis of transverse structure of the dense bottom currents

Umlauf and Arneborg (2009b) made an analysis of a class of shallow, channelised gravity currents, characterised by Ekman numbers of the order of one and subcritical Froude numbers as they are typical for the Western Baltic Sea. Geometry for the analysed channelised bottom gravity current is given in Fig. 2.9. The analysis provided substantial support for the mechanism of frictional control as suggested in the theoretical model by *Wåhlin* (2002, 2004): the down-channel velocity is adjusted exactly such that friction balances the down-channel pressure gradient, and the cross-channel Ekman transport is compensated by the oppositely directed geostrophic transport due to the down-channel tilt of the interface.

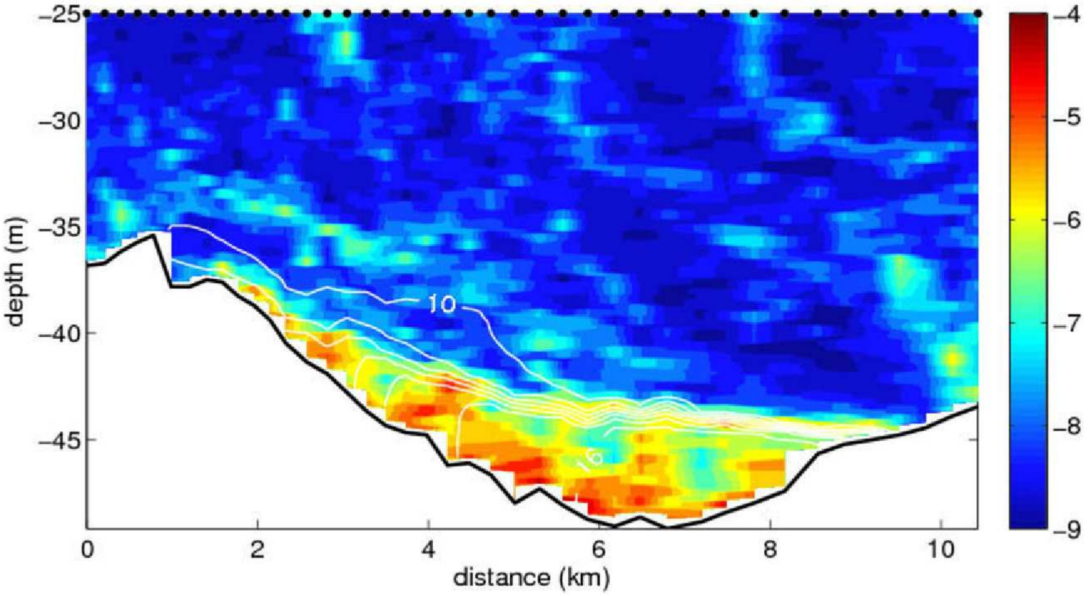

Figure 2.8: As Fig. 2.7 , for a transect across the north-western part of the Bornholm Channel, as indicated in Fig. 2.6, on November 19, 2005 between 10:20 h and 12:30 h UTC, south-east is to the left and north-west is to the right. The salinity contours are drawn as intervals of 1 g/kg here. The upper 25 m of the transect are not shown. The Fig. was taken from *Reissmann et al.* (2009).

Apart from the condition of vanishing cross-channel transport, however, the simple model of *Wåhlin* (2002, 2004) does not explain the vertical structure of the transverse circulation associated with the different types of transverse transport. *Umlauf and Arneborg* (2009b) suggested that the key role is played here by a nearly geostrophically balanced jet in the interface, transporting interfacial fluid to the right of the down-channel flow with a number of important implications for the evolution of the density field and the entrainment process. First, the transverse component of the vertical shear in the interface was shown to be proportional to the Ekman number, E_k, defined as

$$E_k = \frac{C_D u}{f D}, \tag{2.2}$$

with u being the depth-averaged plume velocity in the along channel direction, D denoting the plume thickness, f denoting the Coriolis parameter, and C_D denoting the bottom drag coefficient for related to vertically averaged flow. It became comparable to the down-channel shear for $E_k = O(1)$, i.e. for the range of values observed by *Umlauf and Arneborg* (2009b). The transverse component of the vertical shear therefore is an important source of interfacial turbulence, and may

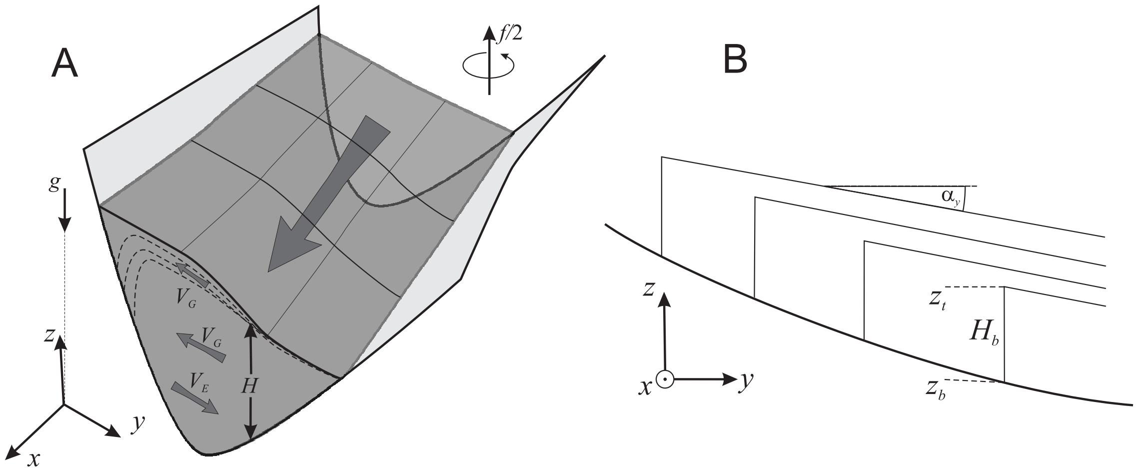

Figure 2.9: Geometry for channelised bottom gravity current rotating at a constant rate, $f/2$ with down-channel velocity indicated by large arrow. Dashed lines illustrate the density structure, and the directions of the cross-channel Ekman transport, V_E , and the geostrophic transport, V_G , are indicated by small arrows. H is the gravity current height. This figure has been taken from *Umlauf and Arneborg* (2009b).

explain the strong positive correlation between E_k and the entrainment parameter, $E = \partial D/\partial_x$ (with D being plume thickness and x the along-channel coordinate), found by *Umlauf and Arneborg* (2009b) in cross-sectional data. Second, being laterally confined by topography, the transverse transport inside the interface induces a lateral distortion of the interfacial density structure, visible as a pinching of the interface to the left of the down-channel flow (northern side here), and a spreading of isopycnals to the right (Fig. 2.10).

From this, and from a simple budget for the buoyancy in the southern part of the channel, the following picture emerged, describing the complex role of the interfacial jet in the entrainment process (*Umlauf and Arneborg* (2009b)). The jet transports premixed interfacial fluid of intermediate buoyancy towards the southern part of the channel, thereby providing an advective source of buoyancy that dominates the local entrainment of ambient fluid in the southern part. The advected, buoyant fluid is mixed down by strong turbulence on the southern slope, and is then advected back towards the centre of the channel with the transverse return current in the interior (Fig. 2.10). This process of *entrainment around the corner* also created the wedge-shaped interface, and the characteristic lateral buoyancy gradient in the interior. Interestingly, although it was shown that the thermal wind shear associated with this lateral buoyancy gradient is comparable to the total shear, *Umlauf and Arneborg* (2009b) did not observe any indications for slippery boundary layers as suggested for a (only seemingly) similar situation by *MacCready and Rhines* (1993).

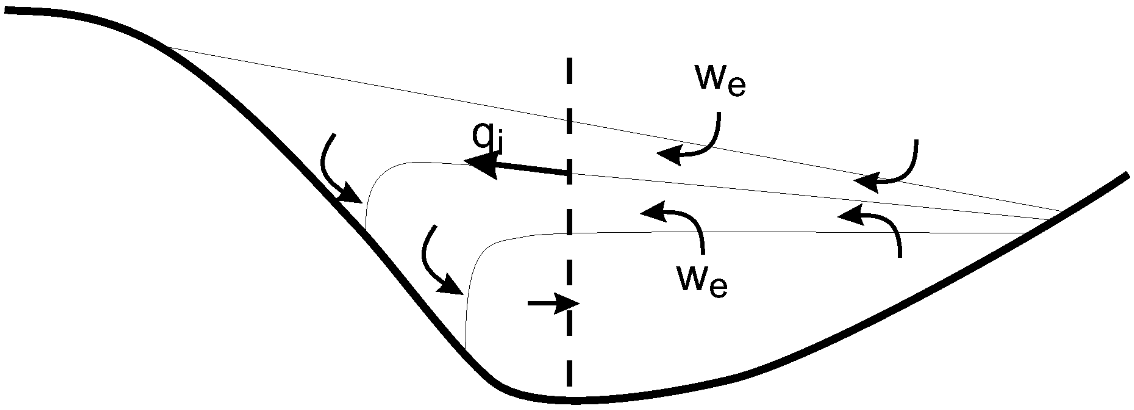

Figure 2.10: Schematic view of the entrainment process and the effect of the interfacial jet. The down-channel flow is directed out of the page. This figure has been taken from *Umlauf and Arneborg* (2009b).

Instead, the flow adjusted in a rather unexpected way to the presence of the lateral buoyancy gradient in the interior: the cross-channel near-bottom velocity reverses, and a new bottom layer appears with transverse velocities and stresses opposite to those predicted from classical Ekman theory.
Given the critical role of the interfacial jet in this picture, one important question arises. Is the transverse transport in the jet limited by entrainment in the northern part of the gravity current, or does the jet control the entrainment process such that a sufficient supply of entrained fluid is always available? The following argument discussed by *Umlauf and Arneborg* (2009b) suggested that the latter is more likely. Without mixing, the draining of interfacial fluid in the northern part would eventually lead to a very thin interface. Since the buoyancy and velocity jumps across the interface are not affected by this process, this would imply that the gradient Richardson number, Ri, (definition of non-dimensional constants are given in *Umlauf and Arneborg* (2009b)) in the interface eventually becomes arbitrarily small, and the interface would thus become increasingly unstable with respect to shear instabilities. There is substantial evidence (see e.g. *Peters and Johns* (2005)), however, that mixing would counteract this interface thinning by adjusting the interface thickness such that the Richardson number always remains above a certain critical threshold, $Ri > Ri_c$.

2.2 Numerical modelling

2.2.1 Idealised modelling of the medium-intensity inflow events

Burchard et al. (2005) combined observational and model results to study of the medium-intensity inflow in January/February 2004. They simulated the dynamics of medium-intensity inflow events over Drogden Sill, using the GETM (*Burchard and Bolding*, 2002; *Burchard et al.*, 2004; *Umlauf and Lemmin*, 2005). For the discretisation, a high-resolution bathymetry (0.5 nm resolution) had been used as well as bottom- and surface-fitted vertical coordinates with 25 vertical layers and a horizontally homogeneous bottom layer thickness of 0.4 m, such that the flow could smoothly advect along the bed. For momentum and salinity, the third-order Total Variation Diminishing (TVD) advection scheme by *Leonard* (1991) was applied by using a directional-split method as suggested by *Pietrzak* (1998). Temperature variations have been neglected in this idealised simulations. The model domain had open boundaries at the northern end of the Sound, towards the West across the Fehmarn Belt and towards the East along $14^o46.5$ E.

The model was forced by a sea surface elevation slightly increased by 0.02 m at the boundary to the Kattegat in the North and a prescribed salinity for inflowing water of 25 psu, whilst the sea surface elevation was forced to zero elevation at the other open boundaries. As initial conditions, flow at rest with a salinity of 8 psu was chosen. At the sea surface a spatially and temporally homogeneous wind stress of 0.22 N m^{-2} from south-west (240^o) is applied to the momentum equations. This value has been calculated from a wind speed of 12 m s^{-1} typical for early February 2004 according to the bulk formula by *Large and Pond* (1981). Compared to full-scale realistic simulations, the idealisations were due to the homogeneous initial and boundary conditions, the stationary and homogeneous surface stresses, and the neglect of surface and boundary heat fluxes.

The observed general structure of the plume was in good agreement with the idealised model simulation. Main features were strong shear and stratification at the interface between plume and ambient water, with a velocity jump of more than 0.5 m s^{-1} and a salinity jump of more than 10 psu over 3 m. Inside the plume, salinity was homogeneous and velocity followed the law of the wall. Cross-sections through the plume showed that the interface between the plume and ambient water is sloping to the right, and the salinity core is displaced towards the left, similar to the theoretical results discussed in the previous section. The comparison of observed and modelled salinity and current velocity north of Kriegers Flak are given in Fig. 2.11.

It was concluded by *Burchard et al.* (2005) that deeper insight into the dynamics of medium-intensity inflow events required more refined modelling, with realistic forc-

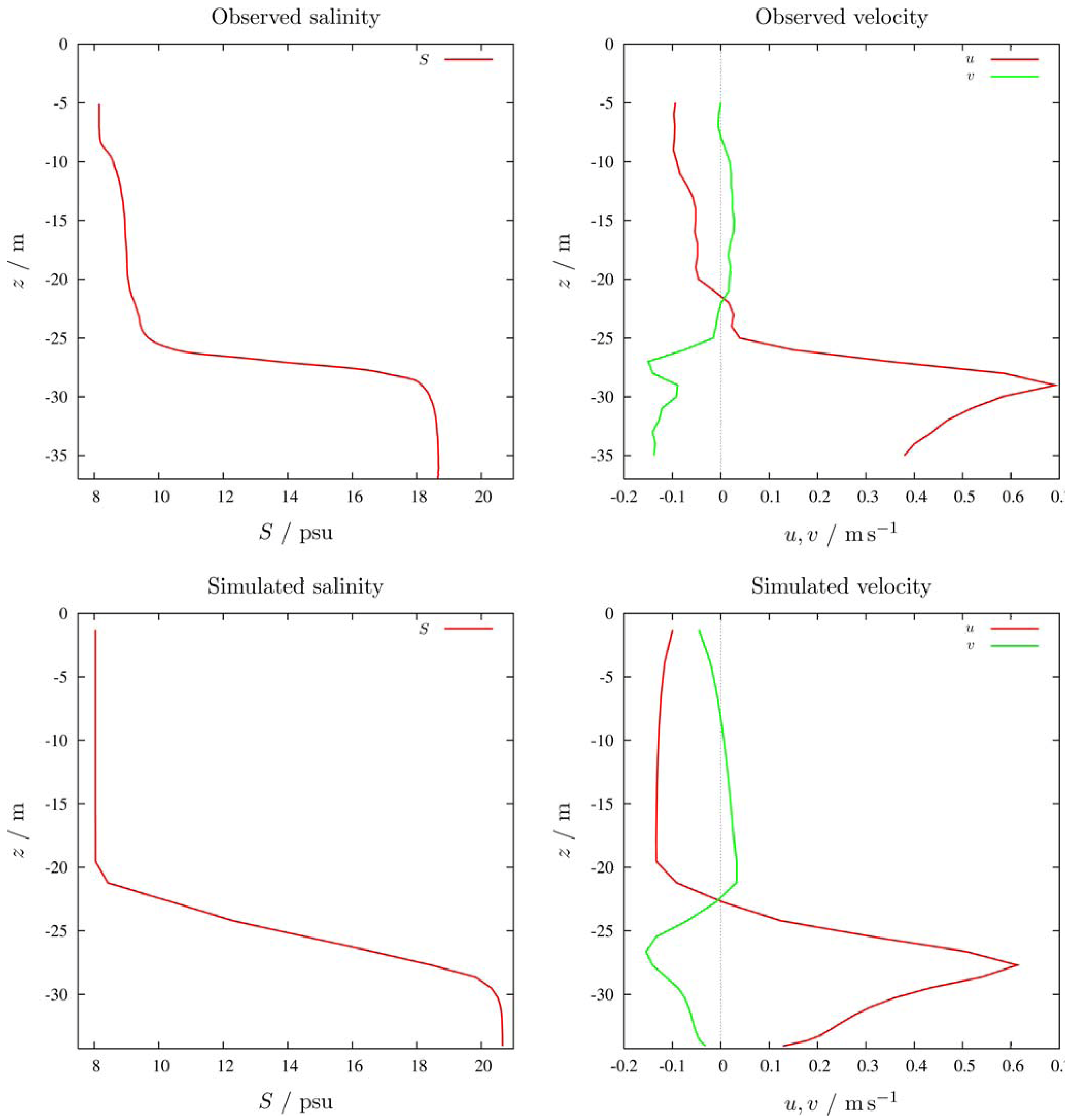

Figure 2.11: Observed salinity and current velocity (upper panels) and simulated salinity and current velocity (lower panels) at a position north of Kriegers Flak during a medium-intensity inflow situation on February 7, 2004 at 4 a.m. Shown for the observations are hourly averages. The figure has been taken from *Burchard et al.* (2005).

ing at the surface and the lateral boundaries and a larger model domain. It was also necessary to analyses and, if needed, to improve the numerical mixing properties of the model. The 25 model layers refined towards the bottom were not sufficient to resolve the sharp gradients at the interface between the plume and ambient water.

In contrast to this, the physical mixing prediction of the model was fairly realistic due to the use of a well-tested turbulence closure model. The realistic modelling of the inflow event was done by *Burchard et al.* (2009) and is described in the following section 2.2.2.

2.2.2 Realistic modelling of the medium-intensity inflow events

The potential of numerical models to reproduce the Arkona Basin dynamics in a qualitatively and quantitatively satisfying way has been demonstrated by *Burchard et al.* (2005) and *Arneborg et al.* (2007). The latter successfully applied a one-dimensional water column model for simulating observations of current, density and turbulence at a 19-hour station in the dense bottom current north of Kriegers Flak.

Inside the QuantAS projects, *Burchard et al.* (2009) used the General Estuarine Transport Model (GETM, see `www.getm.eu` and *Burchard and Bolding* (2002)) for simulating the dynamics of the Western Baltic Sea during 9 months between September 2003 and May 2004, including the period of the field observations (first QuantAS cruise - see sect. 1.4.1.5) obtained in early February 2004, as documented by *Sellschopp et al.* (2006). Since observations of boundary values cannot be obtained in high enough quality, the boundary conditions for the Western Baltic Sea model needed to be generated by the larger scale Modular Ocean Model (MOM-3.1, see *Griffies et al.* (2001) for the general numerical model and *Neumann et al.* (2002); *Janssen et al.* for the Baltic Sea applications).

The Baltic Sea MOM-3.1 model was applied with a horizontal resolution of 3 nm and 77 vertical (geopotential) grid layers, with a near-surface resolution of 2 m, decreasing with depth. The simulation was initialised with temperature and salinity analyses from observations (see *Meier et al.* (1999)) on May 1, 2002, and forced with surface meteorology from ECWMF Reanalysis Project ERA40 with a resolution of 100 km and 6 hours (until August 2002) and the German Weather Service Global Model with a resolution of 60 km and 6 hours (from September 2002). From the large scale Baltic Sea simulation, surface elevations at the open boundaries of the Western Baltic Sea model (between Kattegat and Skagerrak at 57°30'N and east of the Bornholm Basin at 16°30'E) are stored every 15 min. for the surface elevation and every hour for temperature and salinity.

The Western Baltic Sea simulation (see Fig. 1.2 for the bathymetry) was then initialised on September 1, 2003, with temperature and salinity interpolated from the Baltic Sea model, and was forced with the German Weather Service Local Model with a resolution of 7 km and 3 hours. Lateral boundary conditions were interpolated from the Baltic Sea model as discussed above. The model resolution was 1/2 nm in the horizontal, and 50 general vertical coordinate layers, with a non-linear

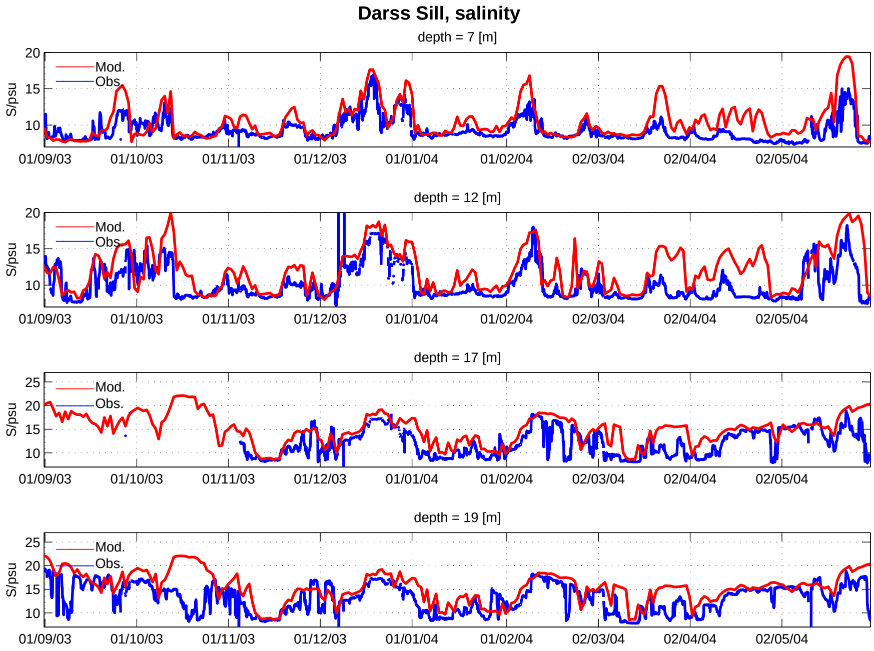

Figure 2.12: Time series of salinity at the Darss Sill buoy. Blue: observations, red: model results. Shown are data at 7 m, 12 m, 17 m and 19 m below the mean sea level. The mean water depth at this station is 20 m. This figure has been taken from *Burchard et al.* (2009).

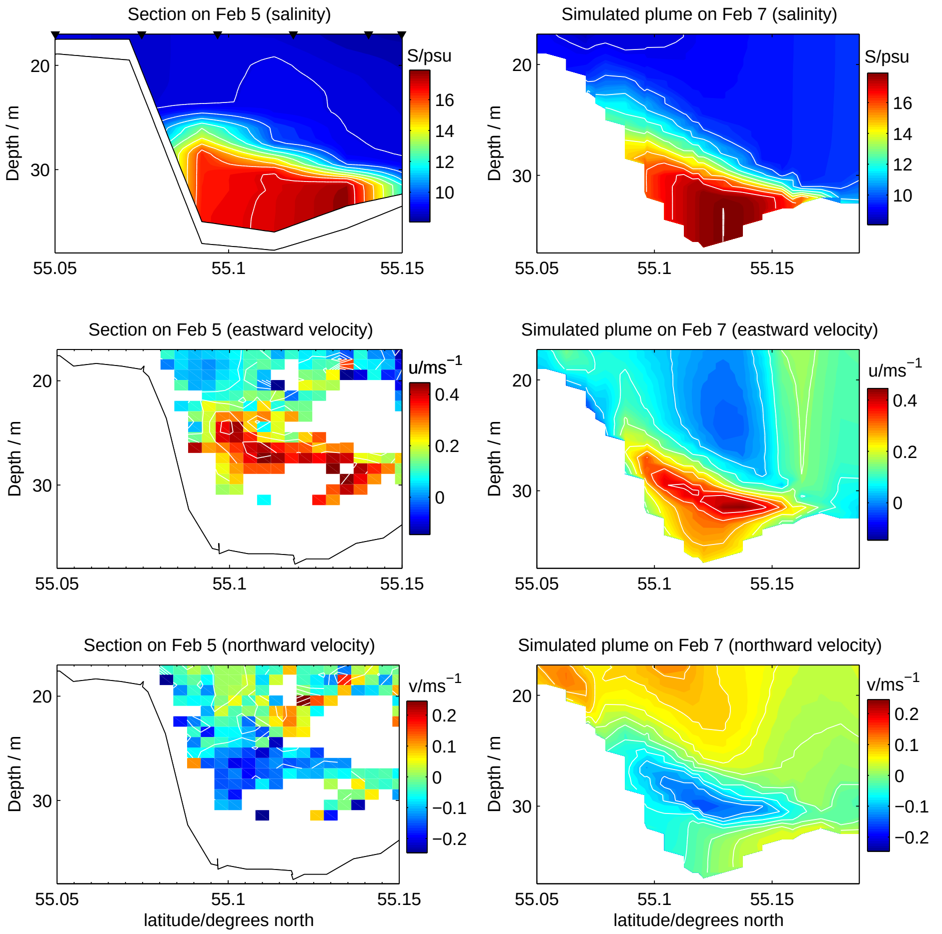

Figure 2.13: Observed (left) and simulated (right) salinity and current velocity on a north-south transect across the channel north of Kriegers Flak, deduced from CTD profiles and Acoustic Doppler Current Profiler. The observations were taken on February 5 from 10:45 h - 12:30 h (UTC). The black triangles in the upper left panel show the positions of the single CTD profiles. This figure has been taken from *Burchard et al.* (2009).

zooming towards the bed.

Problems in simulating the volume and salinity transports have motivated some further adjustments in the model bathymetry and open boundary conditions. The smoothed and unmodified Western Baltic Sea bathymetry turned out to lead to an underestimation of salinities in the Fehmarn Belt and the Drogden Sill. Step-wise bathymetry changes in the Great Belt and the Sound and concurrent model validation with station measurements have resulted in an increase of depth of parts of the Great Belt by up to 35% and in the Sound by up to 15% to obtain reasonable agreement with measured salinities for the Drogden Sill station and the Fehmarn Belt. Due to the two open boundaries at which sea levels from the Baltic Sea model were prescribed the net flow through the Western Baltic Sea had to be adjusted. This was done by increasing the barotropic pressure difference between both open boundaries. An increase of the mean surface elevation at the eastern boundary by 0.05 m turned the unrealistic net inflow into the semi-enclosed Baltic Sea into a net outflow. The original net inflow was probably due to balances between mean surface and bottom stresses which are different between the high- and the low resolution models. Figure 2.12 shows that the simulated salinities over Darss Sill agree well with the observations. Comparison for other moorings are given in *Burchard et al.* (2009).

The simulation results presented by *Burchard et al.* (2009) which had been compared to selected field observations showed that the numerical model has a reasonable predictive capacity. This has been achieved by choosing (i) hydrostatic model equations with a well-tested turbulence closure model, (ii) meteorological forcing from a high-resolution atmospheric model and boundary conditions from a well-calibrated Baltic Sea model, and (iii) high-order numerical methods for discretising the model equations. The observation-simulation comparison of sea levels north and south of the Sound, and the salinities at various depths at Drogden Sill, Darss Sill and the Arkona Basin made by *Burchard et al.* (2009) demonstrated that all significant inflow events are reproduced throughout the nine months of simulation (with the exception of the Drogden Sill, where only three months could be considered). A more detailed inspection of a single inflow event over the Drogden Sill showed that the timing and the intensity of this specific overflow was inaccurate. However, the dynamic structure of the resulting dense bottom current fitted well with observations when shifted in time by a few days. The simulated passage of the Drogden Sill overflow north of Kriegers Flak in early February 2004 was therefore compared to model simulation results for February 7, see Fig. 2.13.

The time shift was necessary in order to account for effects of model inaccuracies in terms of forcing and bathymetry, resulting in a wrong position of the Kattegat front before the inflow. With the Kattegat front displaced too far to the north, high salinity waters reach the Drogden Sill too late after the onset of an inflow event. In Fig. 2.13, the cross-sectional plume structure which had already been discussed for that position in more detail by *Burchard et al.* (2005), *Sellschopp et al.* (2006) and *Umlauf et al.* (2007) can be seen. The plume was to first order geostrophically adjusted and was leaning towards the northern slope of Kriegers Flak, in good agreement with the observations shown by *Sellschopp et al.* (2006).

Thus, *Burchard et al.* (2009) concluded that the model simulations reproduce significant inflow events and their statistics with acceptable accuracy. The modelled inflow propagation is given in Fig. 2.14. The results obtained for vertical mixing are described in sect. 2.2.4.

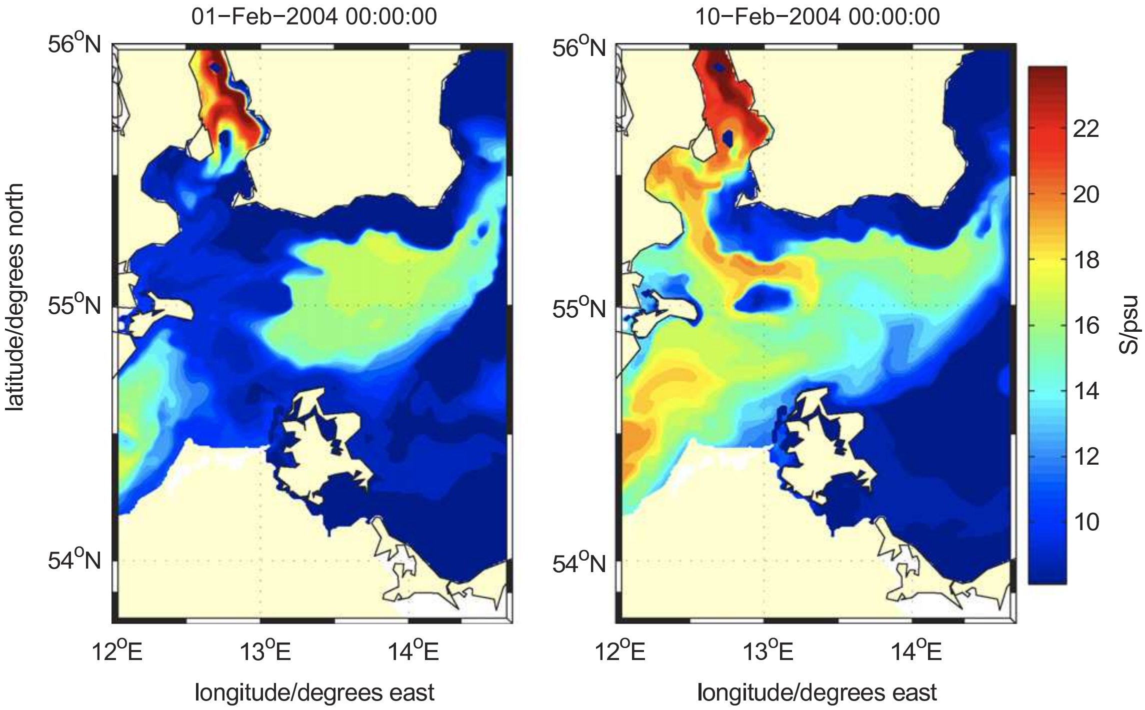

Figure 2.14: Observed salinity and current velocity (upper panels) and simulated salinity and current velocity (lower panels) at a position north of Kriegers Flak during a medium-intensity inflow situation on February 7, 2004 at 4 a.m. Shown for the observations are hourly averages. The figure has been taken from *Burchard et al.* (2009).

2.2.3 High-resolution modelling of transverse structure of channelised dense bottom currents

The transverse structure of the gravity currents were numerically reproduced by *Umlauf et al.* (2010). In order to allow for sufficient resolution of the strong vertical gradients in salinity and velocity occurring at the northern slope of the channel (see Fig. 2.7), the vertically adaptive coordinates by *Hofmeister et al.* (2010) had to be used. The investigated gravity currents were characterised by (a) small entrainment rates, (b) small thickness compared to the Ekman layer thickness (i.e. large Ekman number), and (c) width comparable to the internal Rossby radius. The results were in close agreement with turbulence measurements of channelised gravity currents in the Western Baltic Sea (*Arneborg et al.*, 2007) and numerical results indicate substantial interfacial mixing and entrainment even far below the critical Froude number (for definitions of non-dimensional numbers, see *Arneborg et al.* (2007)). Entrainment in this low Froude number range was in contradiction with the classical experiments (*Ellison and Turner*, 1959; *Turner*, 1986) but consistent with more recent laboratory studies (*Cenedese and Adduce*, 2008), and has considerable implications for predicting the final water properties of dense gravity currents, and thus the basin-scale stratification (*Wåhlin and Cenedese*, 2006; *Hughes and Griffiths*, 2006).

The modelled down channel and cross-channel structure of the velocity field obtained by *Umlauf et al.* (2010) is shown in Fig. 2.15. The down-channel velocity has a general tendency for a reduction of the speed near the edges where frictional

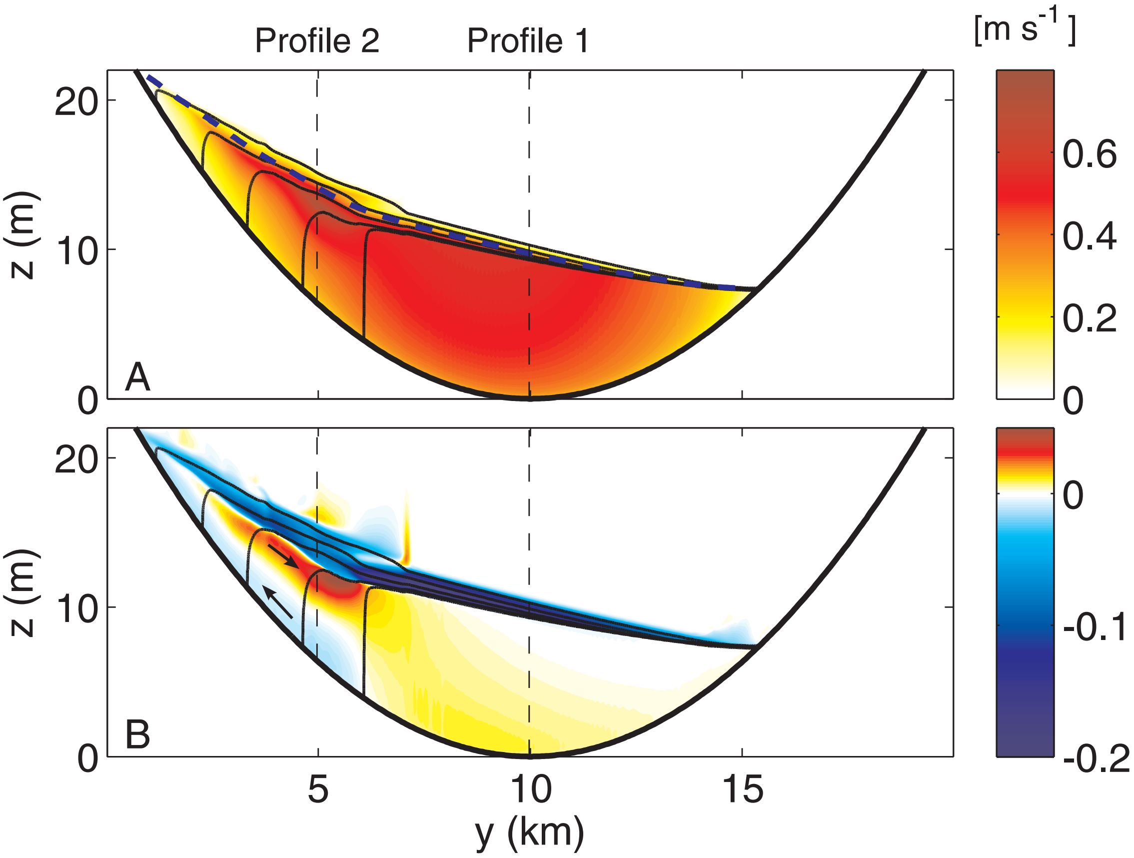

Figure 2.15: Modelled down-channel (upper panel) and cross-channel (lower panel) velocity. Buoyancy is plotted as black contour lines at 0.02 m s^{-2} intervals. The dashed blue line in (a) denotes the bulk interface position. The black arrows illustrate the transverse circulation. This figure has been taken from *Umlauf et al.* (2010).

effects become more dominant. Except in the region with the lateral interior buoyancy gradient, the vertical structure of the cross-channel velocity displayed in Fig. 2.15b shows a strong transverse jet with speeds between 0.1 and 0.2 $\mathrm{m\,s^{-1}}$ which is confined to the wedge-shaped interface, and a weak return current is observed in the bulk. On the left slope, in the region with lateral interior stratification, the situation is rather different. The two-layer transverse circulation is replaced here by a three-layer pattern with a broader but weaker jet in the interface, a strong return current just below the interface, and a third layer with weak up-slope currents in the near-bottom region.

In contrast to the traditional view of entrainment as a strictly vertical mixing process that is governed by the local bulk Froude number, simulations made by *Umlauf et al.* (2010) indicate that for the class of gravity currents, investigated entrainment is a complex, strongly non-local mechanism. Entrainment was demonstrated to occur in a two-stage, spatially separated process with incomplete entrainment of ambient fluid into the interface layer on the deep side of the gravity current, and downward mixing of buoyant fluid into the gravity current's interior occurring on the opposite side of the channel.

This non-local mechanism is largely different from entrainment in non-rotating flows, and clearly cannot be described by any combination of local non-dimensional bulk parameters. In spite of the complexity of the entrainment processes encountered by *Umlauf et al.* (2010), a second-moment turbulence closure model with prognostic equations for k and ε showed a remarkable agreement with measured mixing parameters, in agreement with the conclusions of *Ilicak et al.* (2008) and *Arneborg et al.* (2007). Note that an idetical turbulence model is also used for our three-dimensional simulations described above and in the impact study of offshore wind farms on density currents in the Western Baltic Sea (see section 4.5).

2.2.4 Numerical study of physical and numerical mixing

In the QuantAS project the model results for the Western Baltic Sea were analysed by *Burchard and Rennau* (2008) and *Rennau et al.* (2012) in detail with respect to the mixing during frequent and high-saline inflow events from the North Sea driven by sea level differences between the Kattegat and the Arkona Basin. The model application with general vertical coordinates (gvc) was used by *Burchard et al.* (2009) to investigate the natural mixing on the pathway of these dense bottom currents in the dynamic Arkona Sea. These moving tracer gradients in a complex bathymetry might introduce significant numerical dispersion and dissipation to the advection of salinity. It is therefore of great interest to compare the magnitude and distribution of numerical mixing compared to physically induced mixing. The diagnostic method explained in section 2.2.4.2 is applied to obtain the amount of numerical

mixing within this model simulation. Further experiments were carried out to identify the reasons and locations of high numerical mixing.
The advection scheme for momentum and tracer a TVD (Total Variation Diminishing) scheme with the ULTIMATE QUICKTEST limiter was used, for details, see *Pietrzak* (1998).

2.2.4.1 Physically induced variance decay as measure for mixing

To derive the bulk measure for vertical mixing suggested by *Burchard et al.* (2009), the conservative molecular salinity budget equation is used to derive a conservation equation of the tracer concentration:

$$\partial_t s + \partial_x(us) + \partial_y(vs) + \partial_z(ws) - \partial_z(K_v \partial_z s) = 0. \tag{2.3}$$

Here, s is the tracer salinity, u and v the horizontal velocity components, w the vertical velocity component, K_v the vertical diffusivity, t the time, ∂_t the derivative in time and $\partial_x, \partial_y, \partial_z$ the derivatives in space. In the numerical model GETM, horizontal diffusion is calculated along the sigma layers but is set to zero for all simulations in this work.
After some mathematical transformations, a conservation equation for the square of the mean tracer concentration can be directly derived from (2.3):

$$\begin{aligned}\partial_t s^2 + \partial_x(us^2) + \partial_y(vs^2) + \partial_z(ws^2) - \partial_z(K_v \partial_z s^2)& \\ = -2K_v(\partial_z s)^2.&\end{aligned} \tag{2.4}$$

The last term on the right hand side of eq. (2.4) is the turbulent mean tracer variance decay quantifying the physical mixing measure such that *Rennau et al.* (2012) defined:

$$D^{phy}(s^2) = 2K_v(\partial_z s)^2. \tag{2.5}$$

This is a more appropriate measure for physical mixing than the eddy diffusivity which may result in high values under well-mixed conditions with no tracer mixing. As a second step *Rennau et al.* (2012) add the contributions of vertical molecular diffusion to the physical mixing such that the physical mixing is composed of the turbulent and viscous contributions. For additional theoretical background the reader is referred to the work of *Burchard and Rennau* (2008).

2.2.4.2 Diagnosing numerically induced variance decay

In order to obtain a measure for numerical mixing (*Burchard and Rennau*, 2008) it is helpful to start from the first order upstream (FOU) discretised 1D advection equation for any tracer s:

$$\frac{s_i^{n+1} - s_i^n}{\Delta t} + \frac{u}{\Delta x}\left(s_i^n - s_{i-1}^n\right) = 0 \tag{2.6}$$

with s_i^{n+1} representing a value of the new time level, and s_i^n representing a value of the old (known) time level, the constant positive advection velocity u, the time step Δt and the spatial increment Δx. Now the advection operator A is introduced as:

$$s_i^{n+1} = (1-c)s_i^n + cs_{i-1}^n = A\{s_j^n\}_i, \tag{2.7}$$

with $c = u\Delta t/\Delta x$ being the Courant number for which the stability criterion $0 < c < 1$ must be fulfilled.
Multiplication of (2.6) by $(s_i^{n+1} + s_i^n)$ leads, after some additional mathematical transformations, to the discretised equation calculating the amount of numerical variance decay induced by the first order upstream scheme:

$$\begin{aligned}&\frac{(A\{(s_j^n)\}_i)^2 - A\{(s_j^n)^2\}_i}{\Delta t} = \\ &-2\frac{u\Delta x}{2}(1-c)\frac{s_i^n - (s_{i-1}^n)^2}{(\Delta x)^2}.\end{aligned} \tag{2.8}$$

The term $\frac{1}{2}u\Delta x(1-c)$ is the well-known numerical diffusivity of the FOU scheme (*Smolarkiewicz* (1983)) that can be easily obtained via the truncation error in a Taylor series extension. Hence, the right hand side term in equation (2.8) resembles a discretisation of the right hand side of equation (2.4) for the square of the mean tracer (see also *Morales Maqueda and Holloway* (2006)) with the numerical diffusivity instead of the physical diffusivity. Furthermore, the sink term on the right hand side of eq. (2.8) exactly quantifies the local numerical tracer variance decay for the FOU scheme. Consequently, *Burchard and Rennau* (2008) defined for any advection scheme A:

$$D^{\mathrm{num}}\left\{\left(s_j^n\right)^2\right\}_i = \frac{A\left\{\left(s_j^n\right)^2\right\}_i - \left(A\left\{s_j^n\right\}_i\right)^2}{\Delta t}, \tag{2.9}$$

which is the local rate at which tracer variance is decaying, as the measure for numerically induced mixing. The diagnostics of eq. (2.9) can be easily calculated as the difference between the advected square of the tracer and the square of the advected tracer, divided by the time step. Since the discrete advection of the square of the tracer is conserving the total tracer variance when finite volume schemes are used, this method does indeed calculate the total numerical tracer variance decay in an exact way. Locally, this numerical mixing calculation is subject to discretisation errors, just as the calculation of any tracer such as temperature and salinity. The implementation of this diagnostic method is simple: before the advection step for a tracer, the tracer square is calculated and the advection scheme is applied to the tracer and its square independently. After the tracer advection step, the square of the advected tracer is calculated such that eq. (2.9) can be computed. Afterwards, the squares of the old and the new tracer fields are discarded, and only the advected tracer concentration is used for the further simulation.

In numerical ocean models this generic and non-invasive method for quantifying the numerical mixing should generally be implemented very easily as advection and diffusion are mostly implemented as two different operational steps (*Burchard and Bolding*, 2002; *Shchepetkin and McWilliams*, 2005). In a model with closed boundaries and without any fluxes through the bottom and surface, the loss of salinity squared must be equal to the volume integrated numerical mixing as calculated by eq. (2.9). Here, $S^2(t = t_1)$ denotes the salinity at a certain time t_1 and $S^2(t = t_1)$ at time t_2 and D^{num} the numerical mixing due to the applied advection steps. Up to an uncertainty this can also be applied to a model with open boundaries and fluxes through the surface or bottom. For a domain with open boundaries, the net flux of S^2 through the lateral boundaries would need to be added to the left hand side.

Additionally it should be pointed out that for the model used in this study (GETM; *Burchard and Bolding* (2002)) the spatial discretisation is staggered with the tracer points being located at the centre of each grid cell and the eddy diffusivity being located at the interfaces.

2.2.5 Vertically integrated and time-averaged estimate of numerical mixing

Due to the anti-diffusive contributions of the TVD advection schemes (*Burchard and Rennau*, 2008), the instantaneous spatial distribution of numerical tracer variance decay is quite noisy. Therefore spatial and temporal averaging is applied to obtain an easy to interpret comparison of physical and numerical mixing. Fig. 2.16 demonstrates that the highest numerical mixing generally occurs at moving fronts and is hence located exactly in physically energetic areas where dense bottom plumes are crossing sills and passing channels. A general property of the numerical mixing which can also be seen in Fig. 2.16 are areas of high numerical variance decay along lateral plume boundaries. In these areas, where density gradients are advected vertically through the layers and coincidentally over steep bathymetry, numerical mixing is of the order of physical mixing and even stronger. As one might consider the alignment of terrain-following coordinates on sloping bathymetry as the main problem for the occurrence of high numerical mixing in the model setup used by *Rennau et al.* (2012), such high numerical mixing will also been found in z-level models. This for example can be proven with this model setup for the region of the central Arkona Basin which shows low depth variations. Even here, where the alignment of the vertical coordinates can be nearly neglected and the model behaves nearly like a z-level model, the physical mixing (Fig. 2.16a) still shows same orders of magnitude as the numerical mixing (Fig. 2.16b).

These results demonstrate that numerical mixing has a significant impact on the overall mixing over large areas of the model domain. Fig. 2.16a demonstrates that the numerical mixing plays a major role when salinity is advected through the coordinates vertically in regions where the moving plume front passes areas with steep bottom.

Another point that must be considered is that, additionally, high fluctuations of wind fields push the numerical mixing to high levels as can be seen for the region of the Arkona Basin (Fig. 2.16).

Further relationships can be obtained with the help of Fig. 2.17. Here, the amount of anti-diffusive contributions of the ULTIMATE QUICKTEST scheme are directly plotted. The outcome is that the absolute value of the anti-diffusive contributions makes 6.7% of the positive contributions of D^{num} in the right panel of Fig. 2.16.

Additional information about the strength of numerical mixing is shown in Fig. 2.17. Here, only the model domain regions where the physical mixing is greater than the numerical mixing (obtained by $\log_{10}(\ \max(10^{-10},\ D^{\mathrm{phy}} - D^{\mathrm{num}})\ )$) and vice versa (obtained by $\log_{10}(\ \max(10^{-10},\ D^{\mathrm{num}} - D^{\mathrm{phy}})\ )$) are shown. If we integrate over both fields, the ratio is even $R = 1.7$. With Fig. 2.17 it is demonstrated, that there are large areas in the Western Baltic Sea where physically induced mixing is much higher than numerical diffusion due to discretisation errors of the numerical advection schemes.

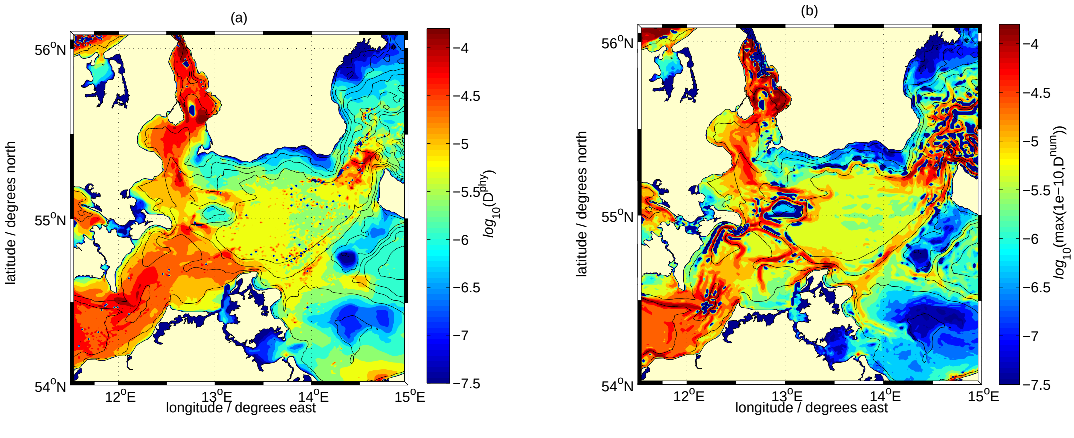

Figure 2.16: Vertically integrated and over nine months time averaged values of (a) physically and (b) numerically induced mixing. This figure was taken from *Rennau et al.* (2012).

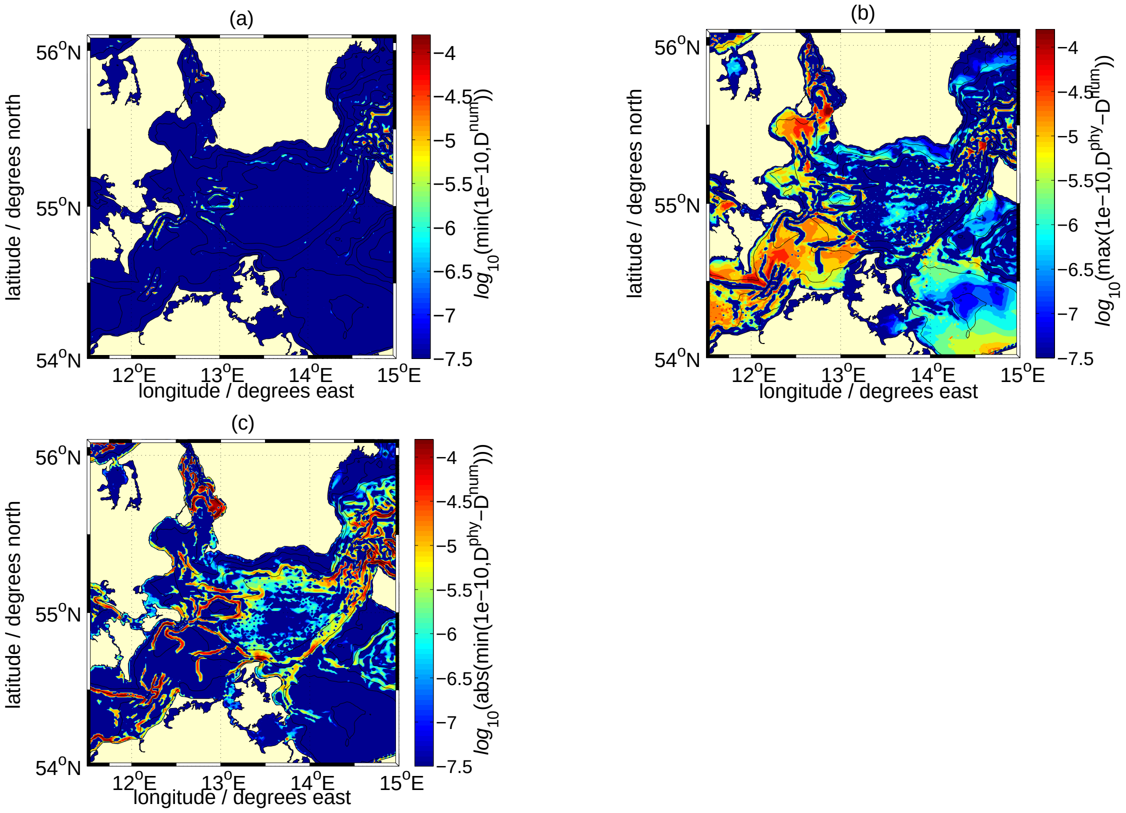

Figure 2.17: All panels show vertically integrated and time averaged (nine months) values of: (a) the anti-diffusive contributions of the numerical mixing, (b) regions where the physical diffusion is higher than the numerical mixing and (c) regions where the numerical mixing is higher than the physical mixing. Here, the ULTIMATE QUICKTEST scheme has been used. This figure was taken from *Rennau et al.* (2012).

2.3 Major conclusion from natural mixing studies

During the course of the QuantAS projects, the understanding of the dynamics in the Western Baltic Sea could be substantially revised. Before 2004, it was assumed that the saline plumes entering the Arkona Sea over the Drogden and Darss Sills were largely geostrophically balanced and thus propagating along the isobaths in an anti-clockwise sense ((*Lass and Mohrholz*, 2003)). Already during the first QuantAS cruise in February 2004 (*Sellschopp et al.* (2006)), this picture could be revised, confirming a model derived hypothesis that the plumes have an additional tendency to follow the thalweg (*Burchard et al.* (2005); *Lass et al.* (2005)), due to the effect of bottom friction. Saline inflows were found to be more energetic and more frequent than assumed before. In contrast to earlier results by *Kouts and Omstedt* (1993), mixing of dense bottom currents exiting the Arkona Sea through the Bornholm Channel may be strong as well. Both facts (plumes tend to follow the thalweg, plumes are energetic) may have strong implications on the mixing due to offshore wind farms which may be built into their pathways. Apart from that, channalised bottom currents (north of Kriegers Flak, Bornholm Channel) showed a complex transverse structure for which a detailed explanation could be derived from field observations and numerical modelling (*Umlauf et al.* (2007); *Umlauf and Arneborg* (2009a,b); *Umlauf et al.* (2010)). The impact of structures such as offshore wind farms erected within these bottom currents would surely be different than expected from simple, horizontally homogeneous bottom currents.

It could be shown by several numerical model studies that numerical models are able to reproduce these complex dynamics in a quantitatively satisfying way (*Burchard et al.* (2005, 2009); *Umlauf et al.* (2010)). However, the analysis of the model results must be carried out with care, since numerically induced mixing may easily be of the same order as physically induced mixing (*Burchard and Rennau* (2008); *Rennau and Burchard* (2009)). It is therefore essential to analyse the total mixing instead of the physical mixing only.

With these basic results (dynamics of the Western Baltic Sea understood and quantitatively reproduce by numerical models), the additional effects of mixing due to offshore wind farms may be parameterised into these models. Before, since such parameterisations did not exist for stratified shear flow at the beginning of the project, basic research is needed to understand the impact of vertical structures on mixing in dense bottom currents. The research related to this question will be highlighted in the following chapter, by means of small-scale laboratory experiments (section 3.1), small-scale modelling (sections 3.1.6 and 3.2) and field observations in a comparable environment (bridge pylons in stratified shear flow, section 3.3).

Chapter 3

Estimation of mixing due to structures

3.1 Laboratory experiments (UNI-HRO)

3.1.1 Special definitions for quantification of mixing

In addition to the mixing quantities, already explained in the chapters before, some special definitions have been used, which are adapted to the quantities that could be measured by directly by the measuring system in the laboratory. For all definitions the same coordinate system has been used, which is shown in figure 3.1.

3.1.1.1 Entrainment

The vertical extension of the mixing layer d_M is defined by the vertical distance of the positions, where the salinity reaches 30 % and 70 % of the maximum salinity (see figure 3.2). The extension of the saltwater layer D is defined by the vertical distance between the bottom and the position, where the salinity reaches 50 % of the maximum salinity. The extensions d_M and D have been computed for each time step and averaged afterwards.

Following *Ellison and Turner* (1959) and *Turner* (1986), the entrainment E can be written as

$$E = \frac{w_E}{U_0} = \frac{1}{U_0} \cdot (\frac{\delta D}{\delta t} + \frac{\delta UD}{\delta x} + \frac{\delta VD}{\delta y})$$

with the entrainment velocity w_E and the averaged incident velocity U_0. The velocity components, vertical integrated over the saltwater layer, are written as U and V. In this case the entrainment can be used to describe the mean change vertical extension of the saltwater layer D and the increase of the mass flux within the saltwater

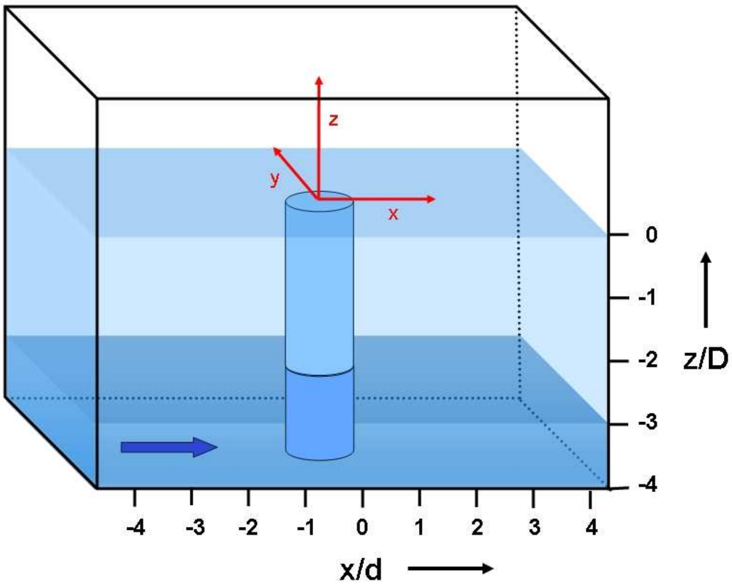

Figure 3.1: Definition of the coordinate system

layer with increasing distance from the inlet. The entrainment velocity-flux

$$\dot{V}_{w_E} = \int\int w_E dx dy$$

is derived from the horizontal integrated entrainment velocity and has the dimensions of volume-flux. Due to symmetry of the cylinder wake to $y/d = 0$, the term $\frac{\delta DV}{\delta y}$ results in zero in the integral. Therewith the entrainment velocity as source for the entrainment velocity-flux can be written as

$$w_E = \frac{\delta D}{\delta t} + \frac{\delta UD}{\delta x}$$

3.1.1.2 Mixing number

The entrainment velocity does not say anything about the vertical extension of the mixing layer or mixing effects within the mixing layer. To get information about the volume-flux within the mixing layer the Mixing number M_a will be used. It is defined in the far field of the cylinder ($x/d \geq 20$) as an increase of the volume flux within the mixing layer as

$$M_a = M_{x/d=a}$$

$$M_a = \frac{[\dot{V}_{mZ,x/d=a}]^{S/S_{max}=0.7}_{S/S_{max}=0.3} - [\dot{V}_{oZ,x/d=a}]^{S/S_{max}=0.7}_{S/S_{max}=0.3}}{\dot{V}_0}$$

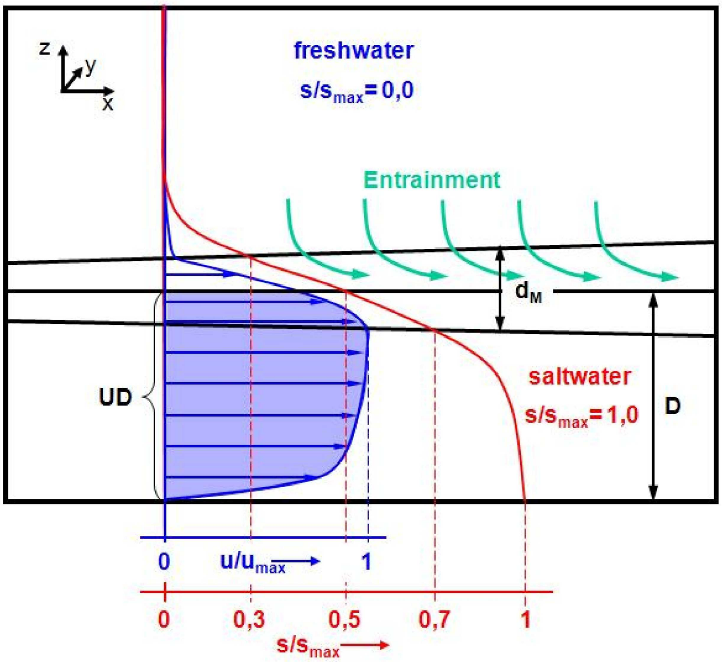

Figure 3.2: principle sketch of a stratified saltwater flow

$$M_a = \frac{\int\limits_{y/d=-0.5}^{y/d=0.5} \int\limits_{z(S/Smax=0.3)}^{z(S/S_{max}=0.7)} dydz(u_{mZ,x/d=a}) \int\limits_{y/d=-0.5}^{y/d=0.5} \int\limits_{z(S/Smax=0.3)}^{z(S/S_{max}=0.7)} dydz(u_{oZ,x/d=a})}{\int\limits_{y/d=-0.5}^{y/d=0.5} \int\limits_{z/D=-4}^{z(S/S_{max}=0.5)} dydz(u_0)}.$$

Here, S is the salinity, u_0 the incident velocity and the indicate ,,mZ" and ,,oZ" mark the cases with cylinder (,,mZ") and without cylinder (,,oZ"). This way M_a describes the additional volume-flux within the mixing layer, that is induced by the cylinder, normalised on the incident volume-flux on the cylinder cross section. The incident volume-flux on the cylinder $\dot{V}_0$ is measured over the cylinder cross section without the cylinder at it's later position and computed from the bottom to the isoline of 50% of the maximum salinity. For the laboratory experiments the Mixing number will be measured at $x/d = 20$ and be called M_{20}.

3.1.1.3 Mixing Efficiency

The entrainment as well as the Mixing number describe the time-averaged observed mixing results without telling anything about the sources of mixing. To quantify the turbulent part of total mixing, smallest spatial and temporal scales have to be observed. For the stratified saltwater flow the turbulent vertical flux of salt is of major interest. Therefore, the vertical Reynolds-flux $\overline{w's'}$ with the turbulent vertical velocity fluctuation w' and the salinity fluctuation s' will be used. To achieve a non-dimensional quantity, the vertical Reynolds-flux was normalised by the incident velocity U_0 and the maximum salinity S_{max} which results in a measure for the vertical mixing. Equivalent to the vertical Reynolds-flux, the buoyancy-flux $\overline{w'b'}$ can be derived. Normalised on the local dissipation of turbulent kinetic energy ϵ it results in the part of dissipated turbulent energy that is used for mixing. The local mixing efficiency γ from the laboratory experiments was therewith derived as

$$\gamma = \frac{\overline{w'b'}}{\epsilon}.$$

Vertically integrated over the saltwater layer it gives the global mixing efficiency

$$\Gamma = \frac{\int\limits_D \overline{w'b'} dz}{\int\limits_D \overline{\epsilon} dz}.$$

This definition is equivalent to the Flux-Richardson number under the assumption that the dissipation equals the production of turbulent kinetic energy. This assumption is not true for regions of strong production, for example in the near wake of the cylinder.

3.1.2 Experimental Setup

Laboratory Experiments will open access to much more information about the flow regime than field measurements can do. Due to very controlled and reproducible experiments, measurements of many quantities at different regions of interest and with different spatial and temporal resolutions can be carried out. This way all three components of the velocity in a three-dimensional volume can be measured as well as the salinity- and density-distribution within this volume. All measurements will give time-resolved information about the flow.

One very important point to mention, when doing laboratory experiments, is that also the characteristic processes have to be scaled, when scaling down the geometry.

For the QuantAS-Off laboratory experiment the densimetric Froude number Fr_D is the ruling number which can be defined as

$$Fr_D = \frac{U_\infty}{\sqrt{gD\frac{\rho_b-\rho_a}{\rho_a}}}.$$

By keeping the densimetric Froude number the Reynolds number Re, defined as

$$Re = \frac{UD}{\nu},$$

will increase. This could change the rate of turbulence due to viscosity effects if the model is scaled to strong. Because of this, the QuantAS-Off laboratory experiment had to be scaled by a factor of 100 to the natural case in the Baltic Sea near Kriegers Flak.

3.1.2.1 Water channel

The QuantAS-Off water channel at the chair of fluid mechanics at the University of Rostock was specially designed to achieve the highest possible Reynolds number by keeping the densimetric Froude number. This and the use of saltwater opens special needs to the facility. The water-channel has an overall length of 17 m and a measuring section of 3 m length, 0.8 m width and 0.8 m depth. The measuring section has optical accesses from 5 sides, as shown in figure 3.3. The water-level is controlled by a dam, following the measuring section. Besides this there are two water tanks with a volume of 5 m^3. The upper one is used as reservoir, the lower one as collecting and mixing tank. In this configuration the maximum measuring time at the maximum volume flow is 2 minutes. Moreover it is also possible to run the system in a circulation mode with the collecting tank also used as reservoir. The pump generates a maximum volume flux of 120 m^3/h. For measurements, the measuring section first has to be filled with freshwater. Afterwards salt, dye and tracer-particle have to be added to the water in the mixing tank. The saltwater can be pumped into the reservoir for a measurement or be used in circulation mode from the mixing tank. During Measurements the saltwater will flow under the still freshwater in the measuring section.

3.1.2.1.1 Specification As already mentioned, the densimetric Froude-number had to be kept. For this purpose the dimensions of the water channel and the idealised model of an Offshore-wind-turbines founding had to be scaled by a factor of 100 to reality. Consequently the wind-turbines founding was displayed as a vertically arranged circular cylinder with a diameter of $d = 8$cm. To minimise

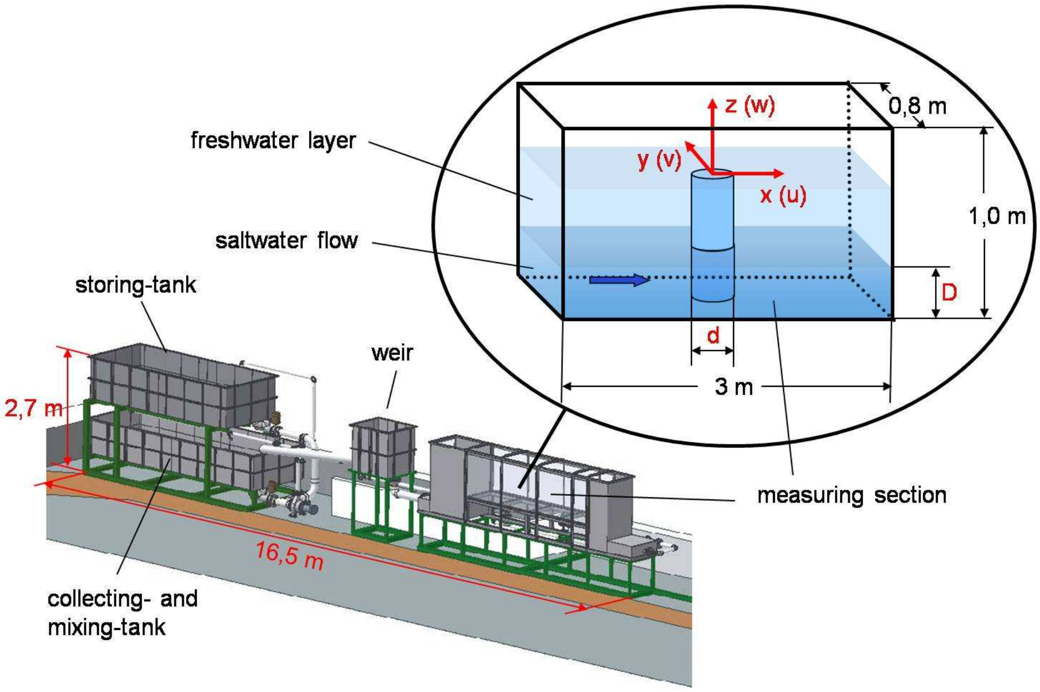

Figure 3.3: Water-channel and definition

blocking effects in the measuring section, it has been designed with a width of 80 cm.

The characteristic numbers and dimensions of the water channel are presented in Table 3.1. More detailed information on the water channel are published in *Menzel et al.* (2006) and *Menzel et al.* (2007). The size of the measuring section as well as the position of the cylinder is shown in figure 3.4. In the inlet region (left) a plexiglas-plate is installed, whose function will be explained later.

3.1.2.1.2 Optimisation The incident flow onto the cylinder is of major importance for the vortex structures in the wake of the cylinder. The strain parameter

$$\beta = \frac{du}{dz} \cdot \frac{d}{u_m}$$

with the velocity u_m at $z = z_{min} + D/2$, defined by *Kappler* (2000) describes the gradient of the linear vertical velocity profile. For small strain parameters (β=0.02 and 0.04) Kappler showed, that the Strouhal number

$$Sr = \frac{f \cdot d}{U},$$

Table 3.1: characteristic numbers

	PARAMETER	ARKONA SEA	WATER-CHANNEL
Wind-turbine	Cylinder diameter [D/m]	8	0.08
	overall depth [z/m]	40	0.4
upper layer	thickness [z_a/m]	30	0.3
	salinity [S_a/psu]	8	0.3
	density [ρ_a/kgm^3]	1006	999
	velocity [U_0/ms^{-1}]	0.0	0.0
saltwater layer	thickness [d/m]	10	0.1
	salinity [S_b/psu]	18	9.8
	density [ρ_b/kgm^3]	1014	1007
	velocity [U_0/cms^{-1}]	≈50	4.3
characteristic number	Reynolds number [Re]	$3.4 \cdot 10^6$	$3.4 \cdot 10^3$
	densimetric Froude number [Fr_D]	0.51	0.51

with the characteristic frequency f, changes significant along the cylinder axis. Figure 3.5 shows two vertical velocity profiles, whereas the black one has been measured by the IOW near Kriegers Flak on 7th February 2004, and the red one was measured in the water channel at the laboratory. The strain parameter for both cases is β=0.57. Due to this, a dominant frequency of the Karman vortex street in the wake of a cylinder can not be expected. The velocity profile, shown in figure 3.5 as red line has been achieved by using a bent nozzle, followed by a profile generator at the inflow and a gap of 10 cm height and 30 cm length (see figure 3.6). To assure that the flow is only two-dimensional, the velocity profile has been measured in the middle of the channel at $y = 0$ cm ($y/d = 0$) at $y = 8$ cm ($y/d = 1$), $y = 16$ cm ($y/d = 2$) and $y = 24$ cm ($y/d = 3$) 5 cm upstream of the planed centre of the cylinder at $x = -5$ cm. The results are shown in figure 3.7. As can be seen, the differences of the velocity profiles are small and the flow can be described as smooth and two dimensional. The velocity gradient profiles have comparable absolute minima. Also the zero crossing, that indicates the vertical distance between the velocity maximum within the saltwater flow and the velocity minimum within the freshwater layer, show equal vertical distances.

Additionally a second velocity profile has been created for measurements at different Froude numbers. The task for this case was to achieve a profile that changes less as possible along the measuring section and at different Froude numbers. Thus a combination of different Grids at the inflow has been used to design the profile. The

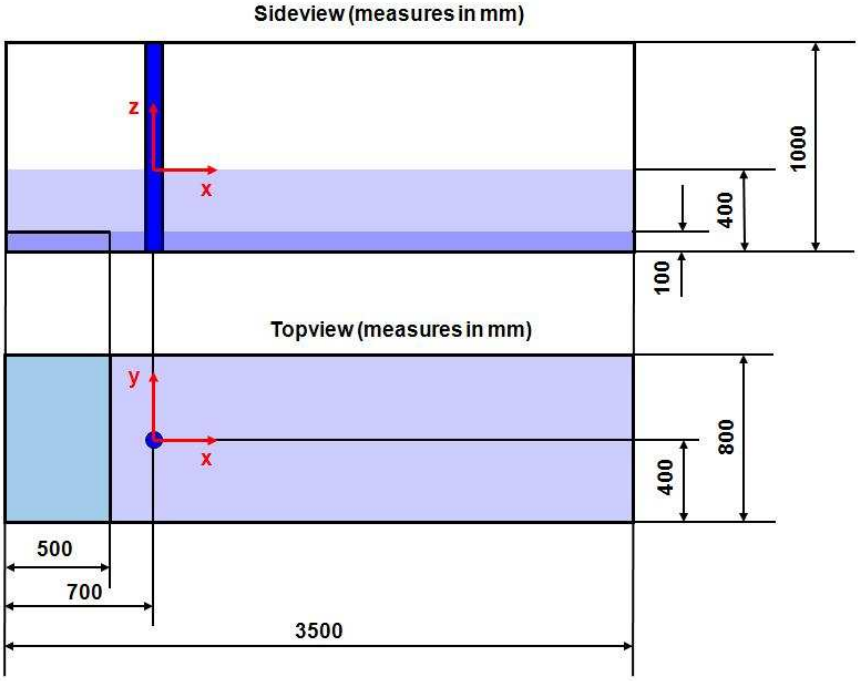

Figure 3.4: Measures of the measuring section and position of the cylinder

mesh size and therewith the blocking was chosen the way that the velocity profile at the inflow equals the profile, measured two meters downstream of the inflow one iteration step before. Figure 3.8 displays the velocity profile 2 at the inflow (red) and two meters downstream of the inflow (black). The difference between these profiles is very small, considering the large distance of two meters.

3.1.2.2 Traversing System

An advanced traversing system has been necessary to guarantee reproducible measurements and to achieve a Volume-Dataset from planar measurements. Due to these recommendations the laser-light sheet had to be traversed along the channel (x-direction) and cross the channel (y-direction), whereas the cameras had to be traversed in all three directions (x,y and z). The laser-light sheet had to be adjustable, in comparison to the cameras in x- and z-direction because of an intensity distribution within the light sheet. By changing the measuring plane in y-direction, the optical way through the water becomes shorter, when the way through air becomes longer. The relation between the distances s (see figure 3.9), expecting the same field of view, is given by the refraction index n as

$$\frac{s_1}{s_2} = \frac{n_1}{n_2}.$$

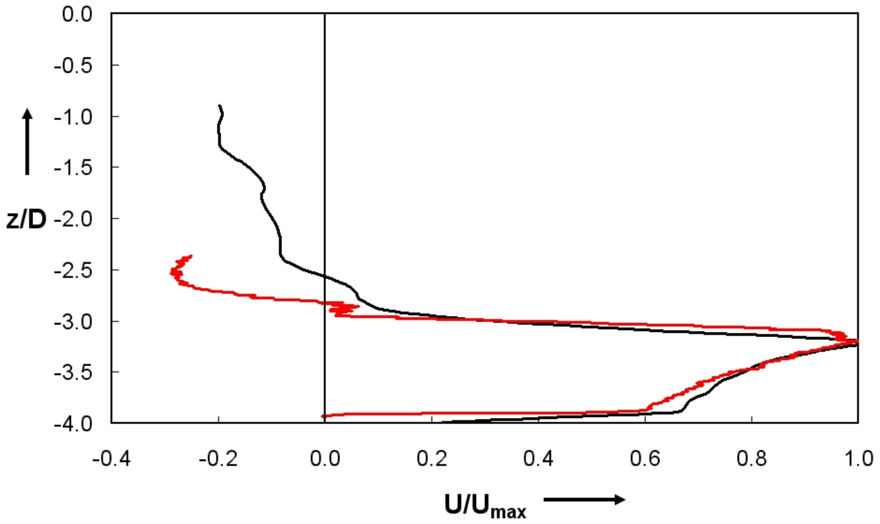

Figure 3.5: Velocity profile 1, measured in the Baltic Sea (black) and in the laboratory (red)

By using a Traversing System with five independently controllable axis, these requirements could be fulfilled. The arrangement of the several traverses is displayed in figure 3.10.

3.1.2.3 Measuring System

Focus of the laboratory experiments was to measure mixing of saltwater and freshwater with a non-intrusive optical measuring system. For this purpose, two planar measuring systems have been combined, which will be explained in the following sections.

3.1.2.3.1 Basics on PIV Particle Image Velocimetry (PIV) is a modern non-intrusive laser-optical principle to measure planar two- or three-component velocity fields. However, the principle of observing the shift of tracer particles in a fluid and measuring the time between the particle observations is known since long times. First developments in direction of PIV were published by *Barker and Fourney* (1977), *Dudderar and Simpkins* (1977) and *Grousson and Mallick* (1977) by the Laser Speckle Velocimetry. Just *Adrian* (1984) and *Pickering and Halliwell* (1984) suggested to observe the shift of on an ensemble of particles and therewith the PIV. Unlike the first experiments, for modern PIV the advantages of CCD and CMOS cameras, up to date laser technology and powerful computers are used. Combined with extensive programmes for digital image processing, modern PIV is a very pow-

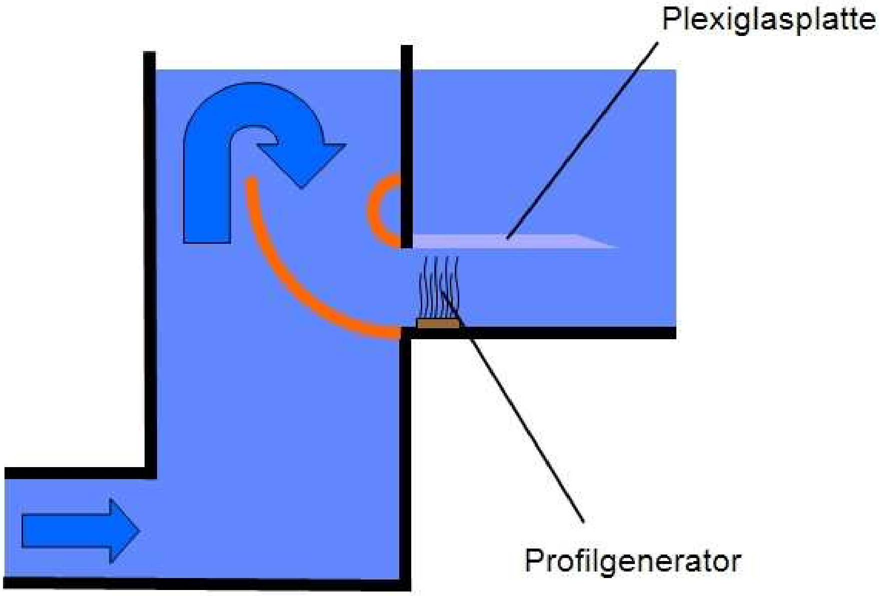

Figure 3.6: Flow-forming facilities at the inlet

erful measuring principle. More information about development of PIV can be found in *Adrian* (2005).

A typical PIV-System consists of a laser-light source, at least one camera, some electronics for signal processing and a PC. For a measurement, the light of the two laser pulses from the double-pulse laser is extended to a planar laser-light sheet as can be seen in figure 3.11. The laser light sheet describes the measuring plane by illuminating the tracer particles, who are following the flow, within this area. The light is backscattered by the process of Mie-Scattering and detected by a special PIV-CCD-Camera that allows the detection two images with a delay of only few microseconds. The two images are stored on a PC. To analyse the images, each image is subdivided into small Interrogation Areas as visualised in figure 3.12. Size and overlap of the Interrogation Areas is chosen the way that at minimum around five particles are visible in one Interrogation Area and at least three particles are visible in both Interrogation Areas. Besides this, several algorithms like the overlap of neighboured Interrogation Areas and shift of the second Interrogation Area by the mean particle shift, computed in a step before, are used to guarantee that a maximum number of particles are visible in both images without leaving the Interrogation Area. The mean velocity vector within an Interrogation Area is computed by using a Cross Correlation between the Interrogation Areas at the same position at different times, which leads to a shift vector. By scaling this image shift to laboratory coordinates (scale factor from a calibration) and dividing the shift by the

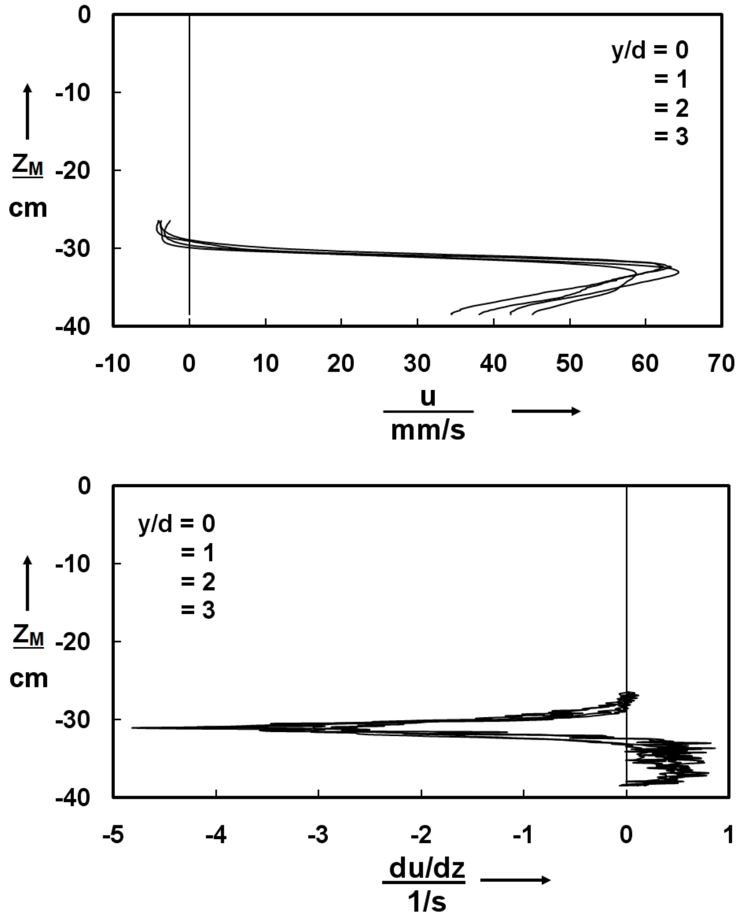

Figure 3.7: Velocity profile 1 and gradient of velocity profile 1 across the measuring section.

time difference of both images, the instantaneous two component velocity vector is derived. More detailed information on the implementation of Cross Correlation for PIV can be found in *Willert and Gharib* (1991) and *Keane and Adrian* (1992). The modified and much more powerful Adaptive Correlation, which has been used for the measurements as well as the different algorithms for validation are described in *Dantec Dynamics* (2002a). For the measurements, done within this work, the Adaptive Correlation with an Interrogation Window of 16 x 16 pixel, 50% and a peak validation of 2.0 has been used in three refinement steps of two runs for the immediate step, one run of the middle step and two runs of the final step with Sub-pixel Interpolation and Deforming Windows. A description of these algorithms can be found in *Dantec Dynamics* (2002b).

Besides these two-dimensional two-component measurements, two-dimensional three-

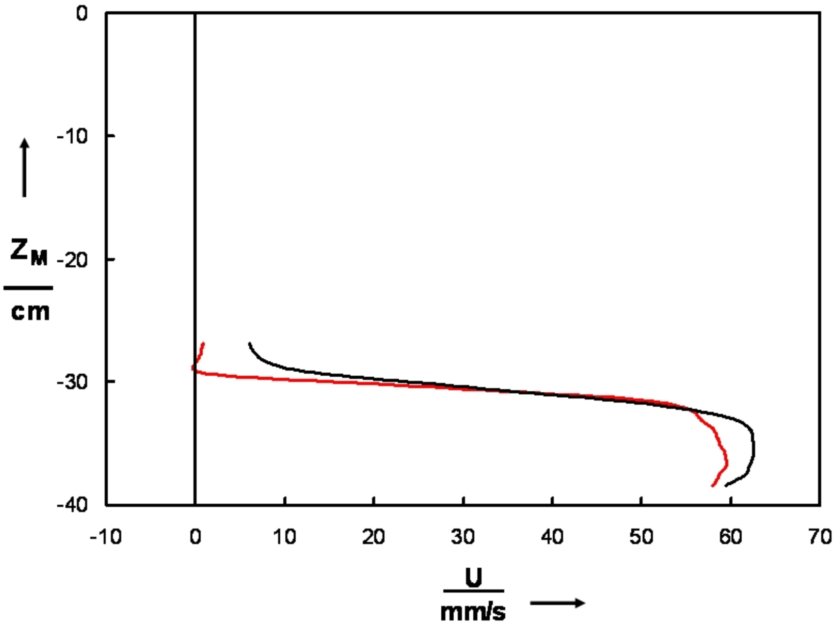

Figure 3.8: Velocity profile 2 at the inflow (red) and two meters behind downstream of the inflow (black).

component measurements have been carried out by using two PIV-cameras imaging the laser-light sheet from two different directions. Therefore a stereo calibration is necessary, where a calibration target is recorded from both cameras. By moving the target in the out-of-plane direction, several images were made at different z-positions of the target while the measuring plane has been a x-y-plane. Using a calibration (f.e. Direct Linear Transformation) leads to the possibility to compute the out-of-plane velocity-component of the observed particles from the two two-component velocity fields. A deep going treatise on Stereo PIV can be found in *Prasad and Adrian* (1993). The description of the Direct Linear Transformation and the calibration, used within this experiment is printed in *Dantec Dynamics* (2002b) and *Witte* (2007).

One of the most important factors on PIV measurements is given by the tracer particles. Those should be as large as possible to cause a maximum backscatter of light but as small as possible to follow the flow as good as possible. In water it is possible to find tracer particles that are of similar density as water, which maximises the ability to follow the flow. For the laboratory experiments, VESTOSINTⓇ2157 has been used. The particles density is $\rho_P = 1016 kg/m^3$ at 23^oC with a mean particle diameter of $d_P = 56\mu m$.

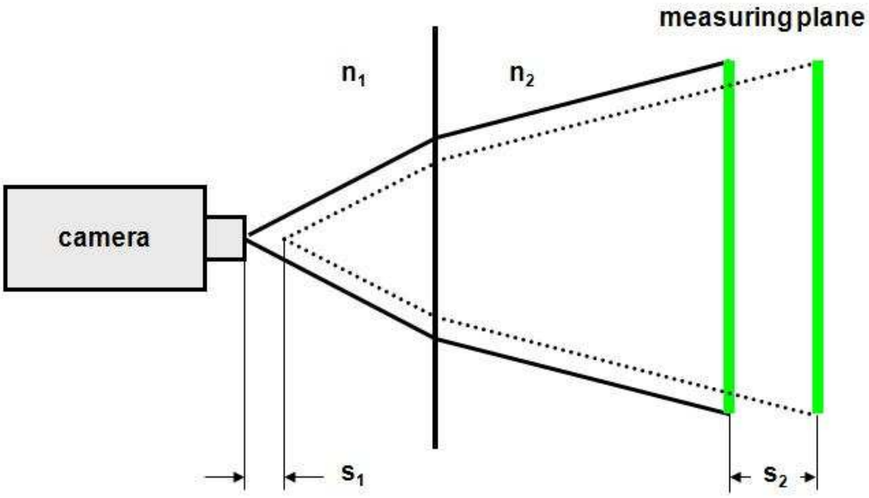

Figure 3.9: Refraction of light between water and air.

3.1.2.3.2 Basics on LIF Like PIV, the Laser-Induced Fluorescence technique uses a laser-light sheet, which illuminates the measuring plane. The laser-light is absorbed by special molecules, which emits the light at a larger wavelength due to the process of fluorescence. The cameras only detect the fluorescence light due to a narrow band optical filter (see also figure 3.11). The intensity of the fluorescence light I_F is dependent on the intensity of the laser-light I_0, the quantum efficiency of the fluorescence Φ, the thickness of the laser-light sheet, the absorption-coefficient ϵ and the dye-concentration c as follows:

$$I_F = I_0 \Phi (1 - e^{-cb\epsilon}).$$

As the laser-light intensity, the quantum efficiency, the thickness and the absorption coefficient are more or less constant, the fluorescence intensity is ruled by the concentration that can be derived from the first order relation

$$c = \frac{I_F}{I_0 \Phi b \epsilon} = \alpha I_F$$

Therewith the light-intensity on the camera is dependent of the concentration. By using a calibration, the constant α can be determined by a linear regression for small concentrations. The temperature dependency of the used dye Rhodamine 6G can be neglected as well as quenching and bleaching.
In the laboratory experiment, a known amount of fluorescence dye was added to the saltwater. By the knowledge that the Schmidt numbers of Salt and Rhodamine 6G are very similar, the Rhodamine 6g-concentration is proportional to the salt-concentration.

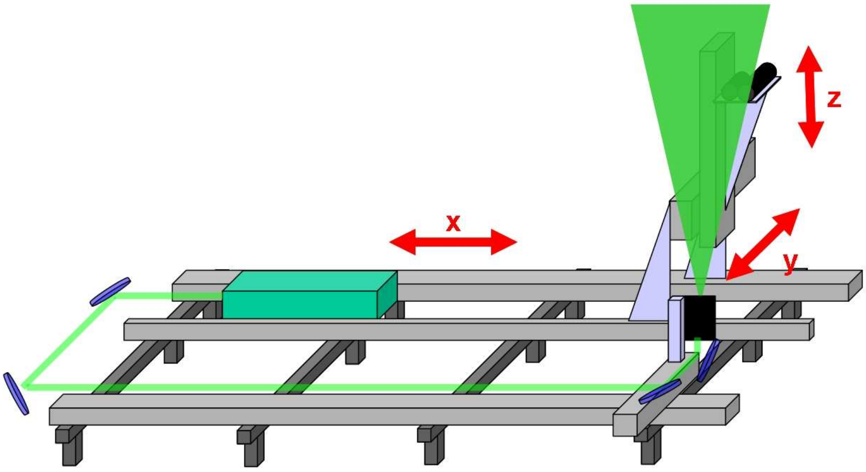

Figure 3.10: Arrangement of the 5-Axis-Traversing-System

3.1.3 Experiments

During the laboratory experiments within the QuantAS-Off project, 207 combined PIV/LIF- and Stereo-PIV-measurements plus around 50 measurements for optimisation of the test facility have been carried out. For each measurement, at first the lower mixing tank had to be filled with 5 m^3 freshwater, the needed amount of salt, tracer particles and Rhodamine 6G. This water than was pumped to the upper storing tank. Afterwards, 4 m^3 of freshwater has been filled into the mixing tank, tracer particles were added and than pumped into the measuring-section until it was filled to the level of the dam. Now the saltwater from the upper storing tank was pumped into the measuring section, where the saltwater flows beneath the freshwater. Five minutes after starting the pump, the measurement could be started and lasted for around 68 seconds.

3.1.3.1 Measurements with velocity profile 1

As already explained in previous sections, the wake of a cylinder and especially the vortex structures are strongly dependent on the incident velocity- and turbulence-profile. Due to this, a velocity-profile was chosen, that is similar to the profile, measured in the Baltic Sea by the IOW. Both velocity profiles are shown in figure 3.5.

For the measurements with cylinder, the cylinder has been installed 20 cm downstream of the inlet.

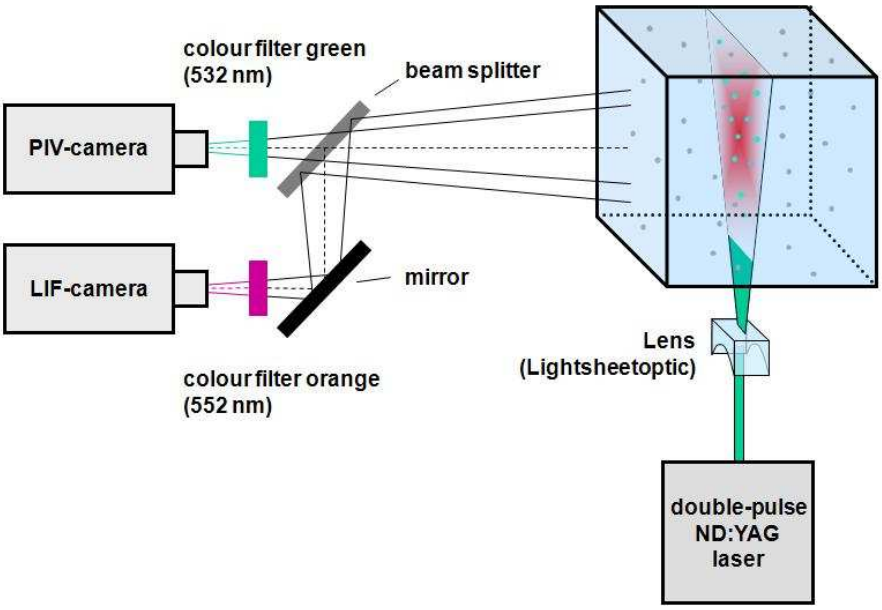

Figure 3.11: Principle of combined PIV/LIF.

Table 3.2: boundary conditions

	BALTIC SEA	LAB	LAB	LAB
velocity profile	profile 1	profile 1	profile 2	profile 2
densimetric Froude number Fr_d	≈ 0.51	0.51	0.51	0.74
added mass of salt [kg]	-	50	50	25
salinity of freshwater s_a [psu]	≈ 8	0.3	0.3	0.3
salinity of saltwater s_b [psu]	≈ 18	9.8	9.8	4.8
salinity difference Δs_{ab} [psu]	≈ 10	9.5	9.5	4.5
thickness of freshwater-layer z_{min}+D [m]	≈ 30	0.3	0.3	0.3
thickness of saltwater-layer D [m]	≈ 10	0.1	0.1	0.1
diameter of cylindrical founding d [m]	≈ 8	0.08	0.08	0.08
volume flux [m^3/h]	-	12.4	12.4	12.4
mean incident velocity U_0 [cm/s]	≈ 50	4.3	4.3	4.3
cylinder-Reynolds number Re	$\approx 3.4 \cdot 10^6$	$3.4 \cdot 10^3$	$3.4 \cdot 10^3$	$3.4 \cdot 10^3$
measuring frequency (PIV/LIF) [Hz]	-	15	15	15
measuring frequency (Stereo-PIV) [Hz]	-	10	-	-
samples per measurement	-	1000	1024	1024

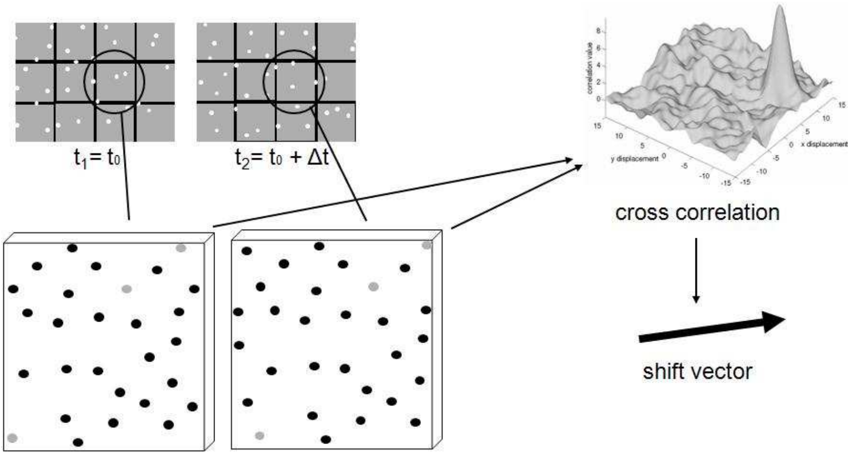

Figure 3.12: Principle of Cross Correlation

Table 3.2 displays the boundary condition in the Baltic Sea and in the laboratory experiments, whereas the numbers for the Baltic Sea were taken from measurements of the IOW near Kriegers Flak. The numbers, measured in the Baltic Sea can not be understood as fixed numbers as the conditions in the Baltic Sea are very variable. It should be pointed out here, that the salinity difference and the densimetric Froude number are kept.
To quantify the additional mixing, caused by the cylinder, the background mixing had to be measured in the water channel. Therefore, measurements in the centre plane ($y/d = 0$) have been carried out along the x-axis in x-z-planes without a cylinder. The results of these measurements were subtracted from the results with cylinder. To identify regions of major mixing, a large set of measurements have been made in several planes (see figure 3.13). These measurements also allows a description of the large vortex structures and periodic phenomena. Figure 3.13 shows a view on the measured x-z-planes from top of the channel, whereas the green lines describe the field of view and the black lines indicate the area, used for analysis. Due to the symmetric geometry, the measurements were reduced to planes of $y/d \geq 0.2$. The spatial resolution of these measurements was 1.09 x 1.09 mm^2 after data processing. For further understanding of the three-dimensional vortex-structures in the wake of the cylinder and the resulting mixing effects, stereo-PIV measurements have been realized. The alignment of the horizontal measuring planes (x-y-planes) can be seen in figure 3.14. The eight planes have been arranged in central to the cylinder axis at $y/d = 0$ from $z/D = -3.7$ to $z/D = -3.0$ and a vertical distance of $z/D = 0.1$ (1 cm). The spatial resolution of the stereo-PIV-measurements had to be 2.2 x 2.2 mm^2 due to the large field of view.

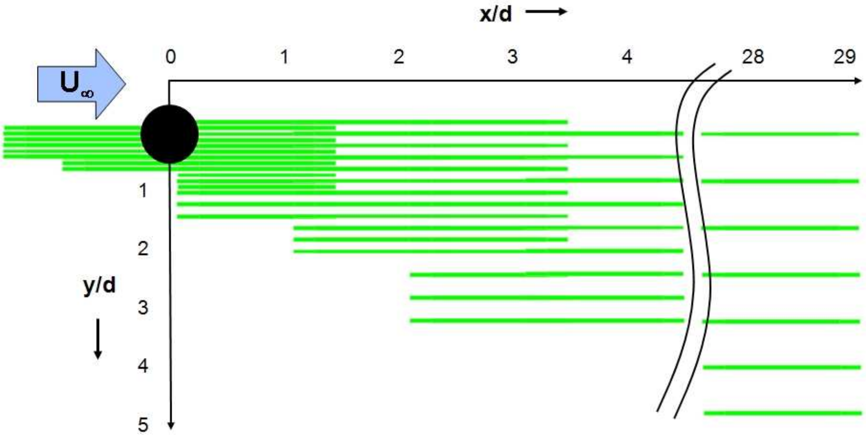

Figure 3.13: measured PIV/LIF-planes with cylinder and velocity-profile 1

3.1.3.2 Measurements with velocity profile 2

The measurements with velocity profile 1, described in the previous section, were focused to reproduce the natural conditions as good as possible. Due to the different Reynolds number and roughness of the bottom, velocity profile 1 changes with larger distances to the inlet of the channel. Velocity profile 2 (see figure 3.8) has been generated to quantify the influence of this change with the distance to the inlet. Furthermore, the influence of different densimetric Froude numbers should be examined by keeping the same velocity-profile. Velocity profile 2 was generated the way, that it changes as few as possible with raising distance to the inlet. The cylinder again was positioned 20 cm downstream of the inlet. The boundary conditions are displayed in Table 3.2. Like for velocity profile 1, here also reference measurements without a cylinder have been made. The measurements took place with densimetric Froude numbers of $Fr_D = 0.51$ and $Fr_D = 0.74$, where velocity and salinity has been measured at $y/d = 0$ for the whole channel ($-2.7 < x/d < 25.3$). For $Fr_D = 0.51$, also measurements with an optimised camera alignment have been made for the volume, showed in figure 3.15 (right). The optimised camera alignment allows a with a spatial resolution of 0.67 x 0.67 mm^2 for the mixing layer region. In addition to these measurements a study of the dependency of mixing on the densimetric Froude number has been carried out at $x/d = 20$ for $Fr_D = 0.5$, 0.57, 0.6, 0.71, 0.81, 0.9 and 1.04 with a spatial resolution of 0.67 x 0.67 mm^2.

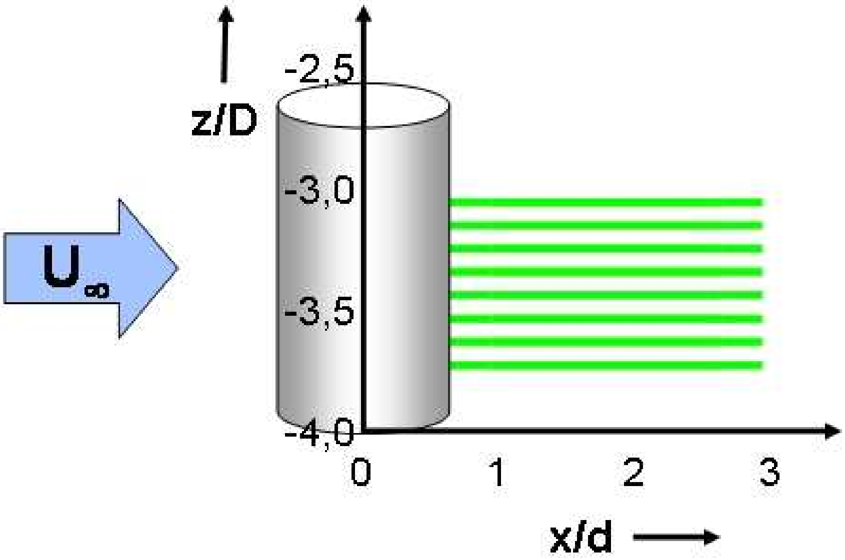

Figure 3.14: measured Stereo-PIV-planes with cylinder and velocity-profile 1

3.1.4 Results

For understanding the additional mixing effects and their reasons it is necessary to understand the processes of the flow around the cylinder. Due to this one part of the experiments is dedicated to figure out the time averaged vortex structures and the turbulence structures in the wake of the cylinder.

3.1.5 Flow visualisation

To understand the mixing processes, caused by the cylinder, it is of advantage to get an overview of the existing vortex structures. The best way to get some impression of these structures is to visualise them. This has be done with the hydrogen bubble method which is described in detail in *Hoyer* (2008) and *Menzel* (2010).
As known from *Sumer et al.* (1997) a horseshoe vortex can be found at a wall mounted cylinder, which is caused by the boundary layer of the wall. The same horseshoe vortex is expected near the mixing layer as it is also a shear layer.
In figure 3.16 the horseshoe vortex beneath the mixing layer is visualised which is, like expected, counter rotating to the bottom near horseshoe vortex, shown in figure 3.17. The diameter of the bottom near horseshoe vortex is around 0.15 d whereas the diameter of the horseshoe vortex near the mixing layer has a diameter of around 0.15 d. The positions to the cylinder also differ slightly. Whereas the bottom near horseshoe vortex begins at around $x/d = -0.75$, the upper one begins at around

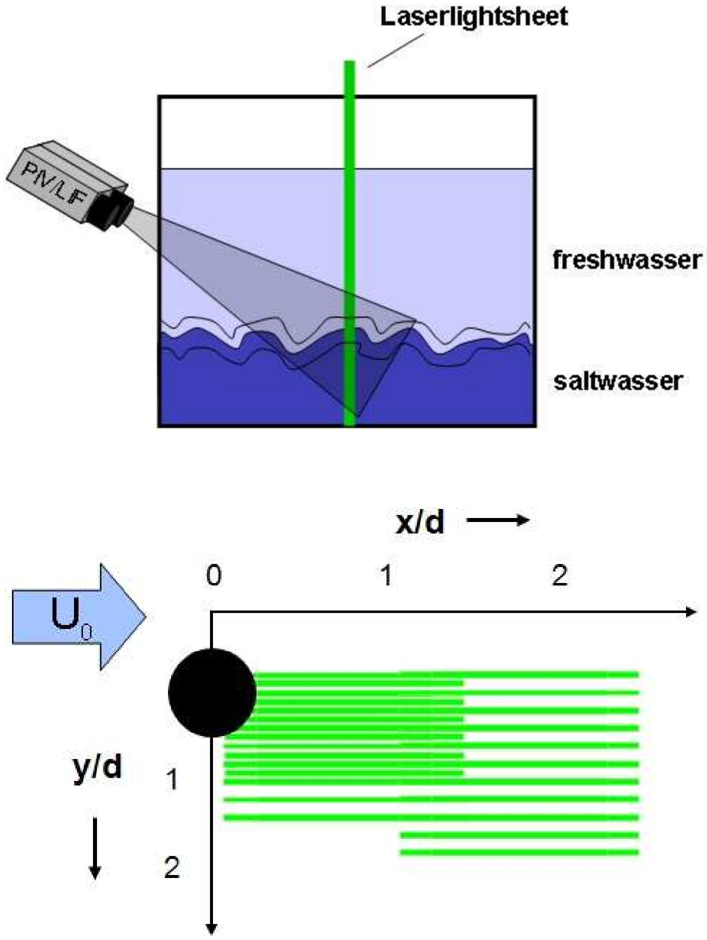

Figure 3.15: Optimised camera alignment and measured PIV/LIF-planes

$x/d = -1$.

One reason for this is the thin boundary layer at the bottom, compared to the thick mixing layer with lower gradients of the velocity. Figure 3.18 shows the bottom near horseshoe vortex. Here, the separation of the vortex is clearly visible. It also is obvious, that the vortex is still rotating at $x/d = 2$. However, the most important result for this work can be seen in figure 3.19. The separation point of the cylinder boundary layers is found at around 110^o. Compared with the angle of 80^o to 90^o that are published f.e. by *Gölling* (2001) and *Zdravkovich* (1997) for the sub-critical Region at $Re \approx 3400$, this angle is an indication for an over critical flow around the cylinder. The reason for this behaviour can be found in the high degree of turbulence of the incident flow, that leaves to a turbulent boundary layer and therewith in the late separation. In nature case, a Reynolds number of $Re = 3.4 \cdot 10^6$ would appear. At this Reynolds number, turbulent boundary

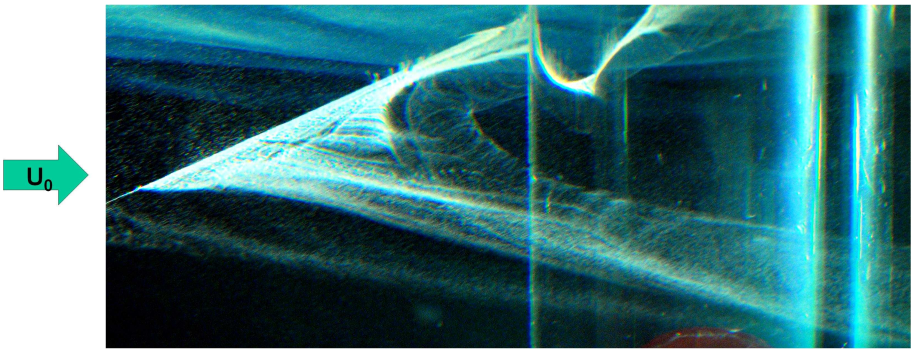

Figure 3.16: Horseshoe vortex at the mixing layer

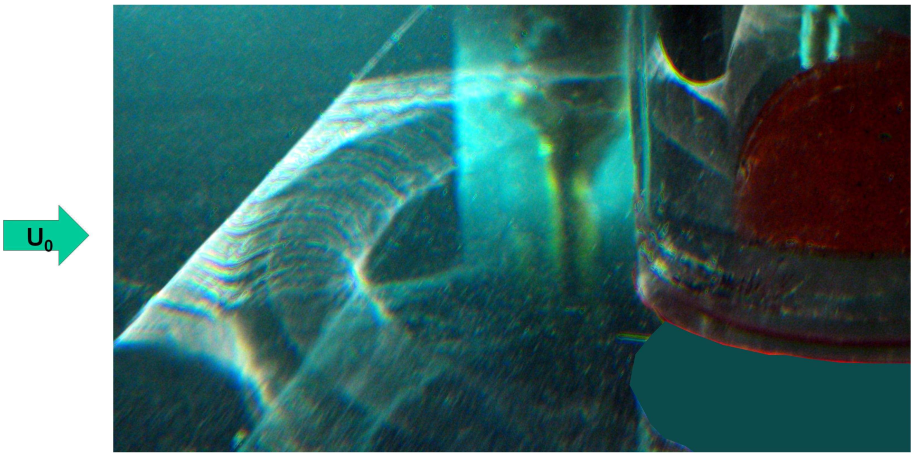

Figure 3.17: Horseshoe vortex near the bottom

layers with a separation at around 120^o would be found (see f.r. *Zdravkovich* (1997) and *Schlichting and Gersten* (2006)). The visualisation experiments show, that the inflow conditions into the water channel were able to reproduce a separation that is similar to the nature case at higher Reynolds numbers. Therewith the size and form of the wake could be reproduced optimal.

3.1.5.1 Measurements with velocity profile 1

The post-processing of the measurements has been carried out for each time step separately. The resulting quantities have been averaged over the whole measurement (1000 samples) afterwards.In the following section, first the measurements in the centre line ($y/d = 0$) will be discussed. The vertical position, where the salinity reaches 50% of the maximum salinity will be used as definition for the thickness of the saltwater layer in the following sections. In figure 3.20, the thickness of the saltwater layer in the case without a cylinder (red line) is horizontal and flat, which

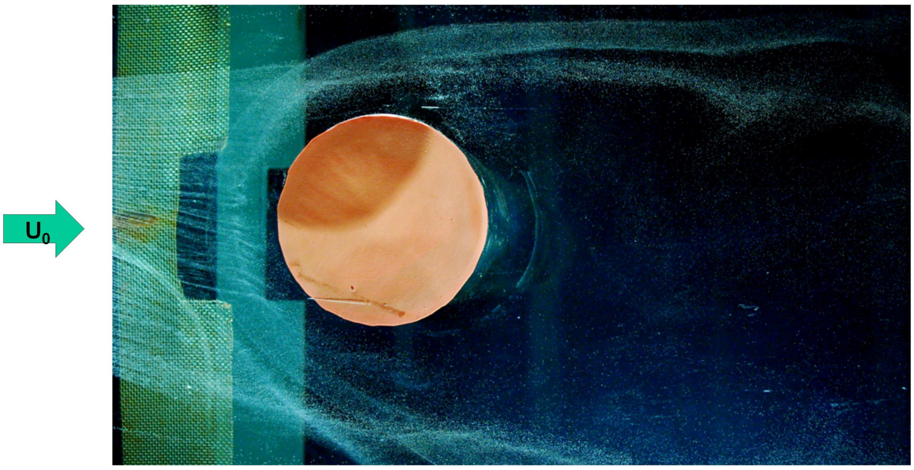

Figure 3.18: Visualisation of the bottom near horseshoe vortex

indicates that the test section and the boundary conditions have been chosen right and allow a good description of the processes, which occur in nature. In the case with cylinder (black line), a lowered halocline is found in the near wake of the cylinder at $0.5 \leq x/d \leq 3.0$. However, in the far field of the cylinder ($x/d \geq 20$), no influence of the cylinder is detectable anymore by observing the thickness of the saltwater layer.

3.1.5.1.1 Mixing quantities in the far field behind the cylinder The mixing in the far field of the cylinder will now be quantified by the use of the Mixing number M_{20}, which was introduced in the sections before. To get an impression about the development of the expansion of the mixing layer, figure 3.21 shows the vertical distance between the point, where the salinity reaches 40% or 60% respectively and the point, where the salinity reaches 50% of the maximum salinity. As can be seen, the expansion with cylinder (raw-data black, linear regression blue) does not differ significantly from the case without cylinder (raw-data red, linear regression green). It should be remarked, that the thickness of the mixing layer is nearly constant within the whole test section for both cases. It should also be noted, that the vertical expansion of the mixing layer of around 4 mm is relatively small. For computing of the Mixing number, the velocity profile at $x/d = 20$ will be used from the bottom to 50% of the maximum salinity. Therewith the Mixing number results in $M_{20} = 0.013$. This means that the volume flux within the mixing layer is increased about 1.3%, normalised on the incident volume flux due to the cylinder.

3.1.5.1.2 Mixing quantities in the near wake of the cylinder The source for the observed mixing in the far field has to be searched in the near wake ($-2 \leq$

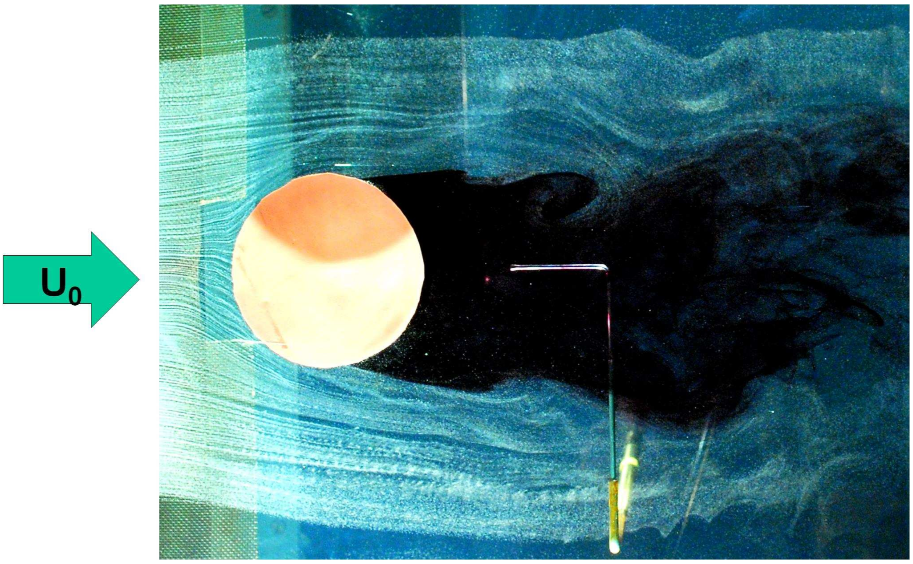

Figure 3.19: Visualisation of the separation point at $z/D = -3.5$.

$x/d \leq 10$) of the cylinder. To quantify the mixing in the near wake and to get a qualitative overview about regions of more or less mixing, the entrainment velocity will be used. To neglect the influence of internal waves, the thickness of the saltwater layer D has been averaged over 30 seconds. Figure 3.22 shows the distribution of the entrainment velocity in the wake of the cylinder. Strong local minima are found at $x/d = 1.5$ in the region of the free shear layers, whereas a maximum is located around the centre line at $1.25 \leq x/d \leq 4$. Downstream of $x/d = 6$ it can be assumed, that no significant entrainment velocity can be measured. The entrainment velocity-flux for the Region, displayed in figure 3.22 results in $\dot{V}_{w_E} = 1.25 l/min$. Normalised on the incident flow from $-1.2 \leq y/d \leq 1.2$, the entrainment-flux is derived with $\dot{V}_E = 0.022$. The reference measurements without the cylinder showed an entrainment-flux of $\dot{V}_E = 0.003$. The additional entrainment-flux is calculated as the difference and can be stated with $\dot{V}_E = 0.019$. This number can be interpreted as an additional increase of the volume-flux within the saltwater layer of about 1.9 %, related to the incident volume-flux.

3.1.5.1.3 Flow structure in the wake of the cylinder

To illustrate the very complex structures in the wake, the measurements from the 2-component PIV will be analysed. Figure 3.23 shows the mean velocity field behind the cylinder at $y/d = 0$ as black vectors and the distribution of salt as colour map. Here again the black isoline of 50% salinity shows the lowered saltwater layer in the near wake. The velocity field shows a strong upward component of the velocity of the saltwater flow in the region of $1.2 \leq x/d \leq 2.5$. Due to this upward component, recirculation

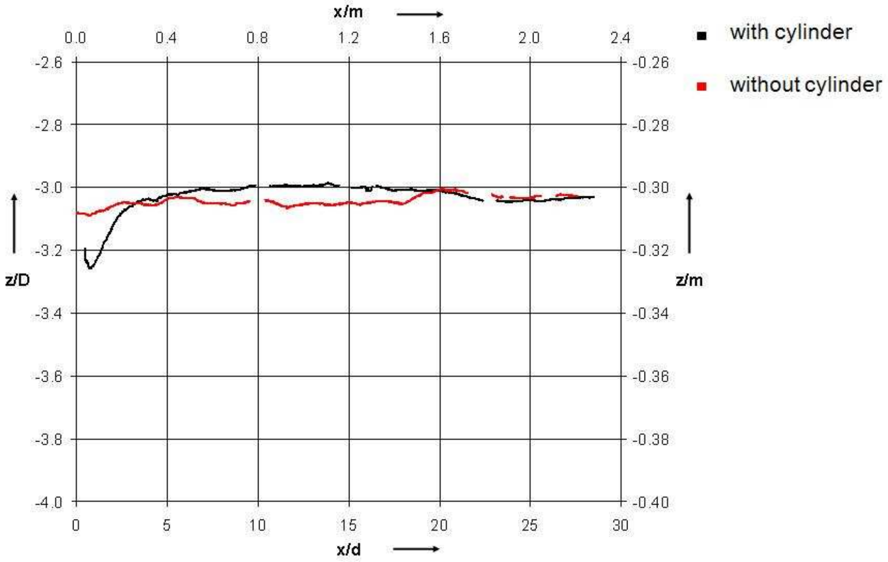

Figure 3.20: Development of the vertical position of the mixing layer with profile 1.

region becomes inhomogeneous along the z-axis. To visualise this, figure 3.24 shows a beige iso-surface, which illustrates the area with the velocity $u = 0$ m/s. It is visible, that the recirculation region has a minimal extension near the bottom. The blue iso-surface of 50% of the maximum salinity is included to illustrate the position of the recirculation region within the saltwater layer. The following part will discuss the Stereo-PIV measurements, taken in x-y-planes. Within each of these measurements, 1024 three-component velocity fields have been measured with a repetition rate of 10 Hz. After averaging over time the Stereo-PIV measurements could be assembled to a three-dimensional three-component velocity volume dataset. Before analysing these measurements, they have been validated by the PIV-measurements, discussed before. A deeper going description of that can be found in *Menzel* (2010). As already discussed, the existence of a dominant frequency in the wake of the cylinder due to the Kármán vortex street has to be investigated. The state of the art method to find this frequency is to analyse the v-component of the velocity via a Fast Fourier Transformation. From the Stereo-PIV measurements this has been done for each measured plane and each position within these planes. This way 26568 points in the wake of the cylinder have been analysed. Figure 3.25 shows an exemplary spectrum of the Strouhal number at $x/d = 1.5$, $y/d = 0$ and $z/D = -3.7$. The black bars show a wide distribution over the whole range of $0.0 < Sr < 0.5$, that indicates that no dominant frequency exists. To neglect high frequencies, which would not be caused by the separating boundary layers, the data have been filtered and displayed as red bars in figure 3.25. Here two very weak but reasonable maxima

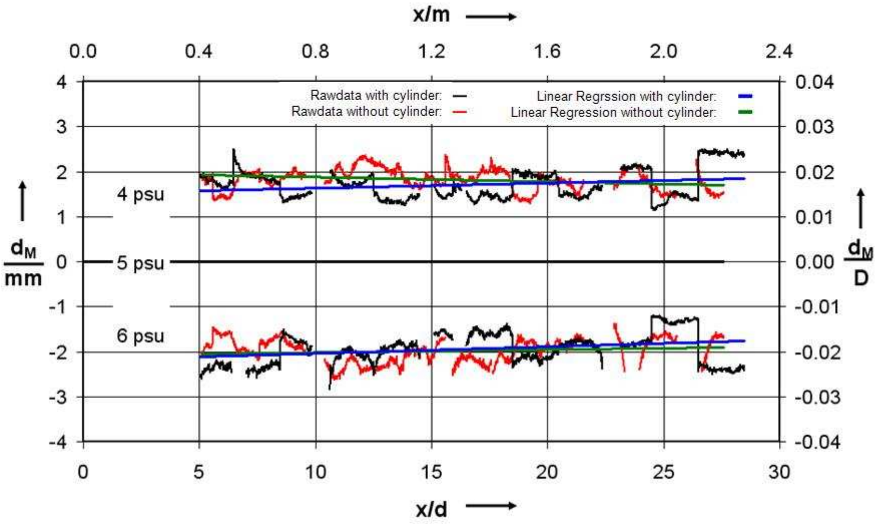

Figure 3.21: Development of the vertical expansion of the mixing layer with profile 1.

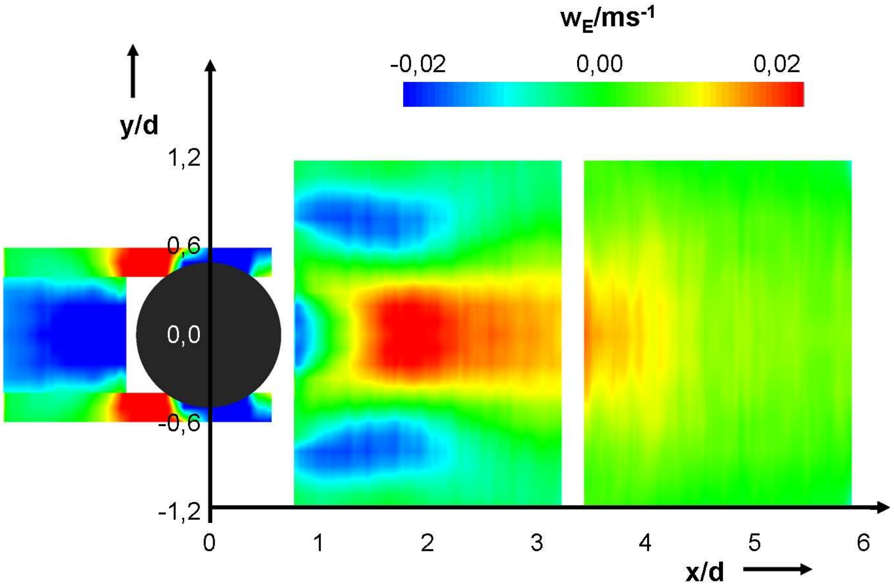

Figure 3.22: Distribution of the entrainment velocity in the wake of the cylinder.

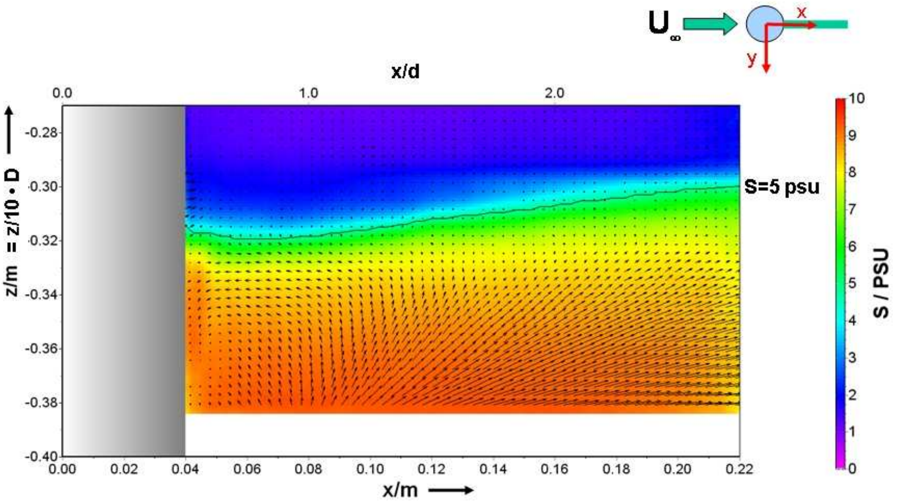

Figure 3.23: Time averaged velocity vector field and salinity distribution at $y/d = 0$ in the wake of the cylinder

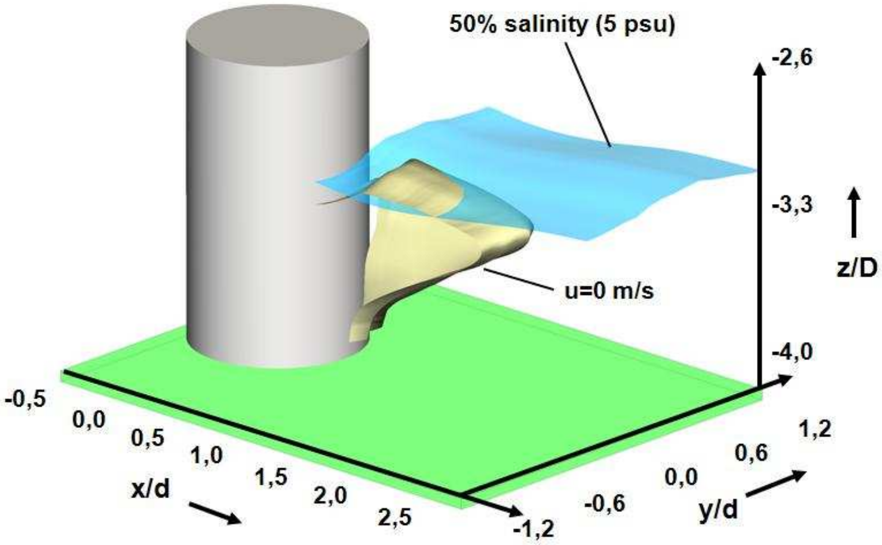

Figure 3.24: Iso-surfaces of the recirculation region and salinity.

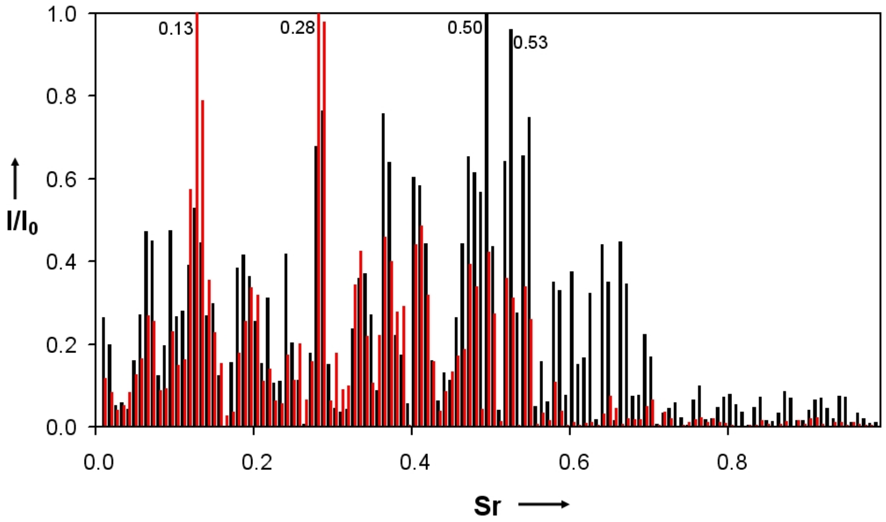

Figure 3.25: Normalised Strouhal-spectrum.

can be found with $Sr = 0.28$ and the half frequency $Sr = 0.13$. These frequencies point to the existence of mutual separating turbulent boundary layers, whereas the Strouhal number of $Sr = 0.28$ is larger than the one, expected for a infinitive long cylinder. The reason for this is the separation which is similar to an over critical flow around a cylinder (see *Cantwell and Coles* (1983)) with a separation angle of around 110^o. As *Kappler* (2000) already found out, a dominant Strouhal number can be found in shear flows, but only local for a limited time. To find a global dominant Strouhal number, the 3321 spectra for each measuring plane have been averaged. These averaged spectra are represented in figure 3.26 for the planes at $z/D = -3.3$ (grey), $z/D = -3.5$ (red) and $z/D = -3.7$ (black). These analysis show, that the Kármán vortex street is present (figure 3.25), but not dominant and global.

Figure 3.27 shows again the iso-surface of 50% salinity and streamlines with their source at $z/D = -3.5$, who are computed as gradients to the time averaged velocity field. The streamlines visualise the mean flow field in the wake of the cylinder whereas an upward directed velocity component ($\overline{w} > 0$) is overlayed to the background flow in the centreline of the cylinder wake ($y/d = 0$) and a downward velocity component at $y/d = \pm 0.6$. The streamlines are coloured by the magnitude of the velocity, which shows minimal values near the mixing layer. To quantify the rotation, found from the streamlines, the vorticity-component ω_x is plotted in figure 3.28. It shows a pair of counter rotating vortices with their vortex axis in x-direction. The maximum of the vorticity is reached at around $x/d = 1$ and $y/d = \pm 0.3$. This "engine for mixing" is located beneath the mixing layer and therewith not strong

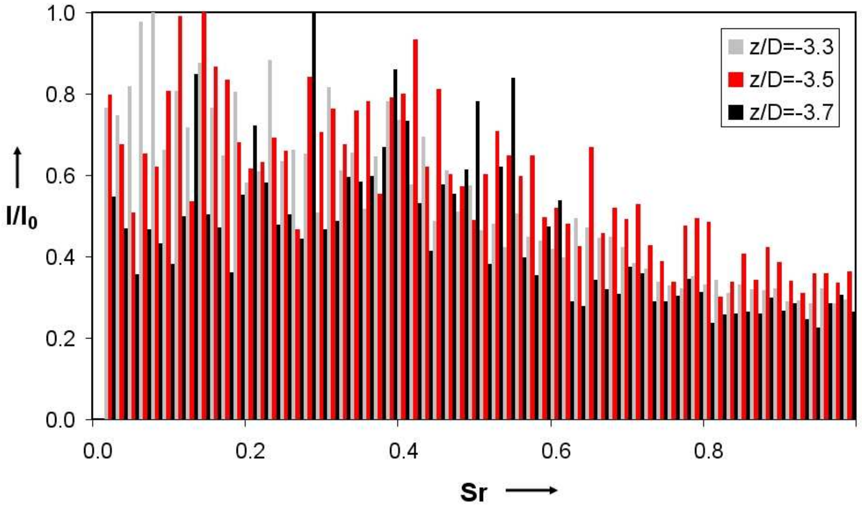

Figure 3.26: Normalised averaged Strouhal-spectra.

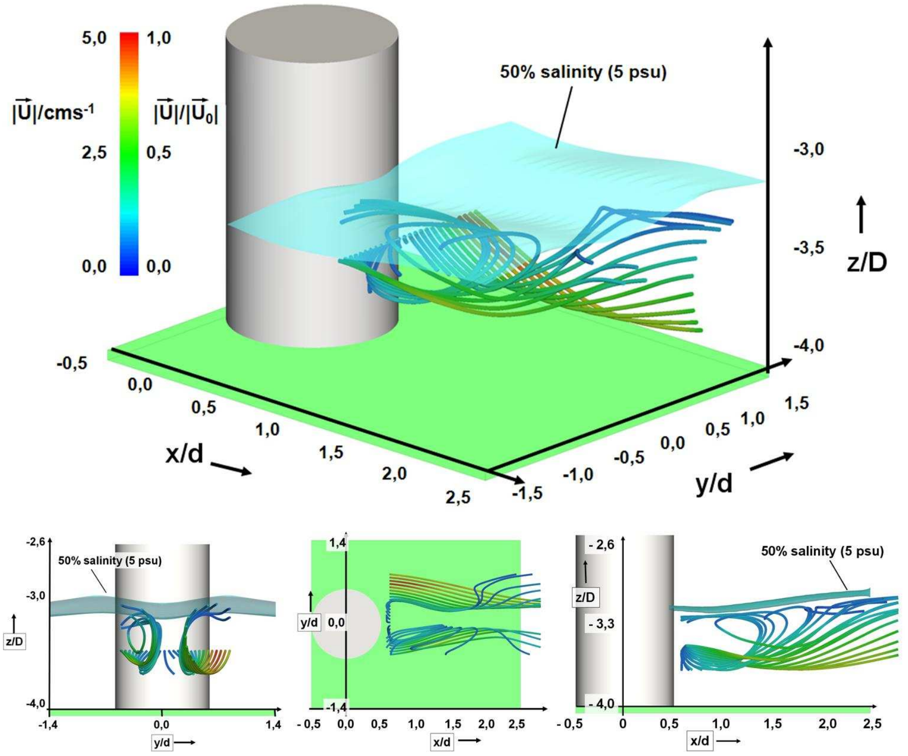

Figure 3.27: Three-dimensional structure of the cylinder wake.

enough to cause a significant exchange of salt between the saltwater flow and the freshwater layer. A scheme of the appearing vortex structures is shown in figure 3.29. It can be seen that the vortex structures are rotating in all three dimensions. The bottom near horseshoe vortex has been found by flow visualisation as well as a horseshoe vortex directly beneath the mixing layer, which is caused by the shear within the mixing layer. This vortex is larger than the bottom near vortex and counter rotating to it. The Kármán vortex street was found, but only parts of it as there is no dominant frequency for the whole wake. Like *Kappler* (2000) also found out, there are fragments of the Kármán vortices which exist local and for short times with quickly changing frequencies. More dominant and therewith the "engine of mixing" is a counter rotating longitudinal vortex pair with their axis in x-direction, which are located within the saltwater layer and who does not disturb the mixing layer. Their sources are supposed to be the separating boundary layers of the cylinder which induce Kármán-like vortices which tip over due to the sheared velocity profile with much higher velocities near the mixing layer than in the bottom near region. This phenomena has also been found by *Jensch et al.* (2010) for a finite, wall mounted cylinder. Also visualised in the figure are the Kelvin-Helmholtz-instabilities, which will occur along the whole mixing layer due to shear. These instabilities induce the main background mixing and can become

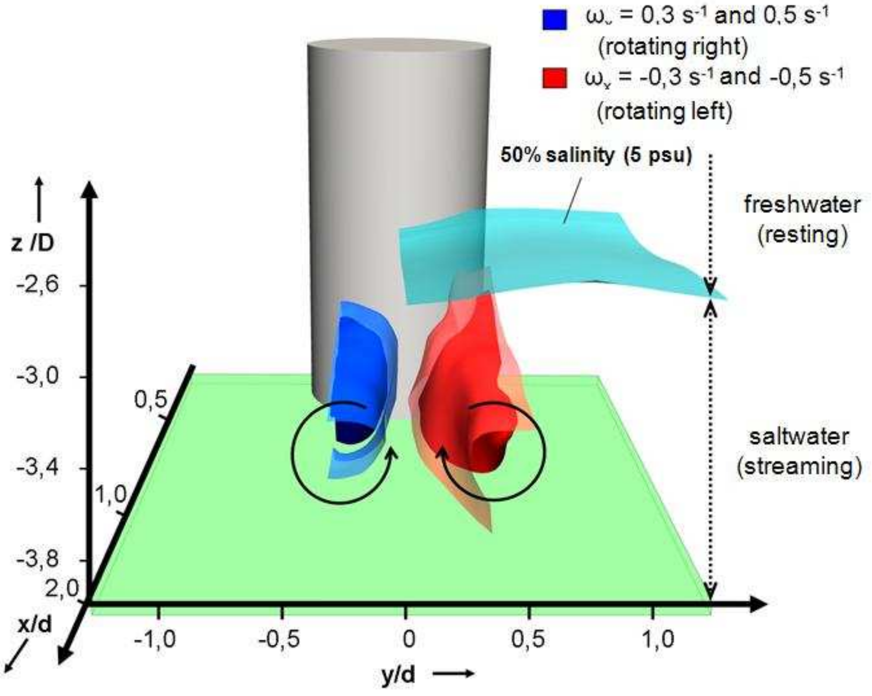

Figure 3.28: The dominant vortex structures

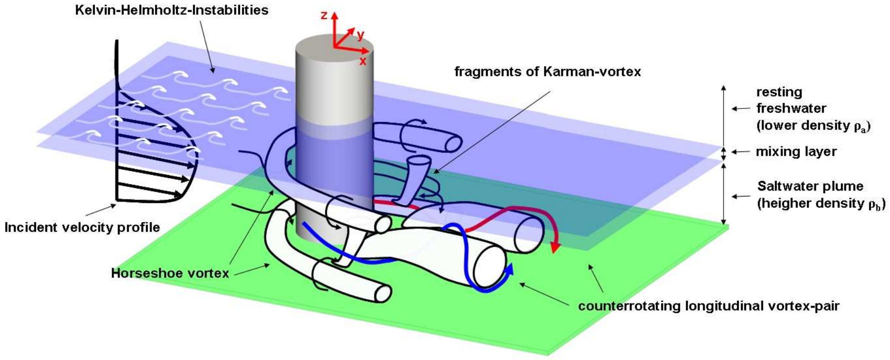

Figure 3.29: Vortex structures in the wake of the cylinder

more instable due to vortex structures caused by the cylinder.

Intensive analysis have been done on the turbulence structure and the separating boundary layers, which will not be discussed in this report and can be found in *Menzel* (2010). Only the main results of these analysis should be presented here. From *Leder* (1992) is known, that different regimes of separating boundary layers can be defined and be detected by the maximum value and the distribution of the Reynolds-stresses in the wake of the body. The analysis of the Reynolds-stresses implies, that the wake of the stratified flow around the cylinder is similar to three-dimensional separation like it can be found in the wake of a finite cylinder (*Richter* (2005)). This result confirms again, that the wake is highly three-dimensional and can only hardly be described by simple models.

3.1.5.2 Influence of the velocity profile on mixing

The following results are taken from the measurements with velocity profile 2. Furthermore, detail measurements will be presented, which have been taken with the optimised camera alignment to zoom into the mixing layer.

These measurements with a densimetric Froude number of $Fr_D = 0.51$ have been done to validate the influence of the velocity profile itself without any other influences. These measurements have been necessary and fundamental for the measurements and analysis that will be done afterwards.

3.1.5.2.1 Mixing quantities in the far field behind the cylinder A comparison of the vertical position of the mixing layer with and without the cylinder with velocity profile 2 shows a similar behaviour as for velocity profile 1. In the near wake a mixing layer, lowered about 0.2 D is found in the near wake of the cylinder (see figure 3.30, black line). Downstream, the mixing layer is slightly lifted and converges to the situation without cylinder (red line) at latest at $x/d = 20$.

The lift of the mixing layer for velocity profile 2 is weaker than for profile 1. In contrast to profile 1, the mixing layer loses 20% of it's vertical expansion within the measuring section, which is caused by an acceleration of the fluid due to the inflow to the collecting section of the water channel, where the densimetric Froude number reaches $Fr_D = 1$ as long as this section is not filled totally with saltwater. This acceleration is followed by a damping of internal waves and therewith to a weaker lift of the mixing layer in the cylinder wake. The influence of this acceleration on small scale turbulent phenomena in the region of the mixing layer can be suggested as negligible small. In contrast to profile 1, the inflow front with profile 2 has been observed to be flatter and of lower turbulence and therewith caused lower mixing at front of the plume. This is caused by the inlet, that has been constructed in another way with the goal to get an optimised velocity-profile which implies a lower degree of turbulence. The visual observations lead to the assumption, that the behaviour of the front of the plume influences directly the density stratification in the collecting area and therewith the flow situation at the border from the measuring section to the collecting section ($Fr_D = 1$ or $Fr_D < 1$). Besides this it can be pointed out, that the mixing without the cylinder is weaker with profile 2 than with profile 1. In figure 3.31, the vertical distance between the point, where the salinity reaches 40% or 60% respectively and the point, where the salinity reaches 50% of the maximum salinity is plotted. Looking at this figure and comparing it with figure 3.21, the acceleration can be seen by the decrease of the vertical expansion of the mixing layer with increasing distance to the inlet for profile 2. The Mixing number

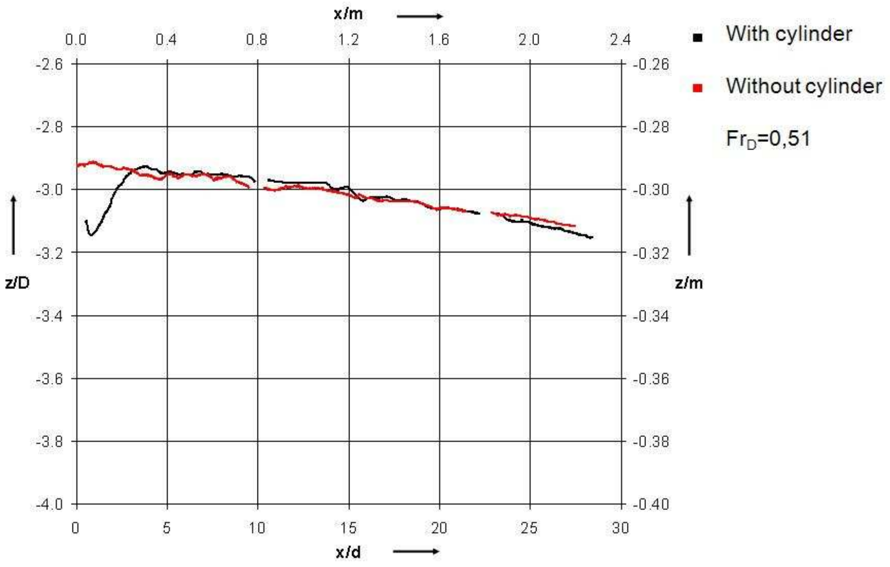

Figure 3.30: Development of the vertical position of the mixing layer with profile 2.

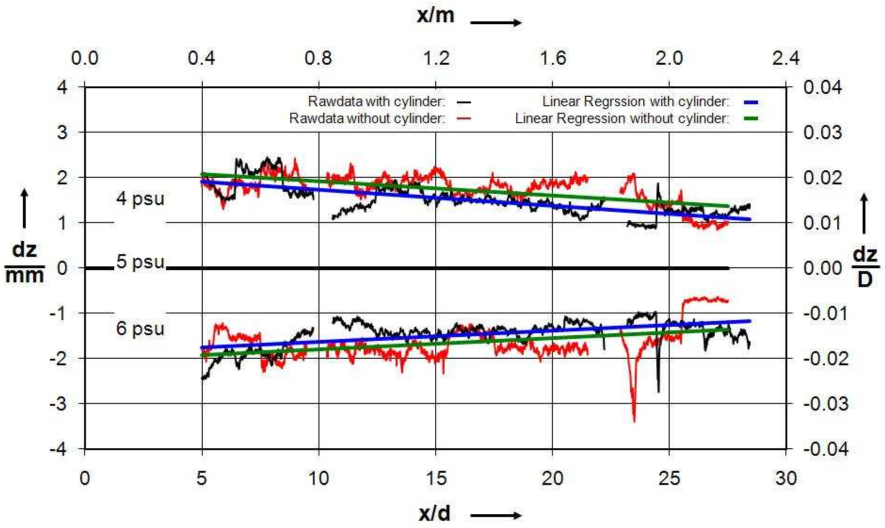

Figure 3.31: Development of the vertical expansion of the mixing layer with profile 2 and $Fr_D = 0.51$.

reaches $M_{20} = 0.005$ with the background mixing already subtracted, which is a little smaller than for profile 1.
It can be concluded, that a stabilising of the mixing layer, compared to the case with velocity profile 1, occurs as a result of the acceleration of the saltwater flow. Due to this, the mixing is determined smaller than with velocity profile 1.

3.1.5.2.2 Mixing quantities in the near wake of the cylinder The measurements with the optimised camera setup allowed a quantification of the vertical Reynolds flux within the mixing layer and therewith a quantification of the turbulent mixing. A quantitative distribution of the vertical Reynolds flux in the centreline of the cylinder is shown in figure 3.32 as colour plot. There a maximum beneath the 50%-isoline (middle black line) can be found. The minima above this line also indicate a turbulent vertical exchange, which is a few lower than the positive values beneath. Positive Reynolds fluxes can be interpreted as a decrease of salinity together with a downward directed (negative) velocity component. This would correspond to an entrainment of freshwater into the mixing layer. Negative Reynolds fluxes can be interpreted as an increase of salinity, together with a negative velocity component. The reason for this can be found in the three dimensional character of the near wake, which has been already discussed before. The whole dataset, presented in figure 3.33, shows the development of the vertical Reynolds flux in the whole wake, whereas negative Reynolds fluxes are not displayed as their impact is quit small. Normalising the vertical Reynolds flux on the product of incident

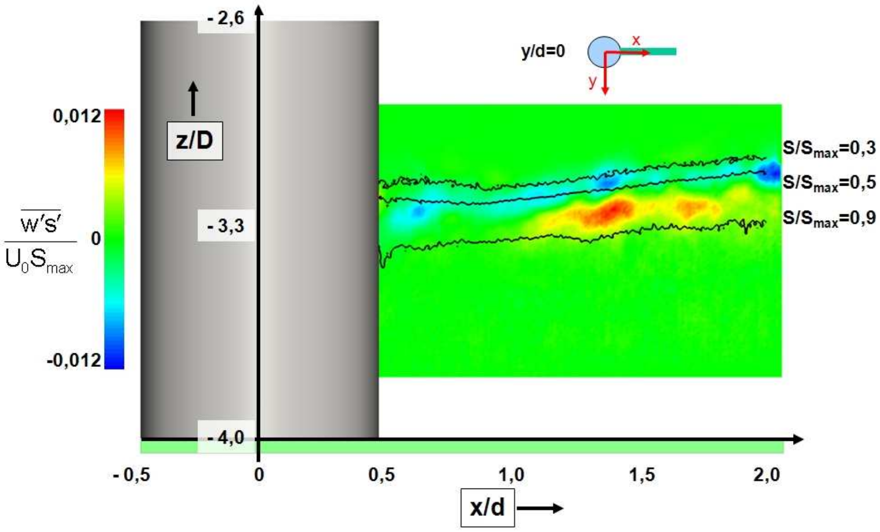

Figure 3.32: Development of the vertical Reynolds flux with profile 2 in the centreline.

velocity and maximum salinity allows a quantification of the maximum turbulent vertical transport, which can be derived as $|\overline{w's'}/U_0S_{max}| \approx 0.012$. Because this quantity is negligible small for the case without cylinder, the additional degree of turbulent transport can be fixed with 1.2%. Additionally to the Reynolds flux, the local and global mixing efficiency has been calculated. Figure 3.34 shows the global mixing efficiency in the near wake of the cylinder. It shows dominant maxima at $y/d = \pm 1.0$ and a small maximum at $y/d \approx 0.0$ with values around Γ=0.15. Regarding the definition of the global mixing efficiency it is expected, that around 15% of the dissipated turbulent kinetic energy contribute to vertical mixing. The local mixing efficiency γ (see upper colour scale in figure 3.35 reaches its absolute maximum at γ=0.6 in a region of small spatial expansion in the centre line behind the cylinder in the region of the mixing layer. Another, weaker maximum can be found in a larger region within the mixing layer around $y/d = \pm 1.0$. In Regions of the undisturbed flow, the local mixing efficiency reaches values around γ=0.2, whereas the global mixing efficiency reaches values of around Γ=0.05. The development of the streamlines (beige lines in figure 3.35) points out, that these maxima are located outside the dominant longitudinal vortex pair. The global mixing efficiency is comparable to the Flux Richardson number Ri_{Fb}, vertically integrated over saltwater layer. From RANS-simulations, published by *Schimmels* (2008), values of $Ri_{Fb} = 0.18$ are given for the scale of the Baltic-Sea at the same densimetric Froude number. The buoyancy production, also published in *Schimmels* (2008), is given with $3 \cdot 10^{-5}$ m^2/s^3. Figure 3.36 shows the buoyancy production, measured in the laboratory at $y/d = 0$ in the wake of the cylinder. The maximum values

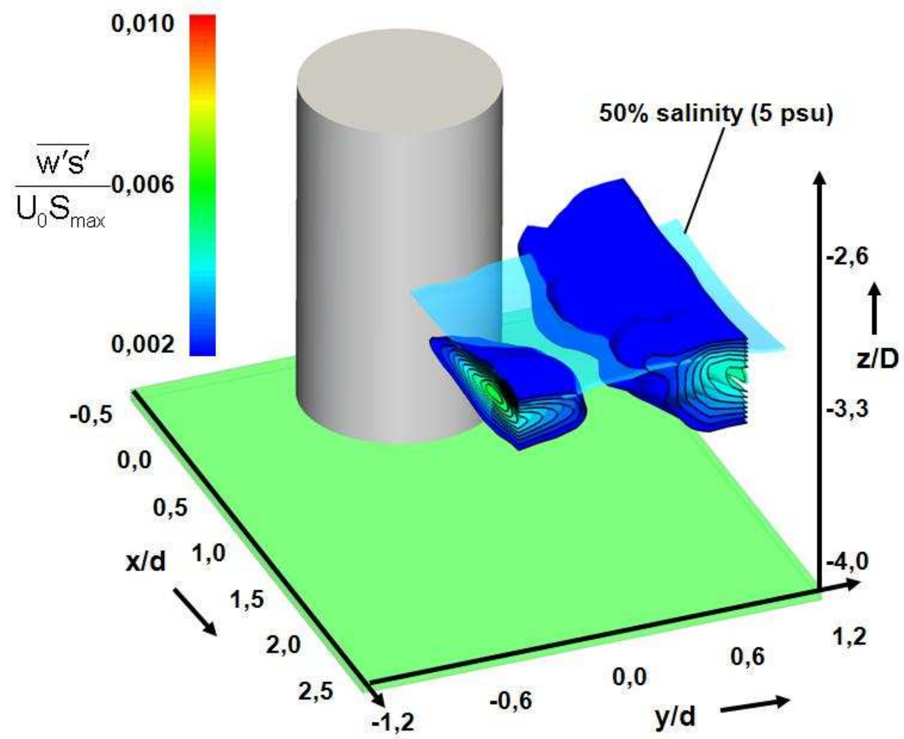

Figure 3.33: Development of the vertical Reynolds flux with profile 2.

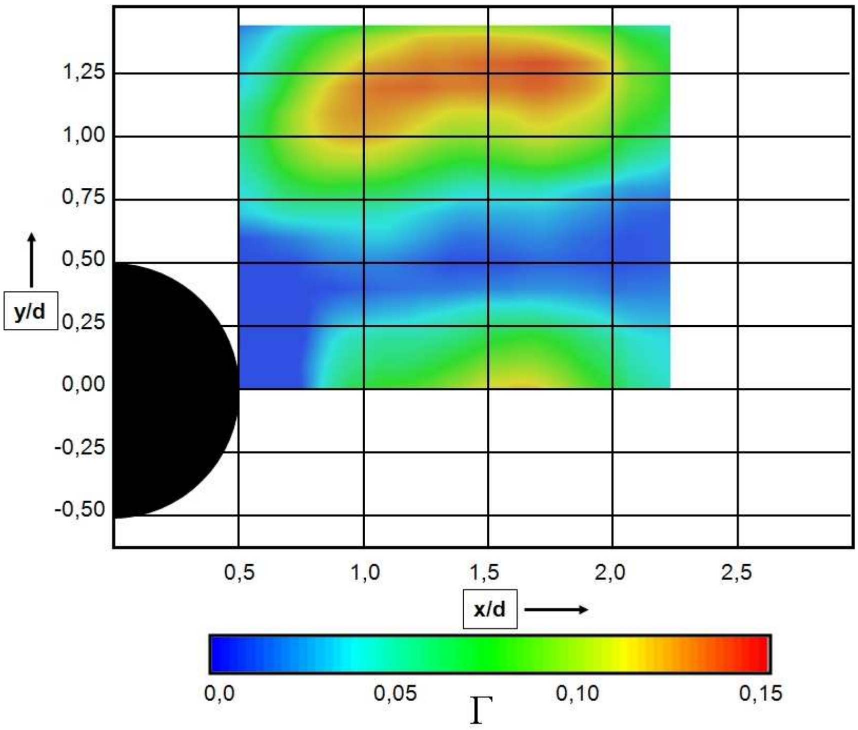

Figure 3.34: Development of the global mixing efficiency with profile 2.

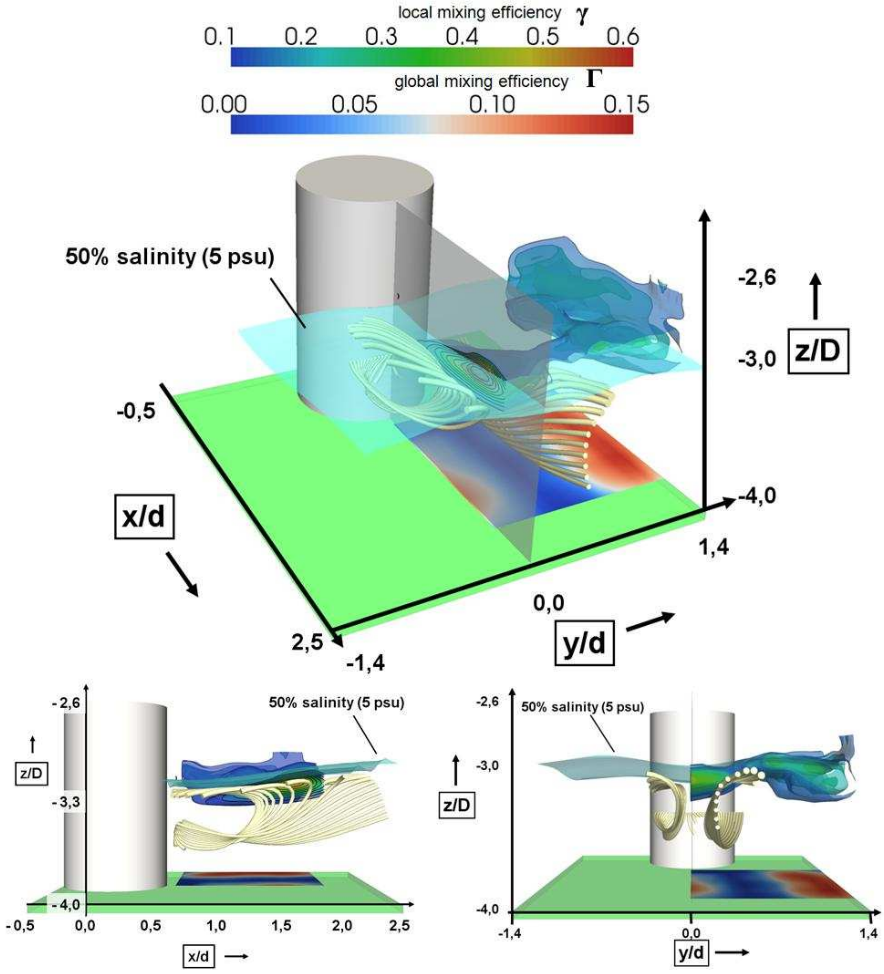

Figure 3.35: Development of the mixing efficiency and streamlines with profile 2.

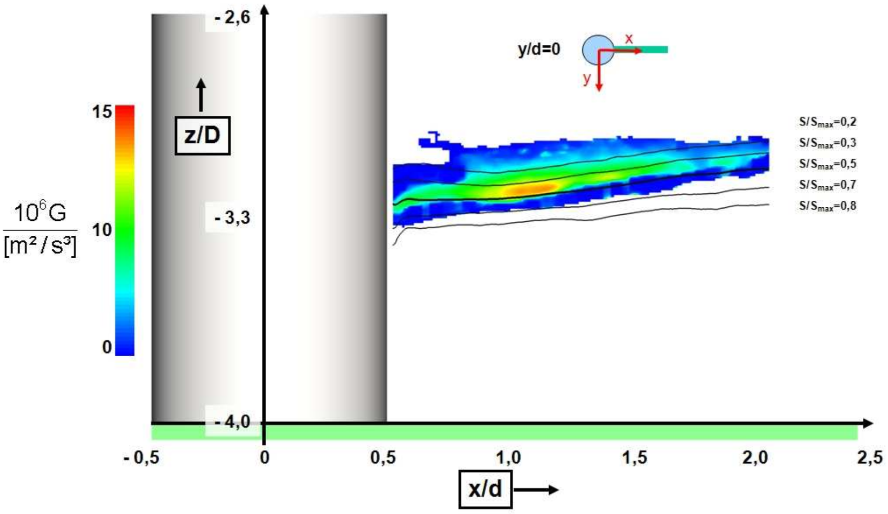

Figure 3.36: Development of the buoyancy production with velocity profile 2

that can be found here is $1.5 \cdot 10^{-5}$ m^2/s^3. Regarding, that the calculation of the buoyancy production is based on time-averaged direct measurable quantities and their derivations, it can be interpreted as the work that has to be done to mix freshwater into the saltwater layer against it's buoyancy. Normalised on the dissipation, a development similar to the buoyancy production is found with a local maximum of $-G/\epsilon$=0.5. Therewith 50% of the dissipated turbulent kinetic energy are used for turbulent vertical mixing, which was already found from the local mixing efficiency. This result confirms, the numerical simulation from *Schimmels* (2008) are comparable to the laboratory experiment by the order of magnitude. By averaging the local mixing efficiency and the buoyancy production over the volume of values higher than the background (estimated as: $0.5 < x/d < 2.0$, $-0.2 < y/d < 1.4$ and $-3.4 < z/D < -3.0$) values of

$$\frac{\int_V -G/\epsilon}{V} = 0.0032$$

and

$$\frac{\int_V \gamma}{V} = \frac{\int_A \Gamma}{A} = 0.001$$

are found. Here the mixing efficiency is based on the turbulent vertical transport whereas the buoyancy production is based on temporal averaged quantities. Here the difference between direct measurements (mixing efficiency) and an approximation by turbulence models (buoyancy production) can be seen.

3.1.5.3 Influence of the densimetric Froude number on mixing

To figure out the influence of the Froude number on the mixing processes, experiments with different densimetric Froude numbers have been carried out by changing the salinity and therewith the density of the saltwater. Due to this, the velocity profile and the Reynolds number have been more or less constant for all experiments. An increasing densimetric Froude number implies the suggestion, that the stability of the stratification will decrease. In figure 3.37, this can be seen, regarding the lowering and later lifting of the mixing layer due to the cylinder (black) in comparison to the reference case without cylinder (red). Here this elongation is stronger than in the case of $Fr_D = 0.51$. But also for this case, no influence of the cylinder can be seen in the far-field of the cylinder by looking at the vertical position of the mixing layer. The development of the vertical expansion of the mixing layer, shown in figure 3.38 stays nearly constant over the length of the measuring section for the case without cylinder (raw-data red, linear regression green), as it has also be seen with velocity profile 1 and $Fr_D = 0.51$. Compared to the case with lower densimetric Froude number ($Fr_D = 0.51$) and the same velocity profile, here an increased mixing can can be seen, as the thickness of the mixing layer stays constant here and decreases at the lower Froude number with increasing distance to the inlet. The case with the cylinder installed shows an increased widening of the mixing layer with increasing distance to the inlet of the measuring section. The Mixing number

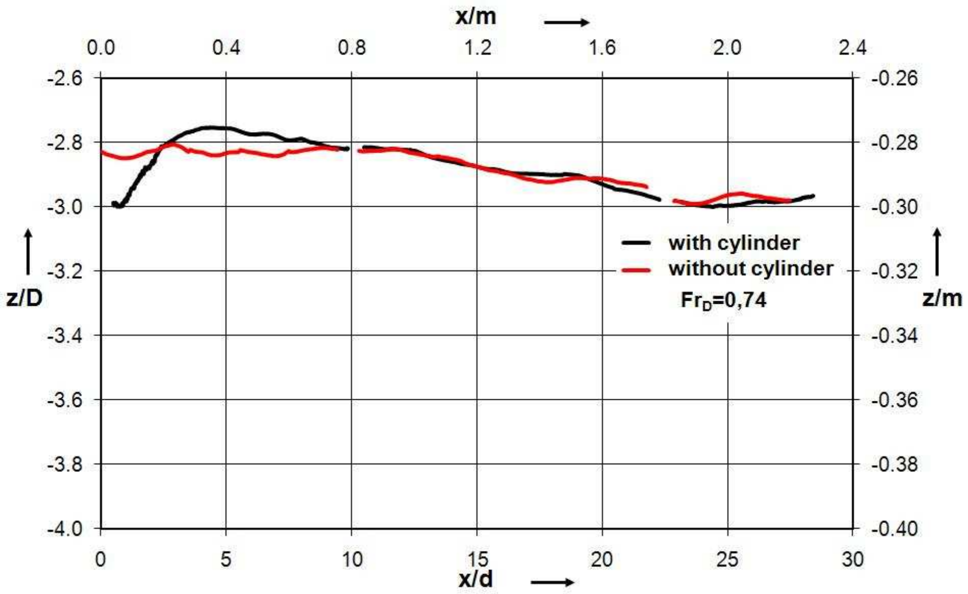

Figure 3.37: Development of the vertical position of the mixing layer with profile 2 and $Fr_D = 0.74$.

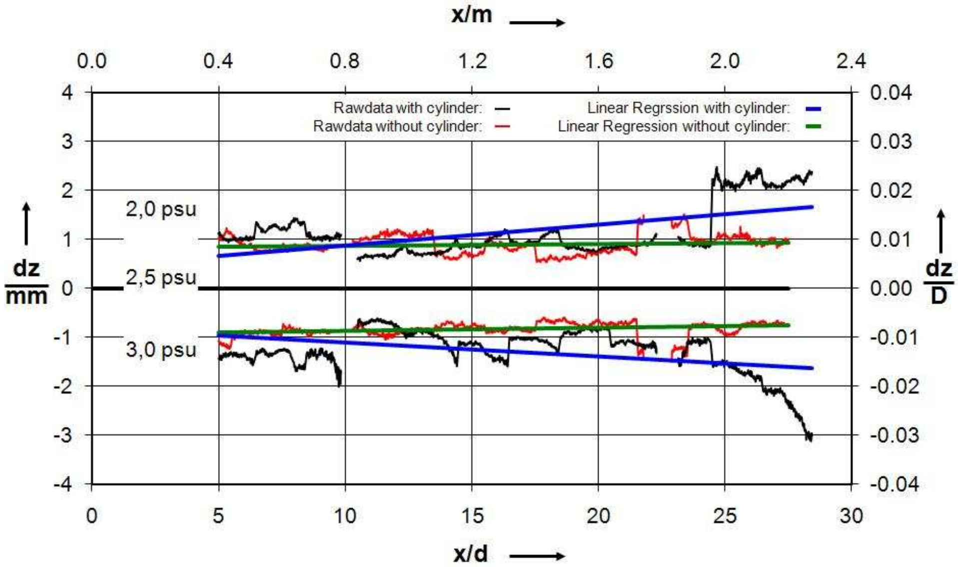

Figure 3.38: Development of the vertical expansion of the mixing layer with profile 2 and $Fr = 0.74$.

is derived with $M_{20} = 0.007$ and is therewith higher but not significantly higher than the value for $Fr_D = 0.51$.
This result implies the tendency, that the mixing increases with increasing Froude number. The results from the chapters before show, that mixing occurs, but it is very weak. An increasing Froude number therewith could increase the mixing, but it is not clear if the additional mixing, caused by the cylinder also increases. To investigate this, measurements with a higher spatial resolution have been carried out at $x/d = 20$ with focus on the thickness and the volume flux within the mixing layer. Figure 3.39 shows the vertical extension of the mixing layer d_M at $x/d = 20$ in dependency of the densimetric Froude number. The black points display the measurements with cylinder, whereas the red ones display the measurements without cylinder. Both regression lines show a significant expansion with increasing densimetric Froude number or decreasing density. The linear regression is used to visualise the effect but not to state a linear law. An influence of the cylinder is again not significantly detectable by this quantity. As already written before, the thickness of the mixing layer can not be used to quantify any mixing and the Mixing number M_{20} has been invented to do so. Figure 3.40 visualises the dependency of the Mixing number of the densimetric Froude number. It is obvious, that very strong fluctuations are present but at small Mixing numbers with a tendency of an increasing Mixing number with increasing densimetric Froude number.

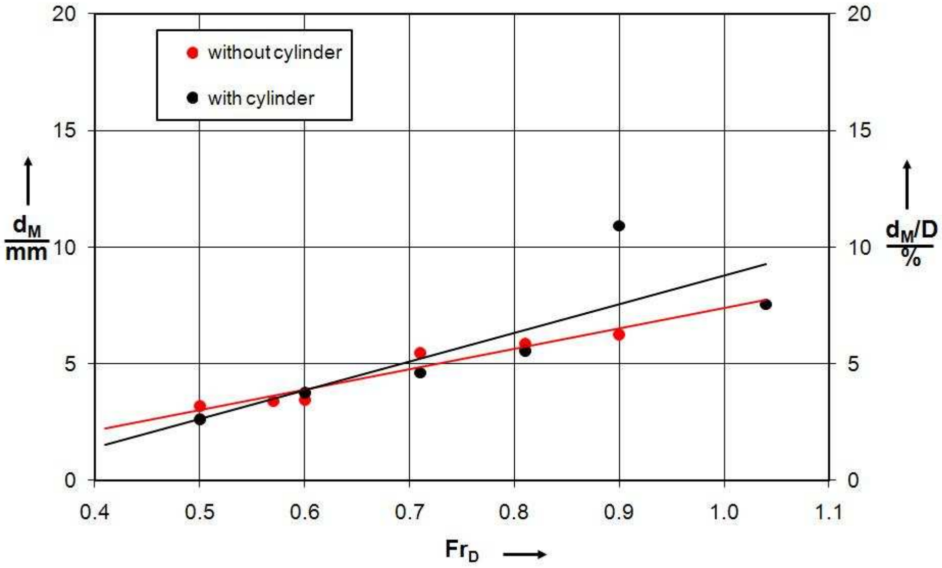

Figure 3.39: Vertical extension of the mixing layer in dependency of the densimetric Froude number with profile 2.

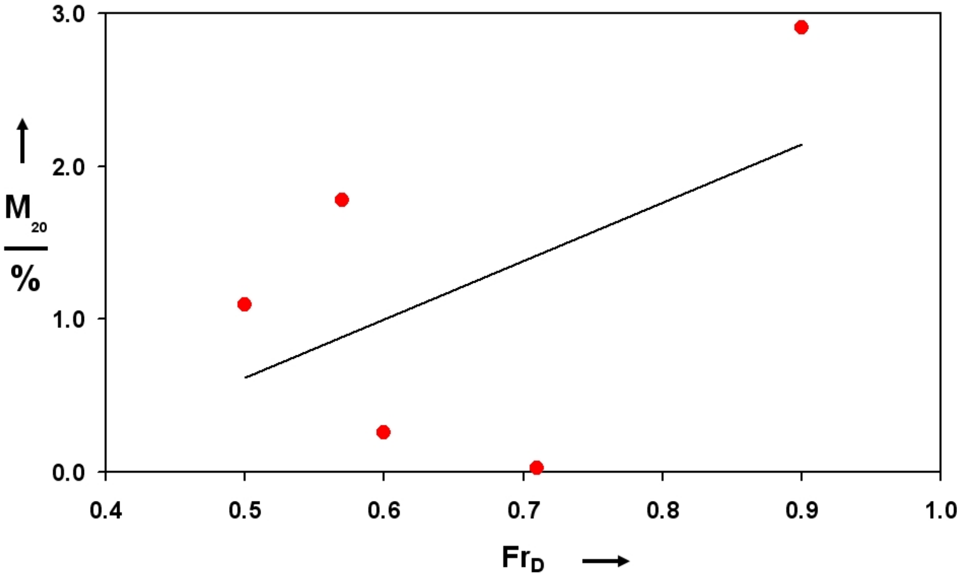

Figure 3.40: Mixing number in dependency of the densimetric Froude number with profile 2.

3.1.6 Numerical Simulation (UNI-HRO)

3.1.6.1 QuantAS-Off: Large Eddy Simulation of the laboratory experiment

Parallel to the laboratory experiments additional numerical simulations are done at the Chair of Fluid Mechanics at the University of Rostock. To provide a highly detailed insight into the processes of the flow regime, the laboratory experiments are emulated in an appropriate method. This means as well to adopt the geometry of the experimental channel as the boundary conditions form the experimental setup. In addition the Large Eddy Simulation (LES) is determined by pre-calculations as the only simulation method to be able to resolve even the smallest structures in the flow *Melskotte* (2007).

A Large Eddy Simulation of the three-dimensional circular cylinder flow in a stratified two-phase-flow in the scale of the experiment has been performed using the boundary conditions "LAB velocity profile 1" (cf. table 3.2). The numerical simulation allowed to overcome resolution limitations in the experiments, concerning the spatial resolution and the available laboratory time budget. The flow- and turbulence structures of the wake were numerically simulated on an block structured domain with 3.8 million hexahedron elements and subsequent compared with the data obtained from the laboratory experiment.

3.1.6.2 Large Eddy Simulation

The turbulent flow results presented in this work are obtained by means of Large Eddy Simulations. LES method is intermediate between RANS and DNS; it resolves the large, energy carrying scales and models the dissipative small ones, supposed isotropic.

The basis of large eddy simulation consists of the application of a spatial convolution filter to the governing equations. This procedure splits a generic turbulent variable into a large scale component and a small scale component. The large scale one can be calculated by solving the basic equations explicitly. The influence of the small scale one on the large scale component can be interpreted as a stress similar to the Reynolds stress, the so-called sub-grid scale stress, which must be modelled *Smagorinsky* (1963); *Fletcher* (1991).

The most commonly used filters are the Fourier cut-off filter, the box filter and the Gaussian filter, among which the Gaussian filter has excellent performance both in physical space and spectral space *Fröhlich* (2006). Thus the Gaussian filter is used in this paper. The physical variable is decomposed into a small scale component and a large scale component as follows :

$$\varphi = \overline{\varphi} + \varphi' \tag{3.1}$$

where $\overline{\varphi}$ is the large scale component; φ' is the small scale component, which is also called the sub-grid scale (sgs) component.

The convolution kernel of the Gaussian filter is defined as

$$G\ (x-x^{*})=\left(\frac{6}{\pi\Delta^{2}}\right)^{2/3}\exp\left(\frac{-6\left|x-x^{*}\right|^{2}}{\Delta^{2}}\right) \tag{3.2}$$

The LES equations are obtained by filtering the Navier-Stokes equations and read

$$\frac{\partial\overline{u_j}}{\partial x_j}=0\ and \tag{3.3}$$

$$\frac{\partial\overline{u_i}}{\partial t}+\frac{\partial\overline{u_i u_j}}{\partial x_j}=-\frac{1}{\rho}\frac{\partial\overline{p}}{\partial x_i}+\frac{\partial}{\partial x_j}\left[\nu\left(\frac{\partial\overline{u_j}}{\partial x_i}+\frac{\partial\overline{u_i}}{\partial x_j}\right)\right]+g_i \tag{3.4}$$

where an over line^{-}denotes filtering at a scale Δ; u_i, p and g mean velocity component, pressure and external forces.
The sub-grid scale stress is expressed by the Smagorinsky model. The Smagorinsky model for the deviatoric part of the sub-grid stress is defined as

$$\tau_{ij}^{sgs}-\frac{1}{3}\,\tau_{kk}^{sgs}\,\delta_{ij}\approx\tau_{ij}^{mod}-\frac{1}{3}\,\tau_{kk}^{mod}\,\delta_{ij}=-2\nu_t\overline{S_{ij}} \tag{3.5}$$

where ν_t is the eddy viscosity and S_{ij} is the resolved strain rate tensor

$$\overline{S_{ij}}=\frac{1}{2}\left(\frac{\partial\overline{u_i}}{\partial x_j}+\frac{\partial\overline{u_j}}{\partial x_i}\right) \tag{3.6}$$

The eddy viscosity v_t is defined as

$$\nu_t=(C_s\Delta)^2\left|\overline{S_{ij}}\right| \tag{3.7}$$

where C is the Smagorinsky coefficient which, in principle, may depend on scale Δ, and typically ranges from 0.1 to 0.23 *Mengler* (2002); Δ is the length scale of the filter which usually depends on the grid size;

$$\nu_t=I^2\left|\overline{S_{ij}}\right|\ with\,\overline{S_{ij}}=\sqrt{2\,\overline{S_{ij}}\,\overline{S_{ij}}} \tag{3.8}$$

Multiphase Flow

To simulate the mixing process in the wake and the mixing layer, the homogeneous Eulerian mixing model for multi-phase flow is used. It is implemented to the governing equations. For each phase α of the total number of phases N_p a variable is denoted *Ferziger and M.Peric* (2002).

$$\Phi_\alpha=\Phi\ \alpha\leq 1\leq N_p \tag{3.9}$$

To fulfil the postulation of continuity, a volume fraction is implemented and the sum of the phase's volume fractions has always to be one for each segment. A common equation for transport with the variable and the volume fraction can be defined as follows

$$\frac{\partial r_\alpha \rho_\alpha \Phi_\alpha}{\partial t} + \frac{\partial r_\alpha \rho_\alpha u_{\alpha_i} \Phi_\alpha}{\partial x_i} - r_\alpha \frac{\partial}{\partial x_i}\left(\Gamma_{\Phi_\alpha} \frac{\partial \Phi_\alpha}{\partial x_i}\right) = S_\alpha^{(\Phi)} + T_\alpha^{(\Phi)} \tag{3.10}$$

3.1.6.3 Computational Model

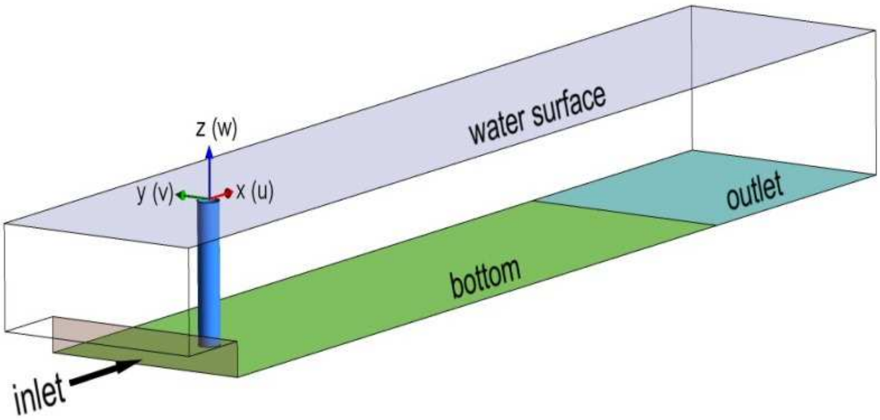

Figure 3.41: Channel with boundaries and coordinate system, computational domain

The computational model of the mixing channel is shown in figure 3.41. The diameter of the cylinder in the figure is defined as d with $0.08\,m$ and the diametric Reynolds number is $Re = 3400$. The saltwater layer thickness is defined as D with $0.1\ m$. The overall length of the domain in x-direction is $4.3\,m$, the width in y-direction is $0.8\ m$ and the height in z-direction measures $0.4\,m$. The stream-wise velocity is defined as u, the cross velocity as v and the upwards velocity as z.

The boundary conditions are as follows:

1. Inlet: Inflow boundary with a mapped velocity profile (figure 3.42) and a mapped salinity profile generated form the laboratory experiments
2. Cylinder and bottom: Solid walls with no-slip boundary conditions are used
3. Water surface: Opening boundary; the dimensionless pressure is chosen to be $p = 0$. Neumann conditions are used
4. Sides : walls with slip boundary conditions are used

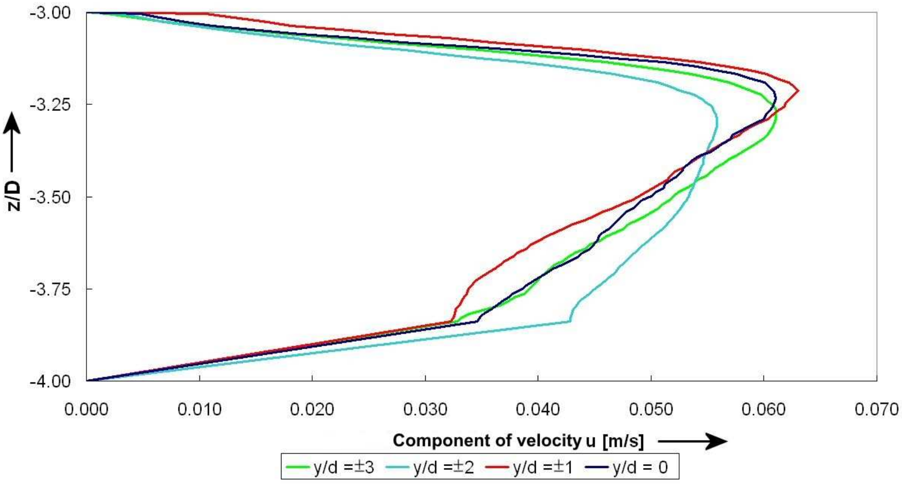

Figure 3.42: Inlet velocity profiles mapped from experimental data to the inlet

5. Outlet: Mass flow: iteratively derived data from pre-calculations

The domain is meshed block structured with hexahedron elements and an O-grid to approximate the cylinder structure. In the region of the mixing layer the cells have a height of approximately $2\,mm$ by an aspect ratio of under 25. To resolve the viscous sub-layer around the cylinder the cell-depth decreases progressively to $0.05\,mm$ directly on the wall; this means dimensionless wall distances of $y^+ \leq 5$ are abided in the significant regions of the cylinder and the mixing layer. The mesh setup is done in Ansys Icem, Release 11.0 and contains about $3.8\,million$ cells.
The simulations are carried out with a constant time step corresponding to a Courant number $C \leq 1$ in the significant parts of the domain, especially around the cylinder, in the sub-layer and the wake. The mean quantities presented in result section are obtained by averaging on about 100 seconds of time or 10.000 time steps. The presented figures show magnitudes over the longitudinal plane of symmetry (x-z-plane). The computational setup is done in Ansys CFX, Release 11 on 14 parallel working processors with 16 GB main storage.

3.1.6.4 Results

In this case the cylinder is responsible for the structure of the wake. To determine the influence to the mixing process several criteria are shown in the following paragraphs. The values are either displayed as coloured plots in a plane, time lines at one specific point or as graphs over the channel height. All values are dimensionless, therefore they are divided by the saltwater layer thickness D, the cylinder diameter

d or the inflow speed u_∞. The analysis of the data is performed with the same program used for analysing the measurements in the experiment.
As a criteria for the spatial and time wise resolution the energy spectrum can be applied. In this case figure 3.43 shows the spectrum in the wake at $x/d = 1.5$, $y/d = 0.5$ and $z/D = -3.65$. It can be seen that in this region of the mesh with its high spatial resolution the turbulence behaviour is represented quite well by the full spectrum of wavelengths. This means that for the important part of the domain not only the large scale eddies are resolved, but also small scales in the region of dissipation are still clearly resolved. Therefore can be noticed, that the calculations of the flow are sufficient exact to resolve the appearing vortex structures in their different sizes.

A further criterion that has to be determined is the velocity field in the wake of the cylinder. In the calculations it should develop the same way it does in the experiment. So the averaged velocity profiles of the experiment and the numerical setup are compared. Due to the limitations in the experimental setup only the velocities u and w are compared. The validated experimental data for the vertical velocity component v does not cover the entire domain of the simulation, what makes a comparison difficult. There is also the fact that the PIV/PLIV setup can not record velocity and salinity fields down to the ground of the channel. This means all values out of the experiment end 0.15 D above the ground of the channel. The first figure (figure 3.44) shows the form of the averaged and normalised velocity component u in the experiment and the simulation. The values are recorded at $x/d = 1.875$ behind

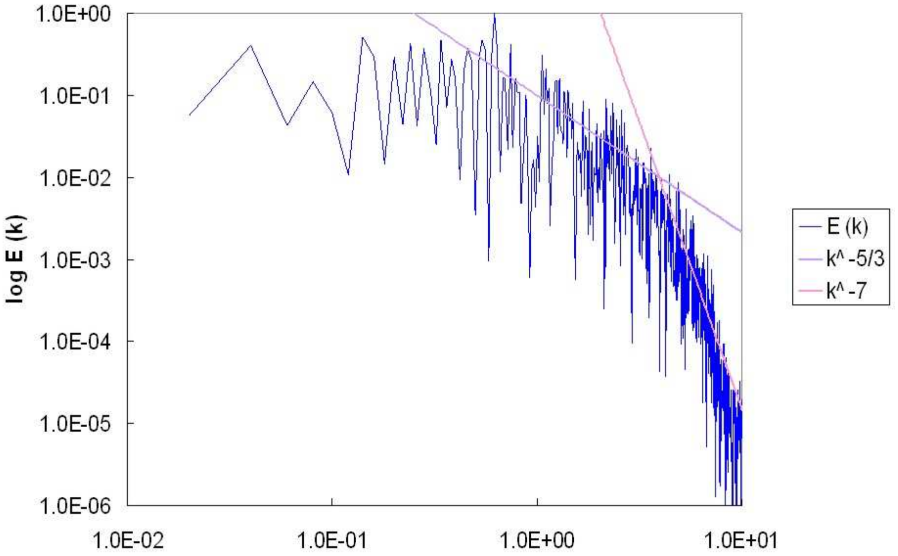

Figure 3.43: Energy spectrum at $x/d = 1.5$, $y/d = 0.5$, $z/D = -3.65$

the cylinder in the wake. Given the fact that limitations in the measuring system of the experiment exist the velocity profile does not reach the ground. In the section above, from $z/D = -3.85$ to $z/D = -3.4$, the two graphs nearly match; thereby not only the slope of the curves is similar but also the maximum values are almost identical. In the section from $z/D = -3.4$ to $z/D = -2.9$ the two graphs differ a little more, whereas the simulation shows a negative velocity which can not be confirmed in magnitude by the experiment. But it has to be considered that within the mixing layer, which is located in this region, the measurements may present some uncertainties. Under these conditions it can be state that the results of the experiment and the simulation match quite well.

A second comparison (figure 3.45) shows the upward component of the velocity w in the experiment and the simulation at the same position at $x/d = 1.875$. Again, the values of the experimental setup end close to the ground. Apart from the maximum values the two graphs look alike in their gradient and form. The differences in the maximum value are well known in numerical simulations. Especially in this setup with the wall mounted cylinder, the stratified flow and the remarkable inflow the demands on absolute identical flow structures between experiment and simulation can not be granted.

A further condition to be determined is the stratification of the two layers with different values of salinity. For establishing the stratification the simulation was originally started with a freshwater filled channel and salty water running into it through the inlet section. The velocity profile at the inlet is mapped from the experiment as mentioned above. After building up a stable stratification the salinity profile data of the channel is recorded and stored. This makes it possible to use the data either to study the averaged values and compare them with the experimental data or to use them as the initial values for further simulations and investigations. As a first step the salinity profiles are drawn over the channel height in a distance of $x/d = 6.25$ and $x/d = 12.5$ behind the cylinder in the wake (figures 3.46 & 3.47). It can be recognised that the gradients of salinity in this case match almost perfect again. The gap between the graphs can be seen as an uncertainty of position determination in the experiment when the stratified flow is setup and the layer thickness varies. These problems protrude in the comparison of the salinity spread in the x-z-centre plane of the channel (figures 3.48 & 3.49).

Beside that it can be determined that both plots show the same structure in salinity distribution. On account of the cylinder and its obstruction to the flow an increase of the saltwater layer thickness in front of cylinder can be ascertained. Just as the increase in front of the cylinder the decrease behind it can be determined on the same scale in the experiment as well as in the simulation. As shown over the channel height in the previous graphs the salinity distribution has the same form in experiment and simulation even over the channel length.

Additionally to the profiles of velocity and salinity the structure of the flow direct

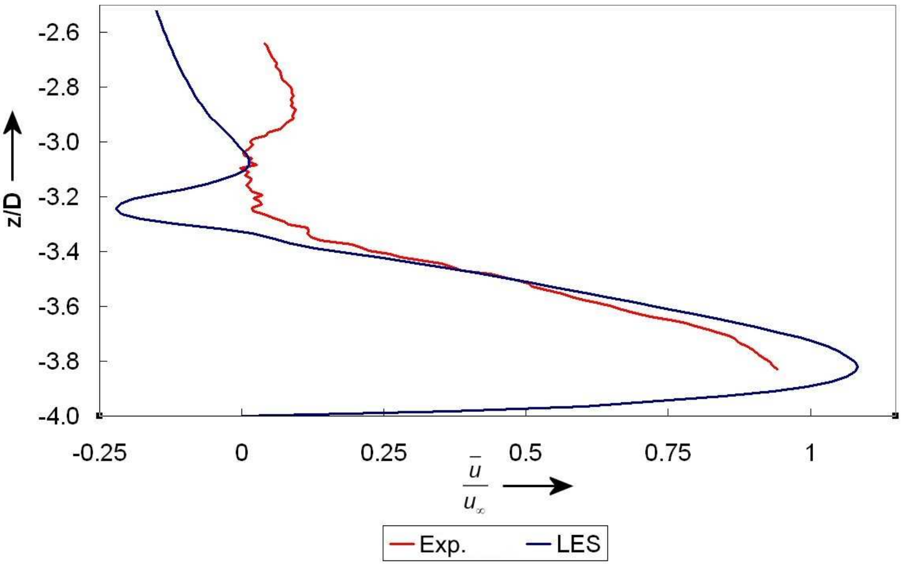

Figure 3.44: Averaged, normalised velocity component $\frac{\overline{u}}{u_\infty}$ at $x/d = 1.875$

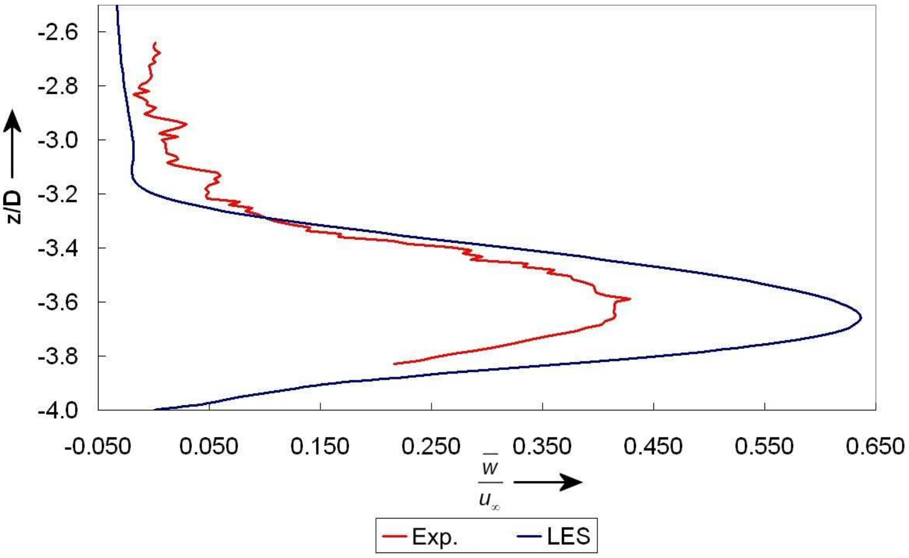

Figure 3.45: Averaged, normalised velocity component $\frac{\overline{w}}{u_\infty}$ at $x/d = 1.875$

behind the cylinder is investigated. The simulation can give a better impression of the spatial range because it not as restricted in the volumetric capacity as the experiment is. As an incentive for the macroscopic mixture between the fresh and salt water layer a special vortex structure can be estimated. It is supposed that due to the inflow velocity profile and the stratification of the two layers with different density the Karman vortices can not develop. Instead of forming a Karman vortex street behind the bluff body the vortices are bent set and form a counter wise ro-

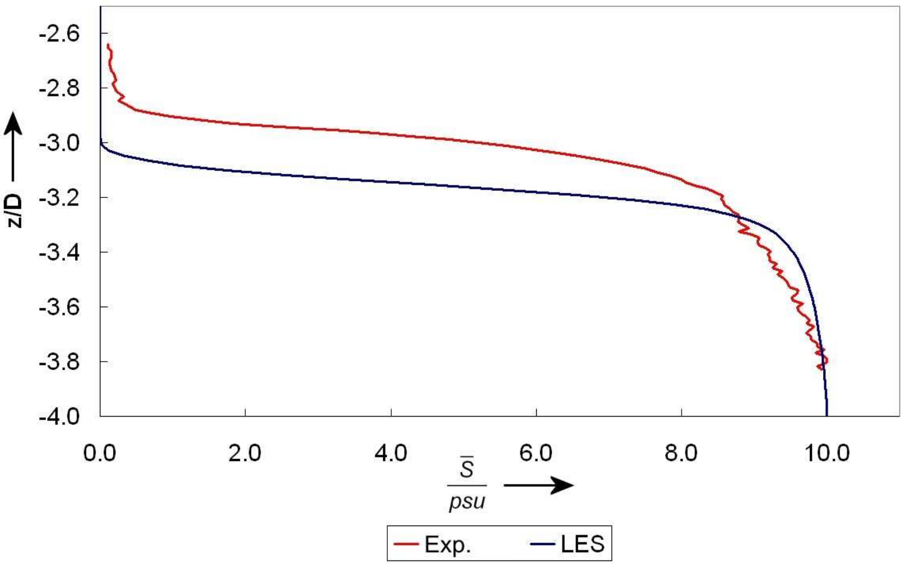

Figure 3.46: Averaged salinity $\frac{\overline{S_b}}{psu}$ at $x/d = 6.25$

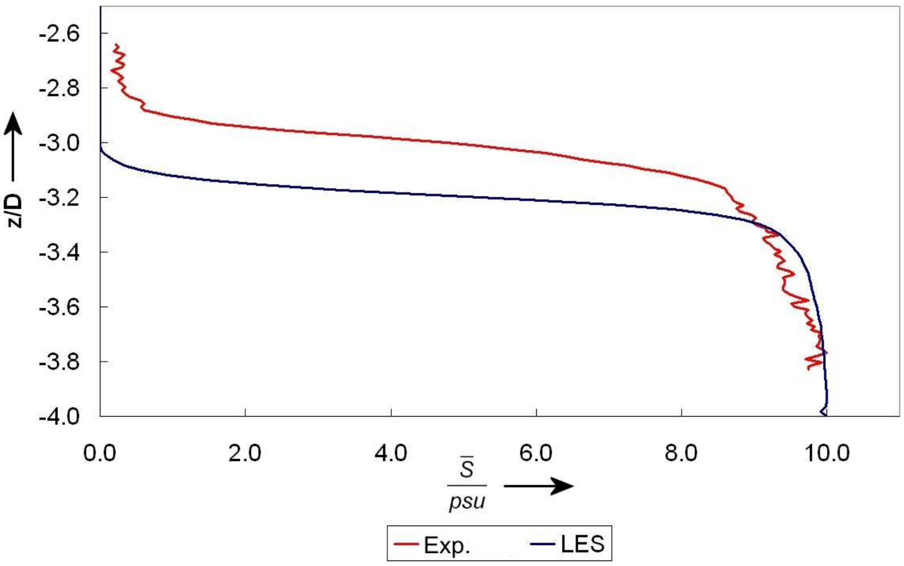

Figure 3.47: Averaged salinity $\frac{\overline{S_b}}{psu}$ at $x/d = 12.5$

tating pair of eddies under the mixing layer, represented by the 5 psu salinity line (figures 3.50 & 3.51). As well in the experiment as in the simulation these structures can be identified in the same scale of values. By the counter wise rotating eddies the strong velocity component w (cf. fig. 3.45) is also explainable. In the simulation the averaged values in the wake are totally symmetrical to the x-z-centre plane which

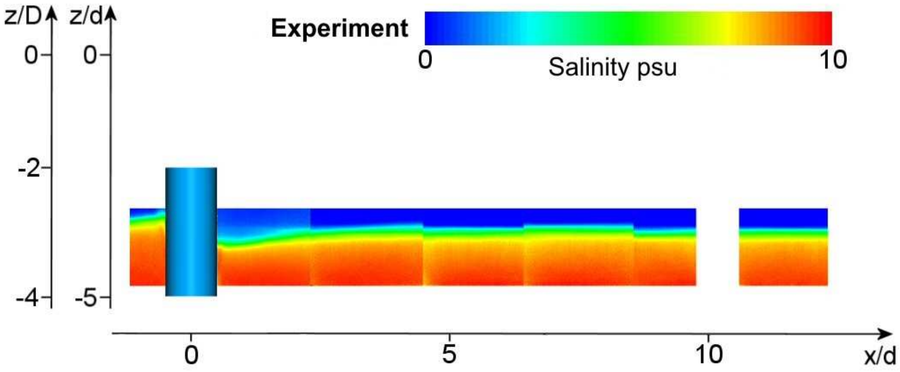

Figure 3.48: Averaged salinity profile $\overline{S_b}$ of the experiment on the centre-plane at $y/d = 0.0$

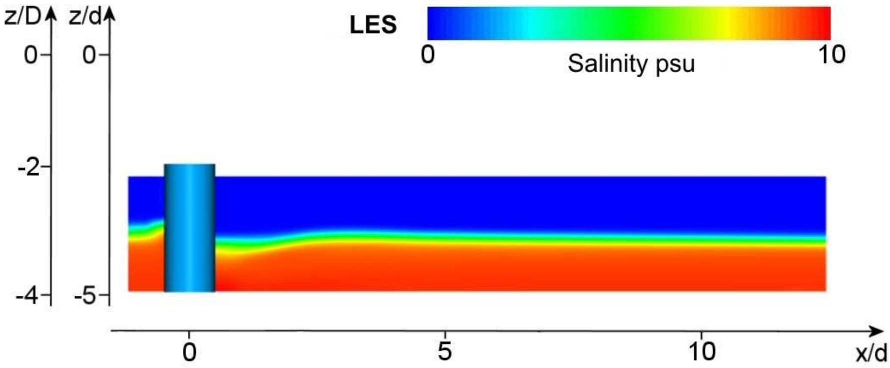

Figure 3.49: Averaged salinity profile $\overline{S_b}$ of the simulation on the centre-plane at $y/d = 0.0$

can not be guaranteed in the experiment. So the differing peak value in figure 3.45 might be due to a non symmetrical wake in the experiment and hence these values do not represent the maximum values as the simulation in this plane does.
A further indication that the eddy structure does not break through the mixing layer is shown in figures 3.52 & 3.53. Here streamlines representing the flow and a contour plane representing the $5\,psu$ level are plotted. It is clearly visible that the contour plane is not touched by the streamlines, but these creep in the mixing layer. The dimensions of the streamline covered region do not essentially differ between experiment and simulation, whereas the experimental data gives an imperfect view due to the measurement system limitations.

Finalising the entrainment velocity w_e is to be evaluated. The entrainment velocity makes it possible to give a transport quantification by considering the layer thickness variation in terms of time and the velocity variation in times of place. In

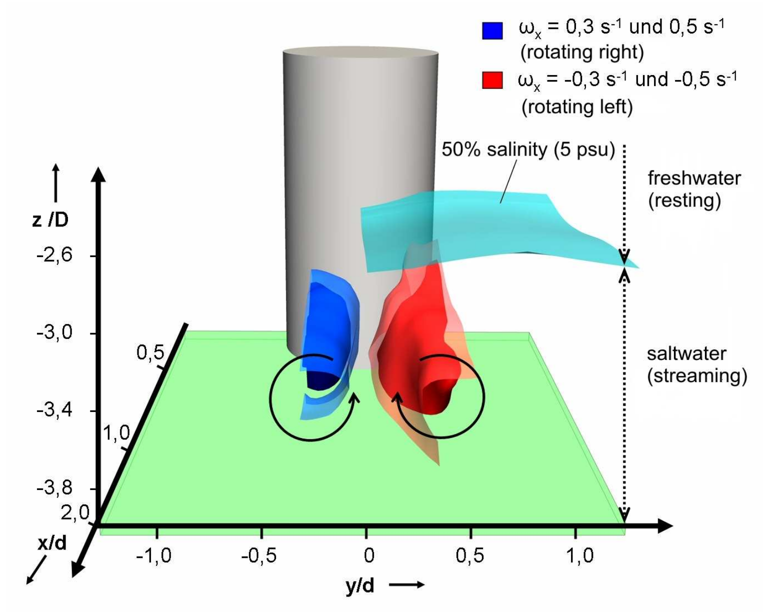

Figure 3.50: The dominant vortex structures in the experiment

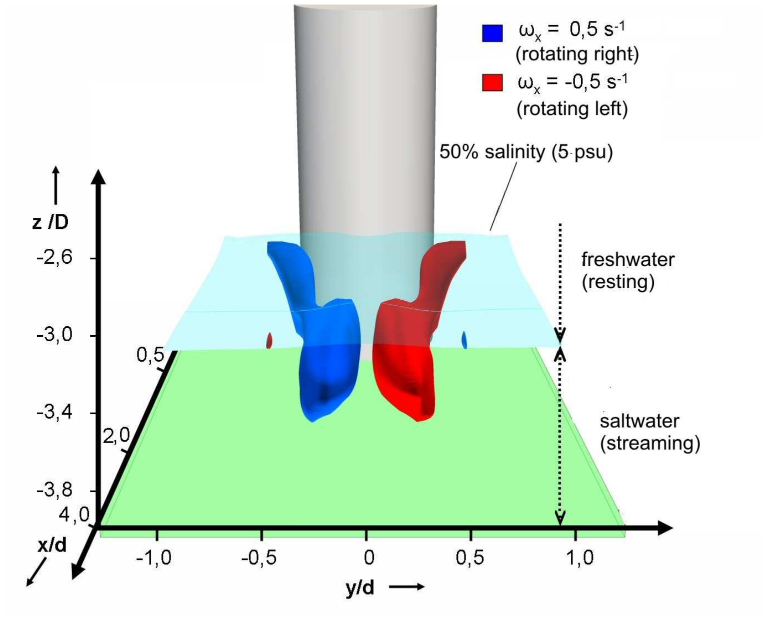

Figure 3.51: The dominant vortex structures in the simulation

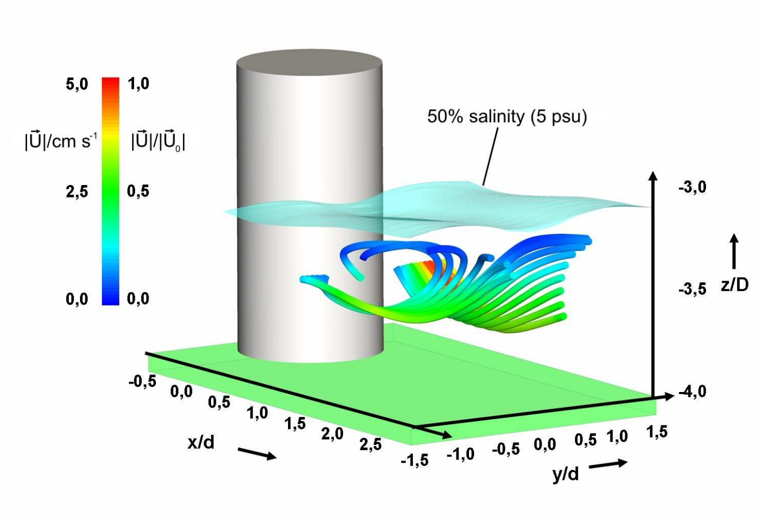

Figure 3.52: Three-dimensional structure of the cylinder wake in the experiment

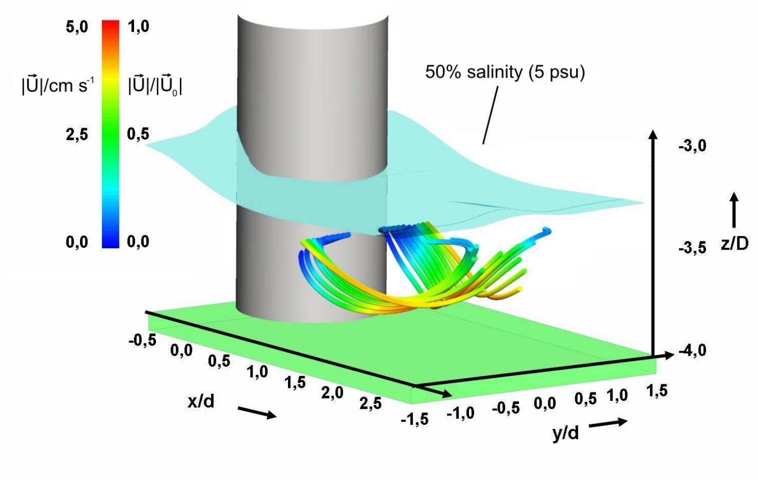

Figure 3.53: Three-dimensional structure of the cylinder wake in the simulation

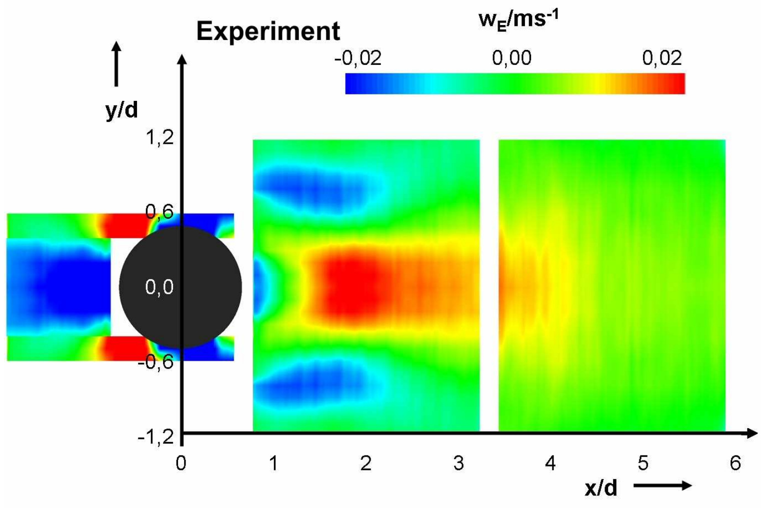

Figure 3.54: Distribution of the entrainment velocity in the wake of the cylinder in the experiment

this case a reduced form is shown due to the only two dimensional experimental setup. The analysis for the simulation is done in the same way (cf. (11)) to ensure comparability to the experiment.

The plots representing the entrainment velocity calculated from the experiment and the simulation (figures 3.54 & 3.55) indicate that the process of transport, thus mixing of the two layers, is detected in the same scales. Again the experimental setup can only give criteria and an approach to the existing structures where transport happens and the magnitude in which it occurs.

Corresponding to the entrainment velocity an entrainment velocity-flux can be derived (cf. 3.1.1.1). By means of this flux it is facilitated to quantify the mixing of the two layers by the exchange and the impact to the layer thickness.

$$w_E = \frac{\delta D}{\delta t} + \frac{\delta UD}{\delta x} \tag{3.11}$$

In the experiment the influence of the cylinder to the mixing process can be estimated by the entrainment velocity-flux to approximately 1.9%. Though the regions of high entrainment velocity in the simulation (cf. Fig. 3.55)) seam to turn out more extensive comparably, the entrainment flux can here be estimated within the same value range with 1,6%.

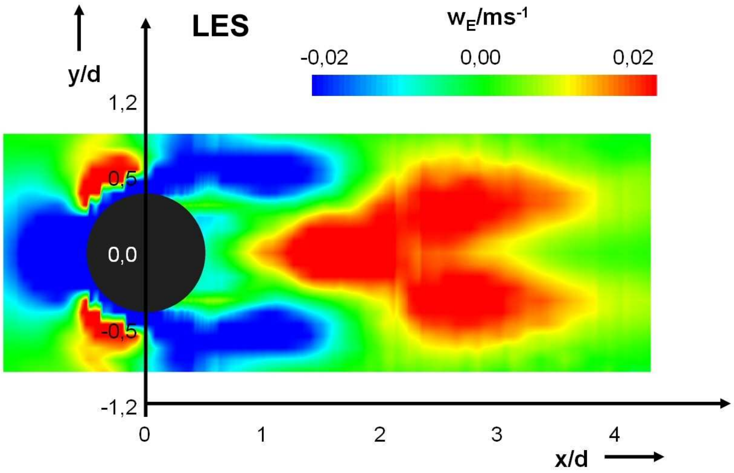

Figure 3.55: Distribution of the entrainment velocity in the wake of the cylinder in the simulation

3.2 Near-field numerical modelling (UNI-HAN)

3.2.1 Project goals

The goal of the near field numerical modelling was the qualitative and quantitative determination of the influence of Monopiles on the mixing of density currents such as they occur in the Baltic Sea. In this context it is not only the goal of investigating the process of the flow around a cylinder but primarily a quantitative determination of the mixing caused by it in order to estimate the near field mixing caused by offshore wind farms. This study was made by QuantAS-Off project partner the Fluid Mechanics Institute of the Leibniz Universität Hannover.

To the knowledge of the authors, this research is the first attempt to quantitatively simulate the structurally induced mixing caused by a circular cylinder in a stratified environment. This involved significant challenges related to the conceptual model, the numerical technique and in particular the turbulence modelling, since turbulence is the primary factor in the mixing process. There are numerous studies presented in the literature on the simulation of the flow around a cylinder in a non-stratified environment. Even here not all of the phenomena are totally understood or numerically simulated.

3.2.2 Model setup

Calculations were carried out using Fluent 6.2 (*Fluent*, 2005). The numerical model solves the fully three-dimensional Reynolds-Averaged Navier-Stokes (RANS) equations using a finite volume method. Although numerous closure equations are possible, the SST k-ω model for turbulence closure was found most applicable (*Wilcox*, 1998; *Schimmels*, 2008). An additional transport equation is solved for the salinity distribution and density is calculated using an equation of state. The model is completely parallelised with almost 100 % efficiency. All of the simulations were made on the HLRN supercomputer (Hochleistungsrechner Nordeutschland).

The transport equations for turbulent quantities are modified to properly account for the effect of buoyancy on turbulence production and dissipation (*Umlauf et al.*, 2003). All simulations were carried out for a vertical cylinder placed in the middle of a computational domain of 40d length, 40d width and 4D depth (fig. 3.56). Fig. 3.56 also shows the boundary conditions which are Dirichlet conditions at the inlet with fixed profiles for velocity, salinity and turbulent quantities. At the outflow boundary velocity, salinity and turbulent quantities are treated by a Neumann condition while pressure is given as a fixed profile. A pressure condition is also applied at the top boundary and the bottom is rigid with an equivalent sand roughness of $k_s = 0.025$ m. The slope of the channel is adjusted to generate the desired Froude number and the velocity and salinity profiles, the turbulent quantities and pressures needed for the inflow and outflow boundary conditions as well as initial conditions were obtained from preliminary simulations without the structure. More information about the details of the numerical model is given in *Schimmels* (2008).

Due to the lack of appropriate measurements for the flow of density currents around a cylindrical structure the numerical model was validated separately for non-stratified flows around a circular cylinder (Fig. 3.57 after *Cantwell and Coles* (1983)), and for the entrainment in undisturbed natural density currents (Fig. 3.58, *Schimmels* (2008)). It could be shown that the specific features of the individual flows are well predicted by the model which is therefore assumed to be equally suited for simulations where the processes are combined. A short summary is given in the next sections.

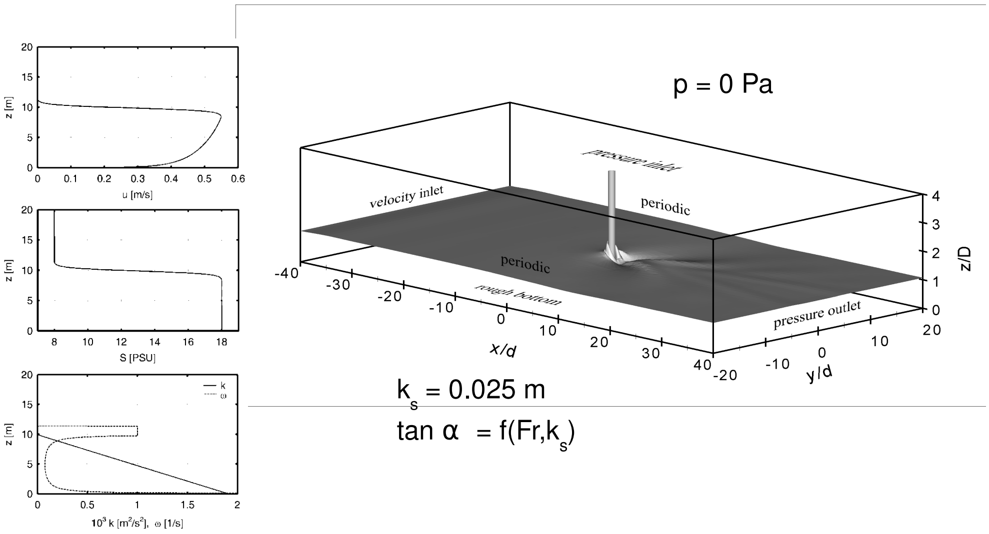

Figure 3.56: Definition sketch of the computational domain with the cylinder in the centre. Boundary conditions are indicated and the current depth indicated by the shaded plane.

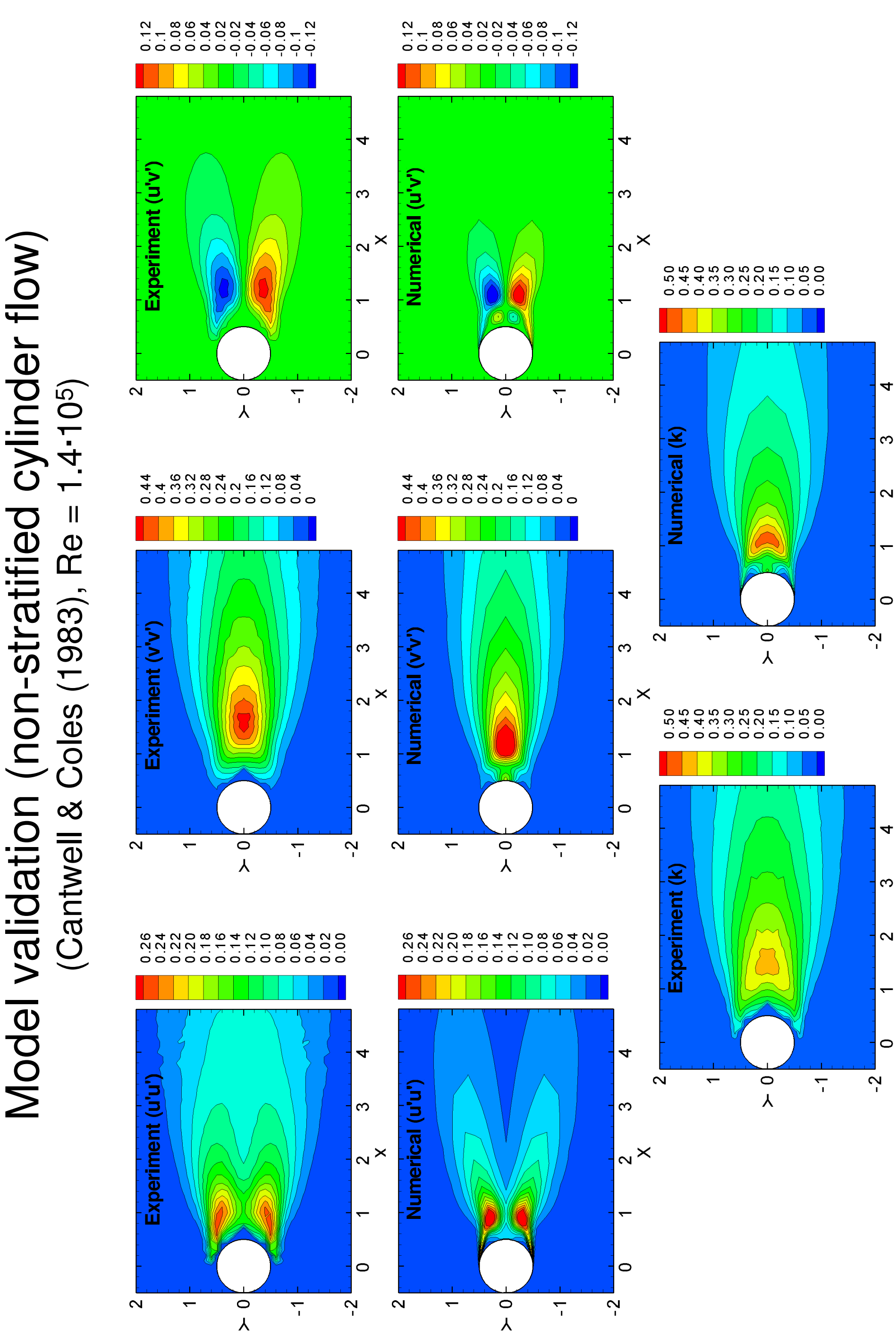

Figure 3.57: Comparison between experimental and calculated values of Reynolds stresses and turbulent kinetic energy.

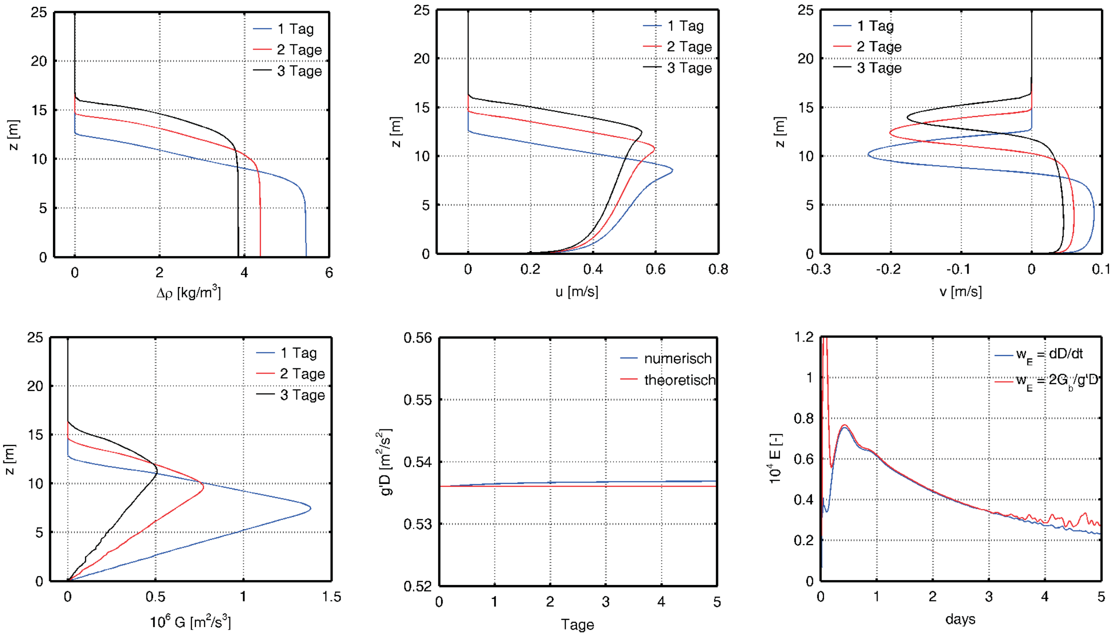

Figure 3.58: Comparison between experimental and calculated values for mixing of a natural density current (*Schimmels*, 2008).

3.2.3 Non-stratified flow around a circular cylinder

Non-stratified flow around structures has been studied for decades. Many laboratory experimental results are available for a circular cylinder. An excellent summary is found in the 2-Volume treatise by *Zdravkovich* (1997). Based on both qualitative and quantitative analysis of the extensive laboratory data he describes the different flow as a function of the cylinder Reynolds number

$$Re = \frac{U_\infty d}{\nu} \tag{3.12}$$

where U_∞ is the undisturbed velocity in front of the cylinder, d the cylinder diameter and ν the kinematic viscosity of the fluid.

For the present work additionally the free stream turbulence and the aspect ratio between length L and diameter of the cylinder L/d are of special interest. The prior because of the bottom induced turbulence in the incoming flow and the latter because of the incoming velocity profile which is not shear free and will cause large scale vertical structures which are sensitive to the aspect ratio.

The flow around bluff bodies is characterised by the detachment of the flow from the cylinder surface and the formation of free shear layers that eventually roll up and form vortices behind the structure in the wake. This pattern is also typical for the flow around a circular cylinder but some distinct features vary significantly with the Reynolds number. *Zdravkovich* (1997) gives an excellent review about experimental evidence for the flow around circular cylinders and suggests expressing the Reynolds number dependence by different flow states, each of which can be split up into some sub-categories.

Non-stratified Flow around a circular cylinder has often been numerically simulated. Major problems had to be solved in order to simulate turbulence and to generate proper conditions on the cylinder surface. Investigations were performed on the basis of the RANS equations (e.g. (*Franke*, 1991; *Bosch*, 1995)) as well as LES (e.g. (*Breuer*, 2000, 2002)).

Although the LES approach seems to be superior to models based on the turbulent viscosity assumption this has to be paid with a very much higher computational effort. In a LES a significant part of the turbulent flow field is directly resolved by the numerical grid. This must be much finer than in case of turbulent viscosity or Reynolds stress models. Moreover, variations along the cylinder span can no longer be neglected and all simulations require a three-dimensional grid to account for the vortex stretching and the energy cascade in the resolved part of the turbulence spectrum. The increase in computational time is estimated to be on the order of magnitude of 100 times higher than for RANS simulations.

Therefore RANS numerical calculations where performed on the high Reynolds number field scale. An extensive set of numerical experiment was performed to see which of the turbulence models available in Fluent was best suitable for simulating the flow around a circular cylinder in this Reynolds number range. The comparison was based on the laboratory experiments of *Cantwell and Coles* (1983), an almost unique data set for the turbulence in the wake of a cylindrical pile at $Re = 140.000$. The following turbulence models were compared:

1. Standard k-ε model
2. Realizable k-ε model
3. RNG k-ε model
4. Standard k-ω model
5. SST k-ω model
6. Reynolds Stress Model (SST)

In addition investigations were made on the influence of the conditions at the cylinder boundary and the detail of the numerical grid.

The simulations were performed on a two-dimensional grid since the approach flow is neither sheared nor stratified and the turbulence models damp variations along the cylinder axis. The cylinder with a unit diameter 1 is placed at $x = y = 0$ in a computational domain that extents 6 diameters left, right and in front of the cylinder and 20 diameters in the cylinder wake. Two different regular grids have been used which are shown in Fig. 3.59. Note that the coordinates have been non-dimensionalised by the cylinder diameter. However, as the diameter had been chosen to be unity this is not important in the present context but for consistency all coordinates will be given in non-dimensional form denoted by capital letters.

The grid is circular up to 3 diameters around the cylinder and then converted to the rectangular shape of the numerical channel. The finest resolution is in the vicinity of the cylinder to account for the wall boundary layer and the free shear layers shed from the cylinder surface. With increasing distance from the cylinder the numerical grid gets successively coarser while the grid size is kept constant after 6 diameters behind the cylinder where the resolution in the wake along $Y = 0$ is kept more compact compared to the less important side regions.

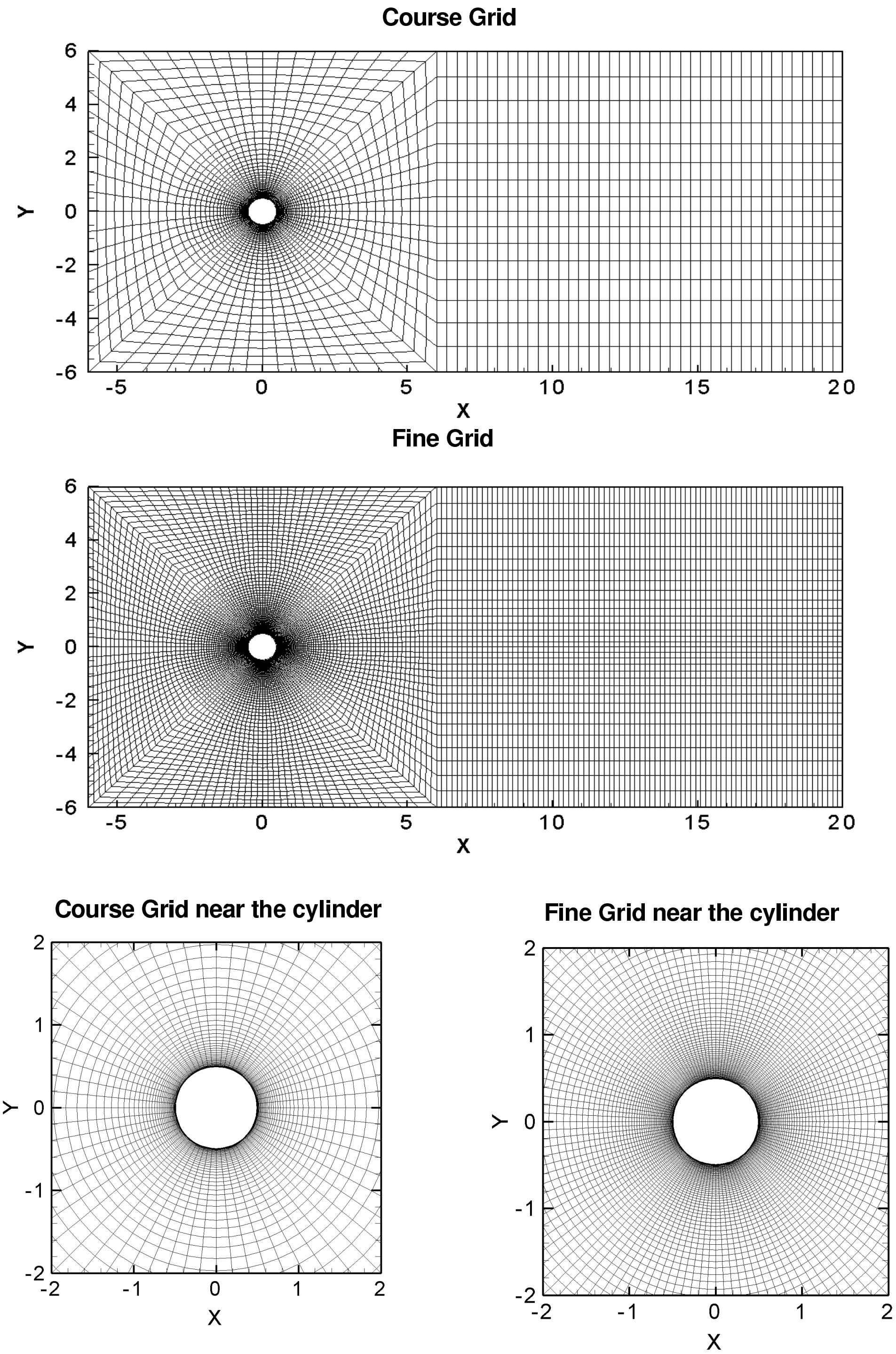

Figure 3.59: Coarse and fine numerical grid for simulation of the non-stratified flow around a cylinder.

The fine grid has twice the resolution of the coarse grid except in the near wall region where the distance of the closest grid point is governed by the near wall treatment method. Both the wall functions and the two layer approach described in *Schimmels* (2008) have been used. For the wall functions approach the non-dimensional wall distance should be slightly above $y+ \approx 30$ while for the two layer approach it should be less than $y+ \approx 5$. To fulfil these requirements on both grids identically the distance of the closest grid point to the cylinder surface has been chosen to be $2.1 \cdot 10^{-3}$ and $2.5 \cdot 10^{-4}$ cylinder diameters for the wall function and the two-layer approach, respectively. As mentioned above the grid is successively coarsened with increasing distance from the cylinder, the stretching factor for the coarse grid being about $f_w \approx 1.11$ and for the fine grid about $f_w \approx 1.06$. The main characteristics of the different grids used in this study are summarised in tab. 3.3.

grid	N	y^+	Δr_{min}	f_W
WF coarse	3.840	32	$2.1 \cdot 10^{-3}$	1.109
WF fine	1.2800	32	$2.1 \cdot 10^{-3}$	1.1062
TF	4.492	3	$2.5 \cdot 10^{-4}$	1.116
TF fine	17.280	3	$2.5 \cdot 10^{-4}$	1.0623

Table 3.3: Characteristics of the different grids used for the simulations. Total number of grid cells N, maximum non-dimensional wall distance $y+$, minimum wall distance $\varDelta r_{min}$ in cylinder diameters and the stretching factor f_w in the near wall region.

All of the results presented here for the non-stratified flow around a circular cylinder and also in later applications are generally presented in non-dimensional form, i.e. lengths are normalised with the cylinder diameter and the turbulent kinetic energy is normalised with the square if the free stream velocity. For details and for a comparison of the results for the parameters c_d, c_l and St with those found in the literature as well as comparison with the mean flow velocities are found in *Schimmels* (2008). Here we have presented exemplary results for a comparison between the numerical results and the laboratory measurements of *Cantwell and Coles* (1983) for the simulated turbulence behind the cylinder.
Following the suggestion of *Reynolds and Hussain* (1972); *Cantwell and Coles* (1983) separated the flow behind the cylinder in a mean, a turbulent and periodic components. It has been shown that both of the fluctuating components, namely the turbulent and the periodic parts are responsible for the mixing. All of the simulations show a time dependent structure with alternating eddy shedding, so that such a description of the flow field is also possible here. The sum of both of these components was used for comparison since the turbulence models are not trimmed

to distinguish between them. Fig. 3.60 shows a comparison between the mean fluctuating kinetic energy along the symmetry axis $Y = 0$. The 4 plots show the results using a coarse and a fine grid with a wall function (WF) and a two layer approximation (TL).

The RSM and the SST k-ω model show the best agreement with the laboratory data while the results for the latter are improved by a refinement of the boundary layer. By contrast, the RNG k-ε model works best with a coarse boundary layer grid and the use of wall functions, as can be seen by the almost identical results compared to the RSM. All models show an increased amount of fluctuating kinetic energy on the fine grids due to the reduced numerical dissipation. The retarded separation on the backside of the cylinder is reflected by the peak values which are always closer to the cylinder than the experimental data. A comparison of the maximum values, which the measurements show to be by ca. $X = 1.5$ indicate that all of the turbulence models show this to be nearer to the cylinder. This is due to

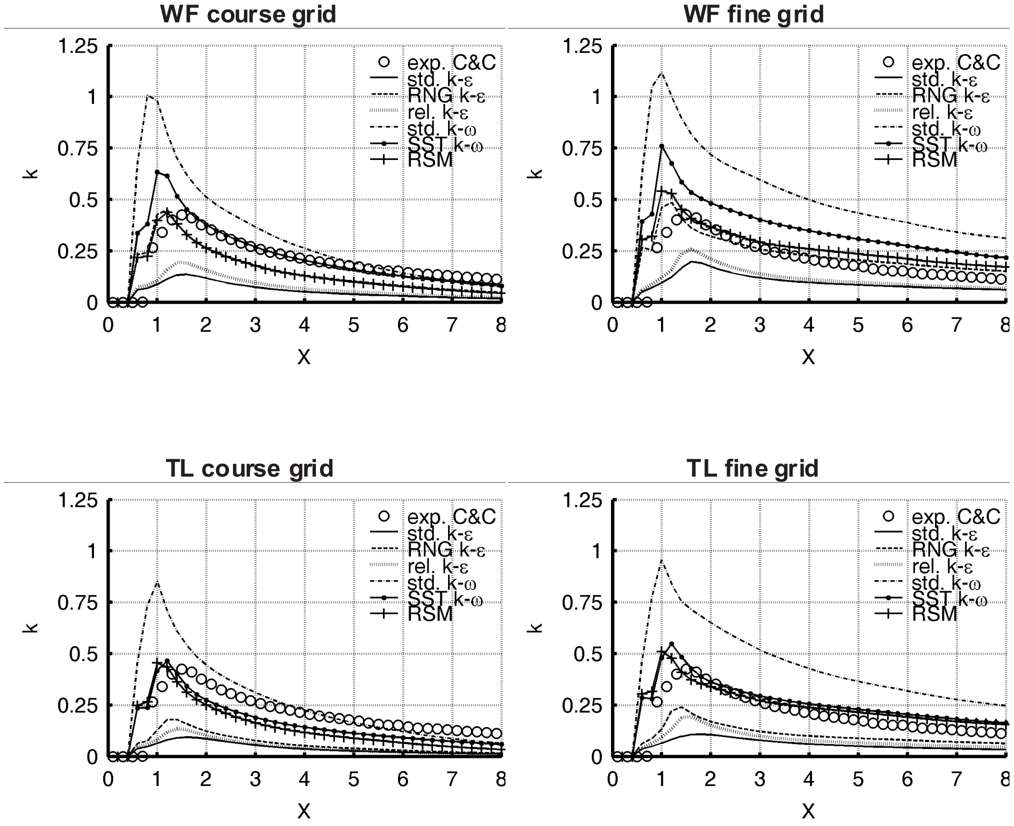

Figure 3.60: Normalised mean total fluctuating kinetic energy along the X-axis at the plane of symmetry ($Y = 0$).

the location of separation in the measurements which at 77^o lies behind the location in of the numerical simulations.

The overestimation of the recirculation length with the standard and realizable k-ε model was attributed above to an underestimation of the total dissipation which is approved by the significantly lower total fluctuating kinetic energy. On the other hand, the standard k-ω model showed a too short recirculation length and higher dissipation in the near wake leading to a reduced mean stream wise velocity compared to the other models. Also this argumentation is manifested by the fluctuating kinetic energy which is always significantly overestimated, especially in the near-wake.

Although no significantly new insights might be expected from the lateral extent of the total fluctuating kinetic energy, it might be interesting to look at the overall distribution. This is shown as contour plots in Fig. 3.61, where the top panel represents the laboratory reference of *Cantwell and Coles* (1983) and the panels below correspond to the presumably best numerical results for each turbulence model. The cross-stream extent is confined for all simulations, particularly very close to the cylinder, which nicely shows the impact of the point of separation. However, despite this fact the agreement of the experimental data with the results of the RNG k-ε model, the SST k-ω model and the RSM is very satisfactory. Qualitatively also the standard and realizable k-ε model and the standard k-ω model agree with the laboratory data as far as they at least show the right distribution. The absolute values are clearly missed which above was assumed to be caused by an over- and under-production of turbulent kinetic energy, respectively.

In summary it is concluded that only the RSM, the RNG k-ε model and the SST k-ω model are suitable for the flow around a cylinder. The advantage of the RSM model is that it is of a higher order and as opposed to the other models and it directly calculates the Reynolds stresses. On the other hand this leads to a significantly greater computer time, since 7 instead of 2 additional equations for turbulence closure need to be solved. All of the models overestimate the separation point and the mean velocities are higher than those measured. This can be explained in that the numerical models have the condition that the flow and the turbulence fields are fully developed although for the Reynolds number in the laboratory experiments the boundary layer is laminar and the transition to turbulence occurs in the shear layers shortly after the point of separation. There it is legitimate to assume that since the turbulence models generated good results despite the just mentioned limitation, that they will provide even better results at high Reynolds numbers when the boundary layer at the cylinder is fully turbulent and the separation point further downstream.

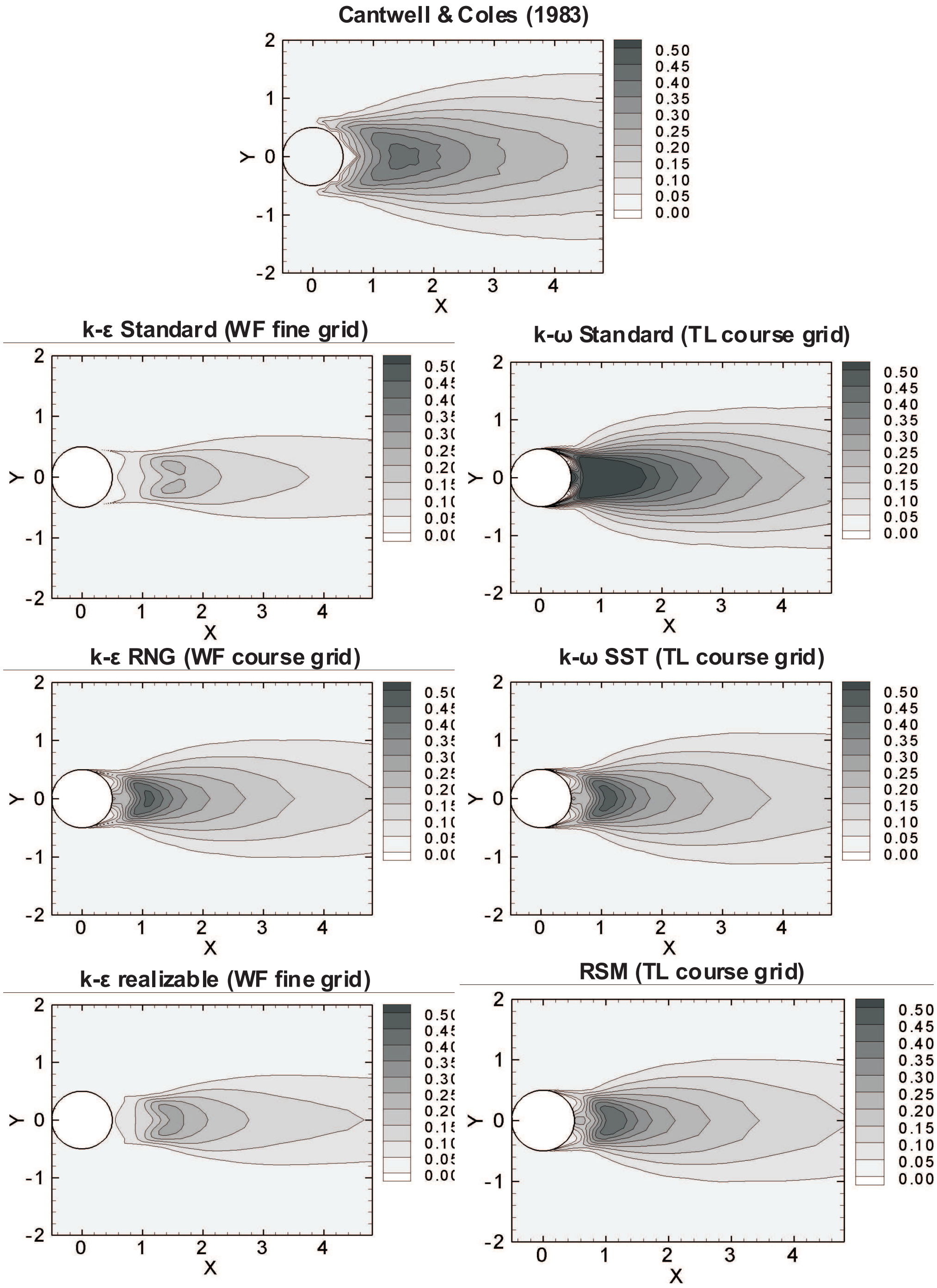

Figure 3.61: Comparison of normalised mean total fluctuating kinetic energy k.

3.2.4 Natural density current

It was shown in the previous section that only three of the tested turbulence models are suitable for simulating structurally induced mixing in a non-stratified flow. In this section results are presented which show which of these models is most suitable for simulating mixing in natural density currents. *Schimmels* (2008) has shown that difficulties arose with the RSM and the RNG k-ε models so that the question was addressed as to whether the SST k-ω model is appropriate. The total set of equations to be solved numerically is as follows:

$$\frac{\partial u_j}{\partial x_j} = 0 \tag{3.13}$$

$$\frac{\partial \bar{u}_i}{\partial t} + u_j \frac{\partial \bar{u}_i}{\partial x_j} - \frac{\partial}{\partial x_j}((\nu + \nu_t)\frac{\partial \bar{u}_i}{\partial x_j}) = -\frac{1}{\rho_o}\frac{\partial \bar{p}}{\partial x_i} + \frac{\rho}{\rho_0} g_i + F_{ij}\bar{u}_j \tag{3.14}$$

$$\frac{\partial k}{\partial t} + \bar{u}_j \frac{\partial k}{\partial x_j} - \frac{\partial}{\partial x_j}((\nu + \frac{\nu_t}{\sigma_k})\frac{\partial k}{\partial x_j}) = P + G - \epsilon \tag{3.15}$$

$$\frac{\partial \omega}{\partial t} + \bar{u}_j \frac{\partial \omega}{\partial x_j} - \frac{\partial}{\partial x_j}((\nu + \frac{\nu_t}{\sigma_\omega})\frac{\partial \omega}{\partial x_j}) = \frac{\omega}{k}(c_{\omega 1} P + c_{\omega 3} G - c_{\omega 2}\epsilon) + c_{\omega 4} D_\omega \tag{3.16}$$

$$\frac{\partial \bar{S}}{\partial t} + \bar{u}_j \frac{\partial \bar{S}}{\partial x_j} - \frac{\partial \bar{S}}{\partial x_j}((\kappa_s + \frac{\nu_t}{\sigma_s})\frac{\partial \bar{S}}{\partial x_j}) = 0 \tag{3.17}$$

$$\rho = \rho(T, S) \tag{3.18}$$

These represent a mass balance, 3 momentum equations, a two-component turbulence model for turbulent kinetic energy (k) and turbulence frequency (ω), a transport equation for salinity and finally an equation of state for determining the density as a function of salinity (temperature dependence has been neglected). Turbulence and mixing are calculated by means of a two-component turbulence model (see (*Schimmels*, 2008) for details).

The basic thought behind all of the turbulence models is that the flow is generated by momentum exchange under the influence of a turbulent viscosity ν_t which is significantly larger than the (normally negligible molecular diffusivity. The same holds for the turbulent kinetic energy (k), the turbulent frequency(ω) and salinity whereas the diffusion coefficient is calculated from the turbulent viscosity using the turbulent Prandtl number σ_t. Normally constant values between 1 and 2 are used for σ_k and σ_ω. Different formulations for σ_S account for the stability of the density current due to both velocity (destabilising) and density gradients (stabilising) on mixing (*Munk and Anderson*, 1948; *Schumann and Gerz*, 1995; *Canuto et al.*, h

$tan\alpha$ **(‰)**	k_S **(m)**	D **(m)**	ΔS **(psu)**	Fr
1.78	0.025	7.0	10.0	0.8

Table 3.4: Initial conditions for the one-dimensional simulations of entrainment in an undisturbed gravity current.

2001). They generally use a gradient Richardson number:

$$Ri_g = -\frac{g}{\rho_0}\frac{\frac{\partial\rho}{\partial z}}{(\frac{\partial\bar{u}}{\partial z})^2 + (\frac{\partial\bar{v}}{\partial z})^2} \tag{3.19}$$

A further important aspect of simulating density currents is the treatment of buoyancy production:

$$G = -\frac{g}{\rho_0}\frac{\nu_t}{\sigma_s}\frac{\partial\rho}{\partial z} \tag{3.20}$$

in the equation for the turbulence frequency.

Wind induced mixing of a stable density field in still water was used to show that the best results were independent of the model for the turbulent Prandtl number. The best results were obtained for so called stationary Richardson number $R_{st} = 0.25$, which is the maximum value for high Reynolds numbers (*Holt et al.*, 1992; *Shih et al.*, 2000). For details see *Schimmels* (2008).

As for the wind entrainment experiment it is sufficient to validate the numerical model for the simulation of undisturbed gravity currents with a one-dimensional model where only the vertical domain is resolved. Therefore the horizontal domain is made up of only one grid cell and periodic boundary conditions applied on the lateral boundaries. To account for the effect of bottom roughness a wall boundary condition with $k_s = 0.025$ m has been applied in all simulations and the free surface at the top is always simulated with a symmetry (slip) boundary condition.

Although the benchmark test has been arbitrarily defined it should at least approximately represent the natural conditions in the Baltic Sea. For this purpose the bottom roughness had been set to $k_s = 0.025$ m to account for realistic conditions at the sea floor. Coriolis forces correspond to a location 55^o longitude North with a Coriolis parameter $f \approx 1.19 \cdot 10^{-4}$ 1/s. The only driving force for the current stems from the bottom slope which has been chosen to be quite steep with tan $\alpha = 1.78 \cdot 10^{-3}$. The total water depth is $H = 40$ m and the initial current depth is set to $D = 7.0$ m. The salinity difference between the current and the ambient fluid is $\mathit{\Delta} S = 10$ psu which implies a density anomaly of $\mathit{\Delta}\rho = 7.85$ kg/m^3 and a reduced gravity of $g' = 0.0765$ m/s^2. The global initial conditions for the benchmark test are compiled in tab. 3.4.

The distribution of salinity is initially approximated by a simple box profile such that a realistic profile will evolve during the starting period of the simulation. In order to keep the initial settling time for the current as short as possible also box profiles for the velocities are applied that approximate the geostrophic balance. The initial profiles of density anomaly and velocity are displayed in Fig. 3.62 where also the resolution of the numerical grid is shown in the left panel.

As can be seen the grid is refined to the bottom in order to resolve the steep gradients of velocity and turbulence quantities in the boundary layer. The interface is initially located at $z = 7$ m and will rise during the simulation due to entrainment. Therefore the region 5 m $< z <$ 15 m has a constant resolution of $\varDelta z = 0.2$ m in order to provide constant numerical settings during the evolution of the current. It should be noted, that the chosen resolution is comparably fine and preliminary tests have shown almost similar results for $\varDelta z = 0.5$ m. However, as the numerical effort for the present grid size of 117 cells over the total water depth is relatively small the finest grid was chosen for the present validation. The region of the stagnant ambient fluid is numerically easy to treat and requires no specific resolution such that the grid for $z >$ 15 m can be made increasingly coarser.

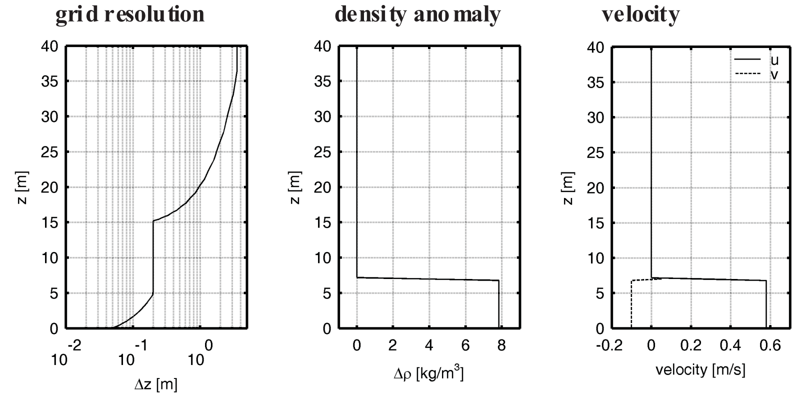

Figure 3.62: Grid resolution and initial conditions for the one-dimensional simulations of entrainment in an undisturbed gravity current.

3.2.5 Comparison of different turbulence models

From the model validation on wind induced mixing it could be concluded that for the simulation of entrainment in a stratified shear layer with two-equation turbulence models the choice of the specific model is rather unimportant as long as the governing parameters (Ri_{st} and σ_t) are adequately incorporated. This shall now be approved by the simulation of a gravity current. For all turbulence models the turbulent Prandtl number is given by the model of *Schumann and Gerz* (1995) and the constant $c_{\Psi 3}$ has been adjusted to fix the stationary Richardson number to $Ri_{st} = 0.25$.

A unique definition of the stationary Richardson number is not possible for the RNG k-ε model due to the additional term in the ε-equation. For the wind induced entrainment simulations this had no significant effect although slightly different results compared to the other two k-ε models could already be noticed. However, for the present simulation of gravity current dynamics this discrepancy is obviously much more severe as the RNG k-ε model was susceptible to instabilities and the results showed very strange behaviour compared to the other models. Therefore this model has not been regarded further and the following discussion is limited to the standard and realizable k-ε model and the standard and SST k-ω model.

All simulations were started with the initial conditions described above and run over 5 days. Fig. 3.63 shows the temporal evolution of the current depth, entrainment rate, Froude number and Ekman number. It is obvious at first sight that the difference between the individual turbulence models is marginal. From the current depth in the upper left panel it can be seen that the k-ε models and k-ω models are pair wise identical and that the k-ω models predict a slightly slower growth of the layer thickness. The same behaviour could be observed in the wind entrainment experiment and is also here attributed to some kind of numerical error.

From the strong variations in the Froude number and entrainment rate at the beginning of the simulation it can be followed that the initial settling time of the current is a bit less than 1 day. The k-ω models also show some random oscillations in the entrainment rate at the end of the simulation for $t > 4$ days. These can be attributed to numerical problems in association with the grid resolution which changes for $z > 15$ m corresponding to the current depth at the beginning of the fluctuations. However, as long as the grid resolution is constant over the interface all models are stable and provide basically the same entrainment rates.

Due to entrainment the current depth increases with time. In this context it should be noted that the entrainment rate in the upper right panel is at first independent from the temporal evolution of the current depth.

The Froude number and the Ekman number decrease with time as shown in the lower panels of Fig. 3.63. The latter indicates that the current is more and more deflected from the straight downhill path and turns into the hill. The temporal evolution of the Froude number together with entrainment rate qualitatively supports the theoretical entrainment laws which predict reduced entrainment with decreasing Froude number. Also this point will be later discussed below.

The similarity of the different turbulence models concerning the depth integrated results is also found in the details. For a current depth of D = 10m after about 1 day of entrainment in the present example Fig. 3.64 displays depth profiles of density difference, buoyancy production, stream wise and cross-stream velocity (in

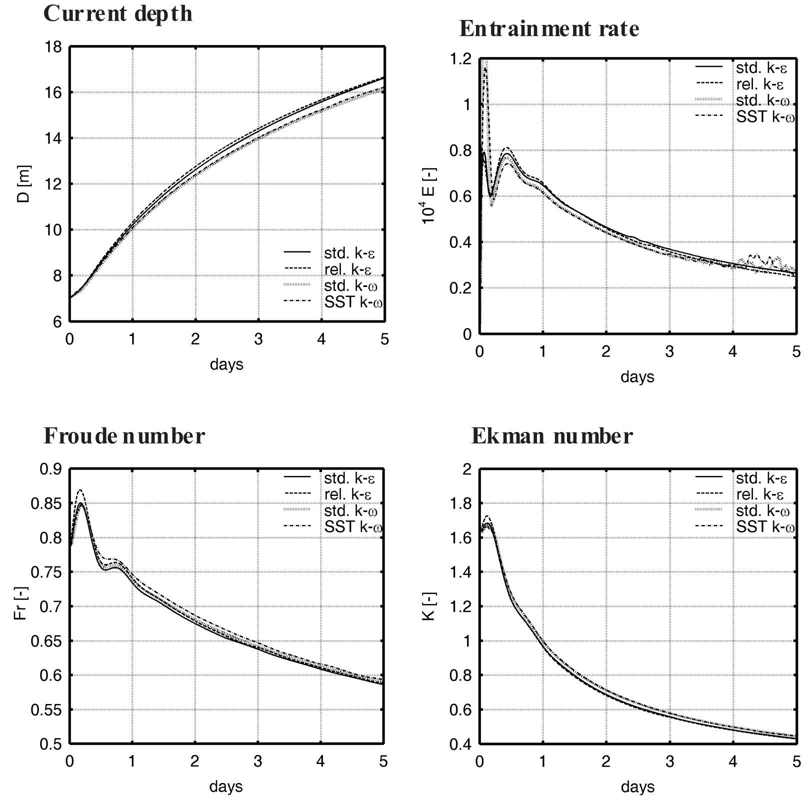

Figure 3.63: Comparison of different turbulence models. Temporal evolution of the gravity current.

the (m, n)-coordinate system), gradient Richardson number and flux Richardson number. As the stagnant ambient fluid is of limited interest only the lower 20 m of the total depth are shown.

Apart from some minor differences in the buoyancy production and Richardson numbers the profiles for all turbulence models are more or less identical. The initial density difference of $\Delta \approx 8$ kg/m^3 decreased by more than 25 % because of the entrainment of ambient fluid. The interface between the current and the ambient fluid is characterised by a more or less constant density gradient ($N^2 \approx 0.01$) which is found in the region 8 m $< z <$ 12 m.

A local mixing rate can be deduced from the buoyancy production in the upper right panel which increases linearly from $G = 0$ at the bottom to its maximum value $G \approx 1.5 \cdot 10^{-6}$ right below the interface and decreases to $G = 0$ again within the interface. This indicates the damping effect of stratification on turbulence and shows that mixing is most intense just below the interface where the ratio between

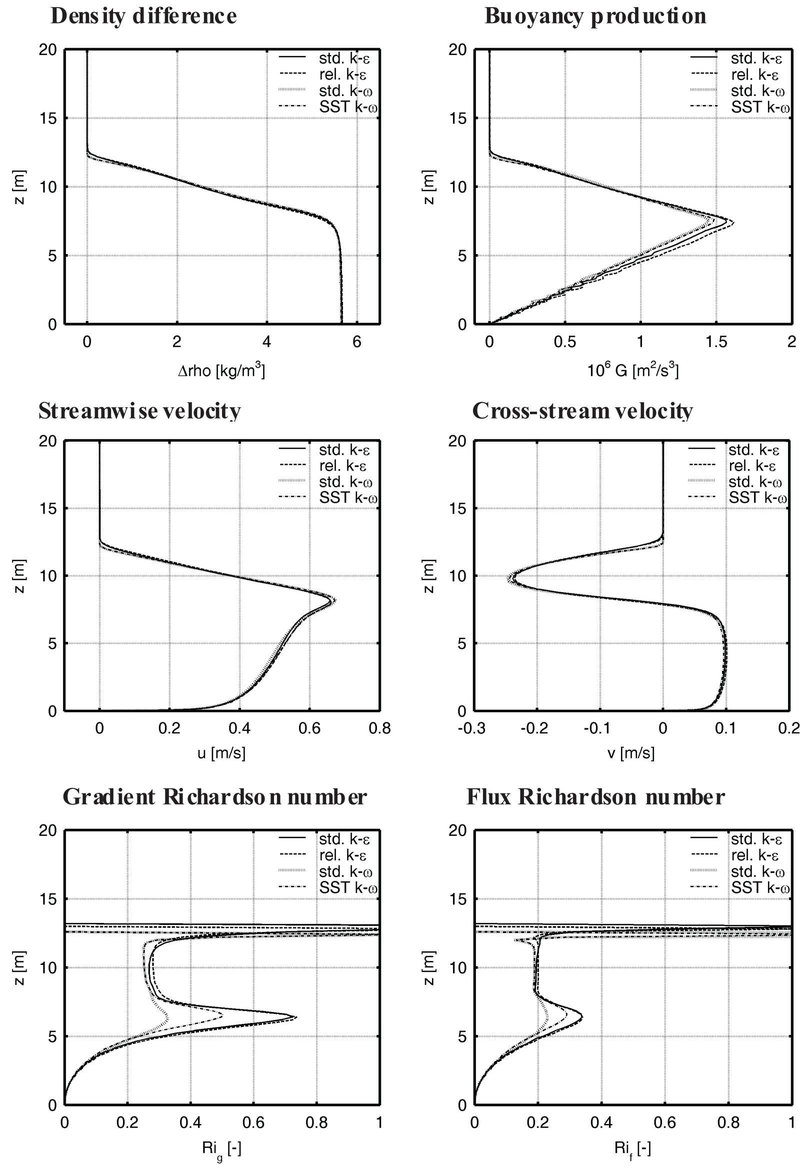

Figure 3.64: Comparison of different turbulence models. Vertical profiles for current depth D=10m.

turbulence intensity and stratification is at maximum.

The velocity profiles in the middle panels show the typical effect of a rotating frame of reference. At the bottom where friction forces are dominant both profiles have the characteristic logarithmic form with mean flow direction downhill. With increasing distance from the bottom, however, the influence of bottom drag decreases and

Coriolis forces become dominant. These accelerate the flow in stream wise direction with the maximum velocity right below the interface. In cross-stream direction the flow is deflected to the right ($v < 0$) with the maximum velocity in the centre of the interface.

From the profiles of the Richardson numbers in the lower panels it can be seen that within the interface the stationary values are reached indicating the validity of the equilibrium assumption in a stratified turbulent shear layer. At the top end of the interface density and velocity gradients tend to zero and the gradient Richardson number becomes ill-defined as indicated by the sudden increase for $z > 12$ m. Also below the interface both increase quite significantly before they approach zero at the bottom. This effect is most pronounced for the k-ε models and least significant for the standard k-ω model. However, the gradient Richardson number is a direct result of the density and velocity profiles which are apparently very similar. The alleged large differences stem from the fact that the velocity gradient enters squared into the numerator (cf. eq. 3.19) such that small deviations in the velocity field can have a large effect on the gradient Richardson number. Hence, it still may be concluded that all turbulence models provide the same results.

For the following validation of the numerical model concerning the simulation of density currents it is therefore sufficient to regard only one turbulence model. In principal the choice of the turbulence model is arbitrary, but in view of the subsequent simulations of the cylinder induced entrainment it seems most appropriate to use the SST k-ω model and ignore the other models from now on.

The validation of the numerical model was performed both by comparison with results from a vertically integrated theoretical model as well as numerical and measured data presented in *Arneborg et al.* (2007). From the mass balance it must be expected that the total buoyancy $g'D$ does not change with time. Furthermore the balance of potential energy requires that the entrainment rate should be identical to that derived from the temporal increase of the current depth. Fig. 3.65 shows the numerically evaluated and theoretical temporal evolution of the buoyancy in the left panel and the entrainment rates in the right panel.

The numerical model predicts a slight increase of buoyancy with time. However, after 5 days the difference to the theoretical value is less than 0.2 % and can therefore be assumed to be negligible. Apart from the deviations at the beginning and the end of the simulation already argued above the entrainment rates in the right panel show perfect agreement and approve the numerical balances of volume and potential energy.

Comparisons of the numerically calculated and theoretical relationships between the Froude and Ekman numbers as well as the dependence of the entrainment rate on the Froude number are shown in Fig. 3.66. Except for the deviations at higher Ekman numbers which are a result of the initial settling of the current, the numerical results almost perfectly agree with the theoretical curves. This confirms both,

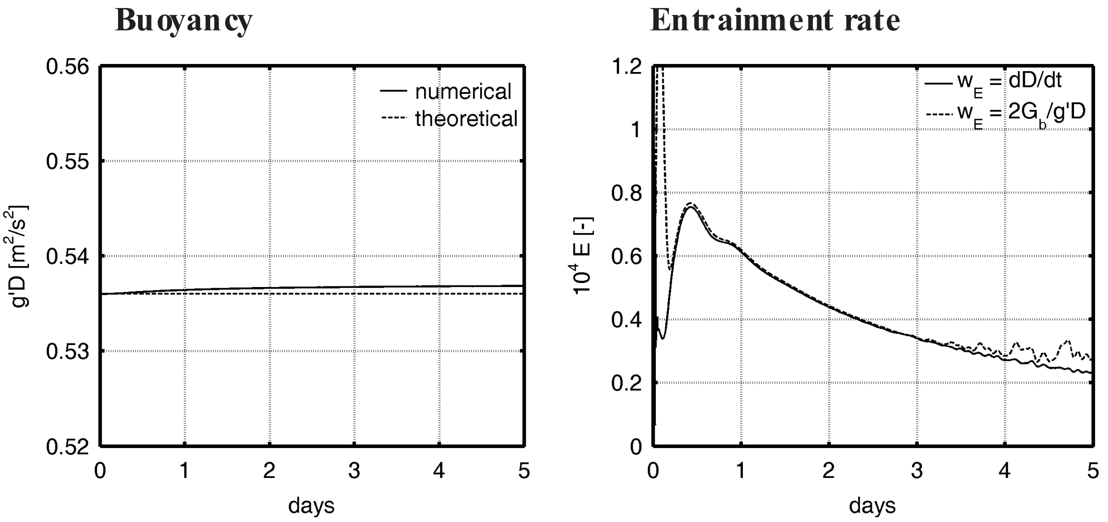

Figure 3.65: Evaluation of numerical errors. Temporal evolution of buoyancy (left) and the entrainment rate (right).

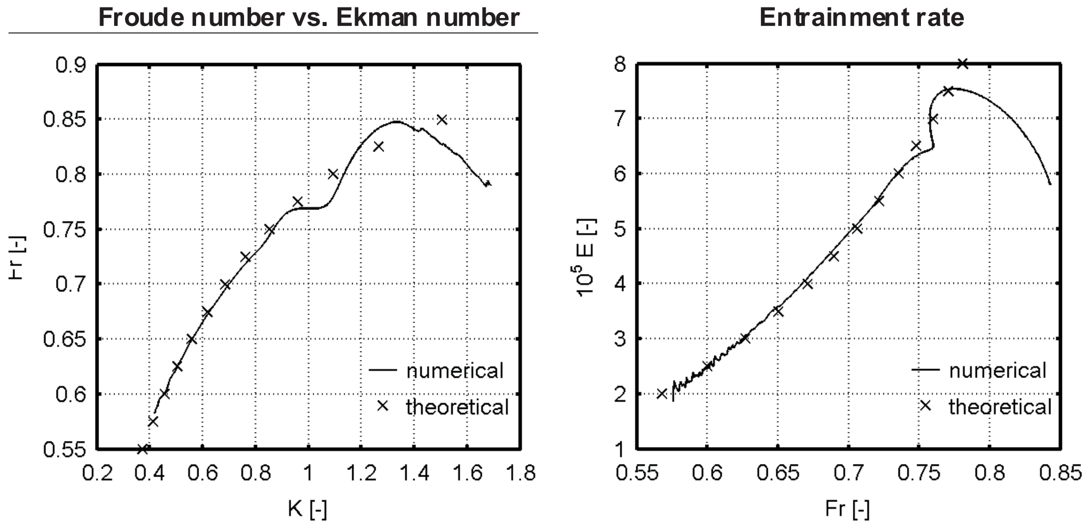

Figure 3.66: Comparison of the numerical and theoretical results for the Froude-Ekman number relationship (left) and the entrainment rate (right) .

the very good performance of the numerical model and that the current is indeed in geostrophic balance after an initial settling time. It is thus concluded that the model has been validated for use in the calculation of structurally induced mixing in the Baltic Sea.

The influence of Coriolis forces on the flow structure significantly complicates a systematic analysis of the mixing process behind a cylinder. It was therefore decided to perform a systematic study first without Coriolis forces and then look at the influence of these forces on the mixing process.

Therefore the same simulations were repeated without considering the Coriolis term. These showed physically unrealistic results after a short time period which eventually led to instabilities. This can be seen in Fig. 3.67 which shows the vertical profiles of density, velocity, turbulence- and buoyancy-production after 5, 10 and 15 hours simulation time.

From the maximum values of density it is seen that obviously some amount of less saline water is entrained into the bottom layer as the density difference between the current and the ambient fluid is constantly reduced. However, compared to the profiles after about 24 hours shown in Fig. 3.64 the reduction is much smaller which can be explained by the strange form of the interface found here. Apparently, the core of the current is more or less unchanged while the region above it is extensively mixed. From the profiles of velocity and gradient Richardson number it can be deduced that the mixed region is constantly growing and turbulence is in equilibrium ($R_{ig} = 0.25$). However, even without Coriolis forces it should be expected that due to the stabilising effect of stratification the interface will reach a quasi-stationary state just as those in Fig. 3.64. In the present case the upper part of the current behaves more like a neutral jet and there is evidence that the interaction of the mean stratified and turbulent flow fields is unbalanced

Indeed the non-physical model behaviour arises due to a wrong prediction of turbulence production and is an inherent problem for all models based on the turbulent viscosity/diffusion assumption. For these models the production of turbulent kinetic energy is proportional to the shear of the mean flow field and if the current is purely two-dimensional there is no production in height of the velocity maximum as the only gradient in the flow field vanishes. The minimal turbulence production inevitably yields a minimum of turbulent viscosity and diffusion which in turn precludes mixing of momentum and salinity and consequently results in the non-physical peak in the velocity profile and the steep gradient in the density profile. Due to the latter the core of the current is somewhat protected against entrainment while the upper part becomes more susceptible to mixing. The currents with Coriolis forcing above show a similar behaviour during the adjustment of the profiles from the initial box shape, but the maxima of stream wise and cross-stream velocity in the balanced state are found in different heights limiting the minimum of turbulence production to finite values. Thus there is no non-physical suppression of mixing,

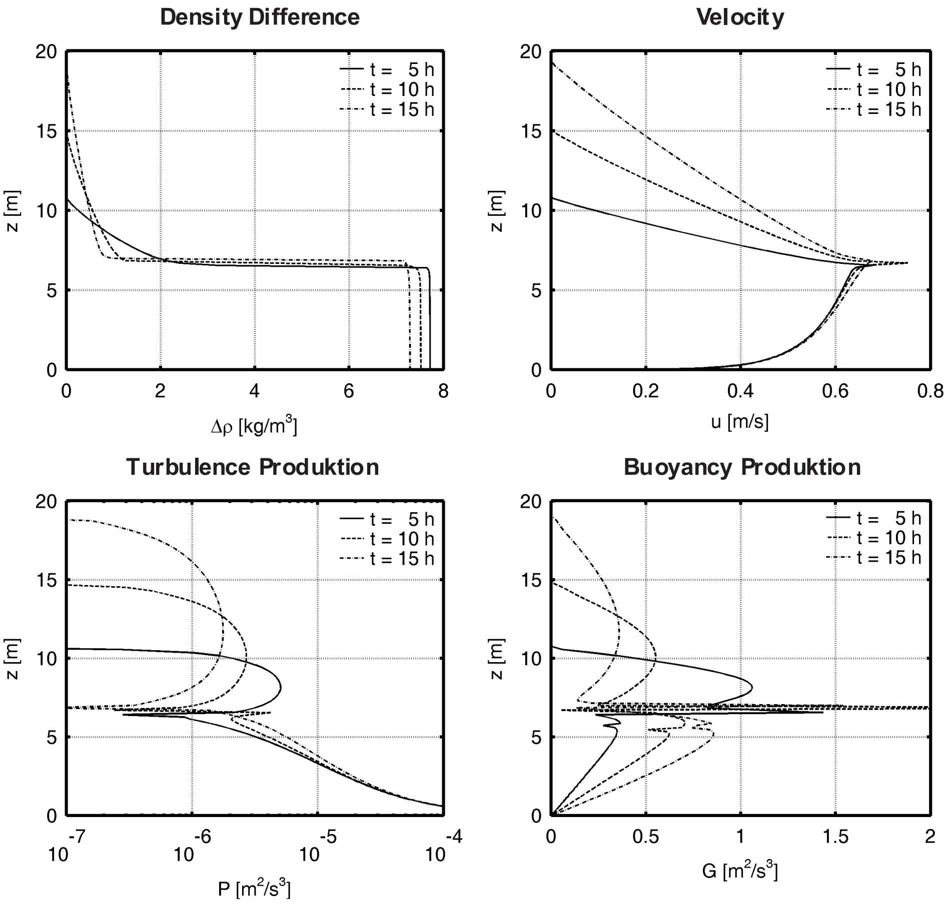

Figure 3.67: Simulation results for vertical profiles of density, velocity, turbulence and buoyancy production at different times without consideration of Coriolis forces.

the profiles stabilise and the numerical model provides reasonable results.

One might argue that in a real current there is also a zero gradient in the mean velocity profile at the maximum and production of turbulence should vanish at this point leading to similar phenomena like above. However, while the first can be assumed to be more or less correct the conclusion is definitely wrong as there is evidence for currents without the effect of rotation to be stable. The reason is found in the nature of turbulence which is always a three dimensional process and in the case of stratified flows is not only produced by shear but also by breaking of internal waves. Simulations based on simple two-equation turbulence models like the one above must inevitably fail as the relevant processes are neither resolved nor adequately incorporated into the model assumptions.

The apparent discrepancy in the model is fortunately not of significance since it only appears for non-structurally disturbed density currents. High shear is generated when the flow is disturbed by a cylinder and the flow becomes highly three dimensional. So that one can well assume that the inherent disadvantages of the turbulence models are negligible in this application.

Based on the above it is important to confirm that the density current is stable over a long reach. This is particularly important having the correct approach flow before the cylinder.

For the following tests a channel with a total length of $L = 1000$ m and a total depth of $H = 40$ m is regarded. With the chosen turbulence models here, however, there will be no lateral variations as long as the global conditions remain constant which is assumed here for simplicity. Hence, it is sufficient to demonstrate the model behaviour for a two-dimensional model with only one grid cell in lateral direction as the results are in the fully three-dimensional case are identical.

The numerical grid is similar to that used for the one-dimensional model above (cf. left panel in Fig. 3.62) with a fine resolution near the bottom to resolve the boundary layer, a constant resolution between 5 m $< z <$ 15 m to account for the gradients in the interface and a coarser resolution towards the top where the stagnant ambient fluid has no specific requirements. Even if the computational requirements for the two-dimensional model here can still be easily handled, the grid was chosen as coarse as possible in view of the much higher demands in the forthcoming fully three dimensional simulations. It was found that for the present simulations a horizontal resolution of $dx = 5$m and a vertical resolution of the interface by $dz = 0.5$m is necessary and sufficient.

In order to more or less reflect realistic conditions found in the Arkona basin the current depth is chosen to be $D \approx 10$ m with a salinity difference of $\Delta S \approx 10$ psu, a target current speed of about $U \approx 0.5$ m/s and a resulting Froude number of $Fr \approx 0.57$. The bottom slope is $\alpha = 1.06$ ‰and the bottom roughness has been set to $k_s = 0.025$ m.

The boundary conditions in this two dimensional model must be chosen such that the flow is in equilibrium. The inflow boundary conditions are the vertical profiles of velocity, salinity and the turbulent parameters k and ω; at the outflow one needs a proper pressure distribution which represents the density distribution.

For simulations without Coriolis forces a theoretical velocity profile was used in order to reduce the development length for the profile within the channel. These are presented in Fig. 3.68.

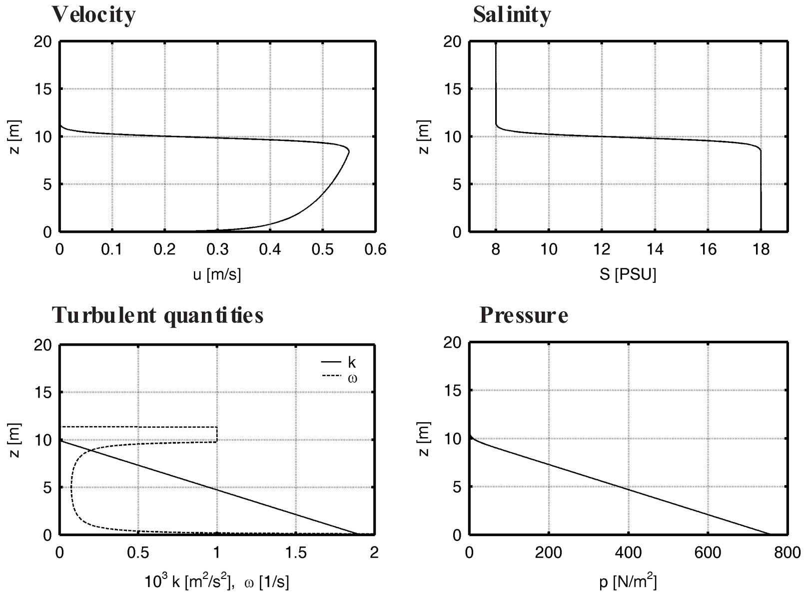

Figure 3.68: Boundary conditions for a density current in a channel without Coriolis forces.

For simulations with a channel in a rotating frame of reference where the current underlies the effect of Coriolis forces the boundary (and initial) conditions can be gained from a preliminary run of the one-dimensional model which is evaluated when the current reached the target depth of 10 m. The lower 20 m of the corresponding vertical profiles for stream wise and cross-stream velocity, salinity, turbulent kinetic energy, specific dissipation rate and excess pressure are shown in Fig. 3.69. Detailed descriptions for the determination of the velocity profiles are presented in *Schimmels* (2008).

It is useful to look at some typical results for depth averaged longitudinal profiles of the current depth, the Froude number, the volume flux and the entrainment coefficient. Fig. 3.70 presents these longitudinal profiles after 5000 s, i.e. a flow path 2.5 times the channel length and such initial disturbances related to the assumed initial conditions are no longer present. One sees the steadiness of the current in the centre part of the channel and shows the effects at the boundaries.

Especially at the inlet the deviations from the steady state are most significant and much stronger than those to be observed in Fig. 3.71 (with Coriolis forces). This could be expected as the inflow boundary conditions here were based on a theoretical analysis and the current adjusts to the quasi-equilibrium state over about the first 200 m.

The strong transformation in the inflow region is associated with large entrainment

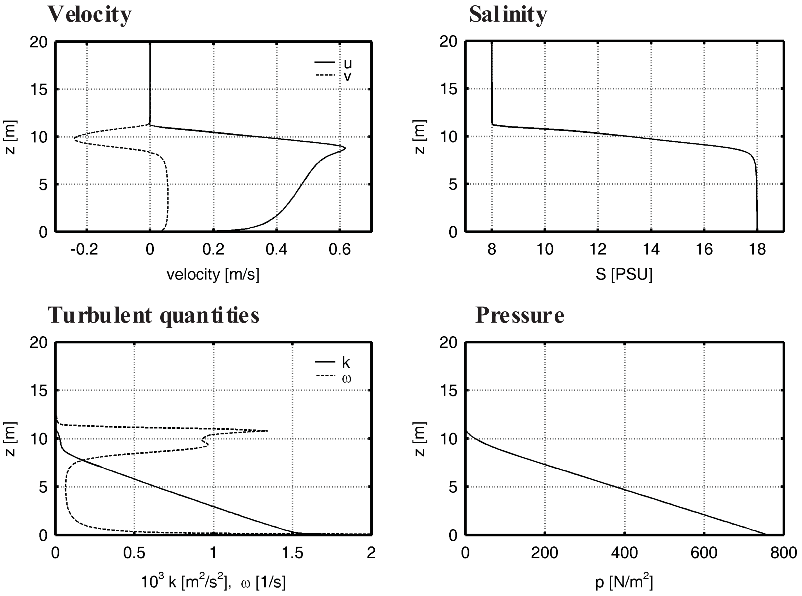

Figure 3.69: Boundary conditions for a density current in a channel with Coriolis forces
.

rates as can be seen from the bottom panel in Fig. 3.70 where entrainment within the first 100 m is even beyond the displayed range. The volume flux is qualitatively consistent with the entrainment rates and shows a large increase in the inflow region. However, in the centre part of the channel, say between 100 m and 900 m the entrainment rate deduced from the volume flux is about $E \approx 5 \cdot 10^{-5}$ and hence almost twice of that based on the bulk buoyancy production.
The following holds for the simulations with Coriolis forces (fig. 3.71): the entrainment rate shown in the lower panel is in the expected order of magnitude of about $E \approx 5 \cdot 10^{-5}$ implying an entrainment velocity of $w_E \approx 1.5 \cdot 10^{-5}$ m/s. In principal the latter could also be determined from the volume balance which reduces in the present stationary stream wise oriented case to

$$w_e = \frac{d(UD)}{dx} \tag{3.21}$$

The expected increase of volume flux over the whole channel length of 1000m should therefore be about $d(UD) = 1.5 \cdot 10^{-5}$m/s·1000m=0.015m^2/s, which is relatively small but can indeed be estimated from Fig. 3.71. However, due to these extremely small values a local evaluation of eq. 3.21 requires a very precise determination of the volume flux which is notably precluded from the present data as can be seen from the along channel profile shown in the second panel from below.

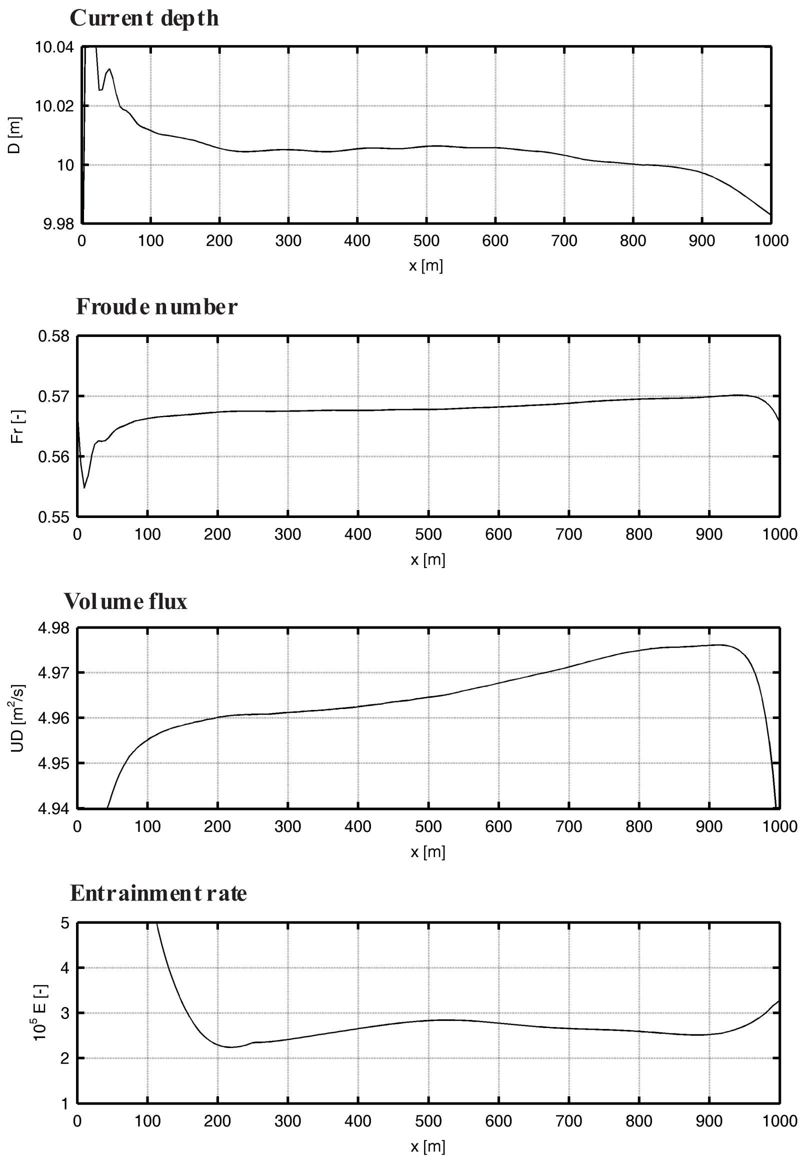

Figure 3.70: Along channel profiles for a density current without Coriolis forces. Current depth, Froude number, volume flux and the entrainment rate .

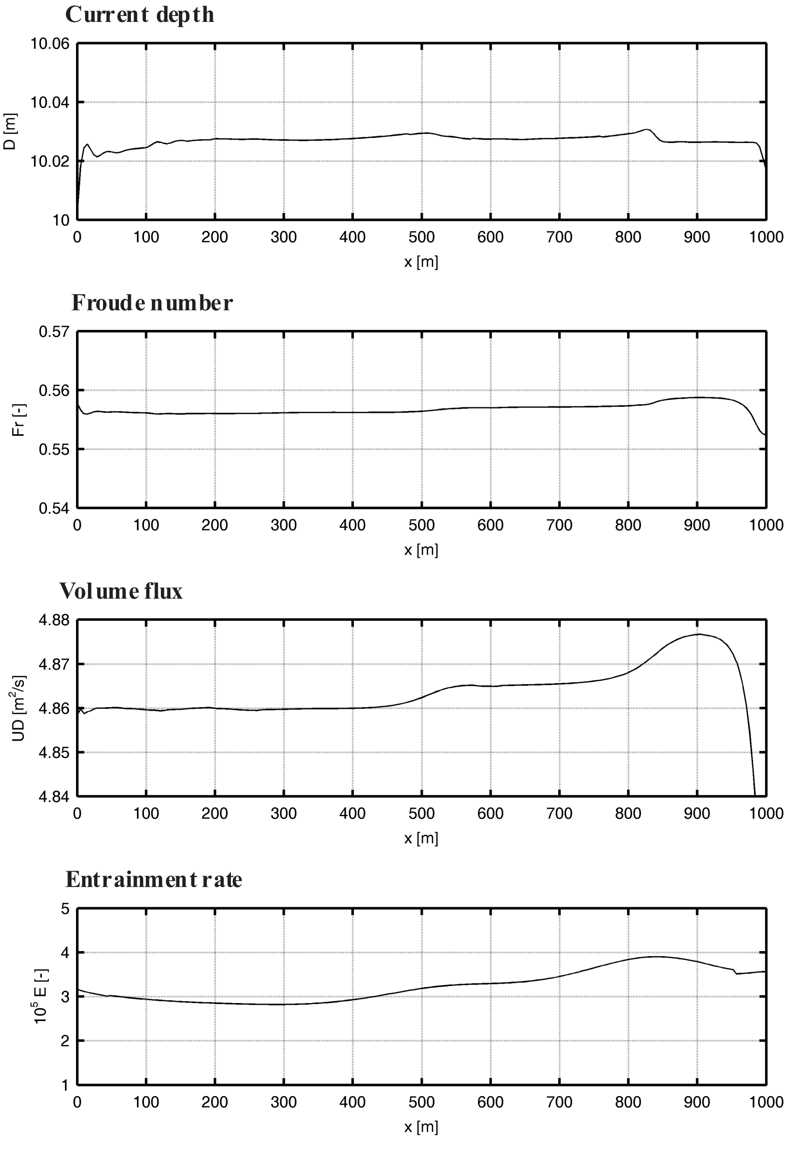

Figure 3.71: Along channel profiles for a density current with Coriolis forces. Current depth, Froude number, volume flux and the entrainment rate.

Compared to the entrainment rate found for the current with Coriolis forces ($E \approx 3 \cdot 10^{-5}$, Fig. 3.71) for the present case without Coriolis forces the entrainment rate can be assumed to be higher following the argumentation by *Stigebrandt* (1985). Thus, the entrainment rate shown in the bottom panel of Fig. 3.70 is obviously underestimated which might have been expected from the non-physical minimum in buoyancy production below the interface.

In conclusion density currents in a channel without Coriolis forces can be principally simulated with the present numerical model. The mean flow field is quasi not affected by the discrepancy of the turbulence model and the results seem to be reasonable although a local determination of the entrainment rate is precluded by the erroneous prediction of turbulent quantities near the interface. However, entrainment in undisturbed density currents is only of minor interest here and it can be assumed that for the flow around a cylinder this drawback disappears due to the presence of secondary currents in the wake.

Without doubt the numerical model can be regarded as validated for the simulation of an undisturbed density current in a channel with Coriolis forces and is clearly suited for the investigation of the influence of a circular cylinder on these currents in the next chapter.

3.2.6 Entrainment induced by a circular cylinder

As mentioned previously the present work is motivated by the intended construction of offshore wind energy devices in the Baltic Sea and the interest to determine the induced dilution of density currents passing these structures. All simulations here were therefore made on a 1:1 natural scale with velocities, salinities and length scales varied in a realistic range representative for density currents in the Baltic Sea and possible foundations of the wind energy devices. However, in order for the results to be of general matter and to be applicable to other situations on different scales, it is useful to define the governing parameters of the flow and to express the results in terms of non-dimensional quantities.

It was shown that the Reynolds number, Re, is the dominant parameter for simulating the flow around a cylinder in a non-stratified environment. For undisturbed density currents the densimetric Froude number, Fr, is the governing parameter for mixing and entrainment and the Ekman number K for considering the influence of rotation. Finally the ratio of the layer thickness to the cylinder diameter D/d is the fourth parameter of concern.

All of the simulations were performed on the fully turbulent field scale of $R_e = O(10^6)$. As such the Reynolds number has no effect on the flow topology and entrainment rates as long as there is no significant change in the flow regime. The Froude number was limited to the sub-critical range $Fr < 1$ and the Ekman number

to $0.4 < K < 1.2$.
A realistic range for Monopiles in the Baltic Sea is $1 < D/d < 2$. For small aspect ratios, say $D/d = 1$, the vortices span over the whole current depth carrying fluid from the interface to the bottom and vice versa. This can be expected to be in association with rather large entrainment rates in contrast to situations with large aspect ratios, say $D/d = 10$, where coherent structures in the wake are of the size of the interface and mixing is restricted to the upper part of the current only leading to comparably smaller entrainment rates.
Although density currents in the Baltic Sea are usually influenced by Coriolis forces it is desirable for the investigations on cylinder induced entrainment to initially neglect this effect. The secondary currents due to Coriolis forces complicate the flow field behind the cylinder and hamper the interpretation of the results. Their neglect facilitates the analysis and furthermore improves the significance of the results for cases in which rotation plays no role.
All simulations were made on the same computational domain which is sketched in Fig. 3.72 with the cylinder in the centre. The shaded plane is the result of one simulation and denotes the current depth which has been added to better visualise the model setup. Horizontal length scales are normalised by the cylinder diameter and the vertical scale is normalised by the current depth. The coordinate system is placed on the bottom in the centre of the cylinder with the z-axis pointing vertically upward, the x-axis pointing in stream wise direction and the y-axis pointing to the left.

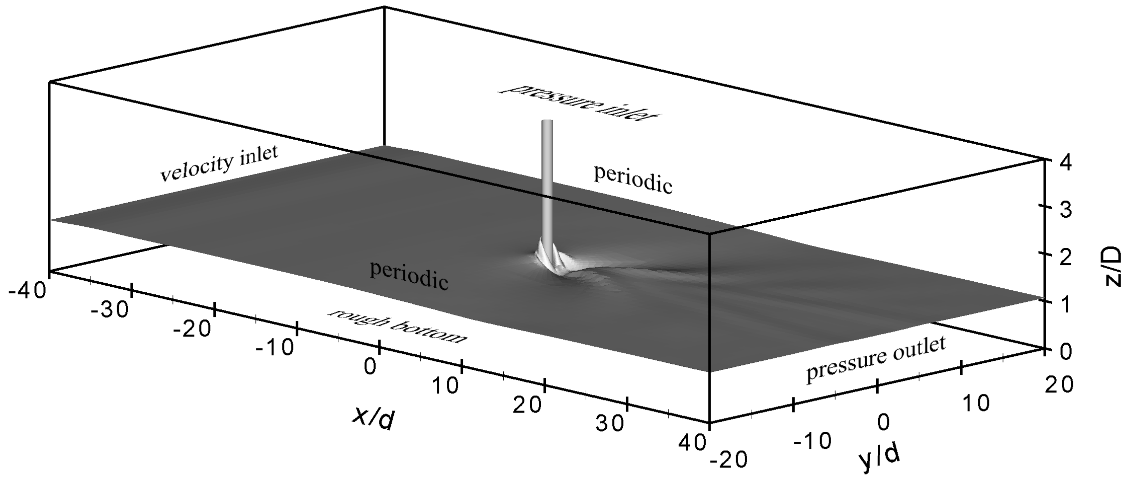

Figure 3.72: Definition sketch of the computational domain with the cylinder in the centre. Boundary conditions are given by the text and the current depth indicated by the shaded plane.

The boundary conditions correspond basically to those used for the simulation of undisturbed density currents in a channel. A pressure boundary condition is used at the free surface. The major difference comes from the new lateral boundaries at which periodic conditions are applied. Like for the top boundary also here symmetry (slip) conditions could have been chosen without significantly changing the results at least for purely two-dimensional currents. However, if Coriolis forces are regarded the resulting secondary flow in y-direction can only be realized with periodic conditions which have then always been used even if they are not the only alternative in cases without Coriolis forces.

The bottom roughness is always set to $k_s = 0.025$ m corresponding to a drag coefficient of $C_d \approx 0.0022$ for all cases where $D \geq 10$ m. The slope of the channel is then found from the definition of the Froude number with tan $\alpha_m = 0.72$ ‰for $Fr = 0.57$, $tan\alpha_m = 0.28$ ‰ for $Fr = 0.36$ and tan $\alpha_m = 1.85$ ‰for $Fr = 0.92$. Please note that these slopes correspond to the inclination in stream wise direction which is identical to the total slope of the channel for currents without Coriolis forces. If Coriolis forces will be regarded later the channel must also be tilted in lateral direction and the respective slopes can be determined from the total slope given by the Froude-Ekman number relation and the angle of deflection.

The profiles for velocity, salinity, turbulent quantities and pressure needed for the inflow and outflow boundary conditions as well as initial conditions were gained from preliminary simulations of undisturbed currents. Just as for currents with Coriolis forces a one-dimensional model has been used to obtain the corresponding profiles. In cases without Coriolis forces, however, this is not possible for reasons mentioned above and the boundary profiles were gained from simulations in a two-dimensional channel.

While the (normalised) size of the computational domain is the same for all cases the grid resolution had to be adjusted somehow to account for the peculiarities of the individual cases. The grid is block-structured and the basic resolution is based on the experiences gained with the validation of the numerical model. The combination of a density current flowing around a cylinder requires a high resolution in both vertical as well as horizontal domain such that the whole problem demands a high computational effort especially because the horizontal domain size must be large for reasons mentioned above. The total number of grid cells N_{tot}, the number cells in the vertical N_z and the normalised minimum grid sizes at the cylinder Δr_{min} and within the interface Δz_{int} are compiled in tab. 3.5.

In the vertical it is necessary to adequately resolve the steep gradients of velocity and turbulence quantities in the bottom boundary layer and of velocities and salinity (density) in the interface. In the range $0.5 < z/D < 1.5$ the resolution of the latter in terms of current depth was chosen to be $\Delta z_{int} = 0.05$ corresponding to 0.5 m for a current depth of 10 m which was found to be sufficient. However, as the thickness of the interface decreases with decreasing Froude number the resolution

case	**Fr**	**D/d**	N_{tot}	N_z	Δr_{min}	Δz_{int}
11xx	0.57	2	338192	47	$5.0 \cdot 10^{-4}$	0.050
21xx	0.92	2	338192	47	$5.0 \cdot 10^{-4}$	0.050
31xx	0.36	2	507288	70	$5.0 \cdot 10^{-4}$	0.025
12xx	0.57	10	299920	47	$2.5 \cdot 10^{-3}$	0.0250
13xx	0.57	1	358800	47	$2.5 \cdot 10^{-4}$	0.050

Table 3.5: Grid characteristics for the different test cases .

has been doubled for the lowest Froude number investigated here to account for this effect.

The horizontal grid topology is the same for all cases and adopted from that used for the simulations of non-stratified flow around a circular cylinder. The grid is circular up to 3 diameters around the cylinder and then converted over the next 3 diameters to the rectangular shape of the channel. The finest resolution at the cylinder Δr_{min} as given in tab. 3.5 corresponds to the wall function approach with y^+ being in the order of 10^2 or slightly below. To reduce the computational effort the resolution in the far field has been chosen much coarser with $\Delta x/d = \Delta y/d = 1$ which is slightly condensed in the wake region. Fig. 3.73 shows a side and top view of the complete numerical grid with details at the bottom and cylinder displayed in the small panels.

In order to cover a realistic range of Froude numbers and aspect ratios a parameter study was carried out. All simulations were run for 8000 time steps. Time steps were adjusted to let the current pass the domain within about 1500 time steps. In order to remove initial disturbances the simulations were first run for 4000 time steps. Subsequently the mean values for the parameters in question were calculated from the following 4000 time steps, corresponding to about 30 shedding cycles.

The total number of grid cells was between $3 \cdot 10^5$ and $5 \cdot 10^5$ and thus required extremely large storage space and computational power. The computations were therefore performed on the Super Computer of Northern Germany (HLRN) in which we used 8 or 16 parallel processors. Despite a practically 100% efficiency, one computer simulation took several days.

3.2.6.1 Structurally induced mixing without Coriolis forces

The goal of the simulation of structurally induced mixing without Coriolis forces is to increase understanding of the underlying processes and to provide a basis for systematically generalising results. Thus detailed investigations were made on the influence of the Froude number and the aspect ratio D/d on the flow field and the

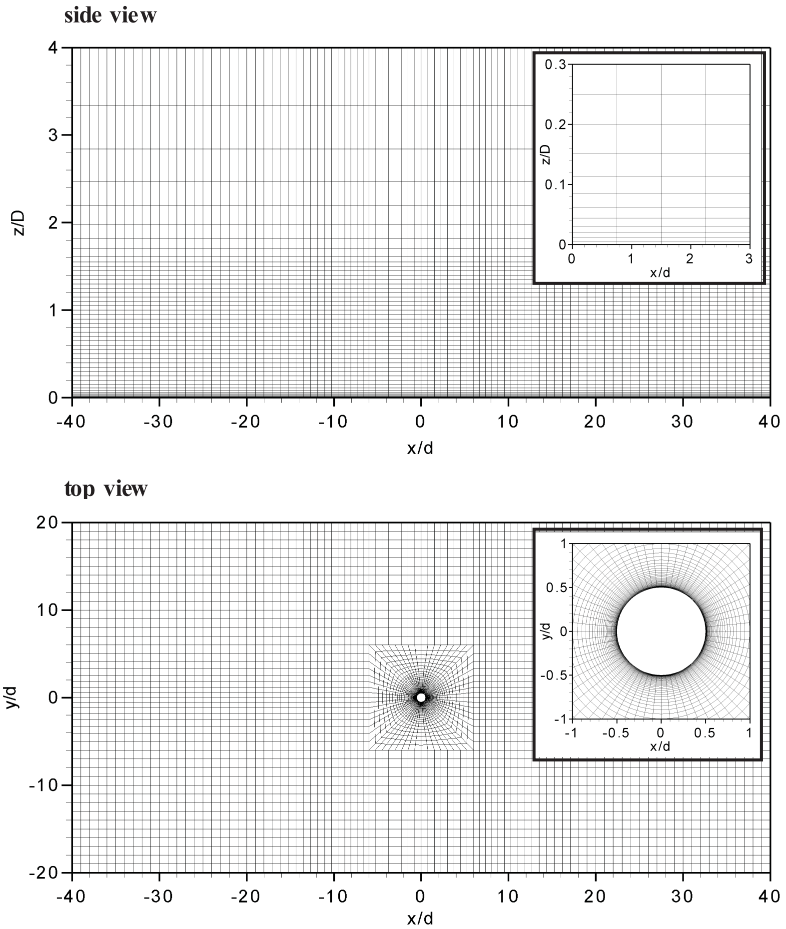

Figure 3.73: Side and top views of the numerical grid. Small panels showing the refined resolution at the bottom and around the cylinder, respectively.

associated mixing process. The major results are presented in this report. The reader is referred to *Schimmels* (2008) for details.

3.2.6.2 Case of reference: Entrainment induced by a circular cylinder without Coriolis forces

The following discussion of a current with $Fr = 0.57$, $Re = 2.5 \cdot 10^6$ and $D/d = 2$ is intended to introduce the peculiarities of the flow and to provide a reference for the succeeding analysis of the influence of the governing parameters. To get a general feeling for the effect of the cylinder on the density current it is useful to have a look at the distribution of the density (salinity) field and the buoyancy production as a measure for mixing intensity. For this purpose Fig. 3.74 shows a contour plot of (dimensional) buoyancy production in four different longitudinal sections in the vicinity of the cylinder at $Y = 0$, $Y = 0.5$, $Y = 1$ and $Y = 5$. The contour lines mark salinity concentrations at 0.5 %, 25 %, 50%, 75% and 99.5% of the complete salinity difference which indicate the interface. The time averaged flow around the cylinder is symmetric and the sections shown here are identical to those for the corresponding negative values of Y.

In the bottom panel at $Y = 5$ buoyancy production and density field are both constant over the whole length of the section and more or less no disturbance of the current is detectable. This indicates that the influence of the cylinder on the current is restricted to the very near field of the structure (at least in lateral direction) and moreover it allows for using this section as a reference. From the contour lines of salinity the vertical structure of the interface can be detected to be of the typical hyperbolic form as found for undisturbed currents. The large density gradients in the core of the interface as reflected by the small distances behind the contour lines at 25 %, 50% and 75% ΔS indicate strong stability against local mixing while the upper and lower part where stratification is weak can be assumed to be more susceptible to mixing. From the distance of the outer contour lines the thickness of the interface can be estimated to be about $0.6d$ corresponding to 3 m for the present case which is consistent with the findings above for a similar undisturbed current. Also the buoyancy production shows the expected behaviour with an increase from the bottom to a maximum value of $G \approx 10^{-6} m^2/s^3$ at the lower part of the interface and a decrease within the interface which, however, is presumably not very well predicted due to the inconsistency of the turbulence model discussed in section 3.2.3. However, as argued there, this discrepancy of the model can be assumed to be unimportant in the wake of the cylinder where secondary currents prevent a singularity in turbulence production. Much more these currents produce a significant amount of additional turbulence in the wake region which is the source for increased mixing as reflected by the high buoyancy production rates behind the cylinder found in the sections at $Y = 0$, $Y = 0.5$ and $Y = 1$.

The spatial evolution of buoyancy production along these sections shows that after 20 diameters behind the cylinder the undisturbed profile as given in the lower panel at $Y = 5$ is almost completely recovered suggesting that the effect of the cylinder on entrainment is restricted to only a few diameters also in stream wise direction. This is supported by the contour lines of salinity which most remarkably change in the near wake, say up to 10 diameters behind the cylinder, and than remain almost constant indicating that entrainment rates recovered to small values.

The evolution of the density field also supports the above assumption that mixing is most efficient in those parts of the interface that are only weakly stratified. The core of the interface where density gradients are large and the upper part where density

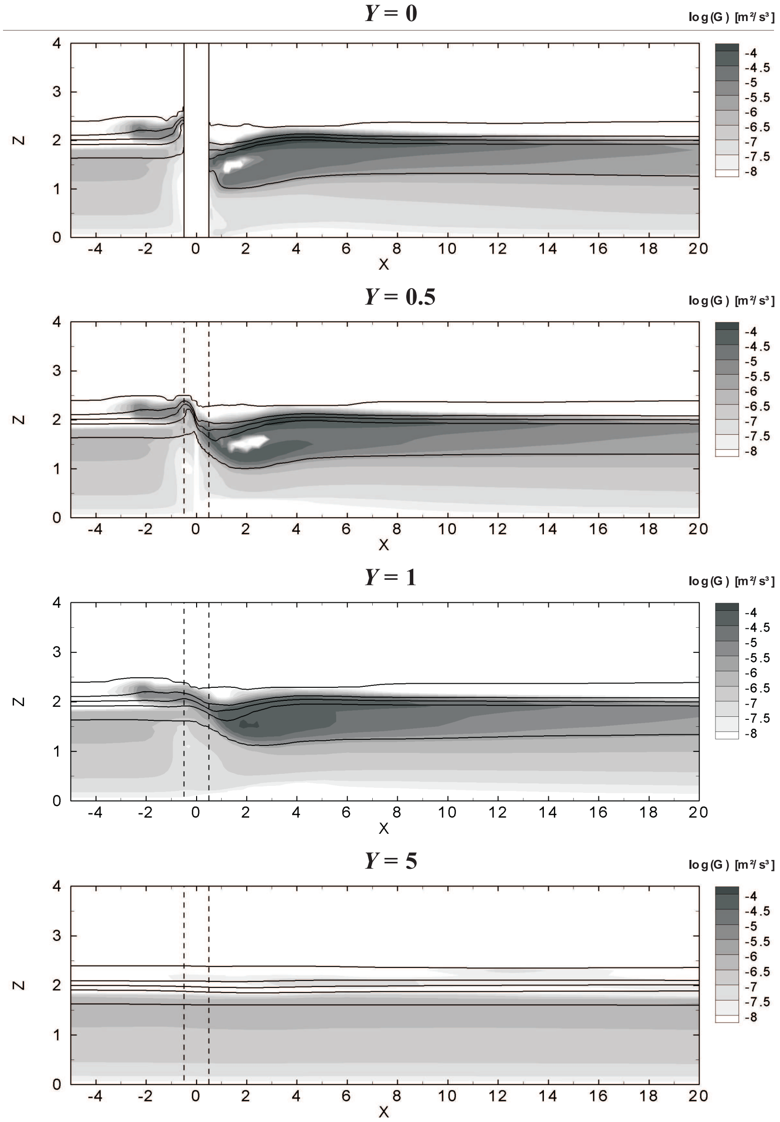

$Y = 0$

$Y = 0.5$

$Y = 1$

$Y = 5$

Figure 3.74: Salinity and buoyancy production at different longitudinal sections for the reference case with $Fr = 0.57$, $Re = 2.5 \cdot 10^6$, $D/d = 2$. contour lines indicating salinities at 0.5%, 25%, 50%, 75% and 99.5 % of ΔS. Buoyancy production is given in logarithmic format.

gradients are small but shear is insignificant remain both basically constant and are only moved up and down by the currents around the cylinder to be discussed below. However, the lower part of the interface where stratification is weak and shear is large is significantly affected by mixing. This is indicated by the distance between the lowest salinity contours which drastically increases behind the cylinder visualising the decreasing density gradient due to entrainment of lighter fluid.

The white spots in the buoyancy production field found in the near wake at $Y = 0$ and $Y = 0.5$ represent areas of negligible buoyancy production and reflect that the fluid in these regions is completely mixed and the vertical density gradient has vanished.

Without doubt the most active region for entrainment and mixing is found in the wake behind the cylinder. However, the flow field in the wake is strongly affected by the situation in front of the cylinder which should therefore not be disregarded in the present discussion. The flow in the section along the cylinder axis at $Y = 0$ is completely blocked by the cylinder which induces a downward current forming a small vortex at the bottom and an upward current lifting the interface. The latter causes an excess pressure to the surroundings driving a back-flow current within the interface in front of the cylinder which is the source for turbulence production and explains the higher buoyancy production found in the upper part of the interface in front of the cylinder.

The excess pressure caused by the lifted interface also induces a strong downward current in stream wise direction which causes an advective transport of the interface as can be deduced from the contour lines of salinity. In the wake upward currents lift the interface again to a maximum level about 5 diameters behind the cylinder before it finally settles to a slightly lower height when secondary currents and mixing rates have diminished.

To get a better idea about the three dimensional flow field around the cylinder Fig. 3.75 shows the velocity field, buoyancy production and salinities at some cross-sections in front of and behind the cylinder. Buoyancy production and salinity are given as in Fig. 3.74 and the velocity field is represented by the vectors which are differently scaled in the individual panels (see reference vector).

The expected symmetry of the (time averaged) flow field can be found in all sections justifying the restriction of the above discussion to longitudinal sections at positive Y only. Moreover it is obvious at first sight that the influence of the cylinder in the lateral direction is indeed limited to a few diameters as directly seen from the pattern of the velocity field and further reflected by buoyancy production and salinity at $Y = \pm 5$ which are identical in all sections, except for $X = 30$.

This is an effect of the increasing width of the wake which is reflected by the velocity and salinity fields in the last four panels and exceeds the width of the section at $X = 30$. The spreading of the wake is associated with a loss of local intensities equalising high gradients in the flow field and smoothing the local effects of entrain-

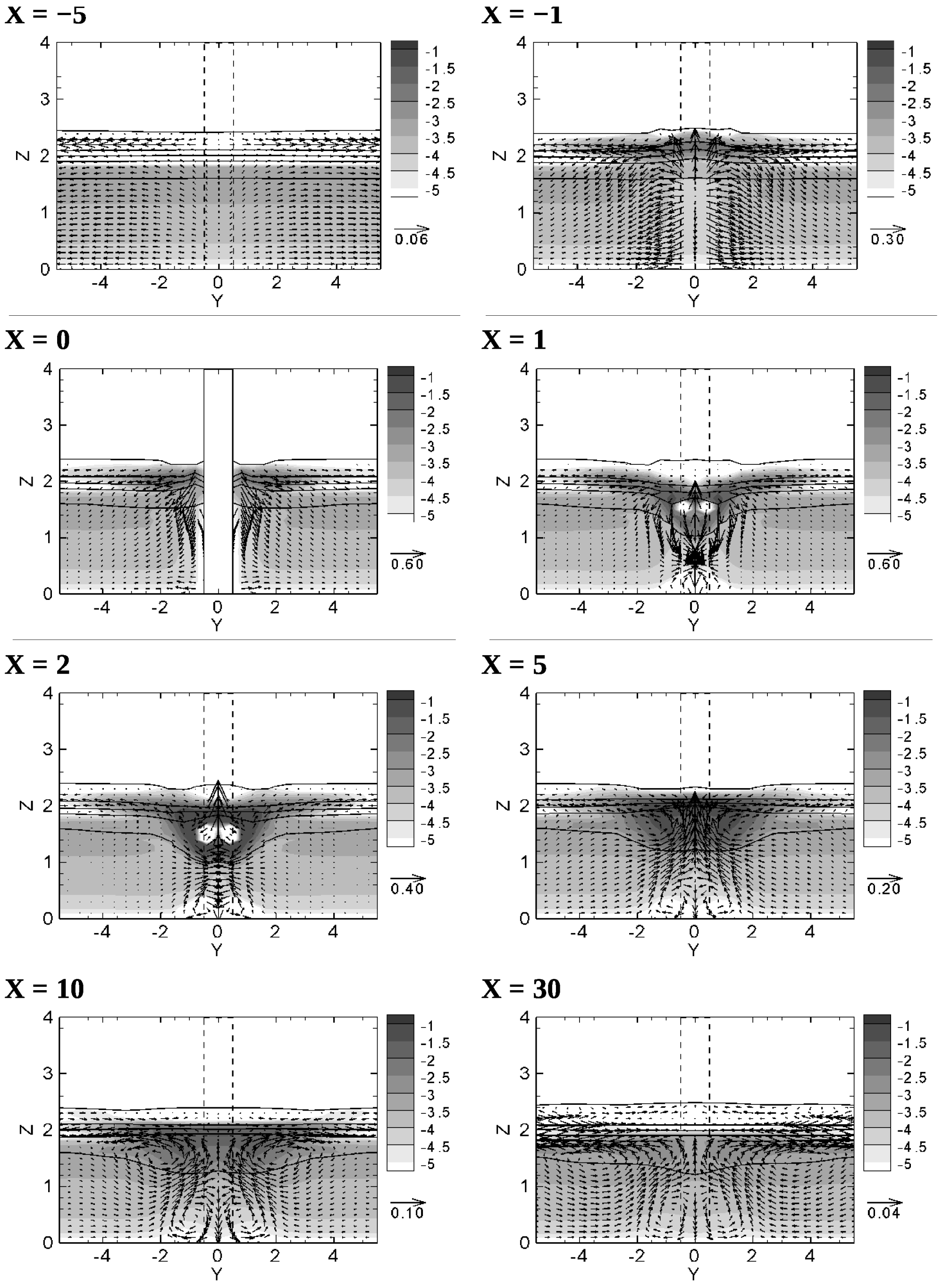
X = −5

X = −1

X = 0

X = 1

X = 2

X = 5

X = 10

X = 30

Figure 3.75: Flow field at different cross-sections in front of and behind the cylinder for the reference case with $Fr = 0.57$, $Re = 2.5 \cdot 10^6$, $D/d = 2$. Salinity and buoyancy production are displayed as in Fig. 3.74. Note the different scaling of the velocity vectors.

ment in lateral direction. Before continuing further it seems to be more useful to align the discussion of the flow field with the pathway of the current around the cylinder starting in the upper left panel of fig. 3.75 and then going from left to right and top to bottom.

Some distance in front of the cylinder at $X = -5$ a clear divergence of the current to the left and right can already be noticed where the highest velocities are found within in the interface but still amount only a few percent of the current speed. Moving closer to the cylinder at $X = -1$ lateral velocities close to the cylinder have significantly increased and the upward and downward current at the cylinder axis is clearly identified from the vectors at $Y = 0$ with the point of inflection being at about $Z = 1.3$ (i.e. 2/3D). The lifting of the interface caused by the upward current can be deduced from the salinity contours and the increased buoyancy production within the interface can be associated with the currents induced by the resulting excess pressure.

Right next to the cylinder at $X = 0$ the downward component of the excess pressure induced current is at maximum and of the same order as the current speed. The interface has been transported back downwards by this current to reach its minimum level behind the cylinder at $X = 1$. Although a significant vertical downward component is still present left and right of the cylinder in this cross-section the highest velocities are found at the cylinder axis and are directed upwards. They cause the transport of the interface in the wake back upwards and induce large vortices which are more clearly identifiable in the following cross-sections farer away from the cylinder. At the bottom another vortex pair is formed which mixes the very low bottom part of the current as can be deduced from the slightly higher levels of negligible buoyancy production at the bottom indicating that density gradients have vanished in that region. However, these vortices are rather unimportant concerning the overall mixing process.

Much more important is the buoyancy production within the interface from which the white spots of zero density gradients and negligible production are found again right behind the cylinder at $X = 1$ and $X = 2$. The highest levels of buoyancy production within each cross-section are located just around these spots with the overall maximum values found at $X = 2$. It can therefore be assumed that the maximum entrainment rates will be found about 2 diameters behind the cylinder and about 1 diameter moved to the left and right, respectively.

Following the current further along the wake at $X = 5$, $X = 10$ and $X = 30$ it can be seen that buoyancy production more and more decreases such that at $X = 30$ additional mixing by the cylinder is no longer detectable and the natural state found in front of the cylinder is recovered. Within the mean flow field, however, the influence of the cylinder remains present much longer as clearly identifiable by the large vortices. This is clear from the fact that mixing induced by the cylinder is actually restricted to a rather small region in the wake which causes quite significant lateral density gradients. These gradients induce lateral currents which drive the vortices and compensate the density difference which will naturally take much longer than the actual local entrainment of ambient fluid.

This homogenisation process can be well identified from a comparison of the two cross-sections in the far wake at $X = 10$ and $X = 30$. Below the interface there is a current directed to the cylinder carrying denser fluid from the lateral far field to the wake region where the lowest salinity contour line is lifted while it is lowered at the sides. A similar pattern is found within the interface where denser fluid in the lower part is transported away from the cylinder while above lighter fluid is added from the sides increasing the amount of low salinity as indicated by the lifted uppermost contour line.

The spatial distributions of the total entrainment rate and the bulk flux Richardson number are given in Fig. 3.76. The entrainment rate of the undisturbed current cannot be determined from the buoyancy production due to the discrepancy of the turbulence model. However, from the volume flux it could be reasonably estimated to be about $E \approx 5 \cdot 10^{-5}$ for the present case which was therefore chosen as the lowest level for the entrainment rate and is the threshold value to determine the effective entrainment induced by the cylinder. The same problem applies to the flux Richardson number which can also not be determined for an undisturbed density current without Coriolis forces. A reasonable value seems to be about $Ri_{f,b} \approx 0.03$ (*Schimmels*, 2008) which has therefore been chosen here as the threshold value to identify the influence of the cylinder.

The distribution of the entrainment rate is almost identical to that of the bulk buoyancy production above. Although there is also some entrainment in the bow wave in front of the cylinder most mixing takes place in the wake where the highest entrainment rates are found at $X = 2$, $Y = \pm 1$ which was already assumed above in the discussion about the depth resolved buoyancy production in Fig. 3.75.

The spatial distribution of the entrainment rate allows for an estimation of the area of influence of the cylinder which can be assessed to be about 20 diameters long and 6diameters wide. Although locally the cylinder induced mixing is very intense with entrainment rates being more than 2 orders of magnitude higher it can be assumed that the overall effect of an offshore wind energy farm on the current is small as long as the structures are not very close to each other. However, this will be discussed in more detail in section .

From the bulk flux Richardson number it is seen that mixing is not necessarily most efficient where the entrainment rates are largest. In contrast the highest mixing efficiency is found where entrainment rates already decay although the pattern of both is quite similar at least in the far wake. It is beyond the scope of the present work to analyse the mixing process in form of the flux Richardson number in more detail as the major interest is on the actual effect which is represented by the entrainment rate. However, it can be concluded that entrainment induced by a

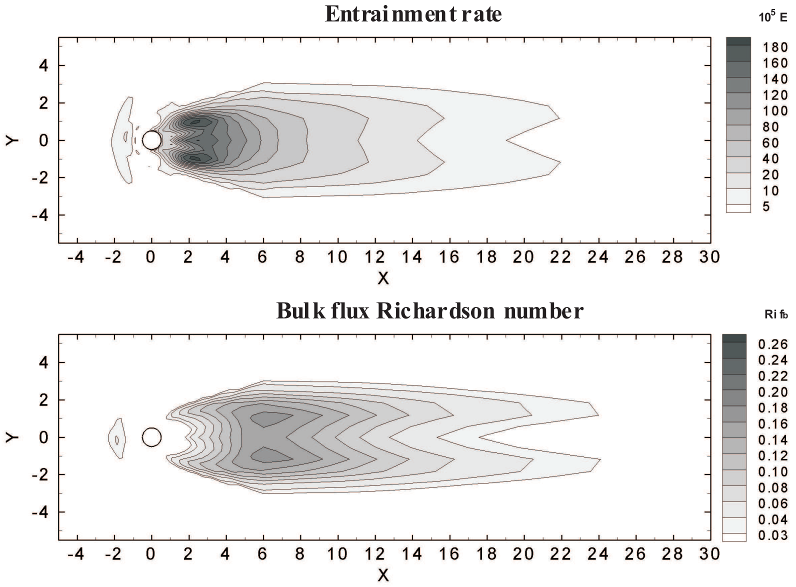

Figure 3.76: Total entrainment rate and the bulk flux Richardson number for the reference case with $Fr = 0.57$, $Re = 2.5 \times 10^6$, $D/d = 2$.

cylinder is generally associated with higher bulk flux Richardson numbers than that found in an undisturbed current. For the present case the maximum values of the bulk flux Richardson number are found left and right of the middle axis and show that buoyancy production can be up to about 16 % of the total produced turbulence.

3.2.7 Parameter Study

The local entrainment is used here to investigate the influence of the governing parameters on the mixing process.

It was previously stated and *Schimmels* (2008) has shown that for realistic conditions in the Baltic Sea and the Reynolds number ($Re \approx 10^6$) is regarded as an unimportant parameter for the present investigation. From a scientific point of view, however, it might be interesting to further investigate the Reynolds number effect by small scale simulations at low Reynolds numbers which would then also allow for a comparison with laboratory measurements. But this is also a task for future work.

The influence of the Froude number can be seen in Fig. 3.77 for $Fr = 0.36$; 0.57 and 0.92. In all cases the Reynolds number was held constant at $Re = 2.5 \cdot 10^5$ and the aspect ratio had a constant value of $D/d = 2$.

Before the spatial distribution of the entrainment rates is discussed it should be recalled that the Froude number for all cases regarded in the preceding sections was $Fr = 0.57$ for which the natural entrainment rate of the undisturbed current was estimated to be $E \approx 5 \cdot 10^{-5}$. In this study the Froude number is changed in the different cases and by that also the natural entrainment rates will change. Hence, for the presentation of entrainment induced by the cylinder it is useful to define other threshold values which are oriented at the natural rates. As these rates cannot be determined with the present numerical model they were estimated from available data in the literature which were compiled in Fig. 3.78. Assuming the lowest limit, the corresponding values could be assessed to be $E \approx 2 \cdot 10^{-5}$ for $Fr = 0.36$ and $E \approx 15 \cdot 10^{-5}$ for $Fr = 0.92$. Fig. 3.77 shows the corresponding representation of the entrainment rates for the different cases with increasing Froude number from

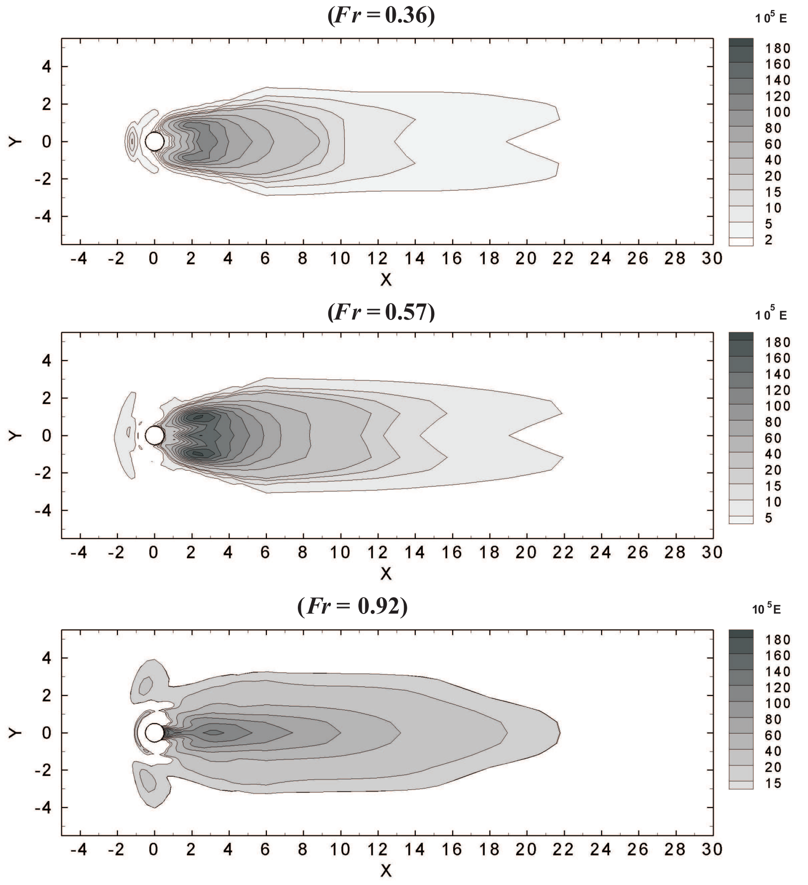
(Fr = 0.36)

(Fr = 0.57)

(Fr = 0.92)

Figure 3.77: Influence of the Froude number on entrainment for cases with constant $Re = 2.5 \cdot 10^6$ and for $D/d = 2$. Note the different lowest contour levels .

top to bottom.

As might have been expected from the similar flow fields in the wake for $Fr = 0.36$

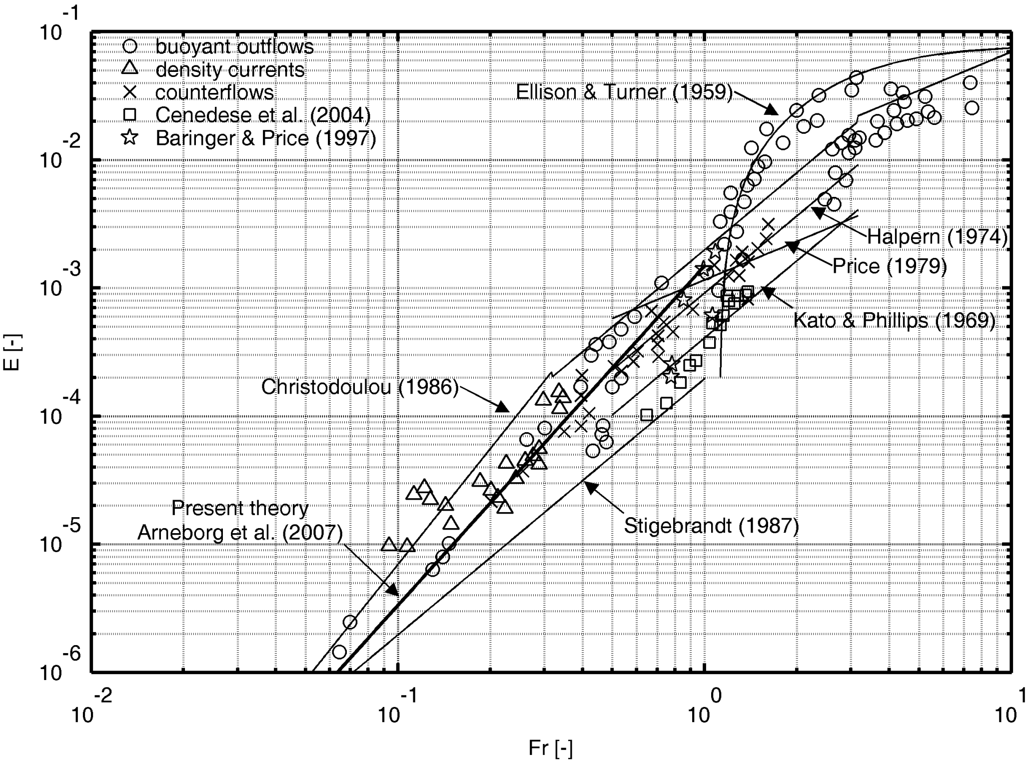

Figure 3.78: Entrainment rate versus Froude number. Comparison of entrainment laws and measurements from the literature.

and $Fr = 0.57$ also the patterns of the entrainment rates in the upper and middle panel are quasi identical except for slightly stronger maxima in the centre of the near wake for $Fr = 0.57$. The absolute values, however, are different and suggest that in analogy to undisturbed currents entrainment induced by a cylinder also increases with Froude number. This tendency seems logical at first sight but is actually not supported by the results for $Fr = 0.92$ where the maximum values are clearly less than for $Fr = 0.57$ and also the pattern has changed. The highest rates are found right in the centre of the wake rather than left and right of it and due to the homogeneity of the flow field discussed above the spatial distribution of the entrainment rates is much more uniform for $Fr = 0.92$.

The area of influence of the cylinder is more or less the same for all Froude numbers which is the result of the different threshold values based on the natural entrainment rates defined above. Also the pattern in the bow wave in front of the cylinder is relatively similar for all cases with the tendency to a larger lateral extent with increasing Froude number. This seems logical from the above argumentation that the potential of a local disturbance to laterally spread increases with decreasing stability of the interface and by that with increasing Froude number. Moreover, the comparable patterns support the preceding findings that the dynamics of the bow wave are presumably associated with the cylinder rather than the current itself.

The influence of current depth to cylinder diameter ratio will be analysed in a similar fashion like the Reynolds number above by comparing the reference case $D/d = 2$ with two other cases, case $D/d = 1$ and 3. All have the same Froude number $Fr = 0.57$. The current depth was kept constant such that the incoming current is absolute identical for all cases and only the diameter of the cylinder has been changed. This implies a significant change of the Reynolds number which, however, was found above to be unimportant as long as the flow is in the same regime.

Fig. 3.79 shows the spatial distribution of the corresponding entrainment rates for the three cases with increasing aspect ratio from top to bottom. In fact, it is seen at first sight that the entrainment rates are largest for $D/d = 1$ and decrease with increasing depth to diameter ratio. For $D/d = 10$ the effect of the cylinder can be quasi neglected as the maximum values are more or less in the order of the natural entrainment rates of the current. So again this case needs no further discussion.

The pattern of the entrainment rates behind the cylinder for the other two cases is very similar especially in the near wake. Apart from the absolute higher entrainment rates for the smaller aspect ratio there is also a tendency to increased mixing in the middle plane along the cylinder axis which is less pronounced for $D/d = 2$. This might be the result of the flow field in the wake which had not only higher velocities but was also more concentrated at the cylinder axis for $D/d = 1$ (*Schimmels*, 2008). Due to the higher intensities in the flow filed, the area of influence of the cylinder is seen to be longer for the lower aspect ratio but the lateral extent is slightly less than for $D/d = 2$. This could also be expected from Fig. 3.75, where the deformation of lowest salinity contour, especially at $X = 10$, is seen to be more confined for $D/d = 1$.

With decreasing aspect ratio entrainment rates not only increase in the wake but also around and in front of the cylinder. While the strong intensities in the bow wave found for the lowest Reynolds number in the preceding section could not conclusively explained, it might be argued that it is a result of the higher blocking ratio and the resulting velocity field around the cylinder. It is noted that higher rates in front of the cylinder are clearly visible, but these make up less than 10 % of the total entrainment. As the conclusions of the present work are not severely affected by this effect, the investigation of the processes involved is left to future research.

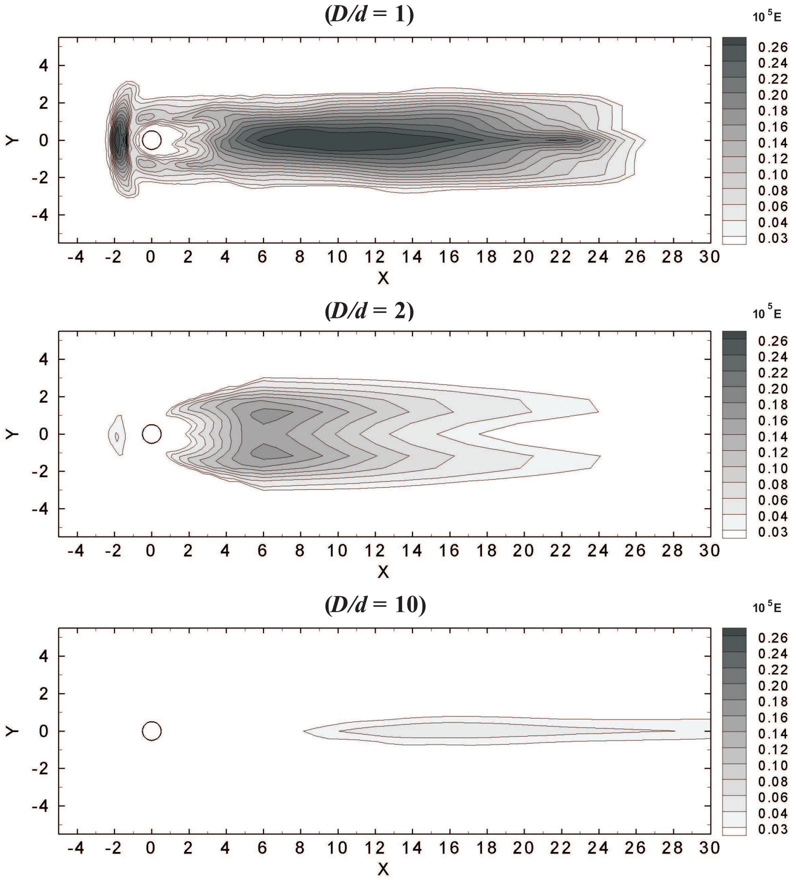

Figure 3.79: Influence of the depth to diameter ratio on entrainment for cases with constant $Fr = 0.57$.

3.2.8 Entrainment Induced by a Circular Cylinder with Coriolis Forces

The previous discussion was focused on density currents without the influence of Coriolis forces and the numerical model could be shown to work very well for their simulation. Coriolis forces induce lateral currents which complicate the flow around the cylinder and make the analysis of the principal processes very difficult. A detailed parameter study was conducted to quantify the effect of the Froude number; Aspect Ratio and Coriolis forces on the mixing process (see Fig. 3.80). For these simulations it is possible to set the channel slope such that the X-direction is parallel to the approach flow, i.e. the vertically averaged lateral velocity in the Y-direction is 0. The strong 3-dimensional flow around the cylinder does not allow the type of analysis presented for the non-rotation case. The entrainment rates can, however,

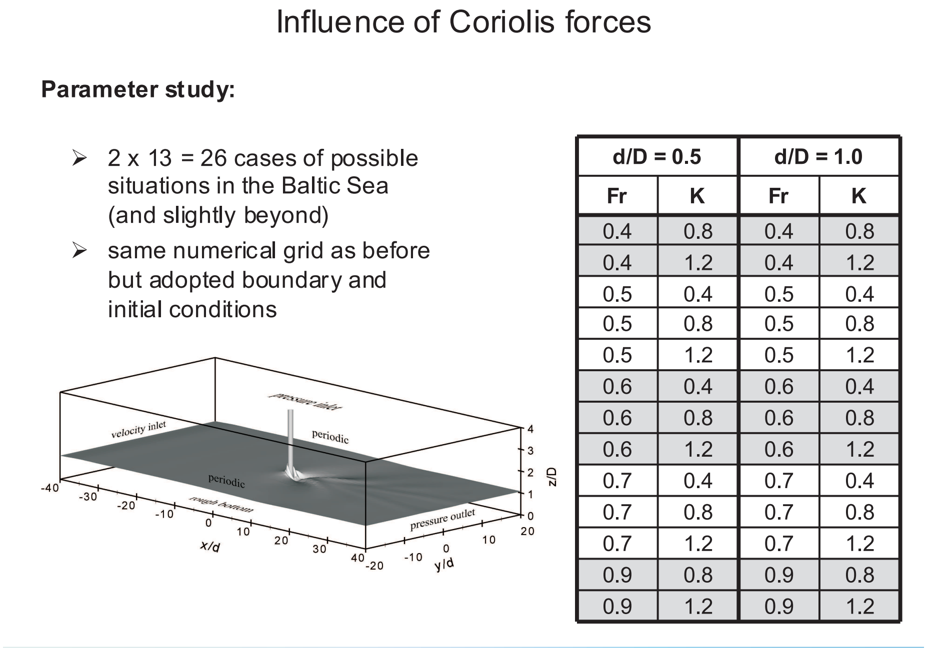

Influence of Coriolis forces

Parameter study:

- 2 x 13 = 26 cases of possible situations in the Baltic Sea (and slightly beyond)
- same numerical grid as before but adopted boundary and initial conditions

d/D = 0.5		d/D = 1.0	
Fr	**K**	**Fr**	**K**
0.4	0.8	0.4	0.8
0.4	1.2	0.4	1.2
0.5	0.4	0.5	0.4
0.5	0.8	0.5	0.8
0.5	1.2	0.5	1.2
0.6	0.4	0.6	0.4
0.6	0.8	0.6	0.8
0.6	1.2	0.6	1.2
0.7	0.4	0.7	0.4
0.7	0.8	0.7	0.8
0.7	1.2	0.7	1.2
0.9	0.8	0.9	0.8
0.9	1.2	0.9	1.2

Figure 3.80: Parameter study of cylindrically induced mixing in stratified flow .

be determined by integration of the buoyancy production over the water depth. In this manner both the local and global influence of the cylinder on entrainment can be quantified.

The complexity of the flow field is demonstrated in Fig. 3.81 which shows the flow field at different cross-sections in front of and behind the cylinder for the reference case but now with Coriolis forces. The results can be compared to those without Coriolis forces presented in Fig. 3.75 but it should be noted that the velocity vectors here are equally scaled in all cross-sections and the lower panels show other cross-sections than those in Fig. 3.75. These differences have their seeds in the lateral current induced by the Coriolis forces which can be very well identified in the upper left panel at $X = -5$ where the influence of the cylinder is not yet intense. It clearly shows the typical pattern with a relatively slow component in positive Y-direction below the interface and a strong flow in negative Y-direction within the interface with velocities reaching up to 50 % of the current speed.

The latter is the reason for the scaling of the velocity vectors and causes any disturbance within the interface to be transported laterally away from the cylinder. Note in this context that the view of all cross-sections presented here is against the flow direction (negative X-direction) which was not important up to now due to the symmetry of the flow patterns. Here, however, it implies that a current appearing to

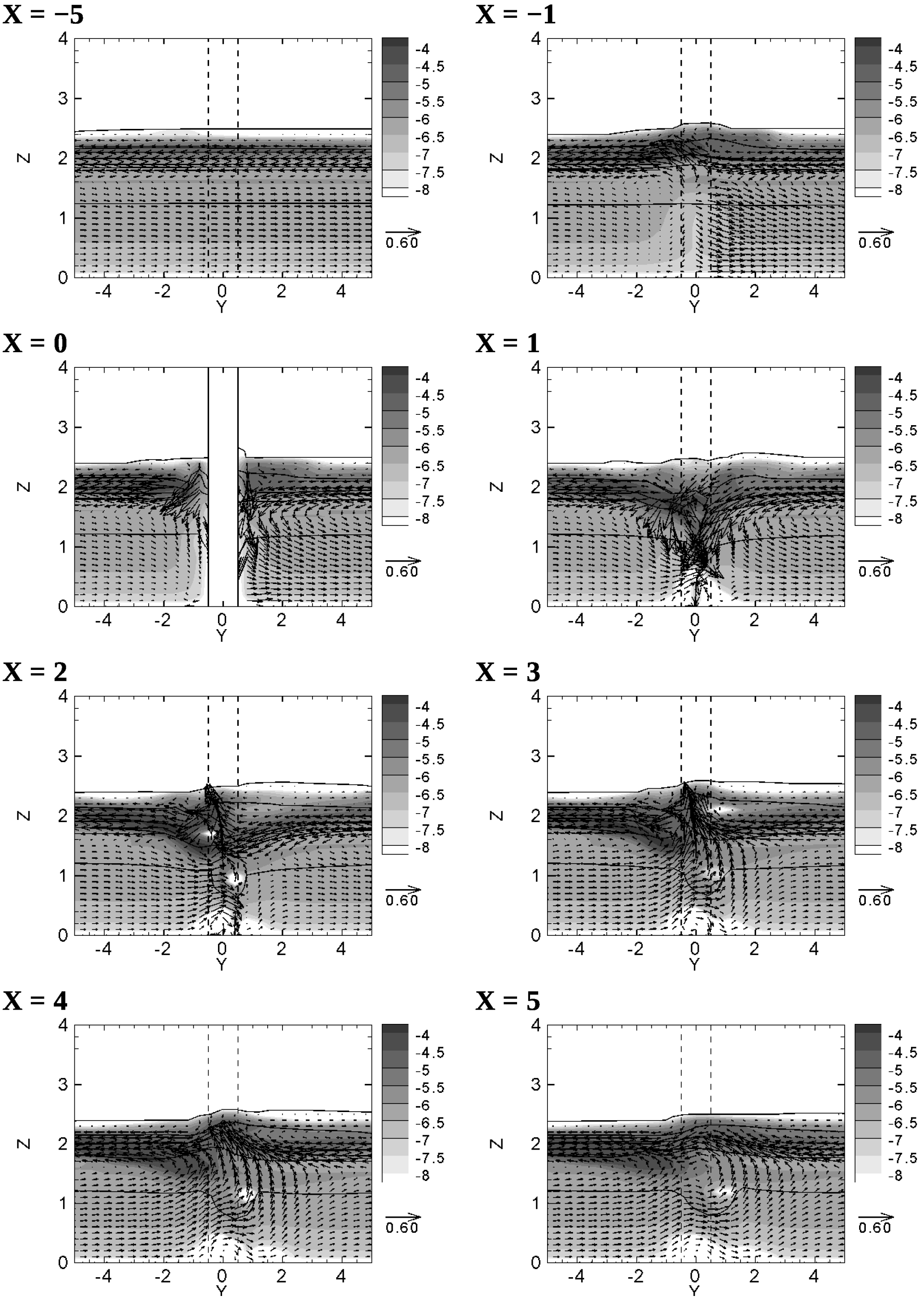

Figure 3.81: Flow field at different cross-sections in front of and behind the cylinder for a density current with Coriolis forces, $Fr = 0.57$, $Re = 2.5 \cdot 10^6$, $D/d = 2$ and $K = 0.92$. Note that in comparison with Fig. 3.75 velocity vectors are equally scaled.

be directed to the left in the cross-sections presented in Fig. 3.81 actually generates a transport to the right in the stream-wise direction.

Due to the strong lateral current within the interface the cylinder wake is deflected to the right (in the downstream direction) and a presentation of cross-sections aligned at $Y = 0$ far away from the cylinder is actually not useful as indicated by the results at $X = 4$ and $X = 5$ showing the rapidly decaying influence of the cylinder. Even closer to the cylinder a sound analysis of the complex flow field based on the cross-sections presented here is also not possible and requires a different methods which were not undertaken within this project.

Some basic features can be extracted from the results in Fig. 3.81.

The lifting of the interface in front of the cylinder at $X = -1$, the resulting strong downward currents around the cylinder at $X = 0$, $X = 1$ and $X = 2$ and the succeeding upward current at $X = 2$ and $X = 3$ can be clearly identified. The motion of the interface and the induced vortices caused by the vertical currents can also be detected and seem to be to be laterally transported like the increased buoyancy production within the interface due to the cylinder.

The complexity of the flow field suggests that the patterns of entrainment rates are also more complicated than the situation without Coriolis forces. This can be seen in the following 2 figures which show the influence of the Froude number (fig. 3.82) and the Ekman number (Fig. 3.83) on the local entrainment. In both figures the left column is for $D/d = 2$ and the right column for $D/d = 1$.

Before the results are discussed it is mentioned that these 2 figures show the cylindrically induced and not the total entrainment. This aids in the discussion since the natural entrainment varies with the Froude and Ekman numbers. One further sees that the lowest contour was set at $E = 10 \cdot 10^{-5}$ and not $E = 0$. This is due to the fact that in some simulations some mostly minor entrainment occurs which was reproducible but did not appear to be physically realistic. This lower limit removed these anomalies in most cases. In two cases further anomalies were removed manually.

The entrainment rates nicely reflect the deflection of the cylinder wake to the right as expected from the discussion of the flow field above. As the lateral velocities due to Coriolis forces increase with the current speed and thus the Ekman number the deflection increased with increasing Ekman number. Comparison of the left and right columns show that the extent of the entrainment is lower for the higher blockage ($D/d = 1$) when compared with $D/d = 2$. This effect becomes less pronounced with increasing Froude number.

This effect is attributed to the increase of the flow velocity with increasing Froude number and is therefore not observed in fig. 3.83 where the Froude number is constant. It is unclear why the blockage effect at the lowest Ekman number $K = 0.4$ shows a counter trend to the other results.

It is also not totally clear why there is increased entrainment directly behind the

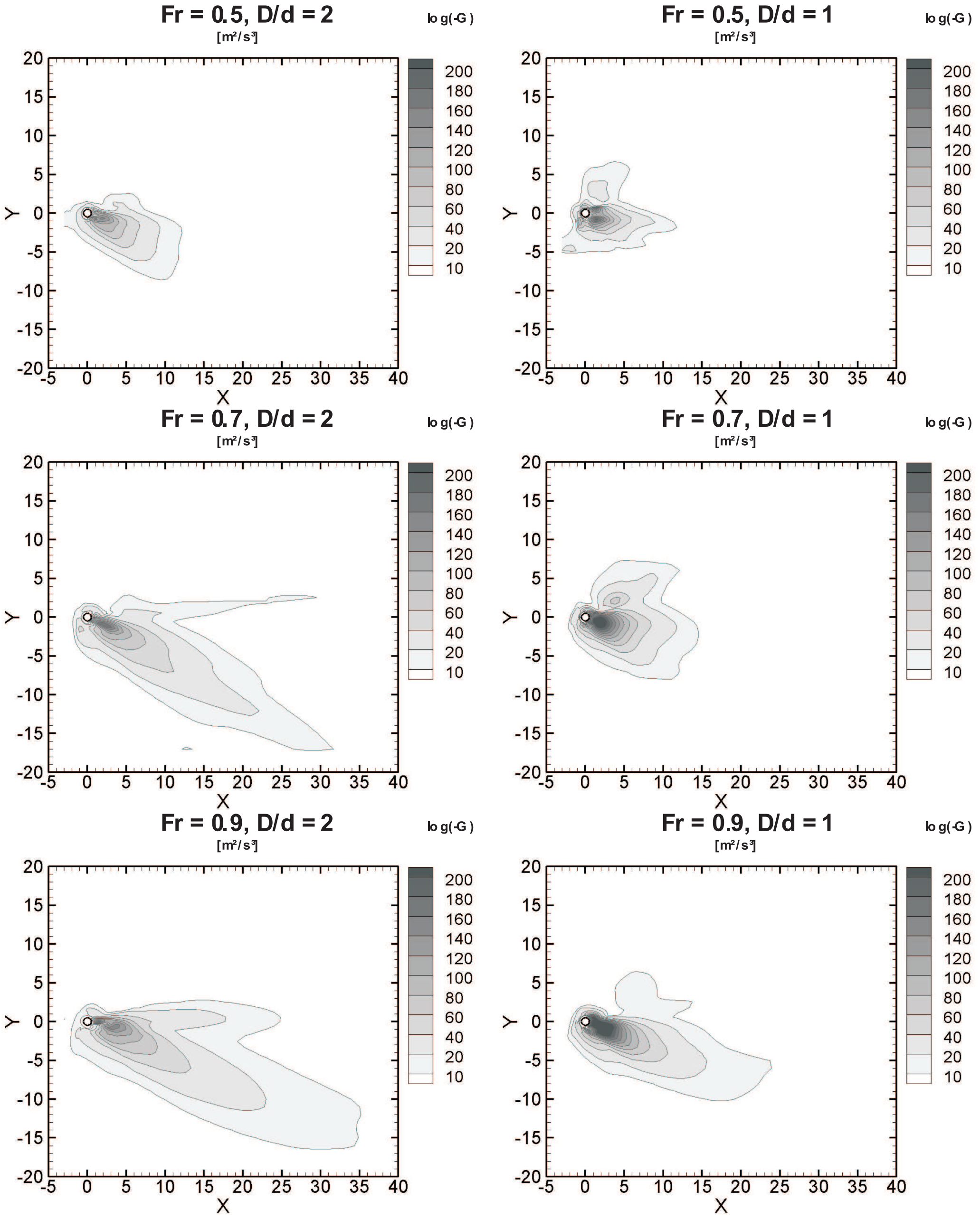

Figure 3.82: Influence of Coriolis forces on entrainment for different Froude numbers, different aspect ratios D/d and a constant Ekman number $K = 0.8$; left column: $D/d = 2$, right column $D/d = 1$.

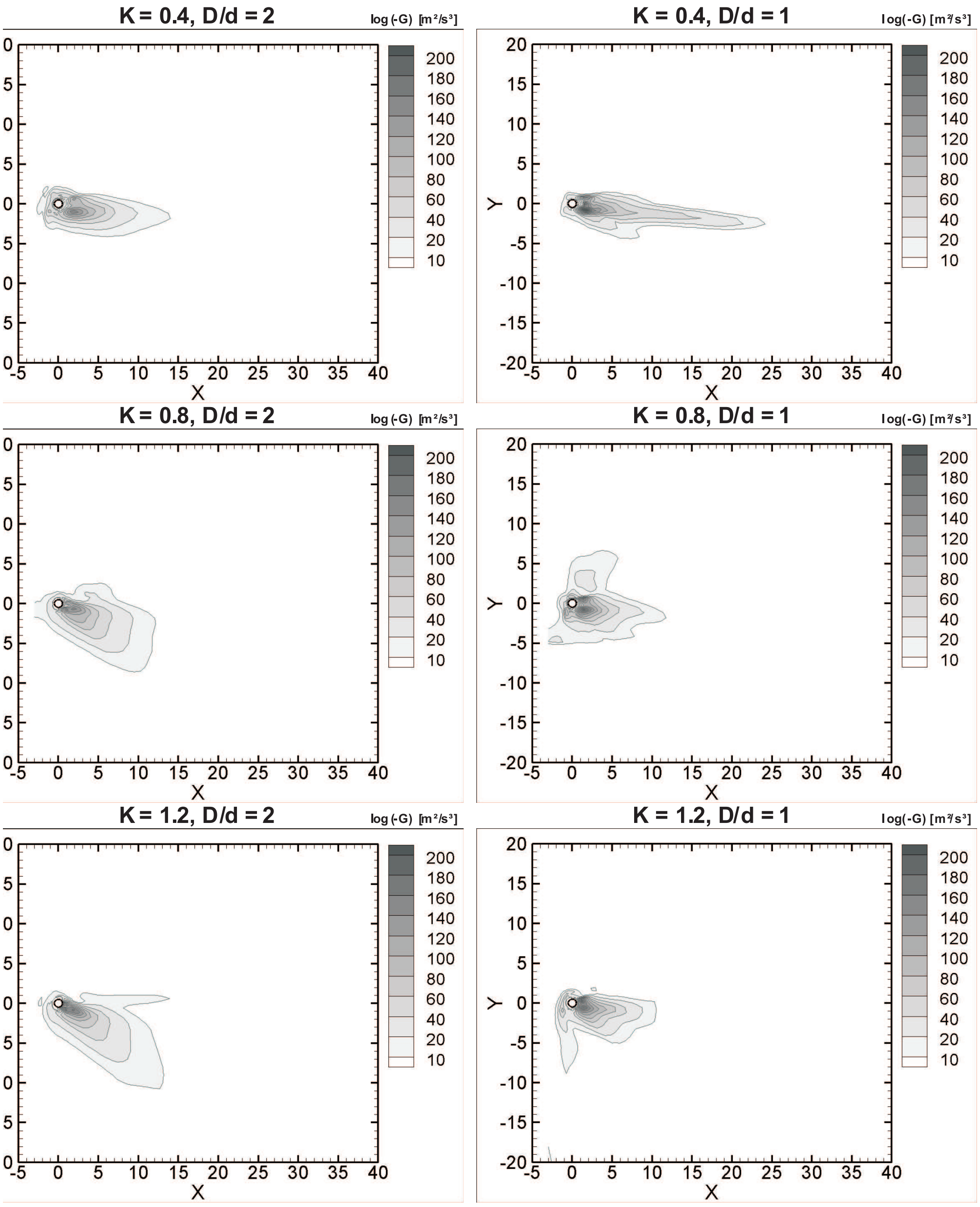

K = 0.4, D/d = 2

K = 0.4, D/d = 1

K = 0.8, D/d = 2

K = 0.8, D/d = 1

K = 1.2, D/d = 2

K = 1.2, D/d = 1

Figure 3.83: Influence of Coriolis forces on entrainment for different Ekman numbers, different aspect ratios D/d and a constant Froude number $Fr = 0.5$; left column: $D/d = 2$, right column $D/d = 1$.

cylinder. This can be particularly observed for $D/d = 2$ at higher Froude numbers and for $D/d = 1$ at lower Froude numbers. It appears that this is due to the vertical velocity profile in the lateral direction through which the flow below the density interface is directed towards the left. The interaction between this flow and the cylinder structure generates the observed complicated flow patterns behind the cylinder.

Fig. 3.82 and Fig. 3.83 clearly show that the local entrainment distribution is not as clearly defined as for the case without Coriolis forces. Nevertheless it is clear that the mixing which takes place in the presence of Coriolis forces is limited to a small reached measured in relatively few diameters from the cylinder with values on the order of $E = 2 \cdot 10^{-3}$, i.e. two orders of magnitude higher than the natural entrainment rates. This statement does not essentially change when the lower limit for the lowest contour level for E is reduced. The main area of influence is still limited to a small reached measured in relatively few diameters from the cylinder. The effect of the cylinder on entrainment is then, however, numerically somewhat higher. The choice of the lowest contour level for E is therefore not considered to be of major significance for the qualitative evaluation of the mixing phenomena. This should, however, be considered in a quantitative analysis (see below).

Even if the area of influence of the cylinder is considerably different for the two cases the absolute entrainment rates are very similar and comparable to those found for the corresponding cases without Coriolis forces above. This significantly improves the credibility of the foregoing results which before might have seemed questionable for the simulation of purely two-dimensional undisturbed currents.

3.2.9 Total Entrainment

In the preceding sections the principal effect of a circular cylinder on the flow field, entrainment rates and mixing efficiencies of a density current has been analysed and the influence of the individual parameters governing the flow has been thoroughly investigated. An analysis of the overall impact of the cylinder on the dilution follows.

The total entrainment induced by the cylinder E_{cyl} is found by integrating the local entrainment rates over the area of influence of the cylinder indicated by the contour plots shown in the preceding sections. This value seems to be rather abstract at first. It is, however, the essential parameter in this study as it allows a reduction of the results of the non-dimensional parameter study to a single value which then can be used to quantitatively evaluate the influence of a Monopile on mixing in the range of the parameters studied ($0.4 \leq Fr \leq 0.9; 0.4 \leq K \leq 1.2$ and $1 \leq D/d \leq 2$). In this way one can directly globally estimate the influence of wind farms on mixing in the Baltic Sea and also present a parametrisation for mixing for use in a large

scale Baltic Sea model.
The lowest contour levels for the case without Coriolis forces were chosen by intention to correspond to the natural entrainment rates of the undisturbed current such that the additional amount due to the presence of the cylinder is clearly identified. However, without the presence of the cylinder the current would still be diluted by the natural entrainment rates which have therefore first to be subtracted from the results presented above before integrating.
The corresponding total additional entrainment rates due to the cylinder are shown in Fig. 3.84 as a function of the Froude number for the non-rotation case. Each of the individual points corresponds to one specific case and the results for the different aspect ratios can be distinguished by the various symbols. The clustering of the individual points reflects the negligible influence of the Reynolds number previously discussed. The curves represent some kind of entrainment law which will be discussed below. They have been added primarily in order to better visualise the results and to simplify their interpretation. The data suggests the general form of

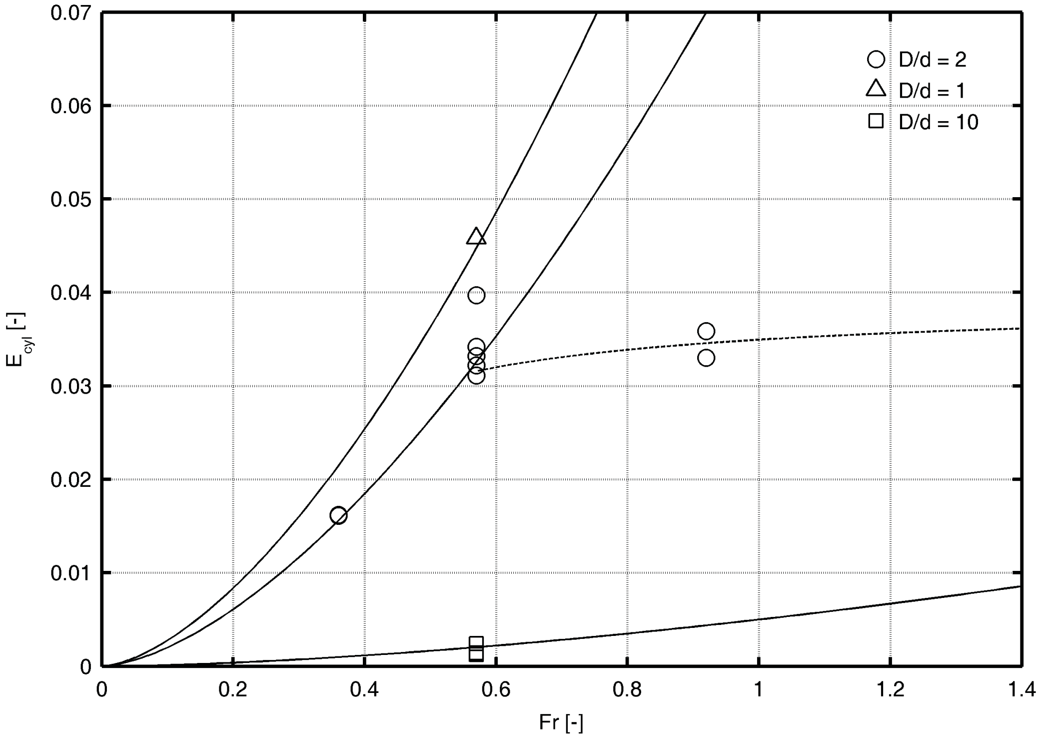

Figure 3.84: Total entrainment induced by a circular cylinder as a function of the Froude number without Coriolis forces.

this law being exponential:

$$E_{cyl} = m_2 e^{(n_2 D/d)} \tag{3.22}$$

The curves in Fig. 3.84 represent the attempt to provide some kind of entrainment law for the present configuration which might at least be valid for the low Froude number range. The data suggests this law to be of the same form like the general entrainment law for undisturbed density currents given by

$$E = mRi_b^{-n} \tag{3.23}$$

Schimmels (2008) which in terms of the Froude can be written as:

$$E_{cyl} = m_l Fr^{n_l} \tag{3.24}$$

From the data for $D/d = 2$ the parameters could be determined to be $n_1 = 1.6$ and $m_1 = 0.08$. For the lack of further data the exponent n_1 was assumed to be independent of the aspect ratio and the other curves were fit through the (single) data points by adjusting the parameter m_1 only, which is found to be $m_1 = 0.11$ for $D/d = 1$ and $m_1 = 0.005$ for $D/d = 10$.

At first sight the curves seem to be a reasonable approach showing that the total additional entrainment induced by the cylinder increases with Froude number. This is consistent with the local entrainment rates discussed above (cf. fig. 3.77) which also increased from $Fr = 0.36$ to $Fr = 0.57$. However, it was also found that for the higher Froude number $Fr = 0.92$ the maximum local entrainment rates in the near wake decrease again while the rates farer away are higher due to a more homogeneous flow field. In consequence, the integrated total entrainment rates do not increase further as suggested by the full curves but seem to approach a maximum value represented by the dashed line.

While the increase of the cylinder induced entrainment for low Froude numbers seems comprehensible, justifying the appliance of eq. 3.24, the cause of the observed effect found for higher Froude numbers is less clear. It might well be the case that the assumption of an asymptotic behaviour for higher Froude numbers is not correct and the entrainment rates will even decrease which, however, can only be clearly judged with additional data. It is therefore inadvisable to provide a mathematical relationship for this effect at this point but in it is assumed at this point that the increase of the cylinder induced entrainment with the Froude number is limited to the lower Froude number range and will quickly approach a maximum value.

It can be expected that the same behaviour also occurs for the other aspect ratios. Unfortunately this assumption cannot be verified here due to the lack of data emphasising the strong need for a complementation of the present dataset. However, as could be expected from the lateral distribution of the entrainment rates in Fig. 3.79, the present data suggests that the total entrainment by the cylinder increases with decreasing aspect ratio (increasing blocking ratio). To allow for a better interpretation of this effect the data has been plotted as a function of the current depth to cylinder diameter ratio in Fig. 3.85 where the curves again represent an entrainment law in terms of the aspect ratio.

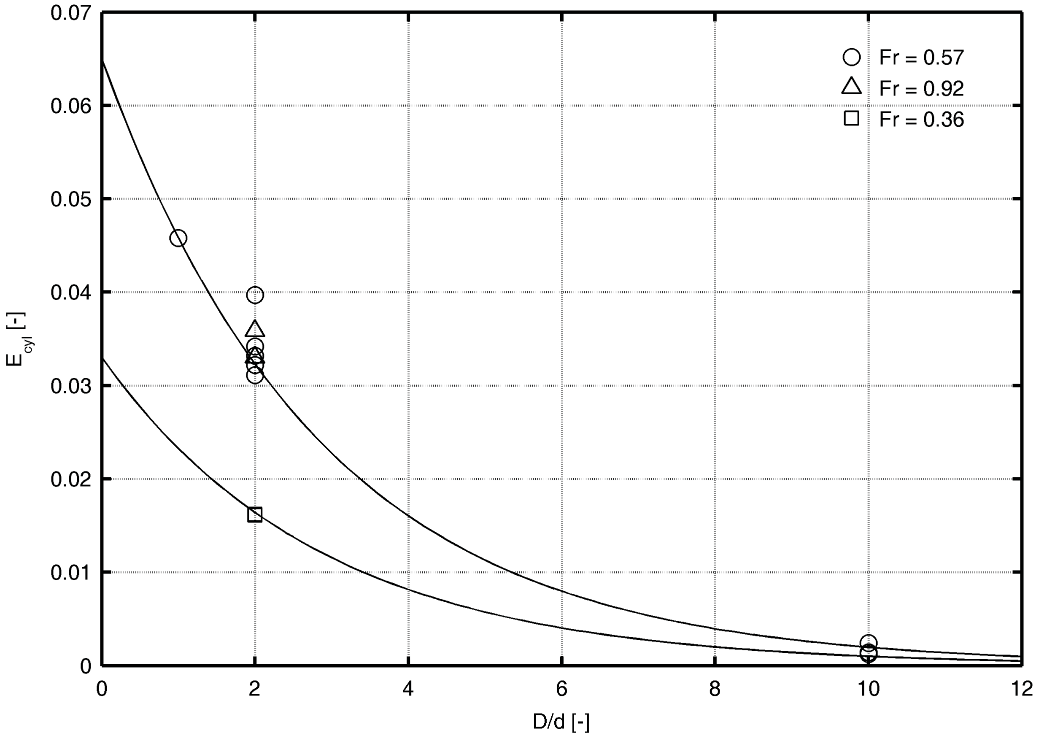

Figure 3.85: Total entrainment induced by a circular cylinder as a function of the current depth to cylinder diameter ratio.

and the parameters found by a fit through the results for $Fr = 0.57$ are $n_2 = -0.35$ and $m_2 = 0.065$.As the increase of entrainment with the Froude number is limited, the parameters for $Fr = 0.92$ are assumed to be the same, with a possibility of a slightly higher value for m_2. The slope n_2 was assumed to be valid for all Froude numbers and the curve for $Fr = 0.36$ was found by only adjusting m_2, which yielded $m_2 = 0.033$.
Although the curves seem to represent the present data very well and nicely show the decrease of entrainment with increasing aspect ratio, the parameters (at least for $Fr = 0.36$) should be verified by additional data. It should also be noted that the entrainment law (eq. 3.22) loses validity for $D/d \to 0$ as at the limit entrain-

ment will naturally vanish and not reach a finite value as shown in Fig. 3.85. Thus, it might be interesting further to investigate the effect of the cylinder for very low aspect ratios in order to assess the ratio with the maximum effect, but also this is left as a task for future work.
Fig. 3.86 shows the influence of the Coriolis forces on E_{cyl}; and presents the dependence of E_{cyl} for different Ekman numbers for the cases of $D/d = 1$ (full lines) and $D/d = 2$ (dotted lines).

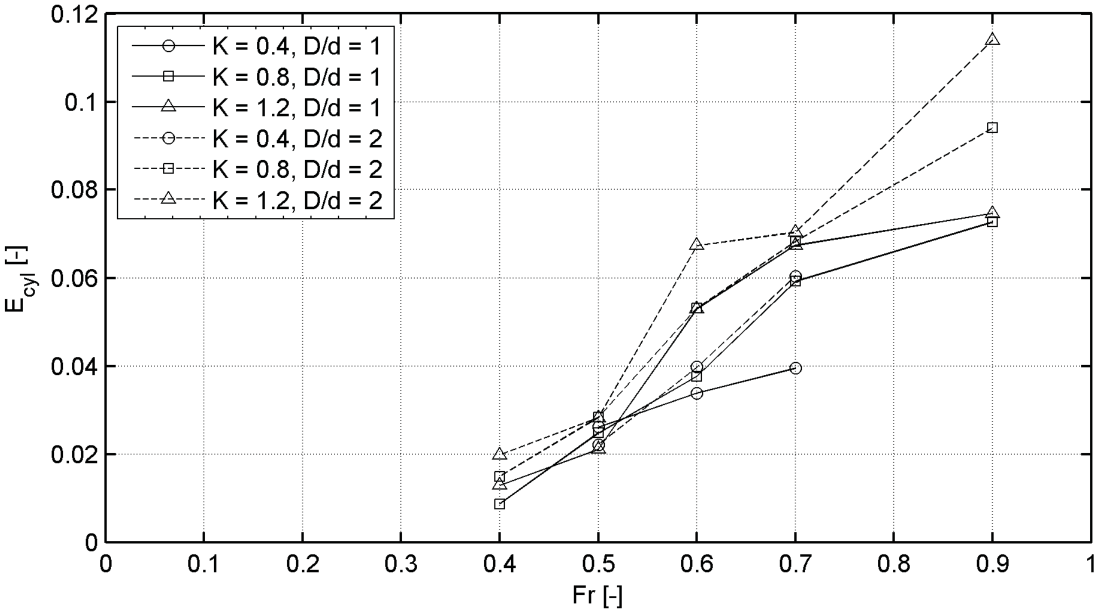

Figure 3.86: Total cylinder induced entrainment rate E_{cyl} as a function of the Froude number for different Ekman numbers.

It clearly shows that the cylindrically induced mixing increases with the Froude number. This is a logical consequence of the result of a reduction of the density induced turbulence damping with increasing Froude number. In addition the entrainment is higher with increased Ekman number although this effect is not so pronounced as the influence of the Froude number. Even if the curves are close together it appears that the total cylindrically induced entrainment is higher for $D/d = 2$ as for $D/d = 1$. This may appear at first strange since that appears to apply that for a given density layer mixing increases for smaller cylinder diameters. That is, however, not the case as the cylinder diameter is also incorporated in the dimensionless parameter E_{cyl}. This will be demonstrated with the following equations and a numerical example.
The total amount of entrained ambient fluid into an undisturbed density current

can be given by

$$Q_{nat} = U_s \cdot E_{nat} \cdot A \tag{3.25}$$

where U_s is the current speed, E is the natural entrainment rate of the current and A is the surface area over which the ambient fluid is entrained. The corresponding absolute amount of entrainment due to the cylinder is

$$Q_{cyl} = U_s \cdot E_{cyl} \cdot d^2 \tag{3.26}$$

where the factor d^2 reflects the fact that the total entrainment rate E_{cyl} given above was found by integration over an area normalised by the cylinder diameter. Fig. 3.87 shows the cylindrically induced flow Q_{cyl} as a function of the Froude number for a 10 m density layer. Two cylinders are compared, namely $d = 10$ m ($D/d = 1$) and $d = 5$ m ($D/d = 2$). It clearly shows that for the same Ekman number the entrainment rate for the 10 m diameter cylinder is higher than that for the 5 m cylinder.

The influence of the cylinder on mixing can be further quantified by comparing the cylinder induced to the natural entrainment. This is done by combining eqs. 3.25 and 3.26.

$$\frac{Q_{cyl}}{Q_{nat}} = \frac{E_{cyl}}{E_{nat}} \cdot \frac{d^2}{A} \tag{3.27}$$

The first term on the right hand side represents the actual impact of the cylinder as it defines the entrainment per unit area related to the natural entrainment without the presence of a cylinder. The corresponding values for the parameters investigated here are given in tab. 3.6, for the case without Coriolis forces where the values in brackets have been extrapolated using Fig. 3.85. The corresponding values for the case with Coriolis forces are given in tab. 3.7. These tables show that the cylinder induced entrainment is in the range of three orders of magnitude higher than the natural entrainment. Although this appears at first glance to be large it is important in the context of total impact to consider that the natural mixing occurs over the total interstitial area of the density current whereas the increased cylindrically induced entrainment is restricted to a reach of diameters from the

	$Fr = 0.36$	$Fr = 0.57$	$Fr = 0.92$
$D/d = 1$	(1130)	920	(330)
$D/d = 2$	800	650	230
$D/d = 10$	(40)	30	(10)

Table 3.6: Total impact of a circular cylinder on a density current in terms of relative entrainment rates per unit area (E_{cyl}/E_{nat}) without Coriolis forces.

Fr	**0.4**		**0.5**			**0.6**			**0.7**			**0.9**	
K	**0.8**	**1.2**	**0.4**	**0.8**	**1.2**	**0.4**	**0.8**	**1.2**	**0.4**	**0.8**	**1.2**	**0.8**	**1.2**
$D/d = 1$	723	864	1633	1181	845	1473	1215	1558	1129	1377	1404	909	858
$D/d = 2$	1241	1323	1384	1350	1131	1728	1712	1981	1725	1588	1466	1176	1310

Table 3.7: Dependence of the cylinder induced entrainment rate to the natural entrainment rate E_{cyl}/E_{nat} for different Ekman numbers.

cylinder.
An offshore wind park consists of numerous units which are spaced far from another. As such, the influence of the wind park on the entrainment is significantly dependent on the diameter of the individual piles and their spacing measured in diameters. This is illustrated by a numerical example for a density current with $D = 10$m, a Froude number $Fr = 0.5$ and an Ekman number $K = 1.2$. The wind park is assumed to have monopiles with a diameter $d = 5$ m and a spacing of $50d$ (250 m). It is noted here that the spacing is generally considerably greater than $50d$. From the spacing $A = 250 \cdot 250 = 62500$ m^2 and from tab. 3.7 $E_{cyl}/E_{nat} = 1.131$. From eq. 3.27 $Q_{cyl} = 45\% Q_{nat}$.
This result can be generalised if one replaces the area A in the eq. 3.27 with

$$A = (Nd)^2 \tag{3.28}$$

where N is the spacing in the number of diameters d, yields

$$\frac{Q_{cyl}}{Q_{nat}} = \frac{E_{cyl}}{E_{nat}} \cdot \frac{1}{n^2} \tag{3.29}$$

This states that the influence of the cylindrically induced mixing decreases with N^2. Eq. 3.29 is given in Fig. 3.88 were the fat lines represent the extreme values in tab. 3.7, namely $E_{cyl}/E_{nat} = 1981$ and 723. All of the other cases (thin lines) are between these two limits. The numerical example is generalises with the thin dotted cure from which one can directly read $Q_{cyl}/Q_{nat} = 45\%$ for $N = 50$. In order to double the entrainment for this case the spacing would need to be reduced to $N = 34$. Even for the highest mixing ($Fr = 0.6$; $K = 1.2$ and $D/d = 2$ (fat full line), a distance of less than $45d$ is necessary to double the natural mixing. For a realistic spacing of 500 m, the entrainment would increase in the worst case by less than 20%. In summary Fig. 3.88 shows that for a spacing $> 50d$ the ratio of the cylindrically induced to natural entrainment $Q_{cyl}/Q_{nat} < 1.0$; for a spacing $> 70d$ is $Q_{cyl}/Q_{nat} < 0.5$ and for a spacing $> 100d$ is $Q_{cyl}/Q_{nat} < 0.2$. These values will normally always be reached for wind farms.

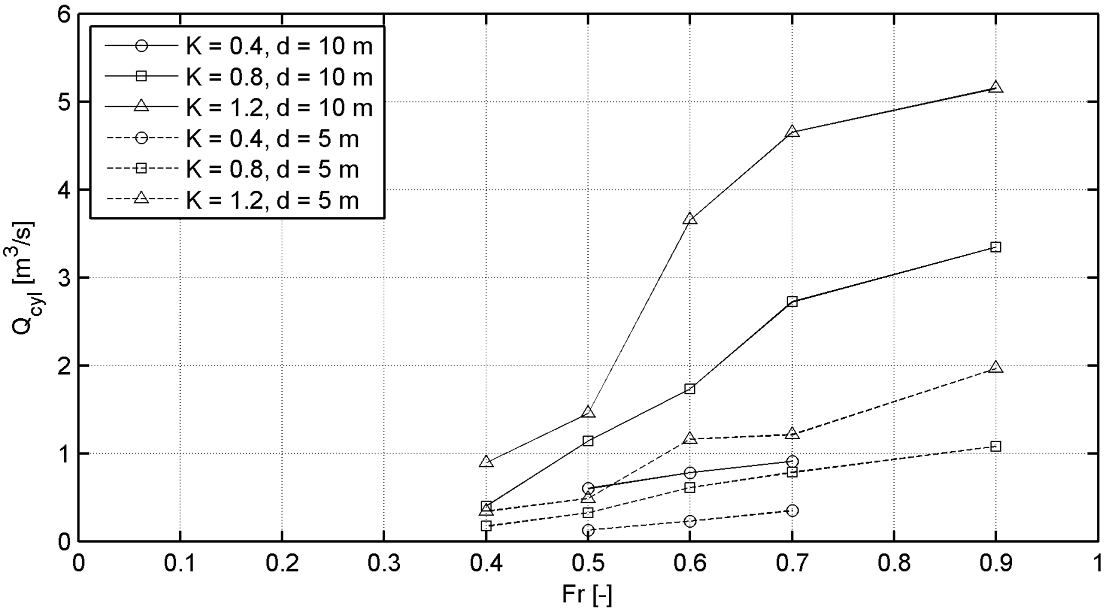

Figure 3.87: Total cylinder induced entrainment Q_{cyl} as a function of the Froude number for different Ekman numbers and cylinders diameters$D = 10$.

A final comment is made here on the effect of the assumption that the lower limit for the evaluation of the entrainment for the case with Coriolis forces was set at $E = 10 \cdot 10^{-5}$. As such the statement is justified that this assumption could lead to an underestimation of Q_{cyl}. Based on the above one can see that even if Q_{cyl} is increase by 50%, which is not the case, the entrainment induced by wind farms appears to be minimal. This is due to the spacing in the wind park and the fact that the area affected by a single Monopile is local and relegated to a small number of diameters from it.

These results give a good estimation of the total effect of entrainment for planed wind farms in the Baltic Sea. The parametrisation can be used as the basis for a more detailed far field analysis using the IOW Baltic Sea model.

3.3 Small-scale in-situ observations (IOW)

While it is evident that vertical mixing may be enhanced in the turbulent wake of the vertically oriented cylinders pylon, internal waves radiated by both the pylon itself and by its wake may enhance the energy level of the natural internal wave field in the environment of the pylon. Turbulence in natural waters below the surface mixed layer occurs in intermittent patches due to pelagic and benthic disintegration

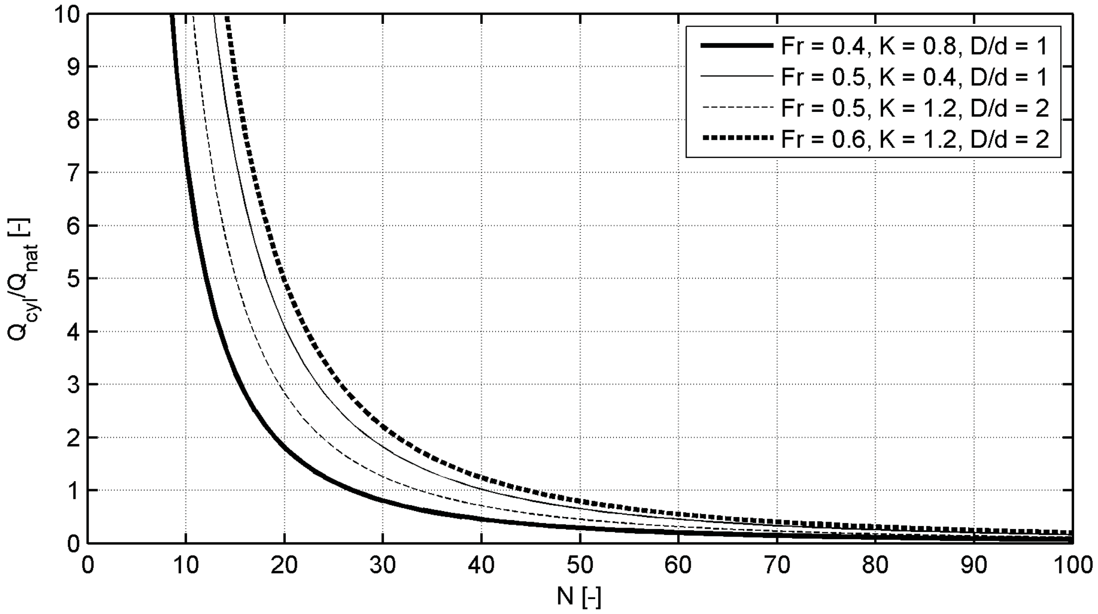

Figure 3.88: Dependence of the cylinder induced mixing to natural entrainment (E_{cyl}/E_{nat}) as a function of the normalised distance between the structures, N based on extreme values.

of internal waves. The general view is that the interaction of internal waves cascades energy to small scales, where it subsequently supports turbulence in the ocean interior (*McComas and Müller*, 1981). Therefore, radiation of internal waves from an artificial pylon in a natural flow may provide additional energy for dissipation of turbulent kinetic energy and vertical mixing in the remote neighbourhood of the pylon.

In this section, evidence of enhanced mixing downstream of a pylon in a moving stratified fluid based on measurements of backscattering and dissipation of turbulent kinetic energy carried out by *Lass et al.* (2008) are presented.

Since no wind power plants are presently established in the saltwater paths of the Baltic Sea, *Lass et al.* (2008) chose to study the pylons of the Western Bridge of the Great Belt Fixed Link, a box girder bridge between the Danish islands Fyn and Sprogø. At first it was planned to investigate ship wrecks, but suitable wrecks could not be identified. *Lass et al.* (2008) used bridge pylons instead as a model of natural scale to study whether pylons in a moving stratified flow enhance vertical mixing. This bridge crossing the Great Belt (the largest of three straits connecting the Kattegat to the Baltic Sea) was constructed under the zero-solution concept (see *Farmer and Møller* (1989)), which requires that any impact of the bridge on the mass and salt flow through the cross section of the Great Belt at the position of the bridge was compensated by corresponding artificial changes of the natural cross section.

There are numerous studies on the flow pattern of homogeneous water around a circular cylinder (see for example *Batchelor* (1967)). In non-rotating, unstratified flow, the form of the wake behind the cylinder is determined by the Reynolds number

$$Re = \frac{Ud}{\nu} \tag{3.30}$$

where U is the undisturbed flow speed, d the diameter of the cylinder, and ν the kinematic viscosity of the fluid.

At low Re the flow is fully attached to the cylinder as a potential flow. At medium Re, eddies form immediately behind the cylinder as counter-rotating pairs. At larger Re, eddies spin off behind the cylinder in a vortex street. The frequency f_e at which the eddies spin off from the cylinder is related to the Strouhal number St (which is about 0.22):

$$f_e = St\frac{U}{d}. \tag{3.31}$$

At very large Re the coherent eddies in the vortex street collapse into a continuum of eddies of different sizes.

The pattern of a stratified shear flow around a cylinder has not been investigated before the QuantAS-Off project (see sections 3.2 and 3.1.6 for numerical model results and section 3.1 for laboratory experiments of stratified shear flow around vertical cylinders). A parameter describing the flow pattern in a stratified fluid is, in addition to Re, the relation between the sheared background flow $U(z)$ and the internal wave speed, the internal Froude number, here defined as

$$\mathrm{Fr}(z) = \frac{U(z)}{c_i} \tag{3.32}$$

where c_i is the phase speed of the gravest mode internal wave in a non-rotating frame.

Ekman (1906) showed that a body moving in the thin upper layer of a two-layered fluid generates internal waves that exert maximum wave drag on the body at $\mathrm{Fr} = 0.77$. Many of the studies on bodies moving in a stratified fluid are devoted to cylinders moving with the axis aligned horizontally. *Arntsen* (1998) studied lee waves and hydrodynamical loads of a submerged horizontal cylinder in a layered fluid experimentally and by means of an analytical model. He found the maximum wave drag at $\mathrm{Fr} \approx 0.5$ where the lee waves have maximum amplitude. The analytical model predicts maximum wave drag at $\mathrm{Fr} \approx 0.8$ in case of deep water in accordance with *Ekman* (1906). The length of the lee waves increase with Fr.

When $Re > 10^3$ and $\mathrm{Fr} > 1$, turbulent wakes develop behind such cylinders and the velocity field outside these turbulent wakes consist mainly of internal waves of different categories, namely waves generated by the body itself and waves produced by the turbulent wake, see *Xu et al.* (1995).

Chashechkin and Mitkin (2001) observed a complex interaction between the internal waves radiated by the moving body itself and the travelling vortices, which may lead to chaotic wave patterns with increasing distance from the body. However, interfaces characterised by strong stratification can bind the elements of the vortex street in a continuously stratified fluid.

Investigations of vertical cylinders extending from the bottom to the surface are by far less common in the literature. The interaction between eddies and internal waves is different compared to a moving horizontal cylinder (see, e.g. *Ozono et al.* (1997)), since eddies with vertical axes do not excite internal waves. Hence, the interaction between eddy streets, the wake of the cylinder, and the internal waves becomes less intense. *Holford and Linden* (1999) have shown that in the wake of vertical cylinders towed through a stratified fluid, the interaction of mostly vertical vorticity with the layered fluid generated several mixed layers at medium *Re*. Entrainment rates into an overflow of a two-layer system caused by obstacles were investigated experimentally by *Møller et al.* (1997). They found that the mixing efficiency of a system with obstacles in the stratified flow was 40% smaller than that without obstacles.

Heywood et al. (1990) found that eddies in the wake of a small ocean island caused cooling of the surface water associated with enhanced chlorophyll concentration, which is evidence of enhanced vertical exchange through the pycnocline in the eddy street behind an obstacle in a stratified flow. In this case, rotational modes of motion may introduce additional properties of the fluid compared with non- rotational hydrodynamics.

3.3.1 Methods

A map of the Western Bridge of the Great Belt Fixed Link between Fyn and the small island Sprogø and its surroundings is given on Fig. 3.89. In this channel-like area, well-stratified water, flowing at up to 1.5 m s^{-1} at a time scale of several days superimposed by semi-diurnal tidal fluctuations is observed in all seasons. Details of the construction of the Western Bridge, the hydrography and the dominating currents in this part of the Great Belt can be found in *Farmer and Møller* (1989). Each bridge pylon from the Western Bridge consists of a rectangular block rising from the bottom to a depth of 3.5 m with a length of 29 m and a width of 7 m (in the centre of the bridge, the length axes of these blocks are turned 25^o counterclockwise from north). On top of this block sit two cylindrical blocks with a diameter of 5 m, of which the southerly is 12 m long and carries the highway bridge, and the northerly is 7 m long and carries the railroad bridge. They are separated by a distance of 10 m above 3.5 m depth. The pylons are about 70 m apart. Due to the orientation of the pylons with respect to the main current direction, the upper northerly, upper southerly, and lower block have effective widths of 7.5 m, 9.6 m, and 18.6 m, respectively. While the bridge pylons themselves are quite similar to those of the planned offshore wind power plants the distance between the pylons is one order of magnitude smaller than those in the wind parks.

Two cruises were performed for this study. The first cruise with R/V Alkor lasted from 24 to 27 January 2006 and the second cruise with R/V Prof. A. Penck went from 3 to 6 April 2006 (see also sect. 1.4.1.5).

CTD chains (*Sellschopp*, 1997) towed behind a ship with a speed of up to 6 knots were used during the first cruise to obtain high-resolution measurements of the upper water column. During the first cruise, two CTD chains were used, one towed from the stern of the ship and the other on the starboard side close behind the bow. Since the CTD chains were not available during the second cruise a Seabird SBE911 CTD mounted in a towed Scanfish was used.

Turbulent kinetic energy dissipation was measured with an MSS 90 descending micro-structure profiler (for details of the profiler see *Prandke et al.* (2000) and section 1.4.1.3). Dissipation profiles were measured along a given track from the slowly moving ship between the surface and the bottom by the freely falling MSS linked to the ship by a slack cable. After arriving at the bottom the MSS was pulled up to the surface and lowered again. This method allowed a sampling interval of about one minute between successive dissipation profiles.

Current profiles were measured from the moving ship by a vessel-mounted 300 kHz ADCP (RD Instruments, see also section 1.4.1.2). A 300 kHz, upward-looking Workhorse ADCP (RD Instruments) was deployed at the 25 m deep bottom north of the Western Bridge in a trawl-resistant bottom mount. Additionally, current profiles were measured by a 600 kHz ADCP (RD Instruments) from a catamaran tethered by a 300 m rope to a bridge pylon during the first cruise.

3.3.2 The hydrodynamic environment of the bridge

3.3.2.1 Stratification

Stratification was measured by two CTD sections aligned parallel to the bridge a few hundred meters from the pylons. One section was located south, the other north of the bridge. The ensembles of salinity, Brunt-Väisälä frequency (BVF), N with

$$N^2 = -\frac{g\partial\rho}{\rho\partial z} = \frac{\partial b}{\partial z} \tag{3.33}$$

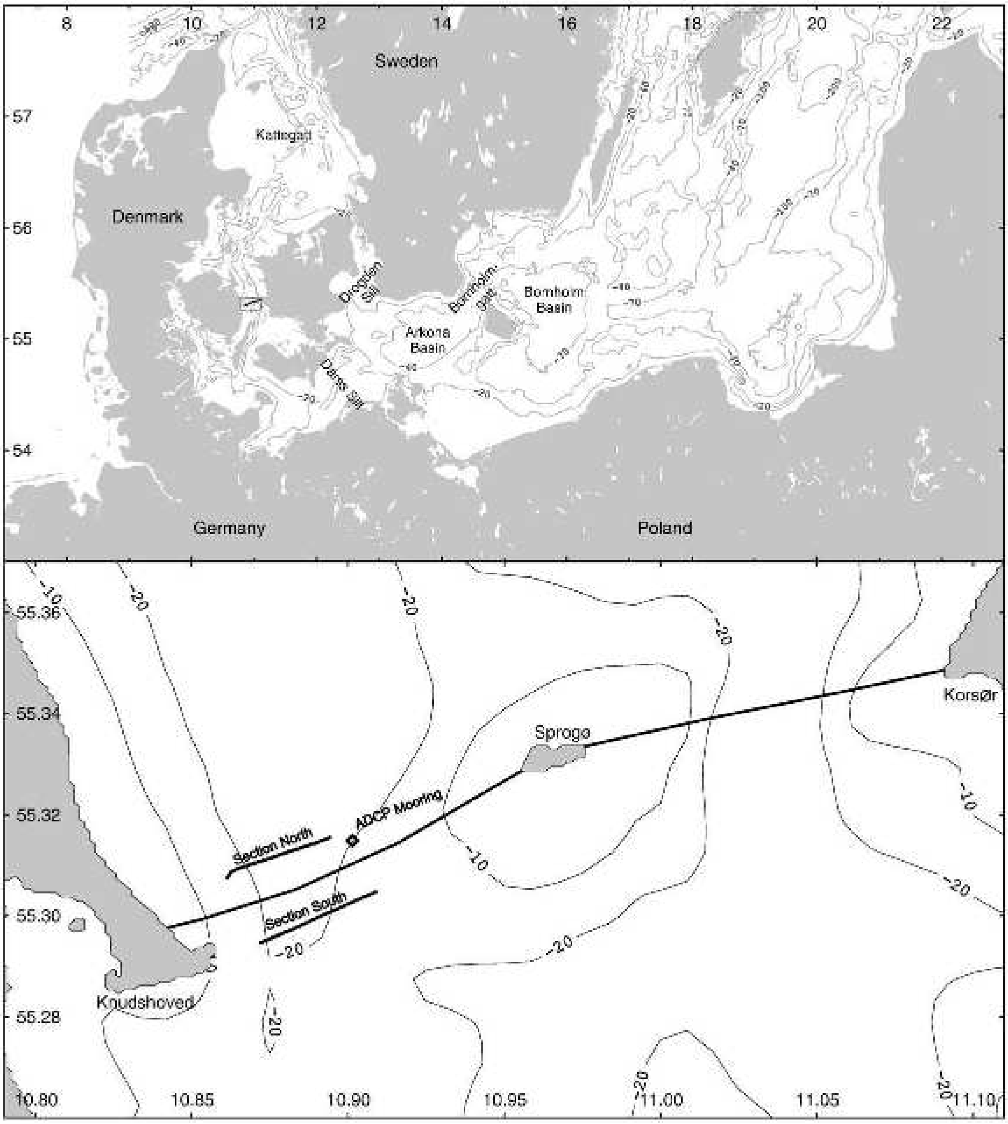

Figure 3.89: Map of the Southern Baltic and the transition zone to the North Sea (upper panel) and map of the Great Belt Fixed Link (lower panel). Depth contours are given in meters. The position of the moored ADCP is indicated by a square and the positions of characteristic tracks of measurements with classical and towed CTD, and dissipation profiler are indicated as black lines. The figure was taken from *Lass et al.* (2008).

(with the buoyancy, b) and density anomaly profiles north and south of the bridge were taken during both cruises. In both cases there is generally a stratification which can be expected in case of an estuarine circulation, namely brackish water in the surface layer and saline bottom water. There are also differences in the stratification in January and April, suggesting that back dating advection and surface mixing processes established differences in the initial stratification at the beginning of each experiment.

During the first cruise, the water column was characterised by a surface layer, a stratified intermediate layer, and a mixed bottom layer. The surface and the intermediate layers were separated by a pycnocline between 5 and about 10 m depth. The bottom water was below approximately 20 m depth. Salinity in the surface layer was slightly higher downstream, while in the intermediate layer, it was significantly lower south of the bridge. The salinity profile of the intermediate layer south of the bridge was rather step-like, while it was fairly smooth north of the bridge. The salinity in the bottom layer south of the bridge was also lower than in the bottom layer north of the bridge, but the difference was smaller than that in the intermediate waters.

Based on the BVF, measured by CTD profiles, the eigen values and eigen functions of the gravest baroclinic vertical dynamic mode (see e.g. *Gill* (1982); *Fennel and Lass* (1989)) of all stations on both sides of the bridge were calculated using a Matlab routine developed by Klinck (available at `http://woodshole.er.usgs.gov/operations/sea-mat/`). The zero-crossings of the first vertical eigen function were all located between 9 m and 13 m depth, and the eigen function depicted opposite directions of the horizontal current in the surface and the bottom layer. The mean of the first baroclinic eigen value of all stations was about $c_1 = 0.6$ m s^{-1} with a standard deviation of about 0.1 m s^{-1}. The corresponding internal Rossby radius $R_1 = c_1/f$ where f is the local Coriolis parameter was $R_1 = 5$ km with a standard deviation of 1 km. No systematic deviations were observed between the eigen values estimated from the CTD profiles north and south of the bridge. The same results were obtained for the estimation of the eigen values during the April cruise. This indicates that rotational effects may occur across the approximately 8 km wide channel formed between the islands of Fyn and Sprogø but not at the scale of the pylons, which are about 70 m apart.

3.3.2.2 Currents

The current regime was characterised by a strong inflow in the upper layer where the southward flow reached up to 80 cm s^{-1} and a weak outflow (northward) in the bottom layer (Fig. 3.90). *Farmer and Møller* (1989) show that this combination of flows is most rare. This general picture was modified by semi-diurnal barotropic and baroclinic tidal fluctuations where the baroclinic tide appears in the zonal current component as internal wave propagating apparently with upward phase speed. This general flow regime was quite similar during both cruises. Fr can be defined locally only in a vertically sheared current. Here Fr is always defined by the current velocity measured at 5 m depth if the depth is not mentioned explicitly. With a maximum flow of up to 0.8 m s^{-1} at 5 m depth, Fr ≤ 1.3 according to eq. (3.32), while $Re \leq 4.8 \times 10^6$ according to eq. 3.30. Here a diameter of 10 m for the bridge pylon is assumed, since the diameter is not unique and varies between 7 m in the upper layers and 19 m in the lower layers. The gradient Richardson number

$$Ri = \frac{N^2}{S^2} \tag{3.34}$$

with the shear squared, $S^2 = (\partial u/\partial z)^2 + (\partial v/\partial z)^2$, was used to find areas of preferred internal wave breaking by Kelvin-Helmholtz instabilities. Ri was calculated from the moored ADCP and the ensemble-averaged BVF north of the Western Bridge, assuming stationary stratification during the deployment of the ADCP. This kind of estimate is quite noisy due to the vertical gradient of the current and the different positions of both the current and stratification measurements. Areas of $Ri < 0.25$ are located permanently in the near-surface layer of the upper 8 m and occasionally in the intermediate layer below 12 m depth. They are apparently associated with the vertical propagating baroclinic tides evident in the measured east component of the current profiles shown in Fig. 3.90. However, these kinds of instabilities cannot account for the enhanced mixing observed downstream of the Western Bridge, since they occurred upstream of the bridge.

Current profiles measured by vessel-mounted ADCP simultaneously with the CTD chain along the tracks north and south of the Western Bridge during the January cruise are shown in Fig. 3.91. They provide information about the vertical and cross-channel structure of the current. The results support the observations made by the bottom-mounted ADCP with respect to the vertical current distribution and with respect to in and outflow.

The cross-channel variation of the current in the upper 15 m was rather weak, while significant cross-channel variation was observed in the bottom layer, obviously caused by the variability of the bottom topography.

3.3.3 The wake of a bridge pylon

Interactions of surface currents in the wake of the bridge pylons with the wind wave field modify the properties of surface gravity waves in the area of the wakes such that they form an optical contrast. Therefore the wakes of the Western Bridge become visible if surface waves are illuminated by sunlight, as shown at

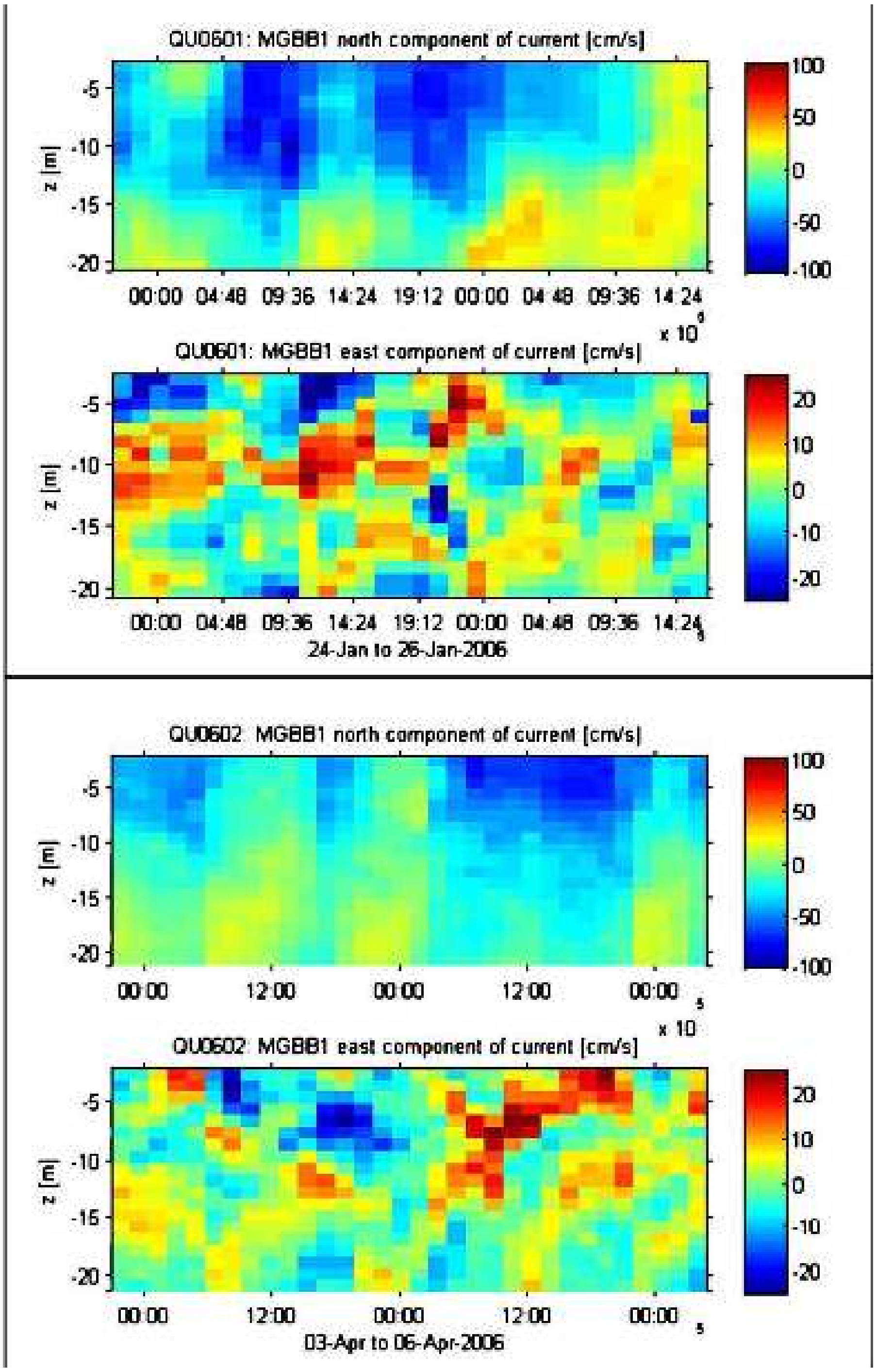

Figure 3.90: North and east component of current, respectively, measured by an ADCP moored north of the Western Bridge of the Great Belt Fixed Link during the January 2006 cruise (upper panels) and during the April 2006 cruise (lower panels). The figure was taken from *Lass et al.* (2008).

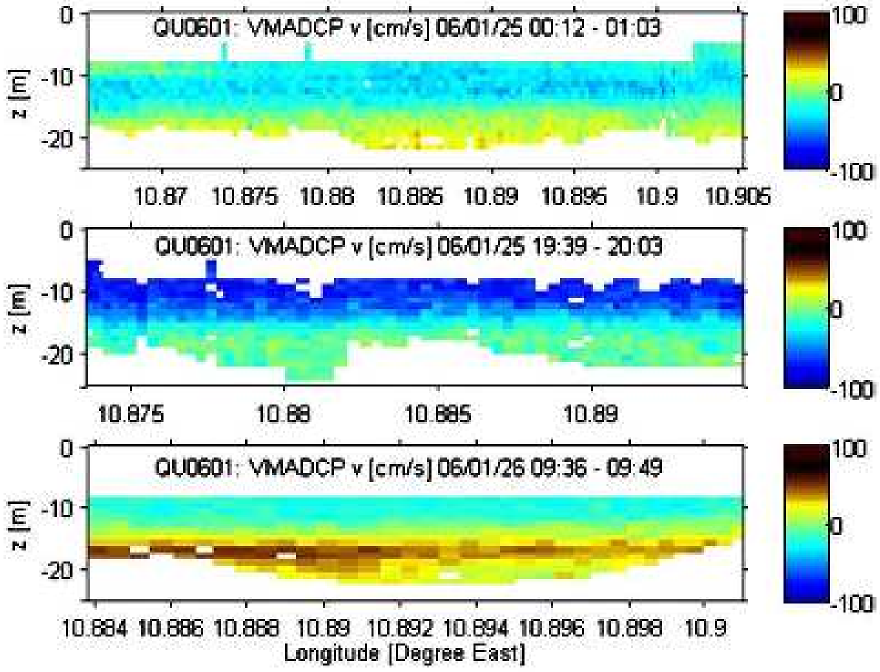

Figure 3.91: North component of velocity measured by the vessel-mounted ADCP on tracks parallel to the Western Bridge of the Great Belt Fixed Link. Upper panel shows the current north of the bridge, middle and lower panels depict currents south of the bridge at different times. The figure was taken from *Lass et al.* (2008).

http://maps.google.com/maps?q=Sprogoe,+Denmark (between the island Sprogø and Nyborg on Fyn using the satellite function at a scale of 50 m). The wakes are visible downstream (northward at the time the image was taken) of each bridge pylon in the centre of the bridge on a length of 4 to 5 times the distance between a bridge pylon (300 to 400 m). This is the most usual situation, according to the results of *Farmer and Møller* (1989). Detailed structures within the wake, however, are not visible on this picture.

3.3.3.1 Eddy streets

In order to study the flow field in the wake of a pylon a catamaran equipped with an ADCP was attached with a 300 m long synthetic rope to a bridge pylon near the centre of the Western Bridge.
In order to study the temporal variations of the current field, a particular period when the catamaran remained relatively stationary was selected (Fig. 3.92). Dis-

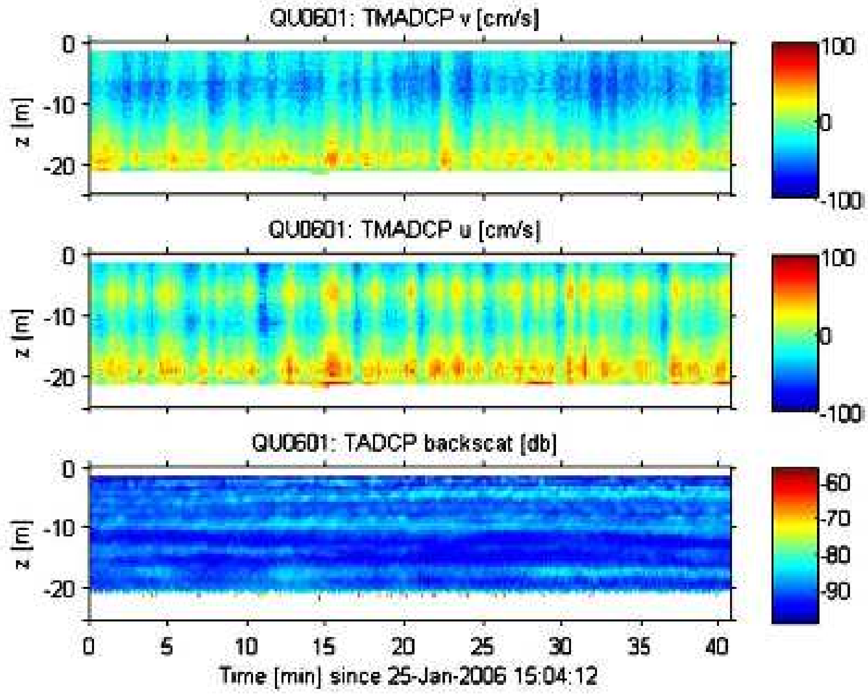

Figure 3.92: North component of the current velocity (upper Panel), east component of the velocity (middle panel), and backscattering intensity measured by an ADCP on a catamaran moored 300 m downstream of a bridge pylon. The catamaran was virtually motionless during the selected time interval. The figure was taken from *Lass et al.* (2008).

turbances were periodically superimposed on the mean current; this was especially visible in the eastward current component with a characteristic period of about 100 s. The EOF analysis of these current measurements revealed that only the first two modes are significant. The first mode was nearly a pure barotropic mode and carried the fluctuations with the 100 s time scale. The real and imaginary parts of the amplitude of the first mode sometimes depicted a 90^o phase shift of changing sign; sometimes no phase shift was observed.

In order to demonstrate the east-west extension of the current disturbances, a time period when the catamaran was moving quite continuously through the wake of the pylon (Fig. 3.93) was selected. The mean current was nearly the same as during the phase shown in Fig. 3.92. Again the disturbances are well exposed in the east component of the current and have a spatial scale of about 10 m, similar to the characteristic diameter of the bridge pylon.

Assuming a 10 m thick bridge pylon and a mean velocity of about 0.5 m s^{-1} a period of eddies shed by the pylon of about $T_e = 100$ s was obtained, according to eq.

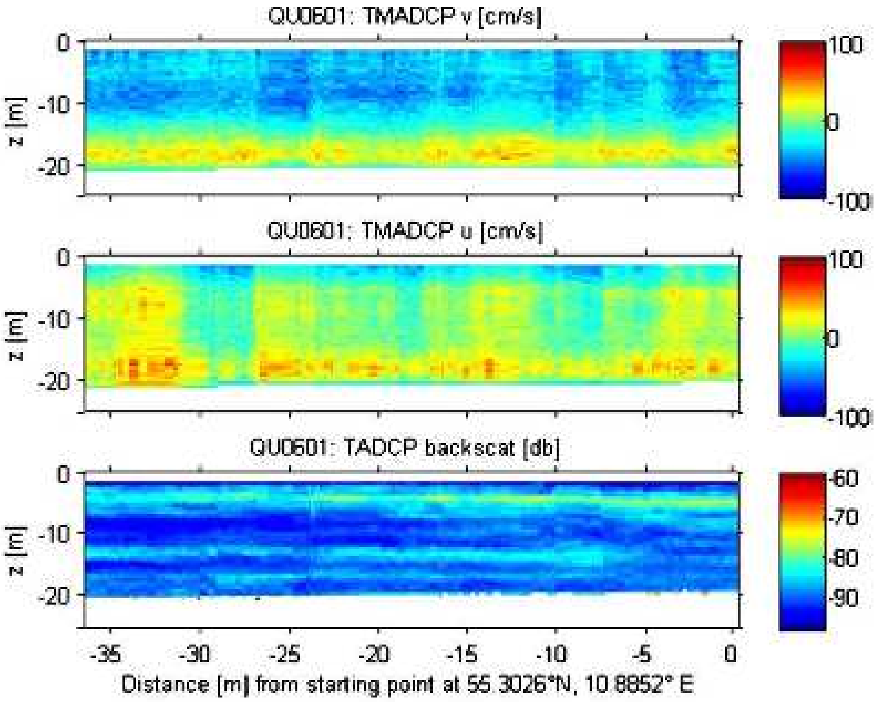

Figure 3.93: North component of the current velocity (upper panel), east component of the velocity (middle panel), and backscattering intensity (lower panel) measured by an ADCP on a catamaran moored 300 m downstream of a bridge pylon. The catamaran was moving in east-west direction during the selected time interval. The figure was taken from *Lass et al.* (2008).

3.31. This agrees quite well with the time scale of the observed current disturbances. Interestingly, this eddy-shedding period is larger than the period of the maximum BVF N_{max} of the water column. This means that besides internal waves excited by the stratified water flowing around the pylon, internal waves can be excited along the whole eddy street in the depth range where the condition $2\pi f_e < N_{max}$ is met, presuming that the eddy street contains a fraction of eddies with a curl which deviates from the vertical direction. It is assumed that the phase velocity of the gravest internal wave mode is

$$c_i = H\bar{N}/\pi \tag{3.35}$$

where H is the water depth and $\bar{N}$ is the vertically averaged BVF (see e.g. *Fennel and Lass* (1989). From eqs. (3.31), (3.32), and (3.35), *Lass et al.* (2008) obtained the range of the Fr at which the von Kármán eddies in the wake of a pylon can excite internal waves,

$$\mathrm{Fr} \leq \frac{1}{2St}\frac{N_{max}}{\bar{N}}\frac{d}{H} \qquad (3.36)$$

with the diameter of the Western Bridge pylons d, the water depth H, and the BVF profiles near the bridge are such that internal waves can be excited by the eddies in the wake of the bridge pylons for $\mathrm{Fr} \leq O(2)$ during the January cruise and $\mathrm{Fr} \leq O(3)$ during the April cruise.

3.3.3.2 Enhanced mixing in the wakes of the bridge pylons

Several tracks with a towed CTD chain were performed parallel to the bridge on its northern and southern sides. Eight tracks were performed north of the bridge; the flow was southward in the upper 15 m and Fr ranged between 0.25 and 1.0 at 5 m depth. All tracks north of the bridge depicted the same general stratification as measured by the conventional CTD. Small-scale perturbations of the pycnocline, which can be interpreted as internal waves, were frequently observed in the western part of the tracks Fig. 3.94. The typical length of these waves was somewhat less than 25 m.

Four tracks were performed south of the bridge. The current at 5 m depth upstream of the Western Bridge was southward at 79 cm s^{-1}. This corresponds to Fr = 1.3. Although the north-south distance between the tracks is only about 500 m, which is about $R_1/10$, the patterns of temperature and salinity structure of both tracks are quite different in both the general and fine structure. The northern tracks were all characterised by a well-mixed layer in the upper 5 to 7 m of the water column, while the southern tracks all depicted a diffusive upper mixed layer, suggesting that warmer saltier water from the pycnocline was mixed into the upper mixed layer. Moreover, the fine structure of the stratification disturbances was different from that of the northern sections, as well. The characteristic fine-scale pattern on the southern tracks consists of pulse-like, increasing salinity and temperature in the surface layer, and lowered salinity at the same location in the intermediate layer. The characteristic horizontal scale of these pulses is about 70 m (Fig. 3.95).

Another ensemble of seven CTD chain tracks was performed south of the bridge, when the upstream, measured surface current was southward at about 13 cm s^{-1} (Fr = 0.22). On these tracks the short starboard CTD chain was deployed just behind the bow of the ship. A well-mixed layer was observed along these tracks with a thickness of about 10 to 14 m. The disturbances of the pycnocline were much less dramatic than those observed on the evening before. They showed deviations characteristic of internal waves.

During the April cruise with R/V Prof. A. Penck the CTD chain could not be used; instead the Scanfish-CTD system in the near surface layer along a few tracks

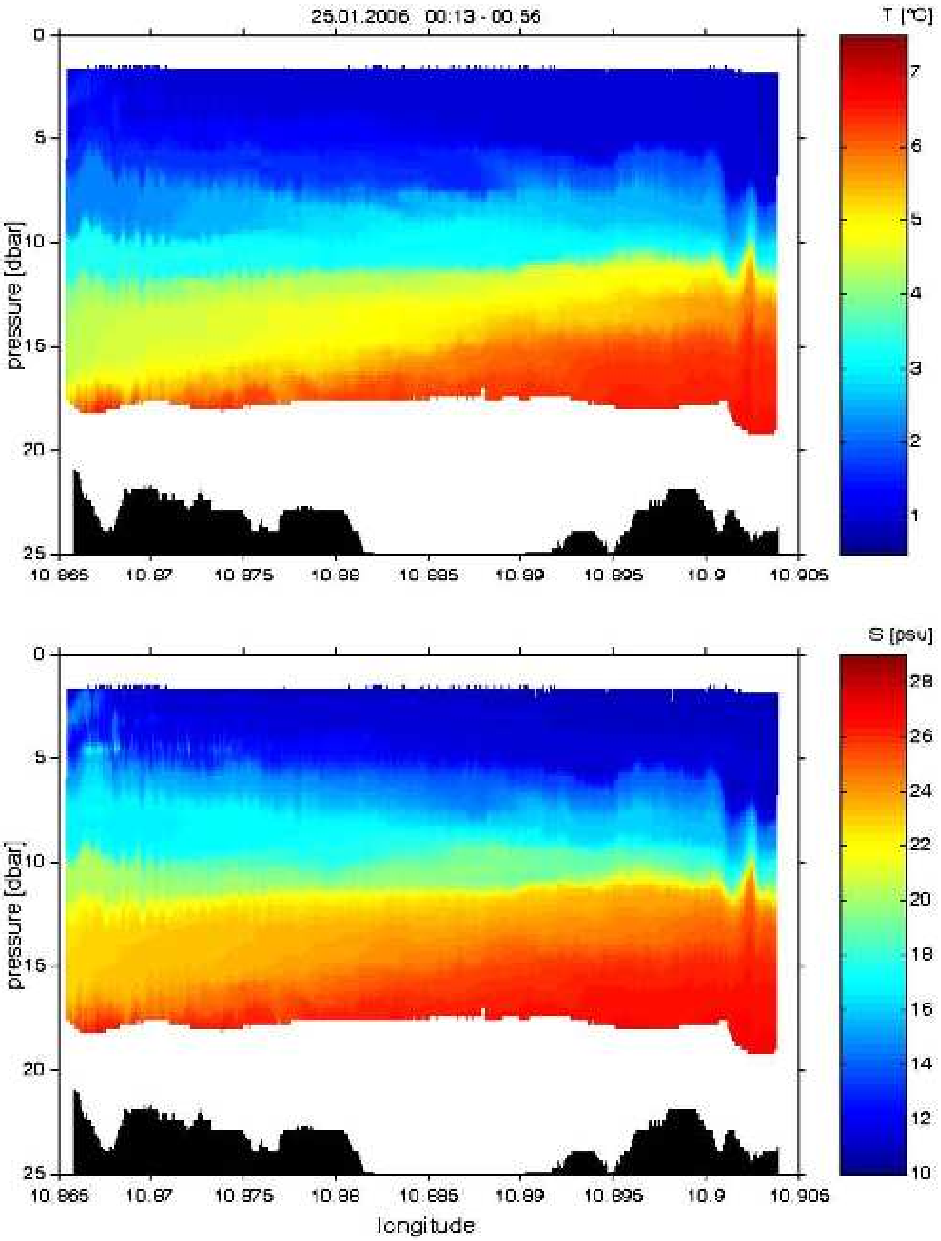

Figure 3.94: Temperature and salinity measured by the towed CTD chain from 00:13 to 00:56 h 25 January 2006 north of the Western Bridge of the Great Belt Fixed Link. The figure was taken from *Lass et al.* (2008).

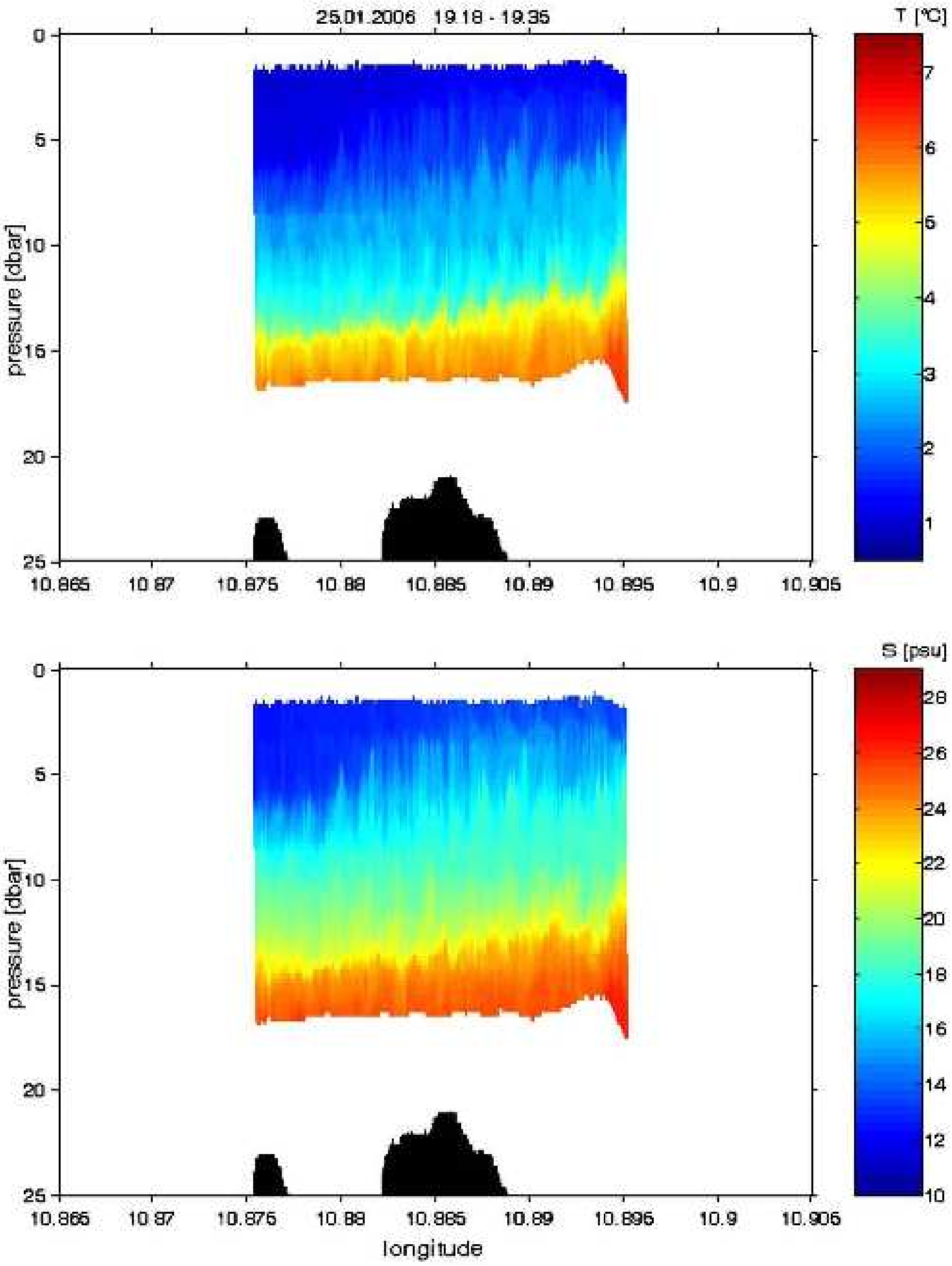

Figure 3.95: Temperature and salinity measured by the towed CTD chain from 19:18 to 19:35 h 25 January 2006 south of the Western Bridge of the Great Belt Fixed Link. The figure was taken from *Lass et al.* (2008).

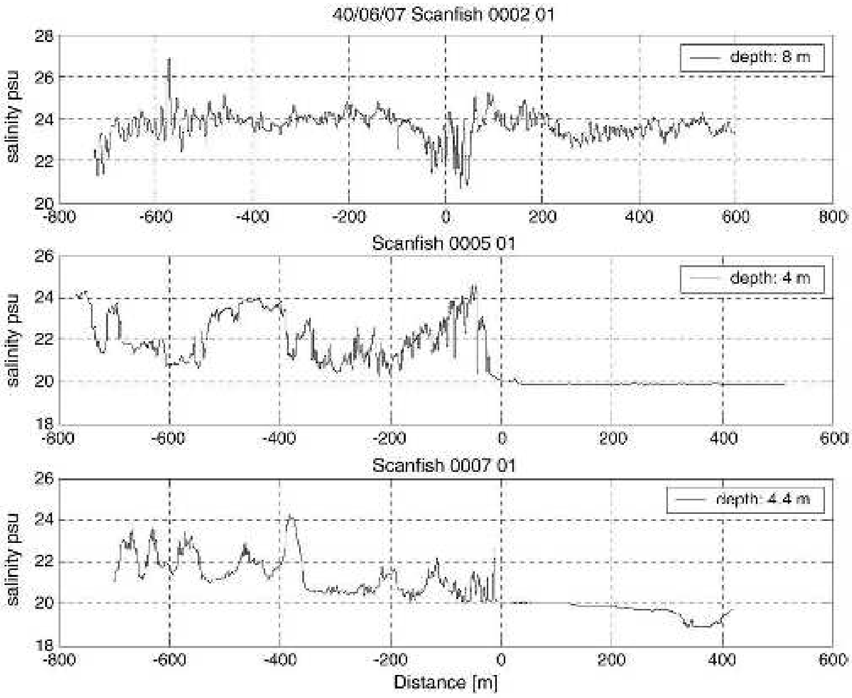

Figure 3.96: Salinity in the surface mixed layer measured with the Scanfish-CTD towed at a given depth level in meridional direction beneath the Western Bridge of the Great Belt Fixed Link. The distance of the Scanfish is given with respect to the middle line of the bridge (northward positive). The measurements in the upper panel were performed at 19:08 h 4 April in the middle panel, at 13:54 h 5 April, 2006, and in the lower panel at 14:48 h 5 April. The figure was taken from *Lass et al.* (2008).

aligned in north-south direction was towed, passing beneath the Western Bridge in the shipping channel between two bridge pylons. The first of these tracks was performed at 8 m depth, just above the pycnocline, when the surface current was southward at 0.4 m s^{-1}. Both the mean value and the variability of salinity were quite similar at distances exceeding 100 m upstream and downstream of the bridge, while close to the bridge, salinity was lower and the variability enhanced (3.96). This suggests that the pycnocline descends quasi-stationary between the bridge pylons, while simultaneously creating vertical oscillations due to inertial waves generated by the pylons in the moving stratified flow. The second and third track beneath the bridge were conducted at 4 m depth, when the surface current was southward at about 0.7 m s^{-1}. Upstream of the bridge the salinity in the surface mixed layer was nearly constant and 1 to 2 psu lower than downstream of the bridge. While upstream the variability in salinity of the surface mixed layer was very low, it exhib-

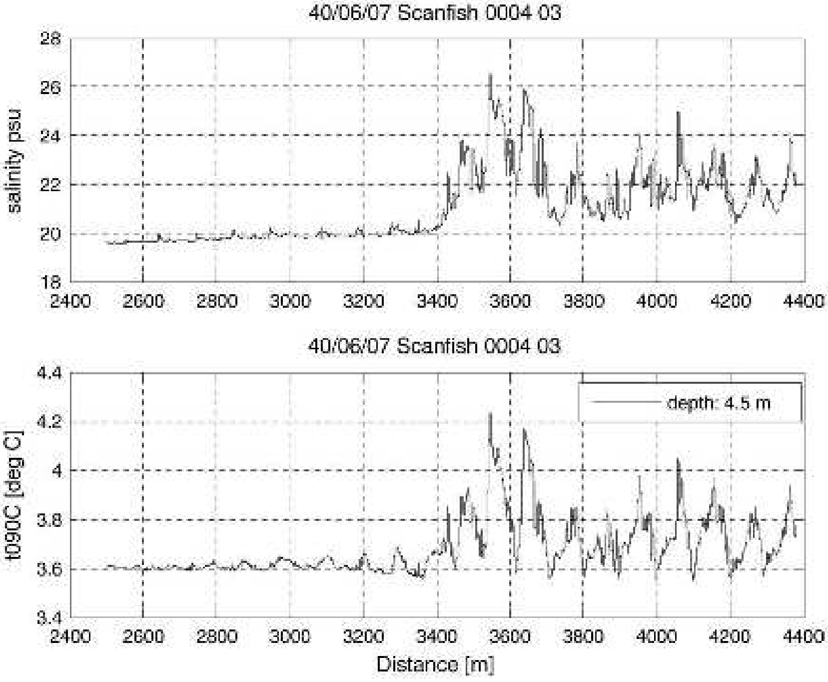

Figure 3.97: Salinity (upper panel) and temperature (lower panel) in the surface mixed layer measured at 12:04 h 5 April 2006 with the Scanfish-CTD towed at a given depth level downstream of the Western Bridge of the Great Belt Fixed Link. The distance of the Scanfish is given with respect to the western end of the bridge. The figure was taken from *Lass et al.* (2008).

ited a maximum just below the bridge, decreasing downstream within a distance of about 400 m. Further downstream the variability of salinity was still high but with a different length scale. These observations suggest that bridge-induced turbulence is enhanced downstream within a distance of at least 400 m, corresponding to an order of 40 diameters of a bridge pylon, when Fr exceeds a certain value close to one. Further than 400 m downstream of the bridge the variability of near-surface salinity may be caused by turbulence generated by a flow of stratified water over an irregular bottom topography on a larger scale south of the bridge (Fig. 3.89). The CTD tows in the near-surface layer upstream on tracks parallel to the bridge support the results of the CTD chain measurements during the first cruise. No variability of salinity was observed in the upper mixed layer upstream of the bridge on a spatial scale of the distance between two bridge pylons, while pulse-like variability on a scale of 70 m was observed 500 m downstream when Fr was close to one (Fig. 3.97).

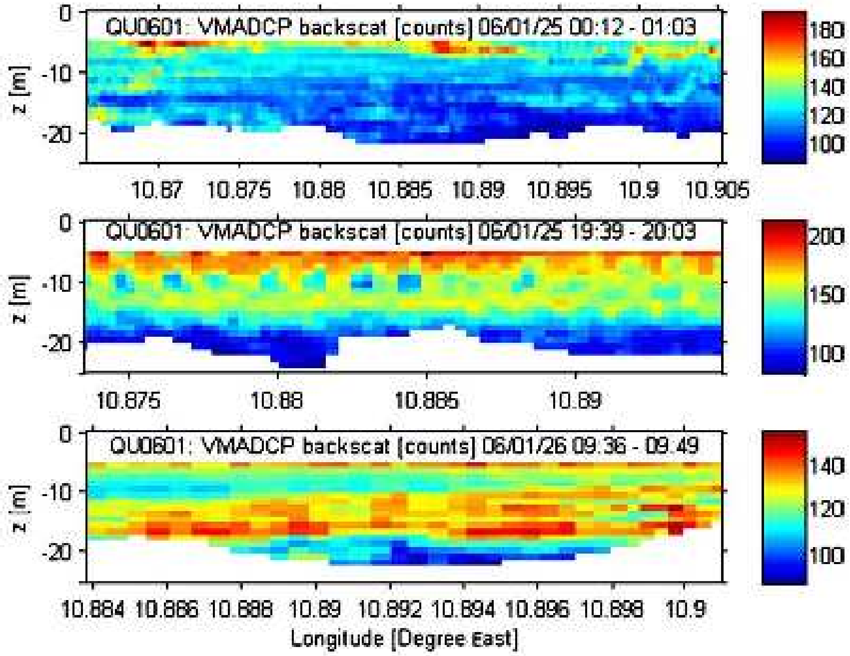

Figure 3.98: Backscattering intensity measured by the vessel-mounted ADCP on tracks parallel to the Western Bridge of the Great Belt Fixed Link. The upper panel shows the backscattering north of the bridge, the middle and lower panels depict backscatter south of the bridge at different times. The figure was taken from *Lass et al.* (2008).

Backscattering of acoustic waves is caused by zoo-plankton as well as by small turbulent inhomogeneities of sound velocity variations. Hence, one can expect that the backscattering signal detected by the ADCP contains certain information on the spatial pattern of temperature and salinity affected by small-scale turbulence.
The pattern of backscattering intensity (Fig. 3.98) differs generally upstream and downstream of the Western Bridge. Backscattering along the upstream track shows strong intensity that decreases with increasing depth in the near-surface layer.

Acoustic backscattering along the downstream track has a secondary maximum in the intermediate layer around a depth of 15 m. This might be evidence of enhanced turbulence in this layer inducing small-scale inhomogeneities of sound velocity by which the sound transmitted from the ADCP is scattered. However, there are significant differences between both downstream tracks. The pattern of acoustic backscatter on the first track south of the Western Bridge, at 19:39 to 20:03 h 25 January, showed well-defined horizontal structures between the surface and the intermediate layer, with a length scale of about 70 m, which agrees well with the pattern of temperature and salinity observed with the towed CTD chain (Fig. 3.95).

These structures were not observed on the downstream track at 09:36 to 09:49 h 26 January. The main difference between both tracks was the current velocity in the surface layer, which amounted to Fr = 1.28 at 19:39 h 25 January and Fr = 0.43 at 09:36 26 January.

The turbulence downstream of the bridge mixes salt from the intermediate layer into the surface layer. This enhanced mixing has implications for general dynamic properties of stratification as mean potential energy anomaly and geopotential anomaly. The downstream mean potential energy anomaly decreased in the water column below 10 m depth by about 50 J m^{-3} as derived from the classical CTD measurements. These measurements might be affected by advection of mean potential energy anomaly. Therefore the mean potential energy anomaly was estimated from the two selected tows of the CTD-chain shown in Figs. 3.94, 3.95 which resolve the disturbances induced by the pylons. The results are shown in Fig. 3.99 and reveal that the enhanced mixing within the wakes of the pylons can lower the mean potential energy anomaly by about 30 J/m^3 in the upper 15 m depth compared with the area between the wakes when Fr is $O(1)$. A time-dependent dynamic equation of the potential energy anomaly, Φ, was given by *Burchard and Hofmeister* (2008). In the case of the water surrounding the Western Bridge, the most significant terms of this equation (besides the advection term) are the differential advection and the vertical mixing term. Since advection of Φ would have a similar effect on positions up and downstream of the bridge, the order of magnitude of the other two terms is estimated. The diffusion term is

$$\frac{\rho_0}{H}\int_{-H}^{0} B\,dz = \frac{\rho_0}{H}\int_{-H}^{0} K_v N^2\,dz \tag{3.37}$$

The vertical turbulent density diffusion coefficient K_ν can be expressed in terms of turbulent kinetic energy dissipation ε according to *Osborn* (1980). With this, it is obtained that

$$\frac{\rho_0}{H}\int_{-H}^{0} B\,dz = \frac{0.2\rho_0}{H}\int_{-H}^{0} \varepsilon\,dz, \tag{3.38}$$

with the buoyancy production, B. Taking $\varepsilon = O(5 \times 10^{-5}\text{ W kg}^{-1})$ and standard sea water density, for the term $O(10^{-2}\text{ W m}^{-3})$ as order of magnitude is obtained.

The significant density spikes in the surface mixed layer observed within the wakes of the pylons form significant horizontal density gradients subject to differential advection in case of a baroclinic cross channel circulation. On one side of the wake, dense water is advected over less dense water, causing unstable stratification and mixing. This term is

$$\frac{g}{H}\,\nabla_h\,\bar{\rho}\int_{-H}^{0} z\tilde{u}\,dz \tag{3.39}$$

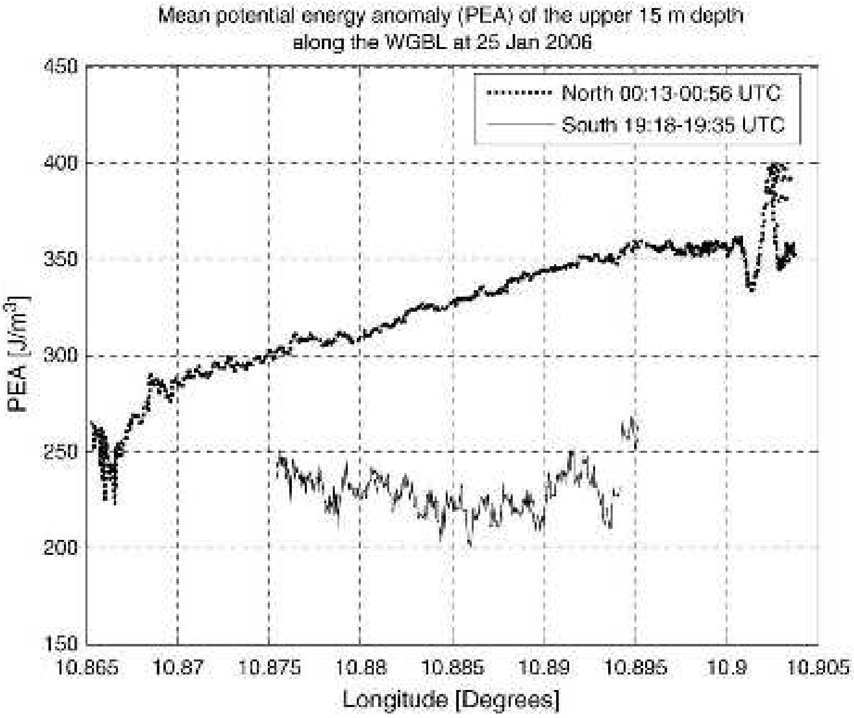

Figure 3.99: Mean potential energy anomaly Φ calculated according *Simpson* (1981) from measurements with the towed CTD-chain north (dotted line) and south (solid line) of the Western Bridge of the Great Belt Fixed Link shown in Figs. 3.94, 3.95. The figure was taken from *Lass et al.* (2008).

Taking the horizontal density gradient as $O(10^{-2}\ \mathrm{kg\,m^{-4}})$, the baroclinic cross channel current as $u = (10^{-1}\ \mathrm{m\ s^{-1}})$, and $H = O(10\ \mathrm{m})$ the order of magnitude for the differential advection term $O(10^{-1}\ \mathrm{W\ m^{-1}})$ is obtained. The characteristic time $T = L/\nu$ is $T = O(10^3\ \mathrm{s})$, taking $L = 500$ m for the length of the wake and $u = 0.5\ \mathrm{m\,s^{-1}}$ for the characteristic long-channel velocity. Then for the change of Φ with time $O(3{\times}10^{-2}\ \mathrm{W\ m^{-3}})$ is obtained, suggesting that it is balanced by both the dissipation and the differential advection term.

3.3.4 Dissipation of turbulent kinetic energy

Dissipation (ε) measurements were performed on twelve parallel sections north and south of the Western Bridge, similar to the tracks of the CTD chain. The distance between two consecutive casts of the dissipation profiler along a section could not resolve dissipation in the wakes of the single pylons of the bridge, since the wakes have a width of $O(10\text{ m})$ in the cross-channel direction.

Five MSS sections were performed north of the bridge between 21:30 h 24 January and 05:47 h 25 January UTC, when a weak inflow in the upper 15 m was observed and weak outflow below 15 m depth. Four sections were performed south of the bridge between 20:51 h 25 January and 02:11 h 26 January, when strong inflow was detected above an interface and outflow was detected below this interface. The depth of the interface decreased from 20 m to 15 m while we were performing measurements six through nine. Two measurements were made north of the bridge between 04:08 and 06:26 h 26 January, during weak inflow in the upper 15 m and strong outflow below this depth. A final meridional measurement was taken south of the bridge during outflow in the whole water column.

During the April cruise, three pairs of dissipation measurements were performed, consisting of profiles along upstream and downstream sections aligned parallel to the bridge. The first pair of sections was performed during medium inflow, the second during weak inflow and the last during strong inflow. Additionally, a time series of dissipation measurements south of the bridge (downstream) was performed on an anchor station during strong inflow that weakened and ceased toward the morning of 6 April 2006.

The dissipation of turbulent kinetic energy north of the Western Bridge during the January cruise (Fig. 3.100) was characterised by high dissipation $O(10^{-4}\text{ W kg}^{-1})$ in the surface layer (upper 7 m), which could have been caused by both wind mixing and the turbulent wake generated by the moving ship. Reduced dissipation was observed in an intermediate layer between 10 and 20 m depth, where scattered patches of dissipation with medium strength $O(10^{-6}\text{ W kg}^{-1})$ were superimposed on a weak background dissipation $O(10^{-8}\text{ W kg}^{-1})$. The dissipation in the bottom boundary layer was slightly higher than in the intermediate layer, in particular during Section 11, when a strong outflow was observed below 15 m depth.

The pattern of dissipation on Section 8, which was performed south of the bridge, was significantly different from the northern sections (Fig. 3.100). Here, no well-defined layered pattern of dissipation was observed. Instead, scattered patches of high dissipation $O(10^{-4}\text{ W kg}^{-1})$ were observed on a background dissipation of $O(10^{-6}\text{ W kg}^{-1})$, in particular in the intermediate water layer.

Dissipation of turbulent kinetic energy is higher in the surface layer upstream than downstream, but in the intermediate layer (10 to 20 m) it is at least 30 fold larger south of the bridge than north. No clear picture emerges in the bottom layer. The stratification, described by salinity, density anomaly, and BVF, during the April cruise was characterised by a very sharp pycnocline at a depth of about 7 m, which separated brackish surface water from very saline bottom water. Generally salinity was higher in the water column compared to the January cruise. This resulted in a thrice-larger maximum BVF during the April cruise.

Assuming turbulence in the water column can also be due to breaking internal

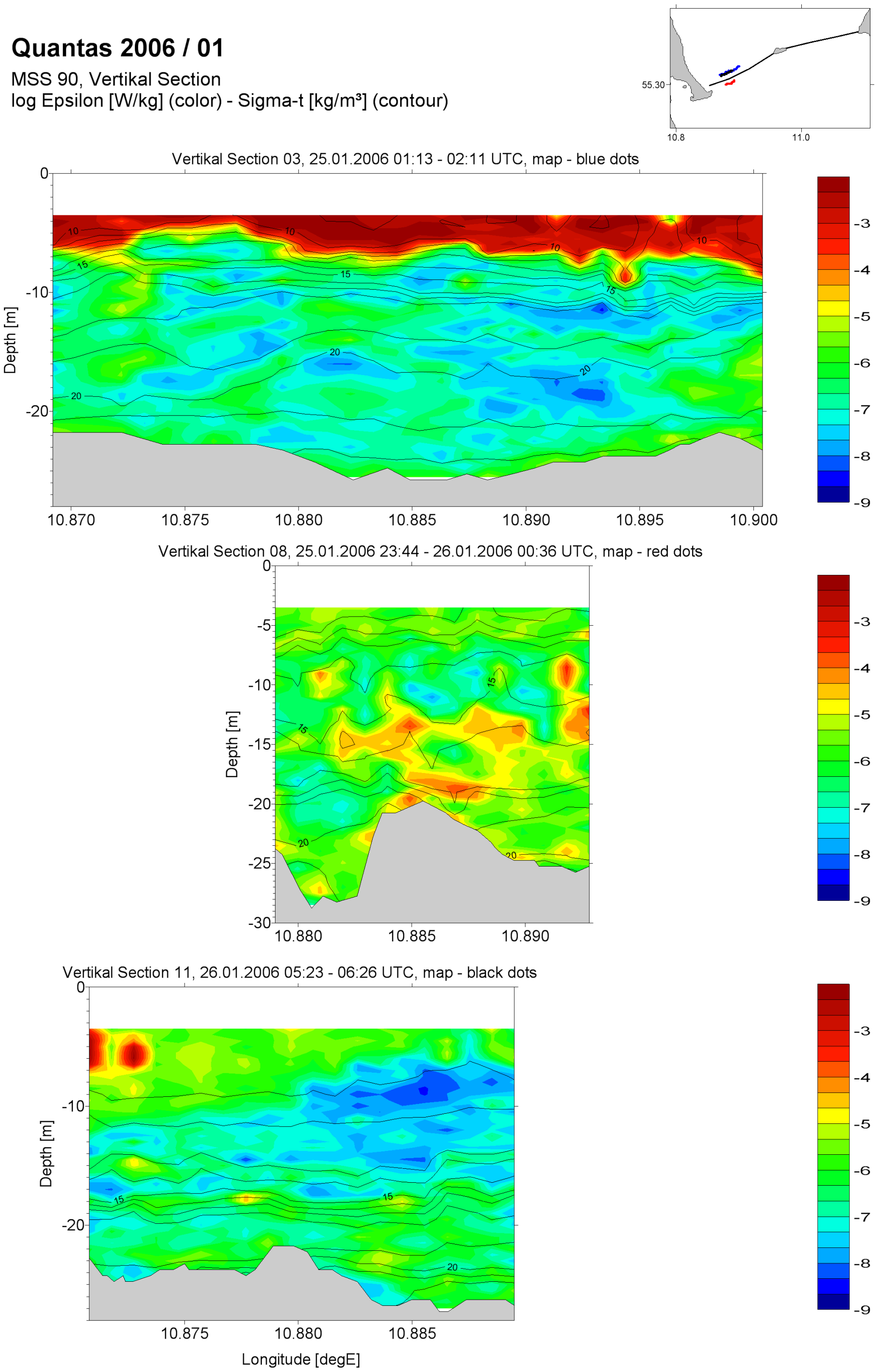

Figure 3.100: Vertical sections of dissipation of turbulent kinetic energy measured north of the Western Bridge of the Great Belt Fixed Link from 01:13 to 02:11 h 25 January (upper panel), south of the bridge from 23:44 h 25 January to 00:36 h 26 January (middle panel), and north of the bridge from 05:23 to 06:26 h 26 January (lower panel). The figure was taken from *Lass et al.* (2008).

waves, one would not expect in this case a local correlation between the generation of internal waves and dissipation of turbulent kinetic energy, since internal waves can transport energy over large distances before breaking. Therefore, *Lass et al.* (2008) averaged dissipation from 10 to 15 m depth, which is separated from the surface mixed layer by the pycnocline and from the turbulent bottom layer by a secondary pycnocline (at least south of the bridge). Dissipation from 15 to 20 m depth, which may be affected by processes in the bottom boundary layer was also averaged. Observations with towed instruments have shown hitherto that the state of turbulence in the area of the Western Bridge depends on surface velocity.

The dissipation upstream during the January cruise ranged between 10^{-7} and 10^{-6} W kg^{-1}, the dissipation downstream was about tenfold larger ($O[10^{-5}$ W kg$^{-1}])$ at least when velocity exceeded 40 cm s^{-1}. Surprisingly, the observed downstream dissipation of the upper layer was lower at 60 cm s^{-1} than at 40 cm s^{-1}. This may be a dynamical effect, since the four ensembles of downstream dissipation measurements were performed within five h of the decelerating current after the maximum southward flow of about 80 cm s^{-1}. Since the energy flux from the mean current to the turbulent flow takes some time to propagate to the spectrum of motions, there may be a delay in the temporal variations of the mean flow and dissipation of turbulent kinetic energy averaged over a significant fraction of the channel cross section.

Enhanced turbulent kinetic energy with turbulent mixing capability can be expected in the turbulent wake of a pylon in a flow of sufficiently high velocity and *Re*. The differential advection by the baroclinic cross-channel circulation is one mechanism to smear out turbulence from the wakes of the pylons. This resulted in enhanced mean downstream dissipation by one order of magnitude in the intermediate depth range between the bottom of the surface mixed layer and the turbulent bottom layer. This depth range is commonly characterised by the lowest dissipation rates in the water column of an undisturbed stratified fluid. The intensity of the downstream enhanced dissipation in the intermediate layer seems to depend on the Fr determined by the surface flow. This enhancement was observed at surface flow speeds with $\mathrm{Fr} > 0.66$ to be at a maximum and to decrease toward larger Fr during January 2006. The downstream dissipation of turbulent kinetic energy was observed to increase dramatically at $\mathrm{Fr} = 0.75$, with a maximum at $\mathrm{Fr} = 1.25$ during the April cruise.

The dependence of mixing, turbulence and dissipation on the Fr suggests that internal waves may distribute energy subtracted by the flow around the pylon from the moving stratified fluid horizontally and vertically into the surrounding undisturbed flow. That means that a part of the energy generated by the drag of the pylon in a stratified flow is distributed over a much wider area than that covered by the turbulent wake itself. This internal wave energy may be converted with a certain time delay into patches of turbulent kinetic energy at remote distances from the pylon where conditions for their breaking exist. The discrepancy between the Fr of maximum mean dissipation in January and April indicates that there might be a time delay between wave drag and generation of turbulent kinetic energy. The maximum energy transfer from the mean flow to the internal waves is at Fr = 0.77 for a constant moving obstacle in a deep stratified fluid according to *Ekman* (1906). However, one can expect that the dynamics of the energy transfer between the mean flow and the internal waves, and their subsequent radiation and breaking causes a certain time delay between generation and dissipation of internal waves. This delay may cause a shift of high dissipation events to lower/higher Fr in case of background velocity decreasing/increasing with time, since the breaking internal waves causing the high dissipation events received their energy from an earlier mean flow of higher/lower Fr. Moreover, the averaged dissipation of turbulent kinetic energy appears higher/lower during decreasing/increasing speed of the mean flow. This dynamic behaviour of the background flow makes it difficult to estimate exact Fr for the transitions of the turbulent state in natural stratified fluids.

The intensified turbulence in the intermediate layer downstream of the bridge led to an enhanced vertical mixing, which reduced the vertical density gradient within this layer. This will lead in case of a constant energy flow from internal waves into turbulenceto a higher turbulent viscosity, since less turbulent kinetic energy is consumed by the buoyancy flux. Indeed, while the dissipation of turbulent kinetic energy increased tenfold downstream in the intermediate layer, the turbulent diffusivity rose by a factor of about 30.

It is rather unlikely that the step-like increase of turbulent mixing with Fr is associated with a constant bulk flux Richardson number as assumed by *Hansen and Møller* (1989b). The enhanced vertical mixing downstream of the bridge at overcritical Fr causes an irreversible density exchange between the saline deep layer and the brackish surface layer, which cannot be completely compensated by dredging and which may have far reaching consequences for the hydrography and ecology of Baltic Sea deep water. Moreover, this mixing causes a baroclinic pressure gradient, resulting in an outflow in the bottom layer during near-surface inflow, which increases the effective resistance factor of the bridge.

3.3.5 Impact of mixing on the baroclinic mean current

The observed significant changes in the stratification and mixing upstream and downstream of the bridge suggest that this might have an effect upon the meridional component of the baroclinic pressure gradient. Therefore, *Lass et al.* (2008) calculated the geopotential anomalies from the temperature and salinity profiles by integrating the specific volume anomaly of the sea water for each CTD profile over pressure. The profiles of the geopotential anomalies calculated north (upstream)

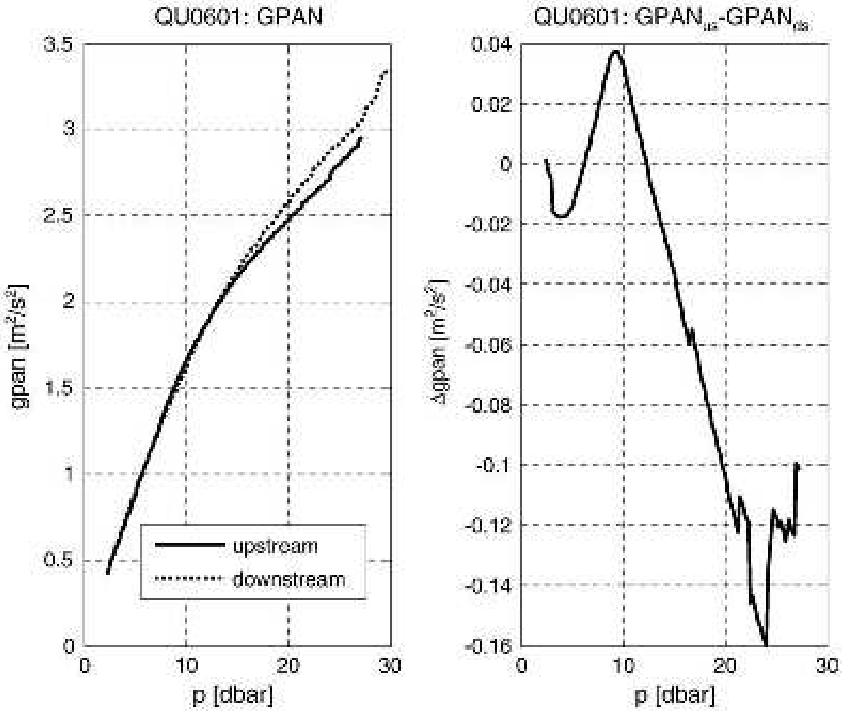

Figure 3.101: Averaged geopotential anomaly (GPAN) north (upstream) and south (downstream) of the Western Bridge of the Great Belt Fixed Link (left panel) and the difference between averaged upstream and downstream GPAN (right panel) during the January 2006 cruise. The figure was taken from *Lass et al.* (2008).

and south (downstream) of the bridge was averaged to one upstream and one downstream profile (Fig. 3.101). In the upper 10 m of the water column the geopotential anomalies are quite similar, while below this, the downstream geopotential anomaly increases much faster than the upstream one. This amounts to a sea level difference of about 1 cm between both positions, which are about 1 km apart. This baroclinic pressure gradient superimposed with the southward-directed barotropic pressure gradient compensated the barotropic inflow at a depth range of 15 to 20 m, such that the resulting flow in the bottom layer frequently appeared as outflow. This current pattern is quite typical for an estuarine circulation, as it was observed at this site before the construction of the Great Belt Fixed Link (see *Farmer and Møller* (1989)). This diffusion-induced baroclinic flow may effectively increase the drag of the Western Bridge on the transport of the Great Belt.

3.3.6 Conclusions

From observations, *Lass et al.* (2008) conclude that bridge pylons in a moving stratified fluid generate at higher than a critical *Re* and Fr downstream, a turbulent wake with enhanced dissipation of turbulent kinetic energy, and enhanced vertical mixing within in a distance on the order of 50 diameters of the pylons. In case of baroclinic cross-channel circulation, this turbulence is exported from the wake laterally. Moreover, the sudden increase of turbulence and mixing at Fr ≈ 0.75 suggests that energy is extracted from the mean flow as internal wave drag and radiated into the remote environment of the pylon. Their findings expand the parameter range of *Re* and Fr covered by the studies of *Møller et al.* (1997) in a laboratory flume, who found no significantly enhanced mixing by vertical cylindrical obstacles in a stratified flow with Fr between 0.19 and 0.33. *Lass et al.* (2008) also did not observe indications of enhanced mixing at the pylons of the Western Bridge in this range.

The observed dependence of mixing in the wake of a vertical pylon in a stratified flow suggests that enhanced mixing can become a matter of importance with respect to the transformation of inflowing water if artificial constructions are build within the pathways of inflowing salt water. The flow velocity is sufficient high only there where the salt water plumes are driven by sea level differences, as between the Kattegat and the Arkona Sea (*Farmer and Møller*, 1989), and by gravity on sloping bottom topography as in the Arkona Sea (*Lass and Mohrholz*, 2003; *Sellschopp et al.*, 2006; *Burchard et al.*, 2005; *Umlauf et al.*, 2007).

Chapter 4

Impact of offshore wind farms on inflows into the Baltic Sea (IOW)

4.1 Introduction

It was first discussed by *Lass* (2003), that structures such as foundations of wind turbines assembled in offshore wind farms could induce additional vertical mixing in stratified shear flow. Such a wind farm induced dilution of the inflowing water could result in a decreased ventilation of the halocline in the Baltic Sea. As a result of this, the region of oxygen depletion in the Baltic Sea could be extended to higher levels in the water column, with significant environmental consequences for pelagic and benthic organisms. It is the goal of the present study to quantify this impact.

An existing high-resolution coastal model of the Western Baltic Sea (*Burchard et al.* (2009) and section 2.2.2) has been used to identify the pathways of dense bottom currents and to quantify the associated amount of natural mixing on their way through the Western Baltic Sea. These results are in good agreement with field observations of medium intensity inflows in the Western Baltic Sea (*Sellschopp et al.* (2006), *Umlauf et al.* (2007)).

Since many years the flow around vertically and horizontally aligned cylinders have been investigated, mainly with the aim to study structural design and flow-induced acoustic emissions and vibrations. Other studies concentrated on the transition area in the wake of the cylinder (see e.g. *Henderson* (1997), *Xu et al.* (1995)). Behind a vertically aligned cylinder a van Karman vortex street may evolve inducing turbulence and mixing far away from the structure. Internal waves may be generated in stratified flow around structures, which propagate away and cause mixing remotely due to dissipation. The main problem concerning previous work is the lack of research on mixing induced by vertical structures in stratified flow. Most of the past studies were conducted on homogeneous water flow without Earth rotation or at horizontally aligned cylinders (*Arntsen* (1998)). Recent field studies conducted by *Lass et al.* (2008) on enhanced tracer (here: salinity) mixing in the Baltic Sea at the Western Great Belt Bridge revealed significantly increased mixing downstream of the bridge. Therefore, it is necessary to develop numerical methods for quantifying structure-induced mixing in stratified shear flows and its impact on larger scales.

To get an impression of the regional dynamics of dense gravity currents in the Western Baltic Sea, two passive tracers were released continuously at transects across the Darss Sill and the Drodgen Sill in such a way that they were set to a value equal to the salinity at these positions when the current was directed into the Arkona Sea and to zero for outgoing currents. After a simulation period of 16 months the mean value of the bottom tracer concentrations were calculated and plotted in Fig. 4.1. It is demonstrated that plumes from Darss Sill show lower salinities but transport higher amounts of salt due to the broader transitions area at the Darss Sill than at the Drodgen Sill. It is also shown that both plumes take different pathways through the Arkona Basin and through the Bornholm Channel. It is hypothesised that structure-induced physical mixing may significantly dilute dense bottom currents generated by inflow events such that their ability to reach deeper parts of the Baltic Sea is reduced as well as the ventilation of these basins.

The existing and validated realistic coastal model setup for the Western Baltic Sea (*Burchard et al.* (2009)) is extended to quantify potential additional dilution of medium intensity inflow events due to vertical structures. Since cylinders of offshore wind farms (OWFs) typically have diameters in the order of 5-10 m, mixing induced by the structures is a sub-grid scale process which cannot be resolved by the coastal ocean models with typical horizontal resolutions of $\mathcal{O}(1\text{km})$. The parameterisation is obtained by calibrating an extended k-ε turbulence closure model by means of results from a set of local high-resolution RANS model experiments as described by *Schimmels* (2008).

This chapter is structured as follows: section 4.2 describes how the parameterisation for the process of sub-grid scale cylinder-induced mixing was obtained by means of high resolution non-hydrostatic RANS modelling; section 4.3 introduces the applied hydrostatic coastal model and the mixing measures used for the investigations; section 4.4 investigates the behaviour and impact of the parameterisation in the hydrostatic model for idealised overflow scenarios and section 4.5 shows the results of realistic simulations on the intensity of diapycnal mixing, dilution and changes on annual mean gradients due to the OWFs for two realistic cases and two cases with over-exaggerated wind farm coverage in the Western Baltic Sea.

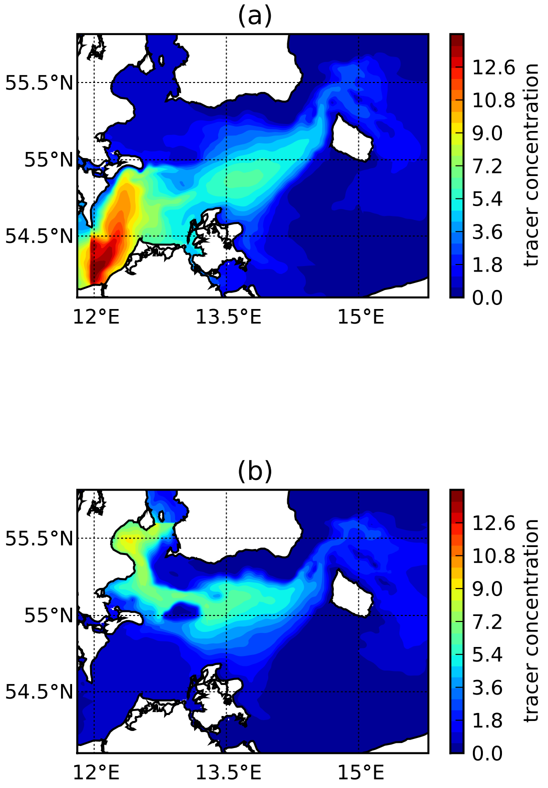

Figure 4.1: Bottom tracer concentration (averaged over 16 months) of the marked (a) Darss Sill and (b) Drodgen Sill plume spreading into the Arkona Sea. The Darss Sill tracer is released at a meridional transect at 12°E and the Drodgen Sill tracer is released at a zonal transect at 55.85°N. Both tracers are equated to local salinity at the release positions if the flow is directed into the Arkona Sea.

4.2 Parameterisation of structure friction in density-driven bottom currents

4.2.1 Model equations

The frictional force per unit height on a cylinder in an unstratified flow perpendicular to the cylinder can be calculated as

$$\vec{F} = \frac{1}{2} C_D \rho_0 d \vec{u} |\vec{u}|, \tag{4.1}$$

with the drag coefficient $C_D = 0.63$ (for a smooth cylinder), the diameter of the cylinder, d, and the undisturbed velocity vector $\vec{u}$ (see e.g., *Sumer and Fredsøe* (1997)). After division by the mass of the reference volume (which in finite volume methods is the mass of the finite volume in which the structure is contained) the frictional deceleration of the vertically resolved horizontal velocity components u and v, respectively, is calculated as:

$$G_d^u = \frac{1}{2} C_D a u \sqrt{u^2 + v^2}, \quad G_d^v = \frac{1}{2} C_D a v \sqrt{u^2 + v^2}, \tag{4.2}$$

with the area density of the structures, $a = X \cdot d/A$, where X is the number of cylinders in the flow and $A = \Delta x \Delta y$ (with the local horizontal grid dimensions, Δx and Δy) is the horizontal area of the finite volume for which the dynamic equations are representative.

Taking the classical u- and v-momentum equations in three-dimensional hydrostatic ocean models (see, e.g., *Burchard and Bolding* (2002), *Shchepetkin and McWilliams* (2005)), and adding the friction terms due to structures in the water column from eq. (4.2), the following dynamic equations result:

$$\begin{aligned} &\partial_t u + \partial_x(u^2) + \partial_y(uv) + \partial_z(uw) - \partial_z\left(A_v \partial_z u\right) \\ &\quad -\partial_x\left(2A_h \partial_x u\right) - \partial_y\left(A_h(\partial_y u + \partial_x v)\right) - fv + G_d^u \\ &\quad = -g\partial_x \zeta - \frac{g}{\rho_0} \int_z^\zeta \partial_x \rho \, dz', \end{aligned} \tag{4.3}$$

$$\begin{aligned} &\partial_t v + \partial_x(vu) + \partial_y(v^2) + \partial_z(vw) - \partial_z\left(A_v \partial_z v\right) \\ &\quad -\partial_y\left(2A_h \partial_y v\right) - \partial_x\left(A_h(\partial_y u + \partial_x v)\right) + fu + G_d^v \\ &\quad = -g\partial_y \zeta - \frac{g}{\rho_0} \int_z^\zeta \partial_y \rho \, dz'. \end{aligned} \tag{4.4}$$

In eqs. (4.3) and (4.4), w is the vertical velocity component. The vertical coordinate z ranges from the bottom $z = -H(x, y)$ to the surface $z = \zeta(t, x, y)$ with t denoting time. A_v is the vertical eddy viscosity, $f = 2\omega \sin\phi$ is the Coriolis parameter, with the angular velocity of the Earth, ω, and the latitude, ϕ, ρ is the potential density, ρ_0 is the reference density, and g is the gravitational acceleration. The horizontal mixing is parameterised by terms containing the horizontal eddy viscosity A_h, see *Blumberg and Mellor* (1987). In realistic hydrodynamic simulations, prognostic equations for temperature and salinity are calculated as well (see *Burchard and Bolding* (2002) for details), using the eddy diffusivity K_v for vertical mixing.

Both eddy viscosity and eddy diffusivity are calculated as functions of the turbulent kinetic energy per unit mass (TKE), k, and the dissipation rate of the TKE, ε:

$$A_v = c_\mu \frac{k^2}{\varepsilon}, \quad K_v = c'_\mu \frac{k^2}{\varepsilon}, \tag{4.5}$$

with the non-dimensional stability functions c_μ and c'_μ containing the algebraic second-moment turbulence closure (see *Umlauf and Burchard* (2005) for details). The TKE and its dissipation rate are calculated here by means of the k-ε two-equation model:

$$\begin{aligned} \partial_t k + \partial_x(uk) + \partial_y(vk) + \partial_z(wk) - \partial_z\left(\frac{A_v}{\sigma_k}\partial_z k\right) \\ = P + P_d + B - \varepsilon, \end{aligned} \tag{4.6}$$

$$\begin{aligned} \partial_t \varepsilon + \partial_x(u\varepsilon) + \partial_y(v\varepsilon) + \partial_z(w\varepsilon) - \partial_z\left(\frac{A_v}{\sigma_\varepsilon}\partial_z \varepsilon\right) \\ = \frac{\varepsilon}{k}\left(c_1 P + c_4 P_d + c_3 B - c_2 \varepsilon\right), \end{aligned} \tag{4.7}$$

with the shear production

$$P = A_v S^2 \tag{4.8}$$

and the buoyancy production

$$B = -K_v N^2, \tag{4.9}$$

with the vertical shear squared, $S^2 = (\partial_z u)^2 + (\partial_z v)^2$ and the buoyancy frequency squared, $N^2 = -(g/\rho_0)\partial_z \rho$.

In the TKE equation (4.6) the loss of mean kinetic energy from (4.3) and (4.4) due to structure-induced friction,

$$P_d = \frac{1}{2} C_D a \left(u^2 + v^2\right)^{3/2}, \tag{4.10}$$

has been included as further production term. Following *Svensson and Häggkvist* (1990), P_d has been included as source term into the dissipation rate equation as well, scaled by the empirical parameter c_4, see eq. (4.7). Other constant empirical parameters are the Schmidt numbers, σ_k and σ_ε and the weighting parameters c_1, c_2 and c_3 for the source and sink terms in the ε equation.

4.2.2 Structure mixing parameterisation

In the turbulence closure model, the parameters c_1 - c_3 all have a clear physical meaning, see, e.g., *Umlauf and Burchard* (2005). For their interpretation as well as the interpretation of the additional parameter c_4, it is instructive to investigate the k-ε model for homogeneous shear layers, e.g., in the absence of gradients except for spatially and temporally constant shear S and buoyancy frequency N (see *Burchard and Baumert* (1995)). Under these conditions, the model reduces to the following system of ordinary differential equations:

$$\dot{k} = P + P_d + B - \varepsilon, \quad \dot{\varepsilon} = \frac{\varepsilon}{k}\left(c_1 P + c_4 P_d + c_3 B - c_2 \varepsilon\right). \tag{4.11}$$

For stationary solutions of (4.11) with $\dot{k} = 0$ and $\dot{\varepsilon} = 0$, the following necessary condition can be derived:

$$\Gamma = -\frac{B}{\varepsilon} = \frac{c_1 - c_2}{c_3 - c_1} + \frac{c_4 - c_1}{c_3 - c_1}\frac{P_d}{\varepsilon}, \tag{4.12}$$

with the local mixing coefficient Γ (see *Umlauf* (2009), *Burchard and Hetland* (2010)). Following *Rodi* (1980), $c_1 = 1.44$ and $c_2 = 1.92$ and following *Umlauf and Burchard* (2005) $c_3 = -0.74$ (when applying the second moment closure by *Cheng et al.* (2002)), such that for $P_d = 0$ a mixing coefficient of $\Gamma = 0.22$ is obtained, a value close to the generic value of $\Gamma = 0.2$ suggested by *Osborn* (1980). It should be noted that the flux Richardson number, $R_f = P/\varepsilon$ (for which $R_f = \Gamma/(\Gamma + 1)$ is obtained for local turbulence equilibrium with $P + B = \varepsilon$), is a measure for mixing efficiency. For non-zero structure-induced turbulence production, the gross mixing efficiency is reduced for $c_4 > c_1$ and enhanced by $c_4 < c_1$ (because $c_3 - c_1 < 0$).

An interesting idealisation is also given by considering homogeneously stratified flow without shear ($P = 0$) for which (4.11) with $\dot{k} = \dot{\varepsilon} = 0$ yields

$$\Gamma = \frac{c_2 - c_4}{c_4 - c_3} \quad \Rightarrow \quad c_4 = \frac{c_2 + c_3\Gamma}{1 + \Gamma}. \tag{4.13}$$

For a mixing coefficient not modified by structure friction, this gives $c_4 = c_1$ (which is consistent with (4.12)), and, again, the gross mixing efficiency is reduced for $c_4 > c_1$ and enhanced by $c_4 < c_1$. The advantage of the formulation (4.13) is that it does not explicitly contain the turbulence production due to structure friction.

However, this formulation can only be used for calibrating c_4 on the basis of shear-free experiments.

Svensson and Häggkvist (1990) estimated for an unstratified atmospheric boundary layer $c_4 = 1.95$, i.e., $c_4 > c_1$ which would induce reduced mixing efficiency for stratified flows.

4.2.3 RANS model simulations

To analyse the process of structure-induced mixing and entrainment more thoroughly, to assess the impact of a cylindrical structure on the dilution of a dense bottom current and finally to provide calibration data for the parameterisation of the regional model described in section 4.2.4, a fully three-dimensional high resolution numerical model based on the Reynolds Averaged Navier-Stokes (RANS) equations has been set up. Besides the balance equations for mass and momentum an additional transport equation for salinity is solved and turbulence is simulated with the SST k-ω model (*Wilcox* (1988)). A detailed description of the numerical model, the model setup, the validation procedure and a thorough discussion of mixing and entrainment induced by a circular cylinder in density currents not influenced by earth rotation, i.e. without the effect of Coriolis acceleration, can be found in *Schimmels* (2008). Simulations of cylinder induced dilution of dense bottom currents with the effect of Coriolis acceleration, which have been used as a reference for the present study are described in *Rennau et al.* (2012), where the results of a parameter study with varying Froude and Ekman numbers are presented and the impact of offshore wind farms is assessed.

All simulations were made on the same computational domain which is sketched in Fig. 4.2a, with the cylinder in the centre. The shaded plane is the result of one simulation and denotes the current depth which has been added to better visualise the model setup. Horizontal length scales are normalised by the cylinder diameter d and the vertical scale is normalised by the thickness of the density current, D.

The boundary conditions are a pressure boundary condition at the free surface, periodic conditions at the lateral boundaries, a closed rough bottom boundary condition with an equivalent sand roughness of $k_s = 0.025$ m, corresponding to a drag coefficient of about $C_d \approx 0.0022$ for $D \geq 10$ m, and open boundaries at the inflow and outflow. The profiles for velocity, salinity, turbulent quantities and pressure needed for the inflow and outflow boundary conditions as well as initial conditions were gained from preliminary simulations of undisturbed currents with a one-dimensional model.

The numerical grid is block-structured and the grid topology is the same for all simulations, as shown in Fig. 4.2b and Fig. 4.2c. In the vertical the grid is refined at the bottom and within the interface between $0.5 < z/D < 1.5$ in order to adequately resolve the steep gradients of velocity, density and turbulence quantities

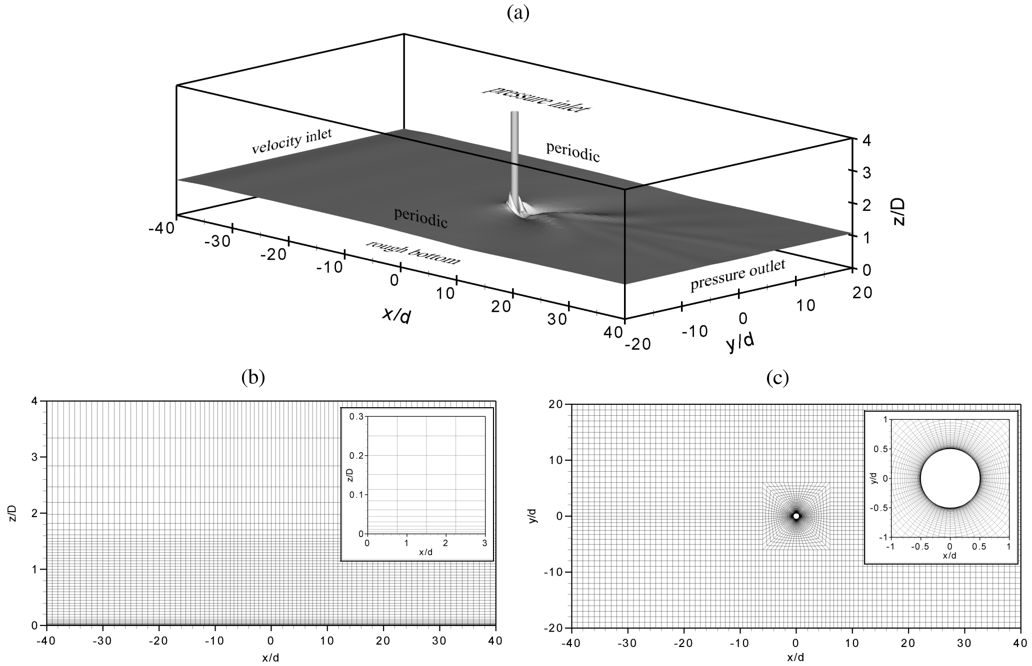

Figure 4.2: Computational domain for three dimensional high resolution RANS simulations. (a) Definition sketch of complete computational domain with the cylinder in the centre, boundary conditions assigned by the text and current depth indicated by the shaded plane. (b) Side view and (c) top view of the numerical grid. Small panels showing the refined resolution at the bottom and cylinder, respectively.

in these regions. In the horizontal the grid is circular up to 3 diameters around the cylinder and then converted over the next 3 diameters to the rectangular shape of the channel. The finest resolution at the cylinder accounts for the requirements of the wall function approach with y^+ being in the order of 10^2 or slightly below and in the far field the resolution is $\Delta x/d = \Delta y/d = 1$ which is slightly condensed in the wake region.

All simulations were run for 8000 time steps which were adjusted to let the current pass the domain within about 1500 time steps. In order to remove initial disturbances the simulations were first run for 4000 time steps and subsequently the mean values for the parameters in question were calculated from the following 4000 time steps, corresponding to about 30 shedding cycles.

With the model described so far *Schimmels* (2008) conducted a comprehensive parameter study to quantify the effect of the Froude number, aspect ratio d/D and Coriolis forces on the mixing process. They focused their analysis on the local patterns of the cylinder induced entrainment rates and gave an estimation of the total impact of offshore wind farms on density currents in the Baltic Sea based on the total entrainment induced by one cylindrical structure.

A direct result of the three dimensional RANS simulations is the total buoyancy flux B_{tot} including the buoyancy flux of an undisturbed current B_{base} and that induced by the structure B_{cyl}. It can either be used to calculate the entrainment rates as done by *Schimmels* (2008) or as a direct reference for the calibration of the parameterisation described in section 4.2.4. Integrating the three dimensional quantity over depth allows for an estimation of the local intensities of mixing induced by the cylinder as well as the area of influence of the cylinder. Before, however, the naturally occurring buoyancy flux B_{base} must be subtracted from the total buoyancy flux B_{tot} in order to analyse the effect of the cylinder alone.

Fig. 4.3 shows the patterns of the depth integrated cylinder induced buoyancy flux for an aspect ratio $d/D = 1$, a constant Ekman number $K = 0.8$ and different Froude numbers ranging from $\mathrm{Fr} = 0.4$ to $\mathrm{Fr} = 0.7$, see equation (4.17) for definitions of these numbers. These can be compared to the patterns for the cylinder induced entrainment rates shown by *Schimmels* (2008), where also a more comprehensive analysis is presented. It is nicely seen from Fig. 4.3 how the buoyancy flux is deflected to the right as a consequence of the lateral currents induced by Coriolis forces. Moreover it is obvious that the influence of the cylinder is generally rather limited and measures only a few diameters. There is also only a relatively small dependence on the Froude number but it can already be guessed that mixing slightly increases with increasing Froude number.

Integrating further over the horizontal plane eventually leads to the total structure-

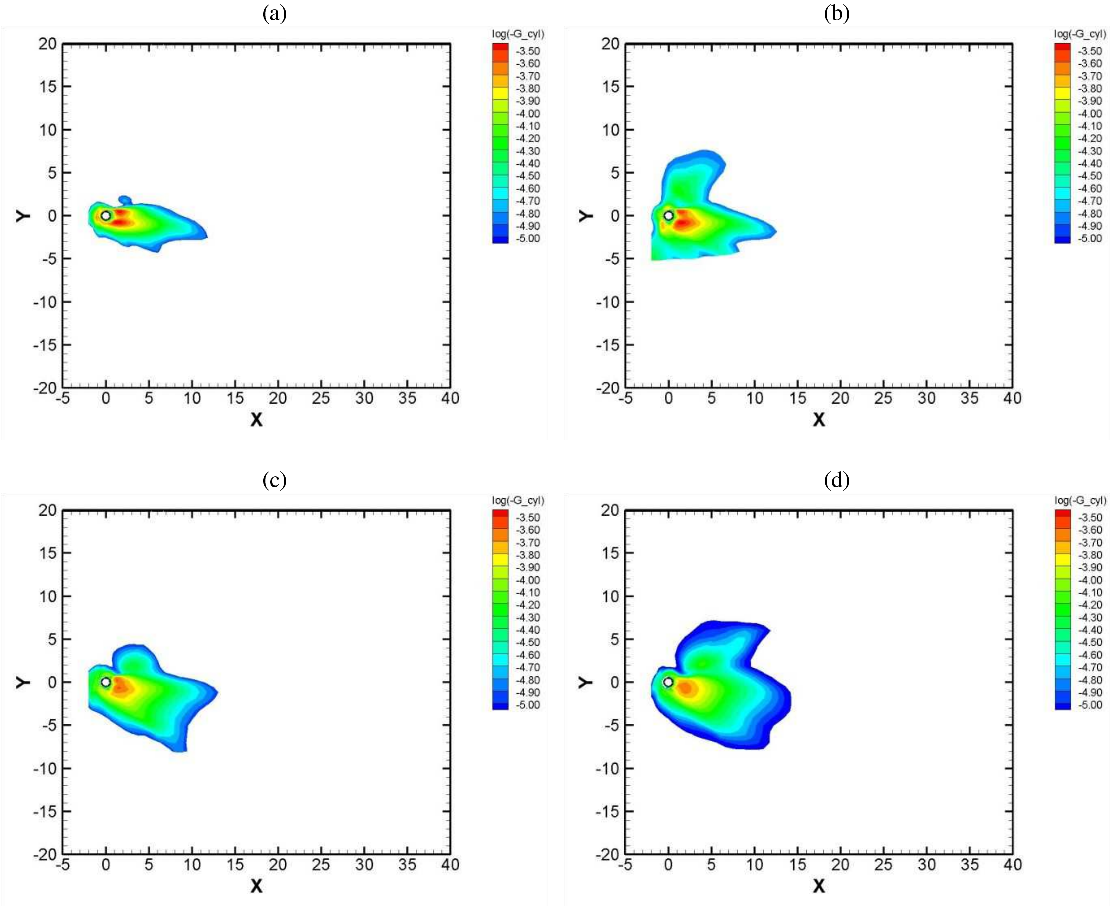

Figure 4.3: Spatial distribution of cylinder induced buoyancy production B_{cyl} for different Froude numbers with the cylinder diameter $D = 10$ m and a constant Ekman number $K = 0.8$. (a) Fr = 0.4, (b) Fr = 0.5, (c) Fr = 0.6 and (d) Fr = 0.7.

induced volume-integrated buoyancy flux

$$\mathcal{B}_s = \int_V B_{cyl}\,\mathrm{d}V = \int_V B_{tot}\,\mathrm{d}V - \int_V B_{base}\,\mathrm{d}V, \tag{4.14}$$

which is a measure for the impact of the cylinder on the additional dilution of the density current and confirms the latter assumption. It is beyond the scope of the present paper to go into further details, which can be found in *Schimmels* (2008), but the results of the RANS simulations for the structure-induced volume-integrated buoyancy flux $\mathcal{B}_s$ are excellently suited as a reference for the calibration of the parameterisation described in the following section 4.2.4.

4.2.4 Calibration

The parameterisation of structure-induced mixing will be calibrated and validated as a function of instantaneous current speed and parameters of a dense bottom current. To determine these numbers, the following bulk parameters have been defined by *Arneborg et al.* (2007):

$$G'D = \int_{-H}^{\eta'} \frac{\rho - \rho_0}{\rho_0} g\,\mathrm{d}z, \quad \frac{1}{2}G'D^2 = \int_{-H}^{\eta'} \frac{\rho - \rho_0}{\rho_0} gz\,\mathrm{d}z, \tag{4.15}$$

$$UD = \int_{-H}^{\eta'} u\,\mathrm{d}z, \quad VD = \int_{-H}^{\eta'} v\,\mathrm{d}z, \tag{4.16}$$

where D is the thickness of the density current, G' its reduced gravity, U and V its velocity components and η' the vertical position of a reference density. With the bottom slope with respect to the direction of the density current, the Froude number Fr and the Ekman number K can be defined:

$$\mathrm{Fr} = \frac{U_s}{(G'D\cos\alpha_s)^{1/2}}, \quad K = \frac{C_d U_s}{fD} \tag{4.17}$$

where

$$U_s = (U^2 + V^2)^{1/2} \tag{4.18}$$

is the depth-averaged speed of the density current.

The calibration is based on the RANS simulations described in section 4.2.3, where the Ekman number is kept at a constant value of $K = 0.8$, and the Froude number was varied as $\mathrm{Fr} = 0.4$, 0.5, 0.6, and 0.7 which is the Fr range of dense bottom currents in the Arkona Sea (*Arneborg et al.* (2007)). Fig. 4.4 shows structure-induced volume-integrated buoyancy fluxes $\mathcal{B}_s$ (see eq. 4.14) between 0.3 $\mathrm{m}^5\mathrm{s}^{-3}$ and 0.6 $\mathrm{m}^5\mathrm{s}^{-3}$, which corresponds to energy fluxes between 300 W and 600 W. As expected already from Fig. 4.3, $\mathcal{B}_s$ increases with Fr in this Froude number range.

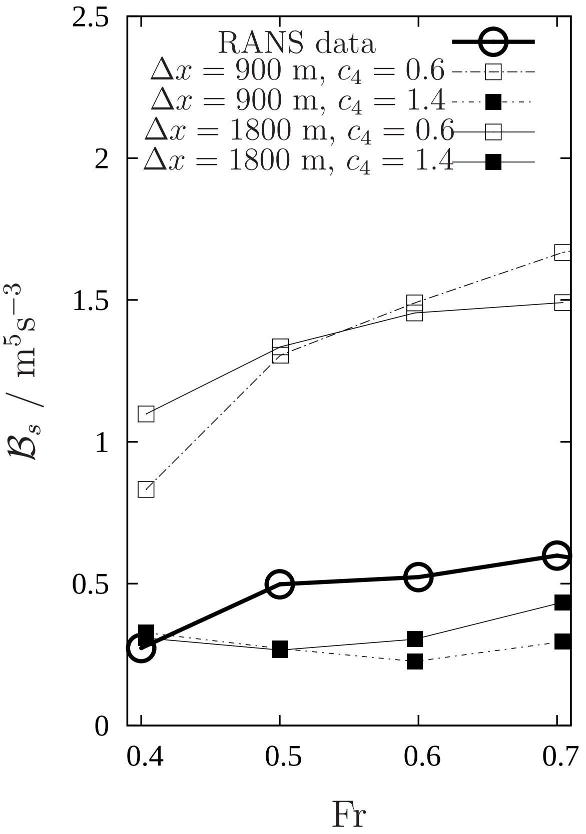

Figure 4.4: Comparison of structure-induced volume-integrated buoyancy flux, $\mathcal{B}_s$, as function of the Froude number, Fr, calculated from RANS simulations (large open circles) and from GOTM using two values of c_4 and references areas with two different sizes, $\Delta x = 900$ m and $\Delta x = 1800$ m.

The strategy for calibrating the parameterisation of structure-induced mixing is to first reproduce with a one-dimensional model the dynamics of pressure-gradient driven dense bottom currents for the same configurations as in the RANS experiments without structure-induced mixing. Then the effect of one cylinder is parameterised into the model by setting the area density to a $a = d/A$ where A is the reference area (corresponding to the area of a grid box in a three-dimensional hydrodynamic model). For each value of c_4 one simulation is then carried out. The vertically integrated buoyancy flux for both experiments (with and without cylinder) is then multiplied with the reference area A, such that the difference between them gives the additional integrated buoyancy flux due to the cylinder. This value can then be quantitatively compared to the structure-induced buoyancy flux $\mathcal{B}_s$ calculated from the RANS experiments.

For this calibration procedure the one-dimensional water column model GOTM (General Ocean Turbulence Model, see `www.gotm.net` and *Umlauf et al.* (2005)) is applied.

In both, the RANS and the GOTM simulations, the Coriolis parameter was set to $f = 1.195 \cdot 10^{-4}\mathrm{s}^{-1}$ (according to a latitude of 55°N, characteristic for the Western Baltic Sea). The initial plume thickness was set to $D = 9.5$ m, with a linear interface of 1 m thickness. Each simulation was run for one inertial period of $2\pi/f = 14.6$ h. With this configuration a pressure gradient driven plume was reproduced, with balanced dynamics and a plume thickness of approximately $D = 10$ m. To reproduce the values of Fr and K under consideration for the end of the simulation period, the interfacial slope, α, and the bottom to surface density difference, $\Delta\rho$ have been varied independently. This was obtained by executing 48 × 48 GOTM simulations with variations in α and $\Delta\rho$, resulting in variations of Fr and K at the end of one inertial period for each simulation. For the calibration simulations, the optimal combination of α and $\Delta\rho$ was then evaluated in terms of the structure-induced integrated buoyancy flux for values of Fr and K close to the prescribed RANS values.

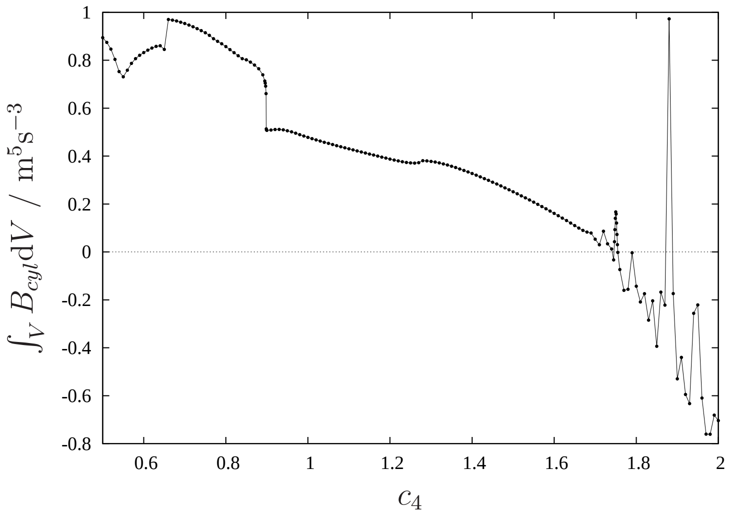

Figure 4.5: Structure-induced integrated buoyancy flux cylinder friction at Fr = 0.4 and $K = 0.8$, as function of c_4, with $\Delta x = 900$ m.

To demonstrate the impact of varying c_4 on the structure-induced integrated buoyancy flux, $\mathcal{B}_s$, c_4 was varied over a wide range for the scenario with Fr = 0.4 and $K = 0.8$. Results for $A = \Delta x^2 = 900^2$ m^2 (with $D = 10$ m yielding an area density of $a = D/\Delta x^2 = 1.2 \cdot 10^{-5}$ m^{-1}) are shown in Fig. 4.5. The structure-induced integrated buoyancy flux is generally increasing with decreasing c_4 which is consistent with (4.12) and (4.13). For $c_4 > 1.75$, $\mathcal{B}_s$ is reduced with respect to the simulations without cylinder friction parameterisation. For this parameter range, numerical instabilities occur. In contrast to that, results are numerically stable for $c_4 \leq 1.75$, with almost monotonically increasing $\mathcal{B}_s$ for decreasing c_4, except for low values of c_4 (strong mixing), where some irregularities occur. The critical value of 1.75 for this two-layer flow is larger than the critical value of $c_1 = 1.44$ which has been theoretically derived for homogeneous shear layers.

The RANS results for $K = 0.8$ and $\mathrm{Fr} = 0.4$, 0.5, 0.6, and 0.7 along with $\mathcal{B}_s$ calculated by means of the one-dimensional model including the structure friction parameterisation for values of $c_4 = 0.6$ and $c_4 = 1.4$ and horizontal resolutions of $\Delta x = 900$ m and $\Delta x = 1800$ m are shown in Fig. 4.4. As expected, the level of structure-induced integrated buoyancy flux $\mathcal{B}_s$ increases with decreasing c_4. Except for the low mixing case with $c_4 = 1.4$, $\mathcal{B}_s$ is generally increasing with increasing Froude number, a feature which is in agreement with the results of the RANS simulations. Furthermore, the resulting $\mathcal{B}_s$ is only weakly dependent on the size of the reference value $A = \Delta x^2$. The latter is a precondition for using the structure mixing parameterisation in three-dimensional models without re-calibrating for each horizontal grid layout.

Concerning the implementation of this parameterisation into the hydrostatic coastal ocean model, the value of $c_4 = 1.4$ is applied into the model as the *weak mixing* case, whereas $c_4 = 0.6$ represents the *strong mixing* scenario. Based on (4.13) which calculates the structure-induced mixing efficiency for flow without shear, the *weak mixing* scenario employs a mixing coefficient of $\Gamma = 0.24$ (mixing efficiency $R_f = 0.19$) and the *strong mixing* case a mixing coefficient of $\Gamma = 0.98$ (mixing efficiency $R_f = 0.49$). Thus, for *weak mixing* about 20% of the structure- induced buoyancy production of turbulence is used for mixing (the rest being dissipated into heat) and for *strong mixing* about 50% of the buoyancy production is used for mixing. It should be noted that compared to the complex processes of internal waves and mixing in stratified flow occurring in the vicinity of the structure the parameterisation suggested here is still quite simple, such that quite some inaccuracy is included in the present approach. Therefore, instead of only using a *best guess* calibration of the structure-induced mixing, two calibrations are used, a reasonably realistic *weak mixing* case, and a *strong mixing* case, for which it can be assumed that the real impact of offshore wind farms in the Baltic Sea is always smaller.

4.3 Methods

4.3.1 Numerical model

The numerical model GETM (General Estuarine Transport Model, see *Burchard and Bolding* (2002) and `www.getm.eu`), which is applied for the present study, is a fully baroclinic and hydrostatic ocean model using terrain-following vertical coordinates. The model is implemented using the Arakawa C-grid (*Arakawa and Lamb* (1977)) for horizontal discretisation. The vertical discretisation of GETM is based on surface and bottom following coordinates, of which σ coordinates with $\sigma = -1$ at the bottom and $\sigma = 0$ at the surface is the most simple example. Characteristic numerical features of GETM are the explicit mode splitting between the fast barotropic and the much slower baroclinic mode, the high-order advection schemes for tracer and momentum-advection (*Pietrzak* (1998)) and the possibility to apply various different turbulence closure models due to the implementation of the well-tested state-of-the-art turbulence model GOTM (General Ocean Turbulence Model, see `http://www.gotm.net`, *Umlauf et al.* (2005)). The turbulence closure model used for the coastal model setup in this study is the k-ε model with transport equations for the turbulent kinetic energy (TKE), k, and the turbulence dissipation rate, ε, extended by production terms due to structure-induced friction, see section 4.2.1. As second-moment closure, the model suggested by *Cheng et al.* (2002) is consistently coupled to the k-ε model (*Umlauf and Burchard* (2005), see section 4.2.1 for details). It should be noted that for simplicity the advection of turbulent quantities is neglected in the simulations presented here. For calculation of the internal pressure gradient the scheme by *Shchepetkin and McWilliams* (2003) is applied. As the advection scheme for momentum and tracer a TVD (Total Variation Diminishing) scheme with the ULTIMATE QUICKTEST limiter is used, for details, see *Pietrzak* (1998). For more details of the model setup, see *Burchard et al.* (2009).

4.3.2 Physical and numerical mixing analysis

Since numerical mixing is a serious issue for all coastal ocean models, it needs to be taken into account when mixing and its changes due to structures in the water has to be quantified. *Burchard et al.* (2009) argued, that for each tracer s the variance decay,

$$D^{phy}(s^2) = 2K_v(\partial_z s)^2, \tag{4.19}$$

is the appropriate measure for turbulent mixing as, e.g., the eddy diffusivity alone may take high values although under well mixed conditions there is almost no tracer mixing, see also the detailed discussion by *Burchard and Rennau* (2008).

Advection of tracers does not change the volume integrated variance of a tracer in a closed domain. However, monotone tracer advection schemes as they are generally required in coastal ocean models do reduce the volume integrated tracer variance in closed domains. *Burchard and Rennau* (2008) suggested an analysis method to quantify the numerically induced mixing: The tracer under consideration is as usual advected with the advection scheme of choice, but additionally, also the square of the tracer is advected with the same scheme. After the advection step, the square of the advected tracer is subtracted from the advected tracer square. This difference is the local reduction of the tracer square due to the advection scheme, and divided by the time step (to get a rate), this is defined as the numerically-induced tracer variance (or short: numerical mixing), $D^{num}(s^2)$.

Rennau and Burchard (2009) showed that numerical mixing for the realistic regional Western Baltic Sea model simulation presented by *Burchard et al.* (2009) amounts to about 50% of the total mixing composed of physical and numerical mixing. They also showed that reductions in numerical mixing due to improved advection schemes lead to increases in physical mixing in such a way that the total mixing is only slightly reduced by improved advection schemes. Therefore, it is the total mixing which needs to be quantified in ocean models and not only physical mixing.

4.4 Impact of parameterisation in idealised 2D and 3D hydrostatic model setups

In this section idealised 2D and 3D model simulations are carried out with GETM to demonstrate the impact of the parameterisation (section 4.2.4) implemented into the hydrostatic model applied for this study. The differences in the simulations are changes in mixing efficiency (set by the parameter c_4) due to cylindric structures as well as different horizontal model resolutions ($\Delta x = 500$ m, $\Delta x = 1000$ m and $\Delta x = 1500$ m). For all simulations a constant diameter of $d = 10$ m was used for the structures. These simulations also had the purpose to demonstrate that the parameterisation is independent on the model resolution and grid layout.

4.4.1 Idealised 2D simulations

The 2D model setup is a simple down-slope lock-exchange scenario, assuming that gradients perpendicular to the 2D plane vanish. The model domain has a length of 50 km with a linear bottom sloping from a depth of 20 m for $x = 0$ km to a depth of 30 m at $x = 50$ km. The horizontal discretisation is 1000 m × 1000 m and in the vertical 80 equidistant σ layers are used. At $x = 19$ km, structure-induced friction is introduced with with $X = 3$ cylindric structures with a diameter of $d = 10$ m, such that the area density is $A = 3 \cdot 10^{-5}$. The model is initially at rest, with a

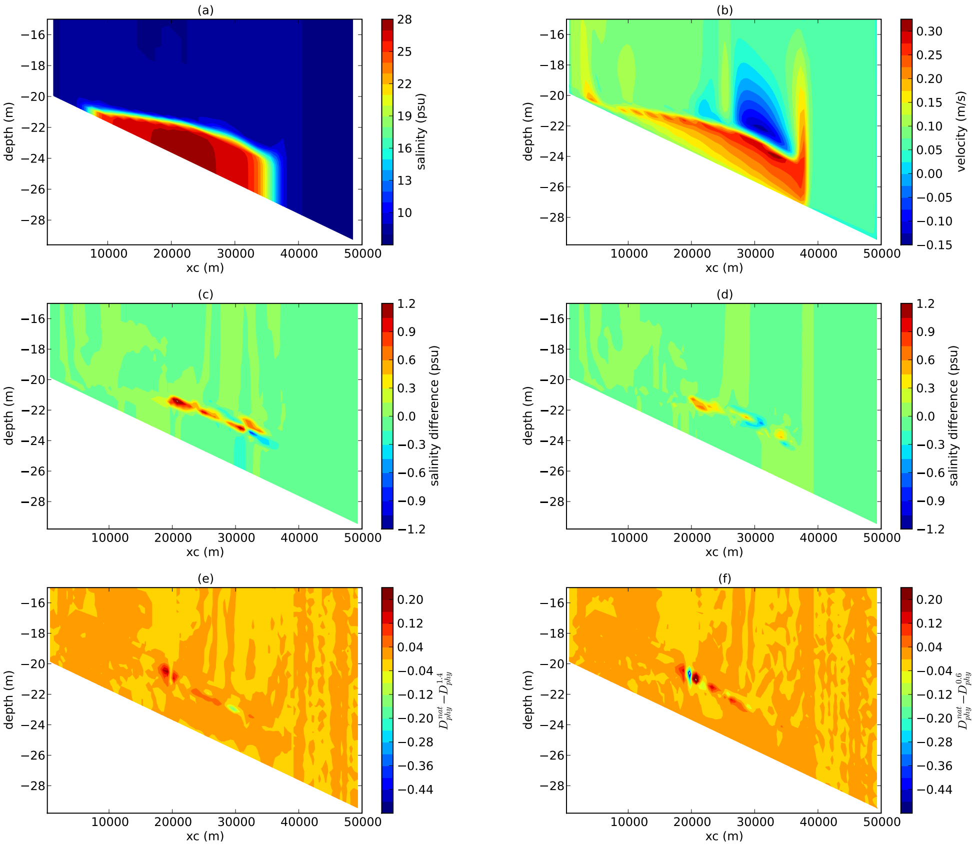

Figure 4.6: Snapshots for 2D downslope plume experiment at $t = 21$ h: (a) salinity and (b) horizontal velocity, (c) salinity difference between reference case and *weak mixing* ($c_4 = 1.4$) and (d) between reference case and *strong mixing* ($c_4 = 0.6$). Panels (e) and (f) show the difference in physical mixing between the reference case and the simulations with $c_4 = 1.4$ and $c_4 = 0.6$, respectively. Note that structure-induced friction is implemented at $x = 20$ km.

salinity of 30 psu for $x < 15$ km and $\sigma < -0.1875$ and a background salinity of 8 psu elsewhere.

Fig. 4.6a shows the salinity distribution after 21 h for the undisturbed reference case without structure-induced mixing. The differences in salinity between the reference case and cases with a cylinder are shown in Fig. 4.6c (weak mixing, $c_4 = 1.4$) and Fig. 4.6d (strong mixing, $c_4 = 0.6$). The current velocity of the plume corresponding to Fig. 4.6a is shown in Fig. 4.6b. It can be seen from panels c and d of Fig. 4.6 that the impact of the structure shows even increased entrainment for $c_4 = 1.4$ compared to the case with $c_4 = 0.6$. This can be explained by the increased blocking effect due to stronger entrainment with $c_4 = 0.6$ inducing baroclinic gradients acting in counter flow direction. Figs. 4.6e and 4.6f show the differences

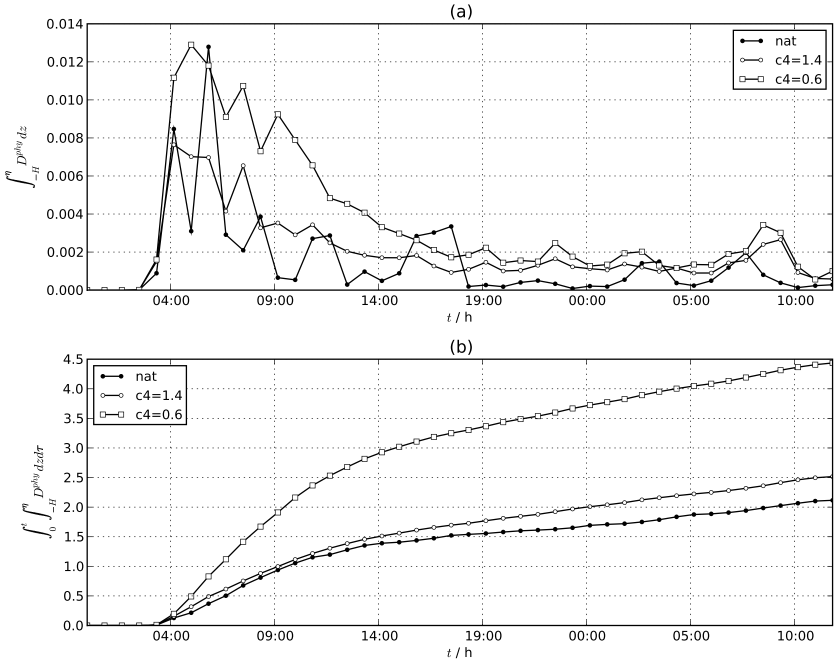

Figure 4.7: Time series of vertically integrated mixing within the water column with the structure implementation for 2D downslope plume experiment: (a) snapshots of vertically integrated physical mixing and (b) physical mixing integrated in time.

between the reference case and each of the cases with increased mixing efficiency and friction. It is found that the *strong mixing* case with $c_4 = 0.6$ indeed shows higher mixing (quantified as physically induced salinity variance decay, $D^{phy}(s^2)$) around the location of the structure than the *weak mixing* case with $c_4 = 1.4$.

Figs. 4.7a,b support increased mixing within the parameterisation, which is strongest when the plume front passes the structure. Since the case with $c_4 = 1.4$ has even shown stronger salinity decrease than the case with $c_4 = 0.6$ (see Fig. 4.6c,d), this is further investigated with the help of Fig. 4.8. Here the vertical integral of numerically and physically induced mixing of the reference case without structure implementation is subtracted by each of the two structure scenarios. It is again been demonstrated that $c_4 = 0.6$ shows stronger physical mixing within the area with structure-induced friction than $c_4 = 1.4$ at $x = 19$ km (Fig. 4.8a). Interesting is the decreased mixing upstream and downstream of the area with structure induced friction for both cases compared to the reference case with even lower mixing for the *strong mixing* case. Fig 4.8b shows the same relation but for the numerically induced mixing. Here, numerical mixing is stronger for the weak mixing case, since the vertical salinity gradients are less reduced by the physical mixing. Still, total mixing (physical & numerical) is stronger for the strong mixing case.

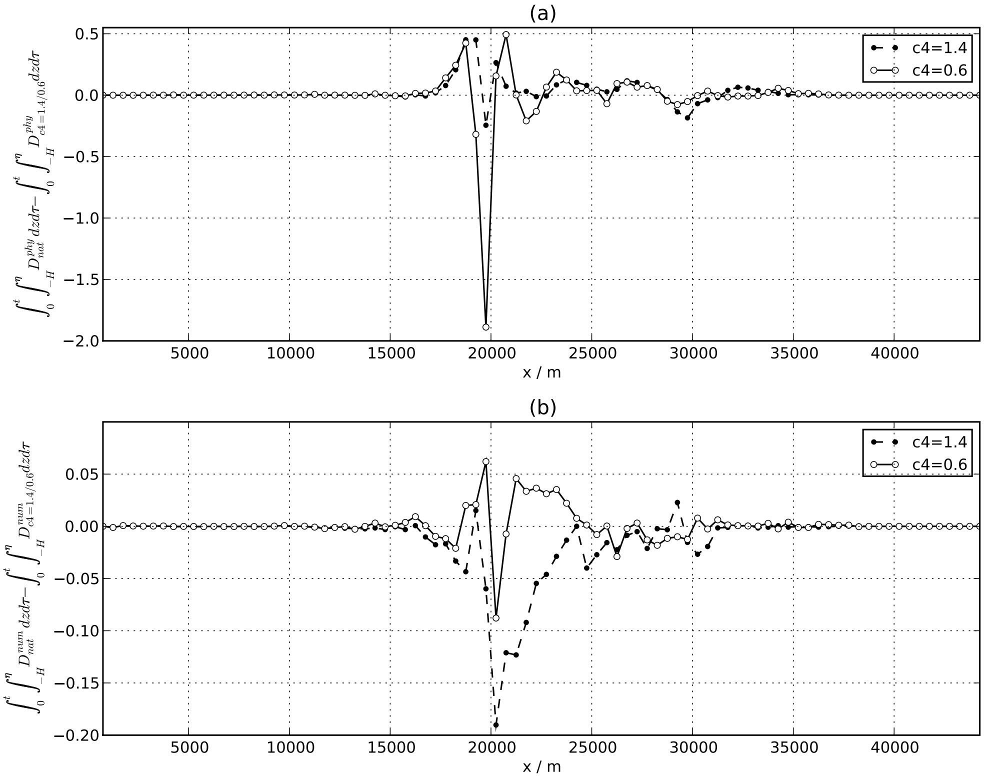

Figure 4.8: Vertically and integrated in time physical and numerical mixing for 2D downslope plume experiment after $t = 19$ h: (a) physical salinity mixing difference between natural case and both c_4 scenarios and (b) numerical salinity mixing difference between natural case and both c_4 scenarios.

4.4.2 Idealised 3D simulations

As a next step before applying the parameterisation in a full 3D realistic coastal model, a simple idealised 3D model similar to the 2D model described in section 4.4.1 is set up to study additional 3D effects such as the flow division around the region of structure-induced friction. Here the domain has a dimension of 80 km × 22 km, with a linear slope in the x-direction descending from a depth of 20 m for $x = 0$ to a depth of 60 m at $x = 80$ km. The model is initially at rest, with a salinity of 30 psu for $x < 2$ km and a background salinity of 8 psu elsewhere. The domain is discretised with $\Delta x = \Delta y = 1000$ m, and 20 vertical layers. The region with structure-induced friction is centred at $x = 18$ km and $y = 39$ km and has an extension of 3 km × 3 km, with an area density of $a = 3 \cdot 10^{-5}$.

Fig. 4.9 shows the expected behaviour of the parameterisation on a stratified flow with: (i) reduced mixing conditions upstream of the cylinder (because of the local blocking effect and reduced velocities), (ii) increased mixing over the whole water column directly in the area with structure friction (mixing is effective over the whole water column) and (iii) reduced mixing downstream of the cylinder.

Fig. 4.10 shows a snapshot of vertically integrated structure-induced mixing calculated as the difference between mixing with and without structures. The snapshot shows how mixing in the wake of the cylinder is reduced and increased at the lateral boundaries of the wake. This is due to decreased vertical tracer gradients downstream of the parameterisation. Locally the mixing within the area with structure-induced mixing is much stronger increased than the decrease downstream compared to the case without structures.

Fig. 4.11a shows the time series of snapshots of vertically integrated physical mixing in the centre (1 × 1 km) area of the structure. Again the scenario with $c_4 = 0.6$ shows more mixing than the scenario with $c_4 = 1.4$. Fig. 4.11b shows the integrated in time physical mixing at the same area (1 × 1 km in centre of structure) with orders of magnitude higher mixing than for the natural case. Fig. 4.12a,b shows the vertically integrated and integrated in time difference between the natural case and the two cases with structures of physical and numerical mixing along a section at $x = 39000$ m after $t = 19$ h. The *weak mixing* ($c_4 = 1.4$) case again shows lower physical mixing than the *strong mixing* ($c_4 = 1.4$) case but it is less pronounced than for the 2D scenario found in the previous chapter (Fig. 4.12a). This is because stronger mixing induces stronger entrainment with the consequence of a baroclinic pressure gradient acting in counter flow direction. This leads to locally reduced velocities having the potential to decrease mixing even for the *strong mixing* case. Again the feature of decreased mixing downstream of the parameterisation is found. The distribution of numerically induced mixing is different to that found in the idealised scenario. Here the numerically induced mixing is increased within the structure and decreased upstream and downstream for both the *weak mixing*

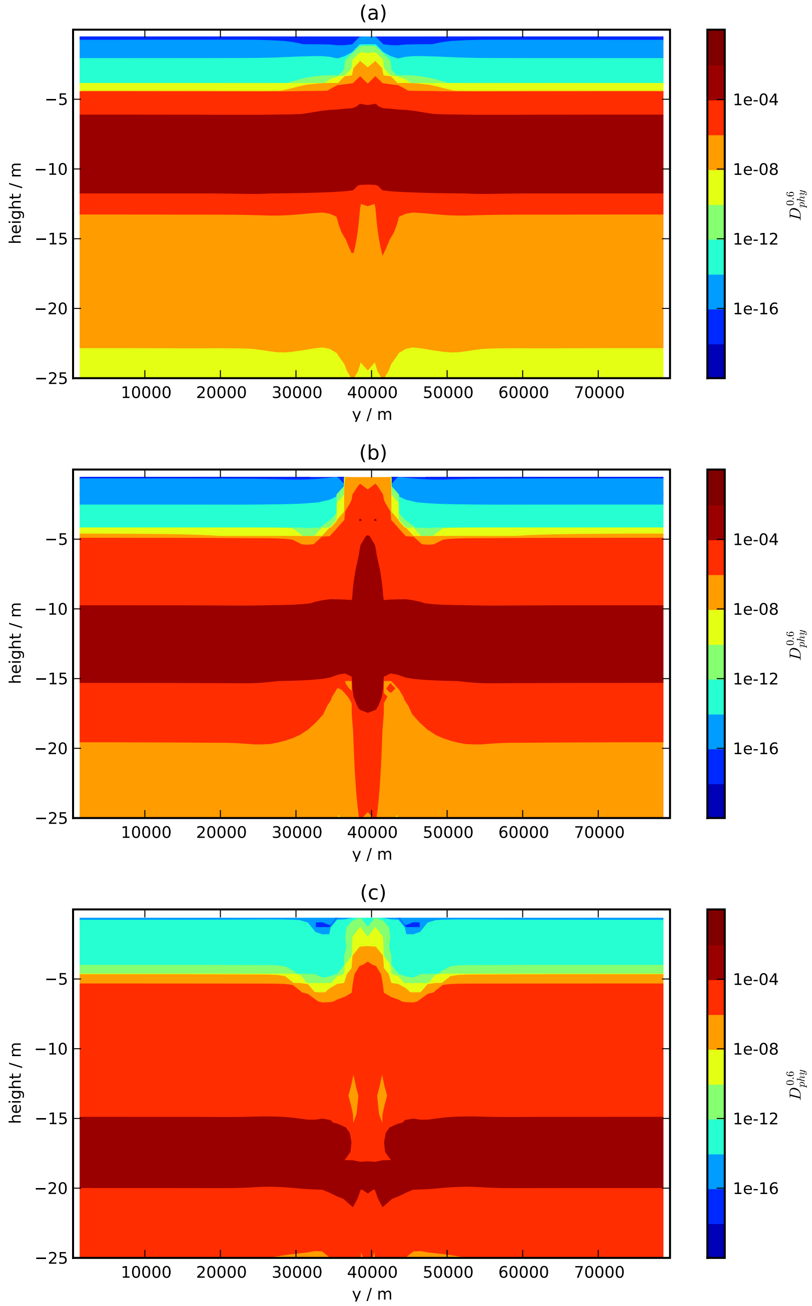

Figure 4.9: 3D downslope plume experiment: snapshots of physical salinity mixing in logarithmic scale at a vertical section 2000 m upstream ($x = 17000$ m, panel a), inside ($x = 20000$ m, panel b) and 2000 m downstream ($x = 23000$ m, panel c) of the area with structure-induced friction. The plot shows the scenario with $\Delta x = 1000$ m horizontal resolution at $t = 12$ h.

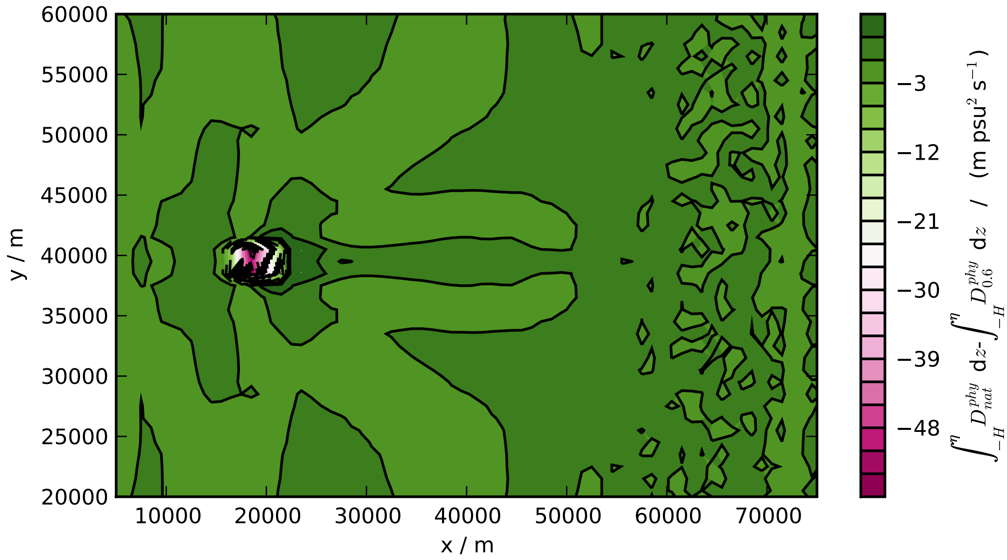

Figure 4.10: Snapshots at $t = 18$ h of the effect of structure-induced mixing for the 3D downslope plume experiment. The figure is showing the difference in vertically integrated physical salinity mixing between the reference case and the *strong mixing* scenario. The plume front for this snapshot is located at $x = 51000$ m.

and the *strong mixing* case and is higher for the *strong mixing* case. The changes in physical mixing compared to the reference case (Fig. 4.12a) are stronger than those in numerical mixing (Fig. 4.12b) and show a different horizontal distribution as already shown by *Burchard and Rennau* (2008) and *Rennau and Burchard* (2009).

4.4.3 Dependence of parameterisation on horizontal grid resolution

Fig. 4.13 shows for the same 3D physical scenario as discussed in section 4.4.2 the dependence of total salinity mixing (physical & numerical) on the horizontal model resolution ($\Delta x = 250$ m, $\Delta x = 500$ m and $\Delta x = 1000$ m) introduced by structure-induced mixing. For each of the three model resolutions close to 100 model simulations with the idealised 3D plume setup described in section 4.4.2 were carried out using different area densities a as well as different values for c_4. For the mixing calculated the volume integral was taken over the area with structure-induced mixing together with a 2 km wide area around to include into the integration areas with decreased mixing upstream and downstream of the parameterisation as shown by Fig. 4.8a too. The values of up to 25% increased mixing (Fig. 4.13) are lower than the increase found in Fig. 4.11 because of integrating an area of 2 km

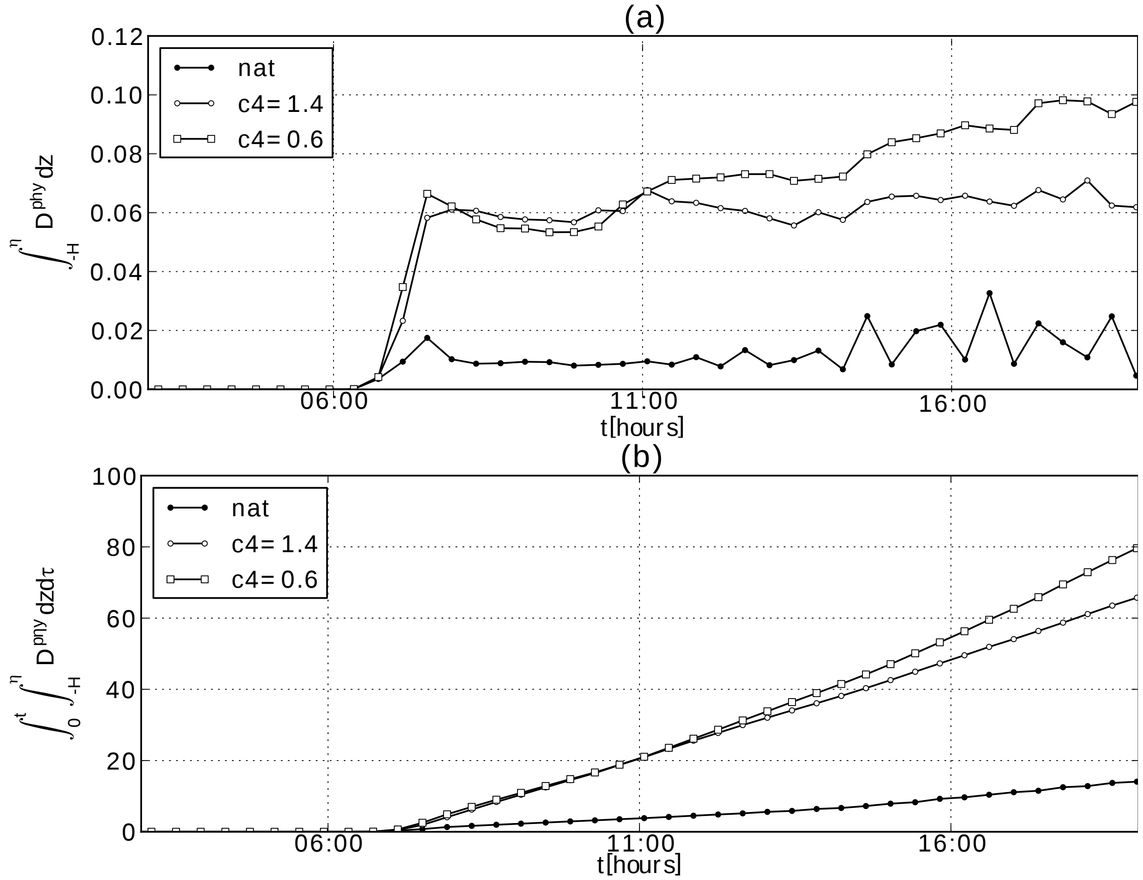

Figure 4.11: Time series of vertically integrated mixing within the centre water column with the structure implementation for 3D downslope plume experiment and $\Delta x = 1000$ m: (a) snapshots of vertically integrated physical mixing and (b) physical mixing integrated in time.

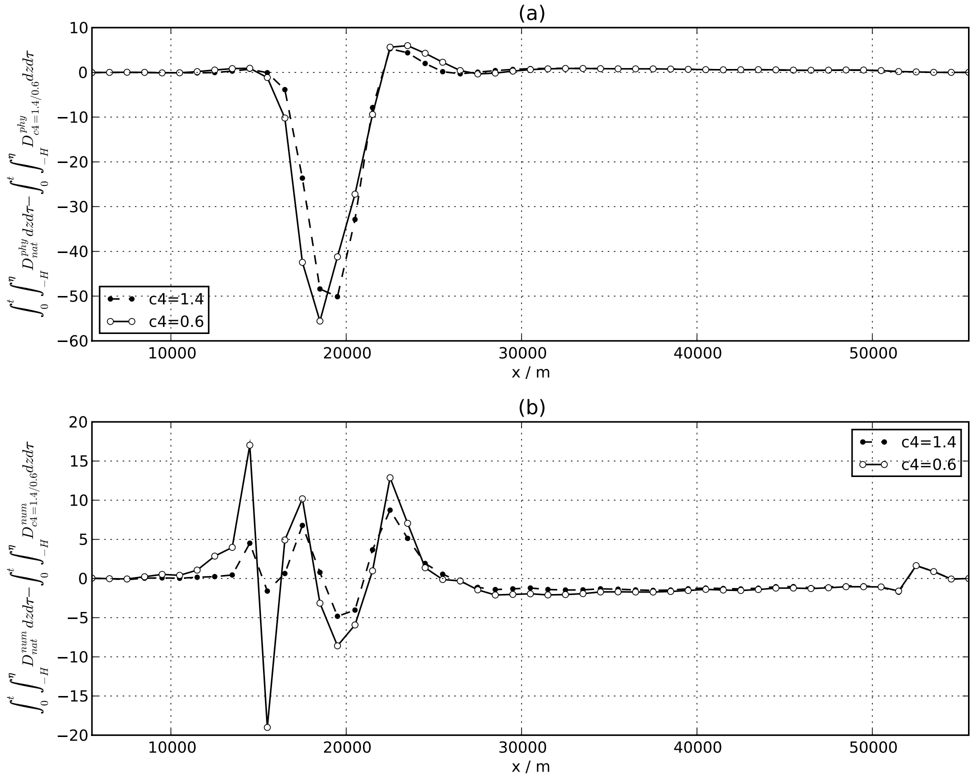

Figure 4.12: Vertically and integrated in time physical and numerical mixing for 3D downslope plume experiment ($\Delta x = \Delta y = 1000$ m) after $t = 19$ h at $y = 39000$ m.: (a) physical salinity mixing difference between natural case and both c_4 scenarios and (b) numerical salinity mixing difference between natural case and both c_4 scenarios.

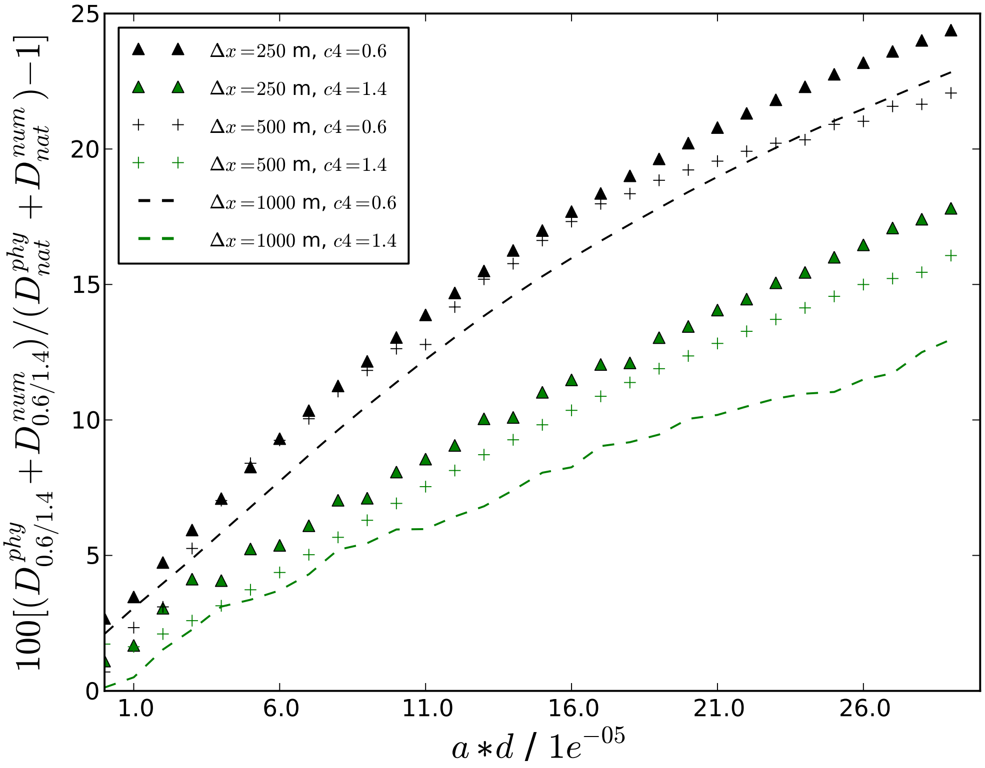

Figure 4.13: 3D downslope plume experiment: Impact of different horizontal model resolutions on the total (numerical + physical) salinity mixing. For this image more than hundred scenarios with different values for the area density a and values of c_4 were calculated.

around the structure into the calculation presented in this section. However, it is found that the total salinity mixing induced by the structure-induced mixing is slightly depending on grid resolution and some convergence of the total mixing for decreased resolution can be noted, except for $c_4 = 0.6$ at high area densities. To summarise, it is found that the dependence of the parameterisation is sufficiently independent on the model resolution.

4.5 Application to the Western Baltic Sea

To quantify the potential impact of offshore wind farms in the Western Baltic Sea, the validated realistic model setup using GETM as presented by *Burchard et al.* (2009) has been used as a reference case. This model setup which has an open

Name	Position	Area [km^2]	# of turbines	Area density a
1. Kriegers Flak	55.00°/13.16°	41.61	80	$1.92 \cdot 10^{-5}$
2. Nystedt	54.53°/11.67°	33.69	72	$2.14 \cdot 10^{-5}$
3. Kriegers Flak 2	55.10°/13.00°	68.37	128	$1.87 \cdot 10^{-5}$
4. Arkona-Becken Südost	54.77°/14.30°	44.59	80	$1.79 \cdot 10^{-5}$
5. Adlergrund GAP	54.83°/14.12°	5.94	31	$5.21 \cdot 10^{-5}$
6. Beltsee	54.41°/11.55°	38.64	25	$6.47 \cdot 10^{-6}$
7. Baltic 1	54.58°/12.61°	15.85	21	$1.32 \cdot 10^{-5}$
8. Ventotec Ost 2	54.86°/14.06°	46.57	50	$1.07 \cdot 10^{-5}$
9. ARCADIS Ost 1	54.83°/13.52°	30.72	70	$2.28 \cdot 10^{-5}$
10. ARCADIS Ost 2	54.82°/14.10°	14.86	25	$1.68 \cdot 10^{-5}$
11. GEOFReE	54.25°/11.38°	5.94	5	$8.41 \cdot 10^{-6}$
12. Rødsand 2	54.55°/11.47°	49.54	≈50	$1.01 \cdot 10^{-5}$
13. Adlergrund 500	54.82°/14.10°	13.87	20	$1.44 \cdot 10^{-5}$
14. ArkonaSee Ost	54.85°/14.00°	9.91	≈40	$4.04 \cdot 10^{-5}$
15. ArkonaSee Süd	54.80°/13.85°	20.81	80	$3.84 \cdot 10^{-5}$
16. ArkonaSee West	54.80°/13.82°	25.76	≈80	$3.11 \cdot 10^{-5}$
17. BalticEagle	54.80°/13.85°	62.42	80	$1.28 \cdot 10^{-5}$
18. BalticPower	54.93°/13.12°	71.34	≈80	$1.12 \cdot 10^{-5}$
19. Adlergrund Nordkap	54.83°/14.03°	39.63	31	$7.82 \cdot 10^{-6}$
20. Sky2000	54.30°/11.38°	21.80	≈50	$2.29 \cdot 10^{-5}$

Table 4.1: Names, geographical position, area, number of turbines and area density of OWFs for the scenarios R1.4 and R0.6. Values with ≈ have been estimated by the authors because no data was available for these OWFs. Area densities have been calculated on the basis of an assumed diameter of $d = 10$ m for each wind turbine.

northern boundary in the Kattegat and an open eastern boundary in the Stolpe sill area, is forced by open boundary values from a multi-annual Baltic Sea model with a resolution of 3 nm (nautical miles) described by *Neumann et al.* (2002) and meteorological forcing from the German Weather Service Local Model with a resolution of 7 km and 3 hours. The Western Baltic Sea model has a horizontal resolution of 0.5 nm and is vertically resolved by 50 general vertical coordinate layers, with a non-linear zooming towards the bed. The simulation is initialised on Sep 1, 2003 and the 16 month evaluation periods end on Dec 31, 2004. For further details, see *Burchard et al.* (2009).

In addition to this natural mixing study, four scenarios with different horizontal distributions of offshore wind farms (OWFs) and different values for c_4 are calculated over a period of 16 months. This period covers a sufficient amount of medium-

Name	Area $[km^2]$	# of turbines	Area density a
A. WP-Fehmarn	645.6	1379	$1.98 \cdot 10^{-5}$
B. WP-Darss	298.8	638	$1.98 \cdot 10^{-5}$
C. WP-KFNE	199.2	425	$1.98 \cdot 10^{-5}$
D. WP-Arkona	6972.6	14886	$1.98 \cdot 10^{-5}$

Table 4.2: Names, area, number of wind turbines and area density of unrealistically extensive OWFs at Fehmarn (WP-Fehmarn), Darss (WP-Darss), Kriegers Flak North-East (WP-KFNE) and at the Arkona Sea (WP-Arkona). A,B,C,D refers to Fig. 4.14. The area density used was the mean value of the area densities used in table 4.1.

Code	OWF distribution	c_4	meaning
R1.4	as planned in 2010	1.4	realistic OWF distribution, *weak mixing*
R0.6		0.6	realistic OWF distribution, *strong mixing*
U1.4	unrealistically extensive	1.4	unrealistic OWF distribution, *weak mixing*
U0.6		0.6	unrealistic OWF distribution, *strong mixing*
REF	none (natural case)	-	reference case

Table 4.3: Specifications of different Western Baltic Sea simulations with and without OWFs.

intensity inflow events to provide enough statistical certainty concerning the impact of structure-induced mixing. For the four different scenarios two distributions of OWFs (a realistic distribution with all existing and planned wind farms, see table 4.1 and a very extensive distribution, see table 4.2) and two degrees of structure-induced mixing efficiencies with *weak mixing* ($c_4 = 1.4$) and *strong mixing* ($c_4 = 0.6$) are investigated. Both wind farm distributions are shown in Fig. 4.14. The specifications of these five scenarios are summed up in table 4.3.

The impact of OWFs is quantified by means of calculating net transports of different density and salinity classes through the Bornholm Channel and mean vertical density profiles in this area. The Bornholm Channel is well suited for such a quantification because of the topographic conditions in the Western Baltic Sea which ensure that almost all dense, oxygen carrying bottom water from the North Sea has to pass through this narrow channel on its way towards the eastern basins of the Baltic Sea (see also Fig. 4.1).

4.5.1 Diapycnal mixing

Fig. 4.15a shows a time series (Jan 2004 - Dec 2004) of the bottom salinity at the Bornholm Channel (see Fig. 4.14 for the exact position) for the reference case and Fig. 4.15b shows the differences in the time series of the natural case (REF) subtracted by each of the four OWF cases (R1.4, R0.6, U1.4 and U0.6). As an expected result it is found, that both U1.4 and U0.6 cases show higher difference values than the realistic scenarios R1.4 and R0.6. With a few exceptions, maximum differences are below 1 psu for all cases.

Plotting these data as a probability distribution reveals that both positive and negative differences show a similar distribution around zero (Fig. 4.15c, only shown for R1.4). The mean values for the bottom salinity differences over these 12 months are $\Delta s_b = 0.0059 \pm 0.491$ for R1.4, $\Delta s_b = 0.0222 \pm 0.469$ for R0.6, $\Delta s_b = 0.1728 \pm 0.595$ for U1.4, and $\Delta s_b = 0.4222 \pm 0.560$ for U0.6. This indicates a small net decrease of bottom salinity due to a realistic distribution of OWFs in the Western Baltic Sea which is even for the *strong mixing* case more than one order of magnitude smaller than the standard deviation of the impact. As expected, the signal is much clearer for the scenarios with unrealistically extensive OWF distributions, but even for the most extreme case the standard deviation is larger than the signal.

Since the statistics for one position shown in Fig. 4.15 do not conclusively show the net effect of OWFs in the Western Baltic Sea on the ventilation of the Baltic Sea basins, changes in salinity distribution during one month (June 2004) with relatively strong saline inflows through the Bornholm Channel are shown in Fig. 4.16. Clearly, highest monthly mean salinities occur at the bottom of the eastern part of the Bornholm Channel. There, the decrease of salinity due to OWFs are between 0.05 psu (R1.4) and 0.1 psu (R0.6). Above the bottom mixed layer, a relative increase of salinity due to OWFs is detected, which indicates that additional entrainment diluted these dense bottom currents further upstream in the Arkona Sea and consequently elevated the density interface.

Fig. 4.17a shows results of an investigation of water mass transport within certain density classes (with $\Delta\rho = 0.2\ \mathrm{kg\,m^{-3}}$) for the reference case (REF). The expected behaviour of dense bottom water propagating into the Bornholm Basin (positive values) and lighter near-surface water flowing out of the Baltic Sea can be clearly seen. The model derived water mass transport averaged over 4 months with significant inflow events (Nov 2003, Mar 2004, Jun 2004 and Jul 2004) amounts to about $0.42 \cdot 10^6\ \mathrm{kg\,s^{-1}}$ which is consistent with the findings by *Reissmann et al.* (2009). The inflowing water mass transport is distributed over more density classes than the outflows, because inflow events show a strong variability in salinity. Fig. 4.17b shows that water mass transport within the highest four density classes is strongly reduced (by up to 100%) and moved downwards the density class scale (with some increases and decreases of water mass transport in respective classes).

As only higher densities have the ability to ventilate the deeper layers in the eastern parts of the Baltic Sea, this may have some theoretical ecological impact. However, Fig. 4.17b shows that the total salt flux reduction in the highest four density classes is small. In the following section 4.5.2 an inflow in Mar 2004 which causes a significant decrease in bottom salinity for the scenario with extensive wind farms but weak mixing (U1.4) is investigated in detail with regard to changes in depth of interleaving of dense bottom currents in the Bornholm Sea.

4.5.2 Impact of one single inflow

As seen in Fig. 4.15a and discussed in the previous chapter, there may be certain events with higher densities that are strongly diluted by the OWFs (density differences of up to 3 psu for the U1.4 scenario in Mar 2004). Although the strong mixing during this inflow event can be regarded as a single extreme event, we analyse it to see how a strong mixing signal affects the ventilation in the Bornholm Sea. In average, as shown by Fig. 4.17c, the change in transport of highly saline water is negligibly small. It can be assumed that a complete dilution of the highest density classes has a negligible ecological effect as the total transport into the Bornholm Sea connected to these classes is small.

When considering a time-series of bottom salinity at the Bornholm Channel as demonstrated by Fig. 4.15a it is seen that the differences between the REF case and all four cases is positive in average, meaning a net decrease in salinity due to OWFs. In Mar 2004 bottom salinity is decreased by 3 psu for the U1.4 case. In order to study the impact of this decrease on the ventilation of intermediate layers in the Bornholm Sea, a passive tracer is released in the Bornholm Channel with a concentration of unity in the REF case and also in the U1.4 case. The resulting bottom tracer concentrations on Mar 31 are shown in Fig. 4.18a for the reference case and in Fig. 4.18b the difference in bottom tracer concentration for the U1.4 scenario is shown. The decrease in bottom tracer concentration due to the extensively distributed OWFs is up to 30%, which indicates that the detachment of the tracer from the bottom is taking place higher in the water column. Fig. 4.18c demonstrates for a cross-section through the Bornholm Sea how this interleaving process with a typical interleaving depth of 60 m happens. To quantify the changes in interleaving depth due to the extreme OWFs case (U1.4), the centre of gravity of the tracer cloud for each scenario has been calculated as function of the tracer concentration on Mar 31. Clearly, for a wide range of tracer concentrations the interleaving depth is decreased by up to 3 m due to OWF mixing in the Western Baltic Sea. One should however keep in mind that this is an extreme case (compare to Fig. 4.15a) and that for scenarios with realistic OWF distributions (scenarios R1.5 & R0.6) changes in interleaving depth are substantially below 1 m.

4.5.3 Impact on annual time scale

To investigate on how mean salinities are affected for the four OWF scenarios, the bottom salinity of the reference case (REF) is compared to the four OWF scenarios by taking the 16 month mean bottom salinity of the natural case and subtracting the mean bottom salinity of each of the four cases (see Fig. 4.19). The bottom salinity differences found for the cases with realistic OWF distribution, R1.4 and R0.6, are in the order of up to 0.2 psu. Interestingly, in the Arkona Sea the saline bottom waters seem to be less diluted by OWFs when strong mixing is assumed (R0.6). This may be explained by the fact that dense bottom currents are decelerated by OWFs such that entrainment of less saline ambient waters may be locally reduced. However, for the R0.6 scenario, bottom salinities are reduced more significantly than for the weak mixing R1.4 scenario, which is consistent with a net increase in mixing and which is more relevant for the ventilation of intermediate layers in the Bornholm Sea.

A different picture is found for the two cases with extensive OWF distributions, U1.4 and U0.6, where the mean bottom salinity is decreased by up to 0.3 psu for U1.4 and by up to 0.6 psu U0.6. A similar picture between the four different scenarios arises along a transect through the Bornholm Channel. Fig. 4.20 shows the differences in annual mean salinity between the reference scenario (REF) and the four OWF scenarios. The bottom salinity differences for the two cases with realistic distribution of OWFs are in the order of up to 0.03-0.05 psu and for the extensive OWF cases between 0.15 psu (U1.4) and 0.45 psu (U0.6). All difference plots show a similar behaviour with decreased bottom salinities and stronger impact at the western channel. The feature of decreased mean bottom salinities, increased mean salinities due to the OWFs in the area of the pycnocline and decreased transport above the pycnocline, which has been found investigating monthly differences at this transect (see Fig. 4.16), was not found in the annual mean differences. This is because of the different plume strengths passing the Bornholm Channel which averages away the area of increased mean salinities in the area of the pycnocline.

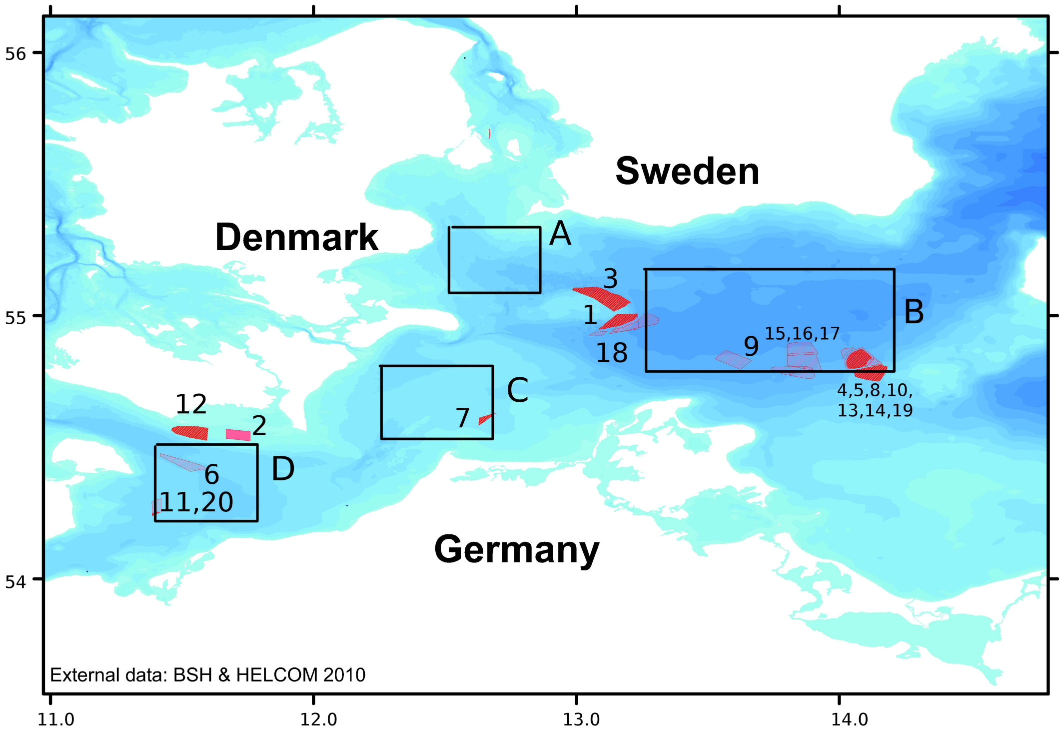

Figure 4.14: Distribution of offshore wind farms (OWFs) in the Western Baltic Sea (external data from Bundesamt für Seeschifffahrt und Hydrographie, see Marnet website at `www.bsh.de`, situation in April 2009) as used for model scenarios R1.4 and R0.6. The status of each of the OWF's is as follows: red: approved, dark magenta: operational and light magenta: projected. Please note that some of the projected OWF sites overlap each other. The black rectangles indicated by A,B,C,D are the OWF's for the unrealistically extensive distribution applied in model runs U1.4 and U0.6. The black line north-west and the black cross west of the Isle of Bornholm indicate locations for model output (see Fig. 1.2 for geographical locations). The numbers in this map refer to the wind farms detailed in table 4.1.

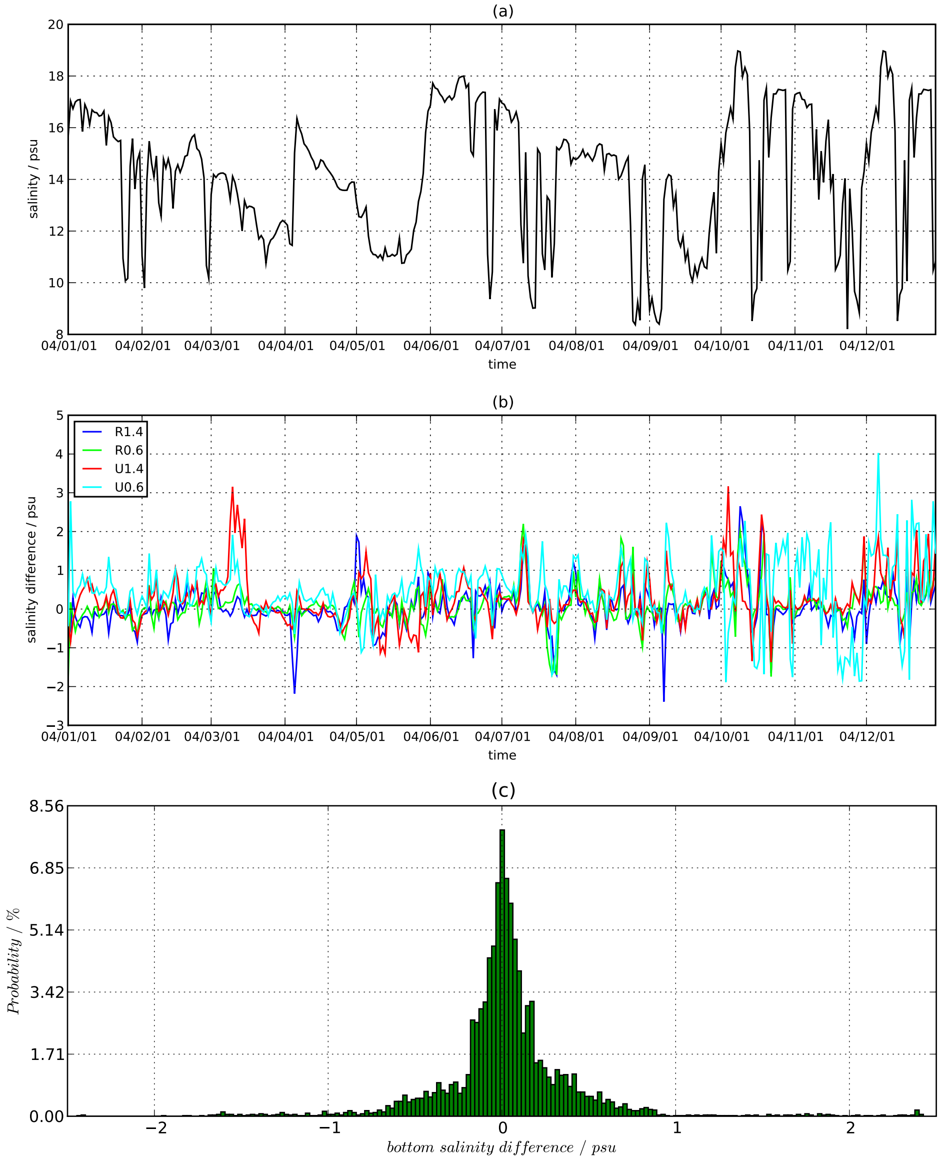

Figure 4.15: Western Baltic Sea simulation: a) Time series of bottom salinity in the Bornholm Channel (see Fig. 4.14 for the location); b) time series of difference in Bornholm Channel bottom salinity between the reference case (REF) and the scenarios with OWFs ($\Delta s_b > 0$ means reduction of salinity due OWF impact); c) probability distribution for this time series for scenario R1.4.

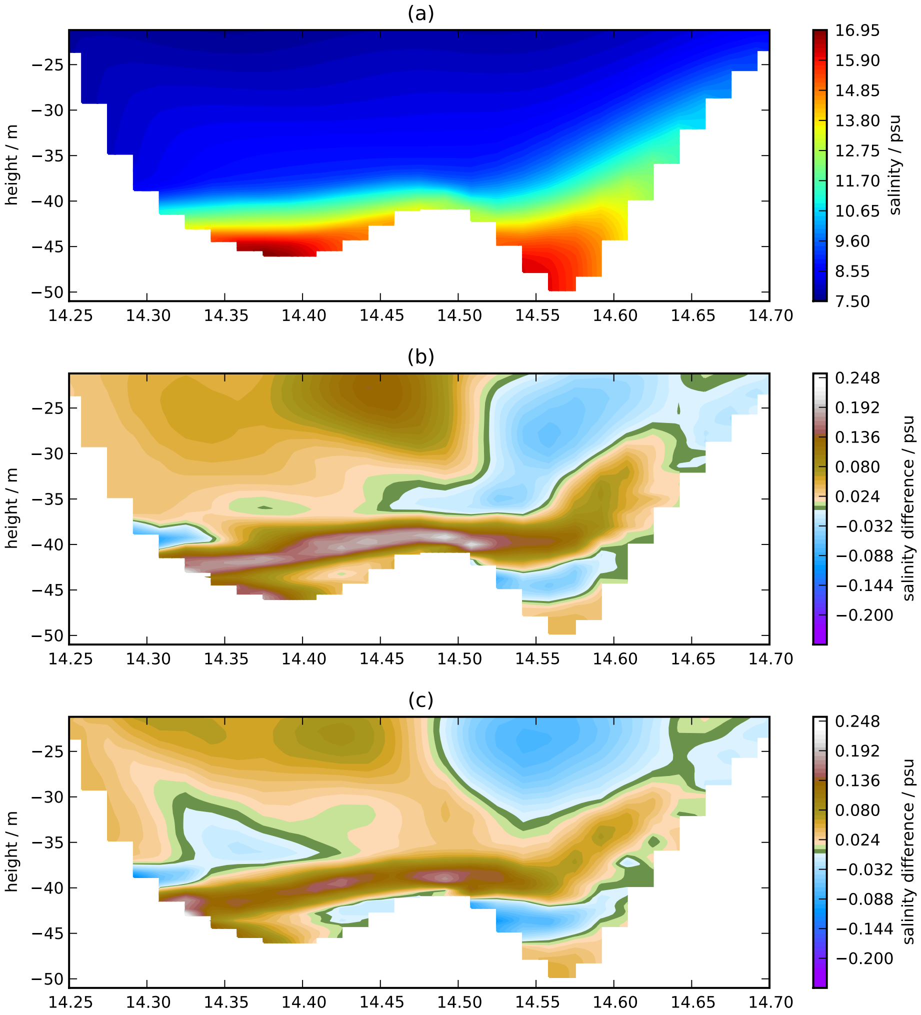

Figure 4.16: Western Baltic Sea simulation: a) monthly mean (June 2004) salinity for the reference scenario (REF) along a transect across the Bornholm Channel (see Fig. 4.14 for the location); b) monthly mean salinity change due to OWF along same transect for the scenario R1.4; c) monthly mean salinity change due to OWF along same transect for the scenario R0.6.

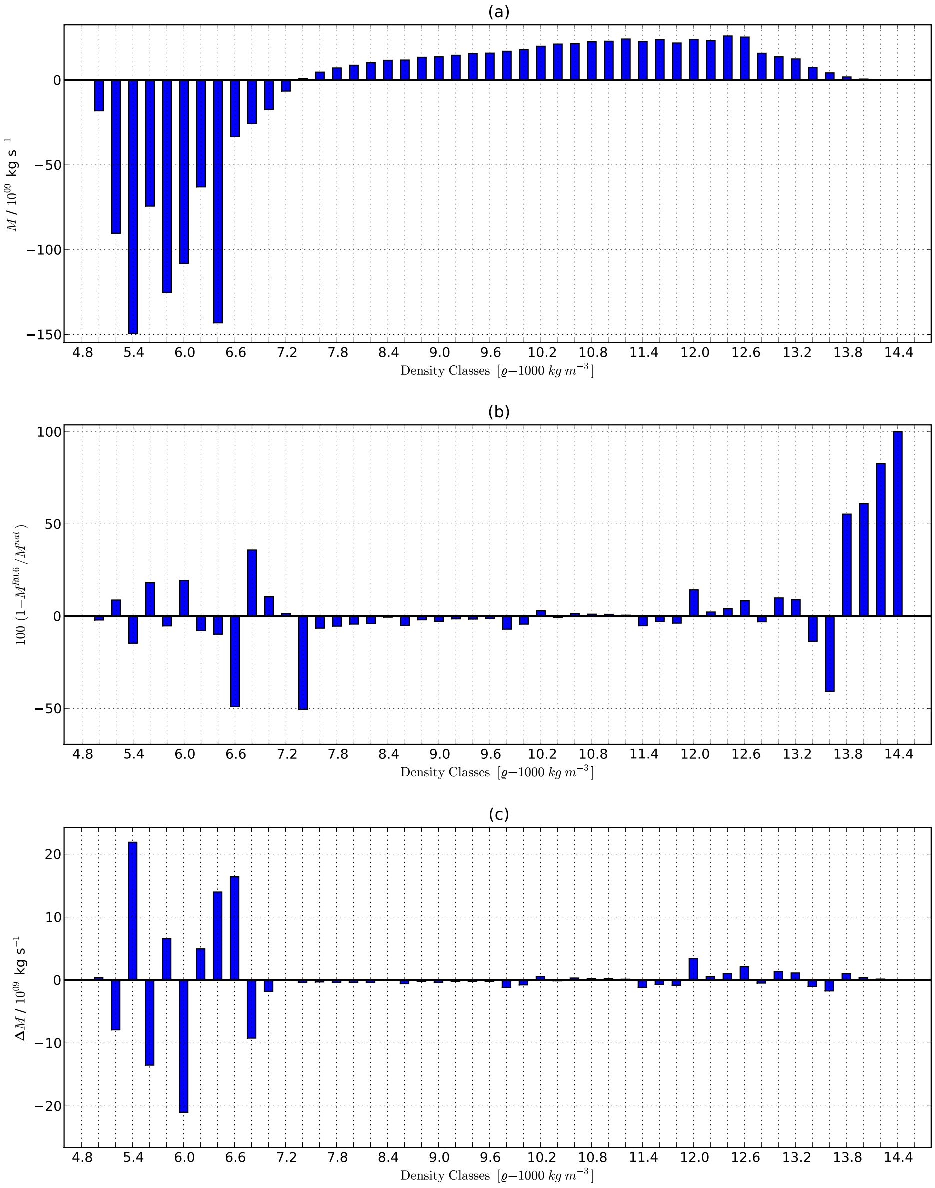

Figure 4.17: Western Baltic Sea simulation: monthly mean (averaged over Nov 2003, Mar 2004, Jun 2004 and Jul 2004 during which relative strong inflow activity was detected) water mass transport M across a transect at Bornholm Channel (see Fig. 4.14 for the location), shown as contributions from density classes. a) water mass transport M for reference scenario (REF); b) difference in % between reference (REF) and R0.6; c) difference in water mass transport ΔM between reference (REF) and R0.6;

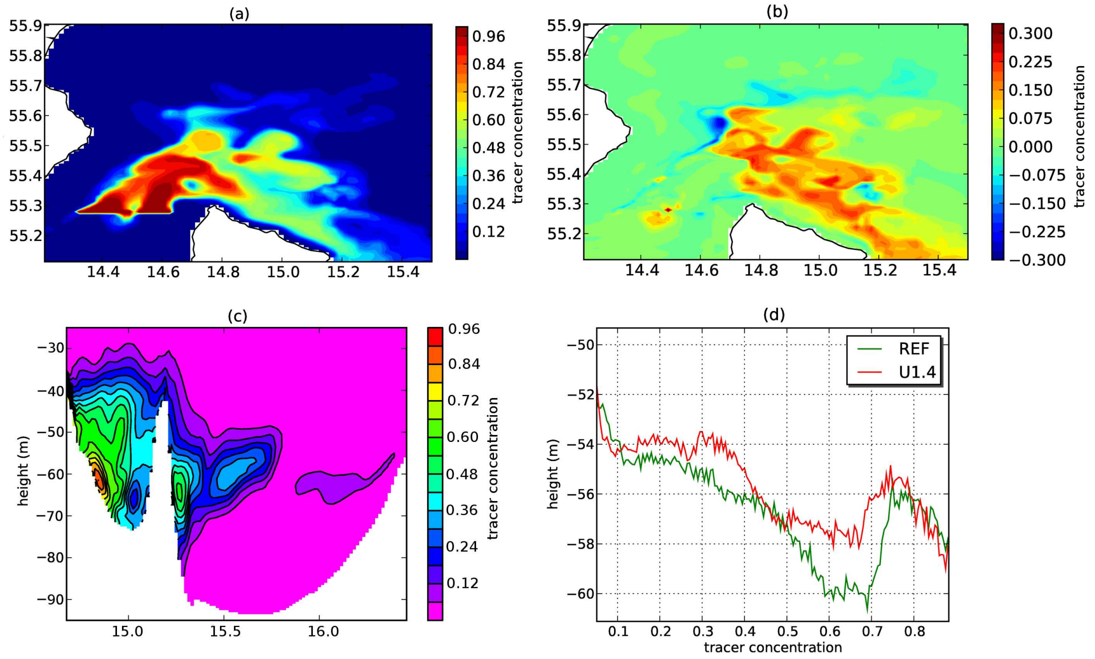

Figure 4.18: Western Baltic Sea simulation, monthly mean (Mar 2004) results from numerical tracer release experiment as example for strong impact of OWF (scenario U1.4): a) bottom tracer distribution for reference case (REF); b) difference in bottom tracer distribution between REF and U1.4 (positive means reduction of tracer concentration due to OWFs); c) tracer distribution along a transect through the Bornholm Sea (see Fig. 4.14 for the location); d) height of centre of gravity of tracer cloud as function of tracer concentration.

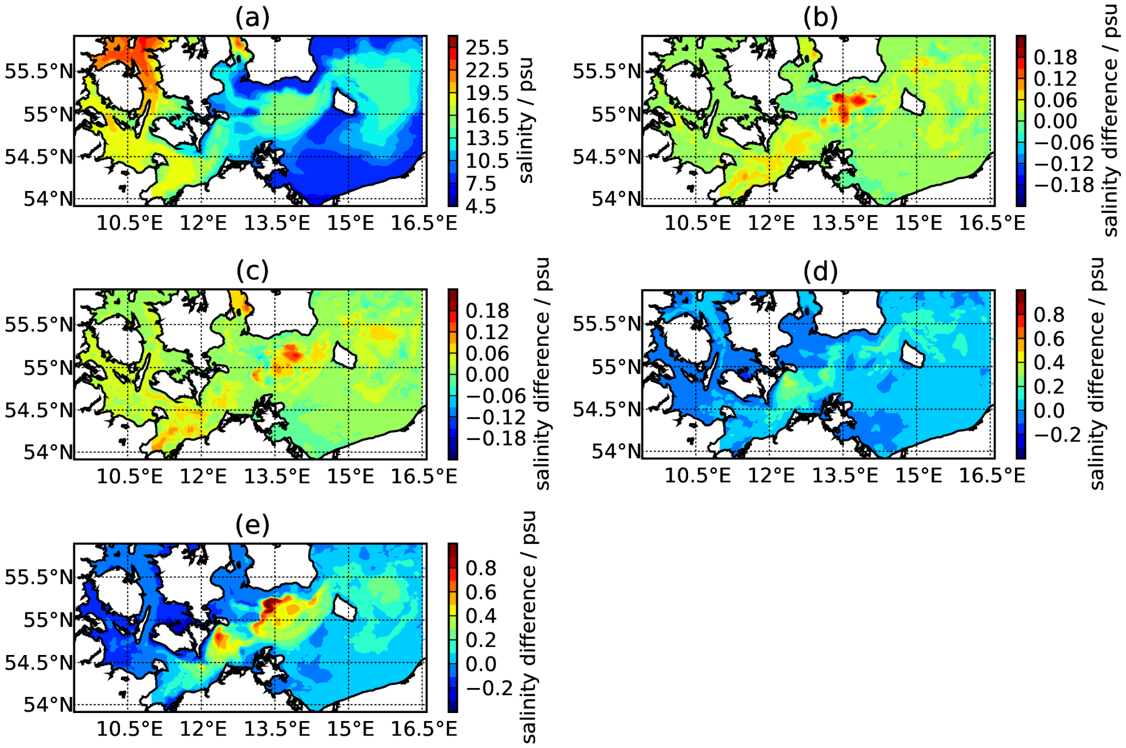

Figure 4.19: Western Baltic Sea simulation; annual mean (year 2004) of bottom salinity and bottom salinity difference due to OWFs: a) reference scenario REF; b) scenario REF - R1.4; c) scenario REF - R0.6; d) scenario REF - U1.4; e) scenario REF - U0.6.

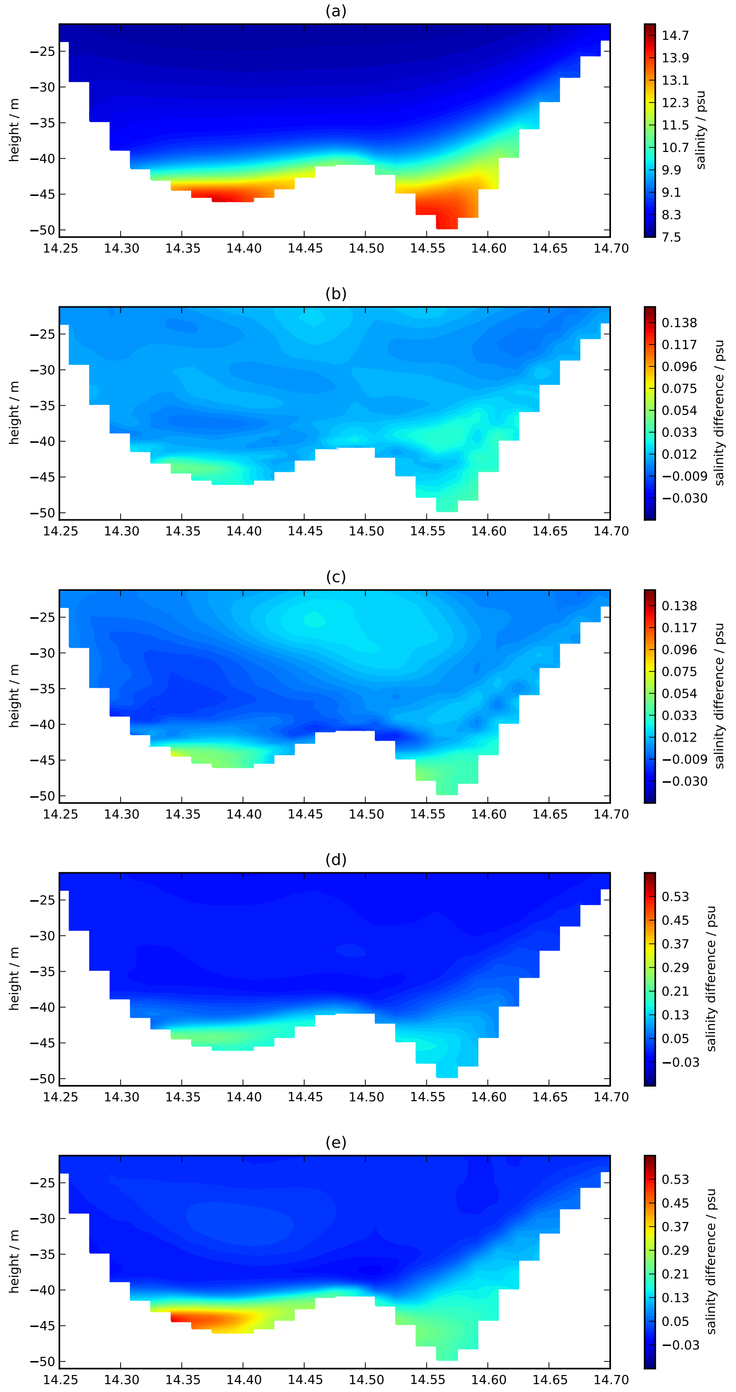

Figure 4.20: Western Baltic Sea simulation: annual mean (year 2004) of salinity difference along a transect through the Bornholm Channel (see Fig. 4.14 for the location); due to OWFs: a) reference scenario REF; b) scenario REF - R1.4; c) scenario REF - R0.6; d) scenario REF - U1.4; e) scenario REF - U0.6.

Chapter 5

Discussion and conclusions

Based on a carefully validated three-dimensional model for the Western Baltic Sea (*Burchard et al.* (2009)), the impact of offshore wind farms on dense water inflows into the Baltic Sea has been studied. To include the effects of these structures which are of a fairly small scale into a regional and hydrostatic ocean model, a parameterisation for structure-induced friction in unstratified flow (*Svensson and Häggkvist* (1990)) had to be recalibrated to properly represent vertical mixing in strongly stratified flow. This parameterisation is based on additional quadratic friction terms in the momentum equations as well as additional production terms in the dynamic equations for turbulent kinetic energy and its dissipation rate, the latter of which includes a calibration parameter (c_4). The physical meaning of this parameter could be identified to be connected to the structure-induced mixing efficiency. The calibration strategy applied here was to compute structure-induced mixing by means of a numerical model resolving the structure as well as the small-scale hydrodynamic processes in the vicinity of the structure. For simplicity and to be fairly general, cylindric structures had been chosen for this purpose. A numerical model based on the Reynolds-Averaged Navier-Stokes (RANS) equations and using a k-ε turbulence closure model to compute eddy viscosity and diffusivity had been found appropriate to resolve the relevant dynamics (*Schimmels* (2008)). Using this model, an idealised dense bottom current as it is typically seen in the Western Baltic Sea during inflow situations (*Burchard et al.* (2005); *Arneborg et al.* (2007)) had been forced in such a model, such that various mixing parameters could be calculated under a variety of Froude numbers and Ekman numbers with an without impact of one cylinder. The volume integrated additional buoyancy flux (difference in buoyancy flux between cases with and without cylinder-induced friction) had been identified as the critical parameter to quantify the mixing impact of a cylinder. For an Ekman number ($K = 0.8$) typical for inflows in the Western Baltic Sea, and a dense bottom current of 10 m thickness with a cylinder of 10 m diameter, structure-induced buoyancy production from the RANS model was compared to equivalent buoyancy production from a high-resolution water column model for a variety of Froude numbers and values for c_4. It was found that a value of $c_4 = 1.4$ resulted in mixing slightly smaller than predicted (20% mixing efficiency) and that a value of $c_4 = 0.6$ (mixing efficiency of about 50%) resulted in an overestimation of mixing by about a factor of two. Due to the uncertainty of the RANS model and the fact that the design of wind turbine foundations often strongly deviates from cylindric structures, it was decided to use both values, i.e. $c_4 = 1.4$ as *weak mixing* case and $c_4 = 0.6$ as *strong mixing* case.

Several idealised numerical experiments showed that the parameterisation is consistent in the sense that mixing is indeed increased for increased structure-induced mixing efficiency. It was furthermore shown that the total mixing (physical & numerical) is fairly independent of the horizontal model resolution. It can therefore be concluded that the approach chosen here has the capability to give reliable quantitative estimates of additional mixing due to offshore wind farms and its ecological consequences for the Baltic Sea.

Besides the reference experiment without structure-induced mixing, four impact assessment simulations have been carried out, with two wind farm distributions, one including all existing, approved and planned wind farms, and a second one with unrealistically extensive wind farms, just to study the potential impact of such a worst case scenario.

First of all, it requires a careful analysis to see any significant changes in saline inflows due to the offshore wind farms. Since almost all inflows into the Baltic Sea proper have to pass the Bornholm Channel just east of the Western Baltic Sea region with potential wind farm impact, a study of the near-bottom salt and mass inflow in that region has been made. One result is that the impact of wind farm mixing leads to spatially and temporally varying changes in bottom salinity, with decreases for realistic wind farm distributions by 0.0059 ± 0.491 psu for weak mixing (R1.4) and by 0.0222 ± 0.469 psu for strong mixing (R0.6). Clearly, these changes are small compared to the natural variability and also small compared to the variability of the impact itself. In contrast to this negligible reduction scenarios with over-exaggerated wind farm distribution led to reduction in bottom salinity in the Bornholm Channel by 0.1728 ± 0.595 psu for weak mixing (U1.4) and 0.4222 ± 0.560 psu for strong mixing (U0.6).

A statistical analysis of the net salt transport into the Bornholm Sea quantified in terms of density classes reveals that the salt transport in the four highest density classes of 0.2 $\mathrm{kg\,m^{-3}}$ width each are partially or completely vanishing in the scenario with realistic wind farm distribution and strong mixing. However, the relative contribution of these high salinity classes to the net salt inflow is small, since only during short single events thee high densities are obtained.

To investigate in depth an event with a significantly strong impact of offshore wind farms, the scenario with the strongest impact on bottom salinity in the Bornholm Channel has been analysed for the month during which this impact happened. During this month, a passive bottom tracer has been released continuously in the Bornholm Channel and it was found that the tracer intruded in the stratified Bornholm Sea water column about 2 m (58 m instead of 60 m depth) higher when wind farm mixing was considered. This means that in such an extreme month ventilation occurs a few percent of the water depth higher in the water column.

In general, bottom salinities in the Arkona Sea are decreased locally by about up to 0.2 psu for realistic scenarios and by about up to 0.3-0.6 psu, depending whether weak or strong mixing is assumed.

It can be concluded that the impact of realistic wind farm distributions on the Baltic Sea ecosystem, according to the present planning state is insignificant compared to the natural variability. Even if a structure-induced mixing efficiency of twice the best guess is assumed, bottom salinities in the Arkona Sea are decreased only locally by about 0.2 psu. In the most extreme month during the entire simulation period, ventilation of the Bornholm Sea occurred about 2 m higher in the water column. This is in accordance with the finding that only the highest density classes vanish due to wind farm mixing. Those contribute however only little to total ventilation. Although only the impact of cylindric wind farm foundations with diameters of 10 m was quantified, potential increase of structure-induced mixing due to more complex foundations (e.g., jacket constructions) or larger numbers of foundations with smaller diameters (leading to the same area density) was accounted for by the consideration of strong mixing (twice the mixing efficiency of the best guess).

It should however be noted that a coverage of large parts of the Western Baltic Sea with offshore wind farms could lead to more significant impacts, such as bottom salinity decreases in the Bornholm Channel by 0.4222 ± 0.560 psu and local bottom salinity decreases in the Arkona Sea of typically 0.6 psu. Therefore, in case of planned offshore wind farm coverages substantially exceeding the present planning state, the ecological impacts would need to be reassessed.

Chapter 6

Publications arising from the joint project

1. Burchard, H., and H. Rennau, Comparative quantification of physically and numerically induced mixing in ocean models, *Ocean Modelling*, *20*, 293–311, 2008.

2. Burchard, H., F. Janssen, K. Bolding, L. Umlauf, and H. Rennau, Model simulations of dense bottom currents in the Western Baltic Sea, *Cont. Shelf Res.*, *29*, 205–220, 2009.

3. Lass, H. U., V. Mohrholz, M. Knoll, and H. Prandke, Enhanced mixing downstream of a pile in an estuarine flow., *J. Mar. Sys.*, *74*, 505–527, 2008.

4. Melskotte, J.-E., Numerische Simulation einer Zweiphasenströmung, Studienarbeit, University of Rostock, chair of fluid mechanics, Rostock, 2007.

5. Menzel, P., *Turbulente Mischungsvorgänge im Nachlauf einer dichtegeschichteten Zylinderumströmung*, vol. 1, Menzel-Verlag, Ostseebad Kühlungsborn, 2010.

6. Menzel, P., F. Hüttmann, and A. Leder, Schichtkanal zur Untersuchung von Mischungsvorgängen in geschichteten Strömungen hinter einem Kreiszylinder mittels PIV/PLIF, in *Lasermethoden in der Strömungsmesstechnik - 14. Fachtagung der GALA e.V. 2006*, edited by D. Dopheide, H. Müller, V. Strunck, B. Ruck, and A. L. (Hrsg.), pp. 55.1–55.8, GALA e.V., PTB Braunschweig, 2006.

7. Menzel, P., M. Brede, F. Hüttmann, and A. Leder, Experimental investigations of mixing-processes in the wake of a circular cylinder in stratified flows, in *AIP Conf. Proc.*, vol. 914,122, 2007.

8. Mohrholz, V., H. Prandke, and H. U. Lass, Estimation of TKE dissipation rates in dense bottom plumes using a Pulse Coherent Acoustic Doppler Profiler (PC-ADP) - Structure function approach, *J. Mar. Sys.*, *70*, 217–239, 2008.

9. Reissmann, J., H. Burchard, R. Feistel, E. Hagen, H. Lass, V. Mohrholz, N. Nausch, L. Umlauf, and G. Wieczorek, Vertical mixing in the Baltic Sea and consequences for eutrophication - A review, *Progress in Oceanography*, *82*, 47–80, 2009.

10. Rennau, H., and H. Burchard, Quantitative analysis of numerically induced mixing in a coastal model application, *Ocean Dynamics*, *59*, 671–687, 2009.

11. Rennau, H., S. Schimmels, and H. Burchard, On the effect of structure-induced resistance and mixing on inflows into the baltic sea: a numerical model study, *Coast. Eng.*, *doi: 10.1016/j.coastaleng.2011.08.002*, 53–68, 2012.

12. Schimmels, S., Numerical simulation of the influence of circular cylinders on mixing and entrainment in natural density currents, Ph.D. thesis, University of Hannover, Hannover, 2008.

13. Sellschopp, J., L. Arneborg, M. Knoll, V. Fiekas, F. Gerdes, H. Burchard, H. U. Lass, V. Mohrholz, and L. Umlauf, Direct observations of a medium-intensity inflow into the Baltic Sea, *Cont. Shelf Res.*, *26*, 2393–2414, 2006.

14. Szewczyk, A., Observation of the medium-intensity inflow into the Baltic Proper in November 2005 and comparison with the model data, Master's thesis, University of Rostock, 2009.

15. Umlauf, L., and L. Arneborg, Dynamics of rotating shallow gravity currents passing through a channel. Part I: Observation of transverse structure, *J. Phys. Oceanogr.*, *39*, 2385–2401, 2009a.

16. Umlauf, L., and L. Arneborg, Dynamics of rotating shallow gravity currents passing through a channel. Part II: Analysis, *J. Phys. Oceanogr.*, *39*, 2402–2416, 2009b.

17. Umlauf, L., L. Arneborg, H. Burchard, V. Fiekas, H. U. Lass, V. Mohrholz, and H. Prandke, The transverse structure of turbulance in a rotating gravity current, *Geophys. Res. Lett.*, *34*, 2007.

18. Umlauf, L., L. Arneborg, R. Hofmeister, and H. Burchard, Entrainment in shallow rotating gravity currents: A modeling study, *J. Phys. Oceanogr.*, *40*, 1819–1834, 2010.

Bibliography

Adrian, R. J., Scattering particle characteristics and their effect on pulsed laser measurements of fluid flow: speckle velocimetry vs. particle image velocimetry, *Appl. Opt.*, *23*, 1690–1691, 1984.

Adrian, R. J., Twenty years of particle image velocimetry, *Experiments in Fluids*, *39*, 159–169, 2005.

Arakawa, A., and V. R. Lamb, Computational design of the basic dynamical processes of the ucla general circulation model, *Meth. Comput. Phys.*, *17*, 173–263, 1977.

Arneborg, L., V. Fiekas, L. Umlauf, and H. Burchard, Gravity current dynamics and entrainment - a process study based on observations in the Arkona Basin, *J. Phys. Oceanogr.*, *37*, 2094–2113, 2007.

Arntsen, O., Lee waves and hydrodynamical load due to the motion of a submerged horizontal circular cylinder in a three layer fluid, *J. Hydraulic Res.*, *35*, 435 – 453, 1998.

Barker, D. B., and M. E. Fourney, Measuring fluid velocities with speckle patterns, *Opt. Lett.*, *1*, 135–137, 1977.

Batchelor, G., *An Introduction to Fluid Dynamics*, Cambridge Univ. Press, 1967.

Blumberg, A. F., and G. L. Mellor, A description of a coastal ocean circulation model, in *Three dimensional ocean models*, edited by N. S. Heaps, pp. 1–16, American geophysical Union, Washington, D.C., 1987.

BMU, Offshore wind power deployment in Germany, *Tech. rep.*, Federal Ministry for the Environment, Nature Conservation and Nuclear Safety (BMU), Berlin, Germany, 2007.

Bosch, G., Experimentelle und theoretische Untersuchung der instationären Strömung um zylindrische Strukturen, Ph.D. thesis, 1995.

Breuer, M., A challenging test case for large eddy simulation: High reynolds number circular cylinder flow, *International Journal of Heat and Fluid Flow*, *21*, 648 – 654, 2000.

Breuer, M., Direkte numerische Simulation and Large-Eddy Simulation turbulenter Strömungen auf Hochleistungsrechnern, *Tech. rep.*, Berichte aus der Strömungstechnik, Shaker Verlag, Aachen, 2002.

Burchard, H., and H. Baumert, On the performance of a mixed-layer model based on the k-ε turbulence closure, *J. Geophys. Res.*, *100*, 8523–8540, 1995.

Burchard, H., and K. Bolding, GETM – a general estuarine transport model. Scientific documentation, *Tech. Rep. EUR 20253 EN*, European Commission, 2002.

Burchard, H., and R. D. Hetland, Quantifying the contributions of tidal straining and gravitational circulation to residual circulation in periodically stratified tidal estuaries, *J. Phys. Oceanogr.*, 2010, in print.

Burchard, H., and R. Hofmeister, A dynamic equation for the potential energy anomaly for analysing mixing and stratification in estuaries and coastal seas, *Estuar. Coast. Shelf Sci.*, *77*, 679–687, 2008.

Burchard, H., and H. Rennau, Comparative quantification of physically and numerically induced mixing in ocean models, *Ocean Modelling*, *20*, 293–311, 2008.

Burchard, H., K. Bolding, and M. R. Villarreal, GOTM – a general ocean turbulence model. Theory, applications and test cases, *Tech. Rep. EUR 18745 EN*, European Commission, 1999.

Burchard, H., K. Bolding, and M. Villarreal, Three-dimensional modelling of estuarine turbidity maxima in a tidal estuary, *Ocean Dynamics*, *54*, 250–265, 2004.

Burchard, H., H. U. Lass, V. Mohrholz, L. Umlauf, J. Sellschopp, V. Fiekas, K. Bolding, and L. Arneborg, Dynamics of medium-intensity dense water plumes in the Arkona Basin, Western Baltic Sea, *Ocean Dynamics*, *55*, 391–402, 2005.

Burchard, H., F. Janssen, K. Bolding, L. Umlauf, and H. Rennau, Model simulations of dense bottom currents in the Western Baltic Sea, *Cont. Shelf Res.*, *29*, 205–220, 2009.

Cantwell, B., and D. Coles, An experimental study of entrainment and transport in the turbulent near wake of a circular cylinder, *J. Fluid Mech.*, *136*, 321–374, 1983.

Canuto, V., A. Howard, Y. Cheng, and M. Dubovikov, Ocean turbulence. Part I: one-point closure model. Momentum and heat vertical diffusivities, *J. Phys. Oceanogr.*, *31*, 1413–1426, 2001.

Cenedese, C., and C. Adduce, Mixing in density-driven current flowing down a slope in a rotating fluid, *J. Fluid Mech.*, *604*, 369 – 388, 2008.

Chashechkin, Y., and V. Mitkin, Experimental study of a fine structure of 2d wakes and mixing past an obstacle in a continuously stratified fluid, *Dyn. Atmos. Oceans*, *34*, 165–187, 2001.

Cheng, Y., V. M. Canuto, and A. M. Howard, An improved model for the turbulent PBL, *J. Atmos. Sci.*, *59*, 1550–1565, 2002.

Dantec Dynamics, *Flow Manager Software and Introduction to PIV Instrumentation*, Dantec Dynamics A/S, P.O. Box 121, Tonsbakken 18, DK-2740 Skovlunde, publication no. 9040u3625 ed., 2002a.

Dantec Dynamics, *Flow Map®3D-PIV System*, Dantec Dynamics A/S, P.O. Box 121, Tonsbakken 18, DK-2740 Skovlunde, publication no. 9040u4113 ed., 2002b.

Dudderar, T. D., and P. G. Simpkins, Laser speckle photography in a fluid medium, *Nature*, *270*, 45–47, 1977.

Ekman, V., On dead water, *Sc. Res.*, *V*, 152, 1906.

Ellison, T. H., and J. S. Turner, Turbulent entrainment in stratified flows, *J. Fluid Mech.*, *6*, 423–448, 1959.

Farmer, D., and J. Møller, Measurements and modelling in the Great Belt: a unique opportunity for model verification, in *Physical Oceanography of sea straits*, edited by L. Pratt, vol. 318 of *NATO ASI series C*, pp. 125–152, 1989.

Feistel, R., G. Nausch, W., V. Mohrholz, E. Lysiak-Pastuszak, T. Seifert, W. Matthäus, S. Krüger, and I. S. Hansen, Warm waters of summer 2002 in the deep Baltic Proper, *Oceanologia*, *45*, 571–592, 2003.

Feistel, R., G. Nausch, T. Heene, J. Piechura, and E. Hagen, Evidence for a warm water inflow into the Baltic Proper in summer 2003, *Oceanologia*, *46*, 581–598, 2004.

Feistel, R., G. Nausch, and E. Hagen, Unsusual Baltic inflow activity 2002/03 and varying deep water properties, *Oceanologia*, *48*, 21–35, 2006.

Fennel, W., and H. U. Lass, *Analytical theory of forced oceanic waves*, Akademie-Verlag, Berlin, 1989.

Fer, I., Scaling turbulent dissipation in an Arctic fjord, *Deep Sea Res., Part II*, *53*, 77 – 95, 2006.

Ferziger, J., and M.Peric, *Computational Methods for Fluid Dynamics*, Springer-Verlag, Berlin, Heideberg, 2002.

Fletcher, C., *Computational Techniques for Fluid Dynamics, Second Edition, Volume I+II*, Springer-Verlag, Berlin, Heidelberg, 1991.

Fluent, Fluent 6.2 user's guide, 2005.

Franke, R., Numerische Berechnung der instationären Wirbelablösung hinter zylindrischen Körpern, Ph.D. thesis, 1991.

Fröhlich, J., *Large Eddy Simulation turbulenter Strömungen*, Teubner Verlag, Wiesbaden, 2006.

Gill, A., *Atmosphere-Ocean Dynamics.*, Academic Press, New York, 1982, p. 662.

Gölling, B., Experimentelle Untersuchungen des laminar-turbulenten Überganges der Zylindergrenzschichtströmung, Ph.D. thesis, University of Göttingen, 2001.

Green, M., and A. Stigebrandt, Instrument-induced linear flow resistance in øresund, *Cont. Shelf Res.*, *22*, 435–444, 2002.

Griffies, S., R. C. Pacanowski, M. Schmidt, and V. Balaji, Tracer conservation with an explicit free surface method for z-coordinate ocean models, *Mon. Weather Rev.*, *129*, 1081 – 1098, 2001.

Grousson, R., and S. Mallick, Study of flow pattern in a fluid by scattered laser light, *Appl. Opt.*, *16*, 2334–2336, 1977.

Gustafsson, B., and H. Andersson, Modeling the exchange of the Baltic Sea from the meridional atmospheric difference across the North Sea, *J. Geophys. Res.*, *106*, 19,731–19,744, 2001.

Hansen, N.-E. O., and J. S. Møller, Zero blocking solution for the Great Belt Link, in *Physical Oceanography of sea straits*, edited by L. Pratt, vol. 318 of *NATO ASI series C*, pp. 153–170, 1989a.

Hansen, N.-E. O., and J. S. Møller, Zero blocking solution for the Great Belt Link, in *Physical Oceanography of sea straits*, edited by L. Pratt, vol. 318 of *NATO ASI series C*, pp. 153–170, 1989b.

Henderson, R. D., Nonlinear dynamics and pattern formation in turbulent wake transition, *J. Fluid Mech.*, *352*, 65–112, 1997.

Heywood, K., E. Barton, and S. J.H., The effect of flow disturbances by an oceanic island, *J. Mar. Res*, *48*, 55 – 73, 1990.

Hofmeister, R., H. Burchard, and J.-M. Beckers, Non-uniform adaptive vertical grids for 3D numerical ocean models, *Ocean Modelling*, 2010, accepted for publication.

Holford, J., and P. Linden, Turbulent mixing in a stratified fluid, *Dyn. Atmos. Oceans*, *30*, 173 – 198, 1999.

Holt, S. E., J. R. Koseff, and J. H. Ferziger, A numerical study of the evolution and structure of homogeneous stably stratified sheared turbulence, *J. Fluid Mech.*, *237*, 499–540, 1992.

Hoyer, H., Froudezahlabhängigkeit der Mischung im Nachlauf eines Zylinders in geschichteter Meerwasserströmung, Studienarbeit, University of Rostock, Chair of Fluid Mechanics, Rostock, 2008.

Hughes, G. O., and R. W. Griffiths, A simple convective model of the global overturning circulation including effects of entrainment into sinking regions, *Ocean Model*, *12*, 46–79, 2006.

Ilicak, M., T. M. Özgökmen, H. Peters, H. Z. Baumert, and M. Iskandarani, Performance of two-equation turbulence closures in three-dimensional simulations of the Red Sea overflow, *Ocean Modelling*, *24*, 122–139, 2008.

Jakobsen, F., M. J. Lintrup, and J. S. Møller, Observations of the specific resistance in Öresund, *Nordic Hydrology*, *28*, 217–232, 1997.

Janssen, F., T. Neumann, and M. Schmidt, Inter-annual variability in cyanobacteria blooms in the Baltic Sea controlled by wintertime hydrographic conditions, *Mar. Ecol. Prog. Ser.*, *275*, 59 – 68.

Jensch, M., M. Brede, F. Hüttmann, U. Grebin, K. Bunse, and A. Leder, Untersuchung der instationären Strömungsstrukturen am einseitig begrenzten Kreiszylinderstumpf, in *Lasermethoden in der Strömungsmesstechnik, Fachtagung der GALA e.V. 2009*, vol. 17, University of Erlangen, 2010.

Johnson, G. C., T. Sanford, and M. Baringer, Stress on the Mediterranean outflow plume: part I. Velocity and water property measurements, *J. Phys. Oceanogr.*, *24*, 2072 – 2083, 1994.

Kappler, M., Experimentelle Untersuchung der Umströmung von Kreiszylindern mit ausgeprägten dreidimensionalen Effekten, Ph.D. thesis, University of Karlsruhe, 2000.

Keane, R. D., and R. J. Adrian, Theory of cross-correlation analysis of piv images, *Applied Scientific Research*, *49*, 191–215, 1992.

Kouts, T., and A. Omstedt, Deep water exchange in the Baltic Proper, *Tellus A*, *11*, 311–324, 1993.

Large, W., and S. Pond, Open ocean momentum flux measurements in moderate to strong winds, *J. Phys. Oceanogr.*, *11*, 324 – 336, 1981.

Lass, H., and W. Matthäus, On temporal wind variation forcing salt water into the Baltic Sea, *Tellus*, *48 A*, 1996.

Lass, H. U., Über mögliche Auswirkungen von Windparks auf den Wasseraustausch zwischen Nord- und Ostsee, in *12. Meeresumwelt-Symposium 2002*, pp. 121–132, Bundesamt für Seeschifffahrt und Hydrographie (BSH), Hamburg and Rostock, 2003.

Lass, H. U., and V. Mohrholz, On the dynamics and mixing of inflowing salt-water in the Arkona Sea, *J. Geophys. Res.*, *108*, 3042, doi: 10.1029/2002JC001,465, 2003.

Lass, H. U., V. Mohrholz, and T. Seifert, On pathways and residence time of saltwater plumes in the Arkona Sea, *J. Geophys. Res.*, *110*, doi:10.1029/2004JC002,848, 2005.

Lass, H. U., V. Mohrholz, M. Knoll, and H. Prandke, Enhanced mixing downstream of a pile in an estuarine flow., *J. Mar. Sys.*, *74*, 505–527, 2008.

Leder, A., *Abgelöste Strömungen: Physikalische Grundlagen*, Vieweg, Braunschweig, Wiesbaden, 1992.

Lehmann, A., P. Lorenz, and D. Jacob, Modelling the exceptional Baltic Sea inflow events in 2002-2003, *Geophys. Res. Lett.*, *31*, 2004.

Leonard, B., The ULTIMATE conservative difference scheme applied to unsteady one-dimensional advection, *Comput. Methods Appl. Mech. Eng.*, *88*, 17–74, 1991.

Liljebladh, B., and A. Stigebrandt, Observations of the deepwater flow into the Baltic Sea, *J. Geophys. Res.*, *101*, 8895–8911, 1996.

MacCready, P., and P. Rhines, Slippery bottom boundary layers on a slope, *J. Phys. Oceanogr.*, *23*, 5–22, 1993.

Matthäus, W., and H. Franck, Characteristics of major Baltic inflows - a statistical analysis, *Continental Shelf Research*, *12*, 1375–1400, 1992.

McComas, C., and P. Müller, Time scales of resonant interactions among oceanic internal waves, *J. Phys. Oceanogr.*, *11*, 139 – 147, 1981.

Meier, H., R. Döscher, A. Coward, J. Nycander, and K. Döös, RCO - Rossby Centre regional Ocean climate model: model description (version 1.0) and first results from the hindcast period 1992/93, *Tech. rep.*, Reports Oceanography No. 26, Swedish Meteorological and Hydrological Institute, Norrköoping, Sweden., 1999.

Meier, M. H. E., et al., Ventilation of the Baltic Sea deep water: A brief review of present knowledge from observations and models, *Oceanologia*, *48*, 133–164, 2006.

Melskotte, J.-E., Numerische Simulation einer Zweiphasenströmung, Studienarbeit, University of Rostock, chair of fluid mechanics, Rostock, 2007.

Mengler, C., *Grobstruktursimulation der Strömungs- und Mischungsfelder komplexer, anwendungsnaher Konfigurationen*, VDI-Verlag, Düsseldorf, 2002.

Menzel, P., *Turbulente Mischungsvorgänge im Nachlauf einer dichtegeschichteten Zylinderumströmung*, vol. 1, Menzel-Verlag, Ostseebad Kühlungsborn, 2010.

Menzel, P., F. Hüttmann, and A. Leder, Schichtkanal zur Untersuchung von Mischungsvorgängen in geschichteten Strömungen hinter einem Kreiszylinder mittels PIV/PLIF, in *Lasermethoden in der Strömungsmesstechnik - 14. Fachtagung der GALA e.V. 2006*, edited by D. Dopheide, H. Müller, V. Strunck, B. Ruck, and A. L. (Hrsg.), pp. 55.1–55.8, GALA e.V., PTB Braunschweig, 2006.

Menzel, P., M. Brede, F. Hüttmann, and A. Leder, Experimental investigations of mixing-processes in the wake of a circular cylinder in stratified flows, in *AIP Conf. Proc.*, vol. 914,122, 2007.

Møller, J. S., N.-E. O. Hansen, and F. Jakobsen, Mixing in stratified flow caused by obstacles, *Coast. Eng.*, *4*, 97–111, 1997.

Mohrholz, V., J. Dutz, and G. Kraus, The impacts of exceptionally warm summer inflow event on the environmental conditions of the Baltic Sea, *J. Mar. Sys.*, *60*, 285–301, 2006.

Mohrholz, V., H. Prandke, and H. U. Lass, Estimation of TKE dissipation rates in dense bottom plumes using a Pulse Coherent Acoustic Doppler Profiler (PC-ADP) - Structure function approach, *J. Mar. Sys.*, *70*, 217–239, 2008.

Morales Maqueda, M. A., and G. Holloway, Second-order moment advection scheme applied to Arctic Ocean simulation, *Ocean Modelling*, *14*, 197–221, 2006.

Munk, W. H., and E. R. Anderson, Notes on the theory of the thermocline, *J. Mar. Res.*, *3*, 276–295, 1948.

Neumann, T., W. Fennel, and C. Kremp, Experimental simulations with an ecosystem model of the Baltic Sea: A nutrient load reduction experiment, *Global Biogeochemical Cycles*, *16*, 10.1029/2001GB001,450, 2002.

Osborn, T., Estimates of the local rate of the vertical diffusion from dissipation measurements, *J. Phys. Oceanogr.*, *10*, 83 – 89, 1980.

Ozono, S., N. Aota, and Y. Ohya, Stably stratified flow around a horizontal rectangular cylinder in a channel of a finite depth, *J. Wind Eng. Ind. Aerodyn.*, *67 - 68*, 103 – 116, 1997.

Paka, V., V. Zhurbas, N. Golenko, and L. Stefantzev, Effect of the Ekman transport on the overflow of saline waters through the Słupsk Furrow in the Baltic Sea, *Izv. Atmos. Ocean. Phys.*, *34*, 641 – 648, 1998.

Peters, H., and W. Johns, Bottom layer turbulence in the Red Sea outflow plume, *J. Phys. Oceanogr.*, *36*, 1763 – 1785, 2006.

Peters, H., and W. E. Johns, Mixing and entrainment in the Red Sea outflow plume: part II. Turbulence characteristics, *J. Phys. Oceanogr.*, *35*, 584 – 600, 2005.

Pickering, C. J. D., and N. Halliwell, LSP and PIV: photographic film noise, *Appl. Opt.*, *23*, 2961–2969, 1984.

Pietrzak, J., The use of TVD limiters for forward-in-time upstream-biased advection schemes in ocean modeling, *Mon. Weather. Rev.*, *126*, 812–830, 1998.

Prandke, H., K. Holtsch, and A. Stips, MITEC technology development: The microstructure/turbulence measuring system mss, *Tech. Rep. EUR 19733 EN*, European Commission, Joint Research Centre, Ispra, Italy, 2000.

Prasad, A. K., and R. J. Adrian, Stereoscopic particle image velocimetry applied to liquid flows, *Experiments in Fluids*, *15*, 49–60, 1993.

Reissmann, J., H. Burchard, R. Feistel, E. Hagen, H. Lass, V. Mohrholz, N. Nausch, L. Umlauf, and G. Wieczorek, Vertical mixing in the Baltic Sea and consequences for eutrophication - A review, *Progress in Oceanography*, *82*, 47–80, 2009.

Rennau, H., and H. Burchard, Quantitative analysis of numerically induced mixing in a coastal model application, *Ocean Dynamics*, *59*, 671–687, 2009.

Rennau, H., S. Schimmels, and H. Burchard, On the effect of structure-induced resistance and mixing on inflows into the baltic sea: a numerical model study, *Coast. Eng.*, *doi: 10.1016/j.coastaleng.2011.08.002*, 53–68, 2012.

Reynolds, W. C., and A. K. M. F. Hussain, The mechanics of an organized wave in turbulent shear flow. part 3: Theoretical models and comparisons with experiments, *J. Fluid Mech.*, *54*, 263 – 288, 1972.

Richter, F., Experimentelle Untersuchungen zur Charakterisierung der Strömungs- und Turbulenzstrukturen im Nachlauf eines Kreiszylinderstumpfes unter Berücksichtigung der Zentrifugalbeschleunigung, Ph.D. thesis, University of Rostock, Verlagshaus Monsenstein und Wannerdat, Münster, 2005.

Rodi, W., Turbulence models and their application in hydraulics, *Tech. rep.*, Int. Assoc. for Hydraul. Res., Delft, The Netherlands, 1980.

Schimmels, S., Numerical simulation of the influence of circular cylinders on mixing and entrainment in natural density currents, Ph.D. thesis, University of Hannover, Hannover, 2008.

Schlichting, H., and K. Gersten, *Grenzschicht-Theorie*, vol. 10. überarbeitete Auflage, Springer-Verlag, Berlin, Heidelberg, 2006.

Schumann, U., and T. Gerz, Turbulent mixing in stably stratified shear flows, *J. Appl. Meteorol.*, *34*, 33–48, 1995.

Sellschopp, J., A towed CTD chain for two-dimensional high resolution hydrography, *Deep Sea. Res. I*, *44*, 147 – 165, 1997.

Sellschopp, J., L. Arneborg, M. Knoll, V. Fiekas, F. Gerdes, H. Burchard, H. U. Lass, V. Mohrholz, and L. Umlauf, Direct observations of a medium-intensity inflow into the Baltic Sea, *Cont. Shelf Res.*, *26*, 2393–2414, 2006.

Shchepetkin, A. F., and J. C. McWilliams, A method for computing horizontal pressure-gradient force in an oceanic model with a nonaligned vertical coordinate, *J. Geophys. Res.*, *108*, 10.1029/2001JC001,047, 2003.

Shchepetkin, A. F., and J. C. McWilliams, The regional oceanic modelling system (ROMS): a split-explicit, free-surface, topography-following-coordinate oceanic model, *Ocean Modelling*, *9*, 347–404, 2005.

Shih, L., J. Koseff, J. Ferziger, and C. Rehmann, Scaling and parameterization of stratified homogenous turbulent shear flow, *J. Fluid Mech.*, *412*, 1 – 20, 2000.

Simpson, J., The shelf sea fronts: implication of their existence and behaviour, *Phil. Trans. R. Soc. Lond. A*, *302*, 531 – 546, 1981.

Smagorinsky, J., General circulation experiments with the primitive equations, *Mon. Weather Rev.*, *93*, 99–165, 1963.

Smolarkiewicz, P., A simple positive definite advection scheme wih small implicit diffusion, *Mon. Weather Rev.*, *111*, 479–486, 1983.

Stigebrandt, A., A model for the seasonal pycnocline in rotating systems with application to the Baltic Proper, *J. Phys. Oceanogr.*, *15*, 1392 – 1404, 1985.

Stigebrandt, A., Bridge-induced flow reduction in sea straits with reference to effects of a planned bridge across øresund, *Ambio*, *21*, 130–134, 1992.

Stigebrandt, A., Regulation of vertical stratification, length of stagnation periods and oxygen conditions in the deeper deepwater of the Baltic proper, *Meereswissenschaftliche Berichte*, *54*, 69 – 80, 2003.

Sumer, B. M., and J. Fredsøe, *Hydrodynamics around cylindrical structures*, World Scientific, Singapure, 1997.

Sumer, B. M., M. Christiansen, and J. Fredsøe, The horseshoe vortex and vortex shedding around a vertical wall-mounted cylinder exposed to waves, *J. Fluid Mech.*, *332*, 41–70, 1997.

Svensson, U., and K. Häggkvist, A two-equation turbulence model for canopy flows, *Journal of Wind Engineering and Industrial Aerodynamics*, *35*, 201–211, 1990.

Szewczyk, A., Observation of the medium-intensity inflow into the Baltic Proper in November 2005 and comparison with the model data, Master's thesis, University of Rostock, 2009.

TRM, Energy strategy 2025. perspectives to 2025 and draft action plan for the future electricity infrastructure, *Tech. rep.*, The Danish Ministry of Transport and Energy, Copenhagen, Denmark, 2005.

Turner, J. S., Turbulent entrainment: The development of the entrainment assumption, and its application to geophysical flows, *J. Fluid Mech.*, *173*, 431–471, 1986.

Umlauf, L., A note on the description of mixing in stratified layers without shear in large-scale ocean models, *J. Phys. Oceanogr.*, *39*, 3032–3039, 2009.

Umlauf, L., and L. Arneborg, Dynamics of rotating shallow gravity currents passing through a channel. Part I: Observation of transverse structure, *J. Phys. Oceanogr.*, *39*, 2385–2401, 2009a.

Umlauf, L., and L. Arneborg, Dynamics of rotating shallow gravity currents passing through a channel. Part II: Analysis, *J. Phys. Oceanogr.*, *39*, 2402–2416, 2009b.

Umlauf, L., and H. Burchard, Second-order turbulence closure models for geophysical boundary layers. A review of recent work, *Cont. Shelf Res.*, *25*, 795–827, 2005.

Umlauf, L., and U. Lemmin, Inter-basin exchange and mixing in the hypolimnion of a large lake: the role of long internal waves, *Limnol. Oceanogr.*, *50*, 1601–1611, 2005.

Umlauf, L., H. Burchard, and K. Hutter, Extending the k-ω turbulence model towards oceanic applications, *Ocean Modelling*, *5*, 195 – 218, 2003.

Umlauf, L., H. Burchard, and K. Bolding, General Ocean Turbulence Model. Source code documentation, *Tech. Rep.*, *63*, 2005.

Umlauf, L., L. Arneborg, H. Burchard, V. Fiekas, H. U. Lass, V. Mohrholz, and H. Prandke, The transverse structure of turbulence in a rotating gravity current, *Geophys. Res. Lett.*, *34*, L08,601, doi:10.1029/2007GL029,521, 2007.

Umlauf, L., L. Arneborg, R. Hofmeister, and H. Burchard, Entrainment in shallow rotating gravity currents: a modelling study, *J. Phys. Oceanogr.*, *40*, 1819–1834, 2010.

Wåhlin, A. K., Topographic steering of dense currents with application to submarine canyons, *Deep-Sea Res. I*, *49*, 305–320, 2002.

Wåhlin, A. K., Downward channeling of dense water in topographic corrugations, *Deep-Sea Res. I*, *51*, 577–590, 2004.

Wåhlin, A. K., and C. Cenedese, How entraining density currents influence the ocean stratification, *Deep-Sea Research II*, *53*, 172–193, 2006.

Wesson, J. C., and M. Gregg, Mixing at Camarinal Sill in the Strait of Gibraltar, *J. Geophys. Res.*, *99(C5)*, 9847 – 9878, 1995.

Wilcox, D. C., Reassessment of the scale-determining equation for advanced turbulence models, *AIAA Journal*, *26*, 1299–1310, 1988.

Wilcox, D. C., *Turbulence Modeling for CFD*, 2 ed., DCW Industries, 1998.

Willert, C. E., and M. Gharib, Digital particle image velocimetry, *Experiments in Fluids*, *10*, 181–193, 1991.

Witte, M., Stereo-MikroPIV-Untersuchung mikrofluidischer Strömungen im Nachlauf einer Seehundvibrisse, Master's thesis, University of Rostock, Chair of Fluid Mechanics, Rostock, 2007.

Wyrtki, K., Die Dynamik die Wasserbewegungen in Fehmarnbelt I, *Kieler Meeresforsch.*, *9*, 155–190, 1954.

Xu, Y., H. J. S. Fernando, and D. L. Boyer, Turbulent wakes of stratified flow past a cylinder, *Phys. Fluids*, *7*, 2243–2255, 1995.

Zdravkovich, M. M., *Flow around circular cylinder*, vol. 1 fundamentals, Oxford University Press, Oxford, 1997.